Qcd and spectroscopy beyond the quark model: the search for the lightest scalar glueball

Au, King Lun

'QCD and spectroscopy beyond the quark model: the search for the lightest scalar glueball'

A thesis submitted for the Degree of Doctor of Philosophy in the Department of Physics University of Durham

King Lun Au, BA (Oxon)

Graduate Society

Durham

September 1986

'QCD and spectroscopy beyond the quark model: the search for the lightest scalar glueball'

K.L.Au

ABSTRACT

The naive quark model has been remarkably successful in classifying the many hadron states so far discovered. The underlying theory for these successes is QCD. This theory, however, not only suggests states made purely of quarks, but also those containing glue. Whether these pure glue states are observable depends on the validity of the notion of valence gluons which has been explored in the earlier part of this thesis. My studies show that the hard and soft gluon components can be distinguished and behave as valence and sea constituents in glueballs. These glueballs, and especially the ground state, must be found in order to establish QCD as a successful theory of strong interactions. Because of the inevitability of mixing, particularly for low mass states, simple parton configurations cannot be expected in practice, so supposedly characteristic decay patterns may not serve as a guide to the existence of new states. The only reliable way to establish the intrusion of extra dynamics is to count the number of states with given quantum numbers. An extensive coupled channel analysis of results on $\pi\pi$ and $K\bar{K}$ final states interactions with I=0 0^{++} quantum numbers below 1.7 GeV has been performed incorporating new data on $pp \to pp\ \pi\pi(K\bar{K})$. Though no poles are imposed on these data, we find that 3 distinct resonances emerge in the 1 GeV region, when the naive quark model requires but two. This clearly indicates for the first time definite evidence for dynamics beyond the quark model in the 0^{++} channel. Our results are consistent with the presence of the ground state glueball $S_1(993)$ together with ideally mixed quark model states $S_2(988)$ and $\varepsilon(900)$.

Acknowledgements

I would like to sincerely thank my supervisor Mike Pennington for his friendship, guidance, advice, collaboration and support throughout the period in which this research was undertaken and for reading the manuscript.

I would also like to thank David Morgan for many enjoyable and fruitful collaborations.

I thank the members of the particle physics group at Durham - Alan Martin, Peter Collins, Fred Gault, Chris Maxwell, James Stirling, Mike Whalley, Stuart Grayson, Neil Speirs, Martin Carter, Tony Peacock, Yanos Michopoulos, Simon Webb and Nick Brown - for providing the friendly atmosphere in which this work was carried out.

Finally and by no means least I would like to thank my parents, my uncle and aunt, Johnny Cheng, Donald Liu and Stephen Pan for their continual support and encouragement. This thesis is dedicated to my parents.

物理

WU LI

CONTENTS

CHAPTER ONE

QCD AND GLUEBALLS

1.1 INTRODUCTION TO QCD

The role of particle physics is to understand the fundamental laws of nature and to unify them into one theory. Any Grand Unification candidate must embed in it the four known fundamental forces ---- Electromagnetism, Weak and Strong interactions plus Gravity. Internal symmetry and gauge invariance are believed to be the underlying principle of physics.

The idea of internal symmetry first appeared when it was realised that the nucleon-nucleon force is charge-independent by observing that nn, pn and pp forces are equal apart from small Coulomb corrections. Therefore the proton and neutron appear to be identical in nuclear reactions and the small difference in their mass is attributable to their different behaviour with respect to electromagnetic interactions because of their charge difference. This internal symmetry is expressed by labelling the proton and neutron as two possible internal 'isospin' states of a 'nucleon'. In analogy with the spin of an electron this isospin symmetry corresponds to the Lie Group SU(2). All strongly interacting particles form multiplets using Heisenberg's concept of isospin [1]. Extending this internal symmetry idea to describe the proliferation of nucleons, Murray Gell-Mann and Y. Ne'eman independently

discovered the higher Lie Algebra SU(3) of flavour [2]. The basic entity in this SU(3) is called a quark [3][4] with spin-1/2 and has three different flavours u, d and s. These quarks carry fractional charges and belong to the fundamental representation of SU(3). The classification of baryons being made up of three quarks into decuplet octet and singlet, and mesons made up of a quark and an antiquark into nonets is called the Eightfold way. The u and d quarks that are degenerate in mass form an isospin multiplet. The heavier s quark carries the quantum number called strangeness which is conserved in strong interactions, but not in weak, and is required to explain the long lifetime of Λ and K particles.

This simple quark model suffers from the following difficulties;

1. It does not explain the absence of fractional charged particles,
2. The wavefunctions for the $J^P = \frac{3^+}{2}$ baryon decuplet are in conflict with Fermi-Dirac spin statistics.

The solution to these difficulties is to give each quark flavour a hidden colour symmetry with Lie Algebra SU(3) of colour [5]. The quarks are in the fundamental representation and only colour singlet states are allowed to exist as asymptotic states (this is the colour confinement hypothesis). From the products of such representation we see that the simplest singlet configurations are $q\bar{q}$ and qqq, since

$$3 \times \bar{3} = 1 + 8 \text{ and } 3 \times 3 \times 3 = 1 + 8 + 8 + 10 .$$

However there are other colour singlet configurations notably the four-quark $q\bar{q}q\bar{q}$ states which have been studied elsewhere [6]. While the badly broken flavour symmetry SU(N) depends on N the number of quark

flavours discovered, the $SU(3)_c$ is taken to be exact such that the singlet configurations of quarks are independent of the number of flavours. The three degrees of colour freedom are supported by experimental evidence e.g. the R ratio of cross sections of $e^+e^- \rightarrow$ hadrons over $e^+e^- \rightarrow \mu^+\mu^-$. It is therefore reasonable to postulate that $SU(3)_c$ is responsible for the strong interaction. This is accomplished by making $SU(3)_c$ a gauge symmetry.

The idea of gauge symmetry originates from the invariance of the classical Maxwell equations under

$$A_\mu(x) \rightarrow A'_\mu(x) = A_\mu(x) - \partial_\mu\theta(x) \qquad (1.1)$$

which is known as a gauge transformation. The vector potential or gauge field A_μ appears linearly with the space-time derivative in quantum electrodynamics, QED [7]. Requiring the same gauge freedom on A_μ as in the classical theory leads to an accompanying local phase transformation for the wavefunction

$$\psi(x) \rightarrow \psi'(x) = \exp[ie\theta(x)]\psi(x) \qquad (1.2)$$

where e is the electric charge and $\theta(x)$ is a local phase factor. This is equivalent to saying that QED has a local U(1) gauge symmetry and the electromagnetic interaction is mediated by the corresponding gauge field. The generalization of this concept to non-abelian gauge symmetries was made by Yang and Mills [8]. The interactions corresponding to these symmetries are mediated by a set of gauge fields, the analogue of A_μ in QED, which carry internal symmetry labels. The

strong interactions can be thought of as an internal $SU(3)_c$ gauge field theory known as Quantum Chromo-Dynamics or QCD [9][10]. The Lagrangian of QCD with N_f flavours of quark is

$$L_{QCD} = -(1/4)G^a_{\mu\nu}G^{a\mu\nu} + \sum_k^{N_f} q^i_k(i\gamma_\mu D^{ij}_\mu - m_k)q^j_k \qquad (1.3)$$

where the quarks fields q_i being in the fundamental representation of $SU(3)_f$ have i = 1, 2, 3, while the gauge fields are in the adjoint representation so a = 1,....,8 .

The covariant derivative is

$$D^\mu_{ij} = \delta_{ij}\partial^\mu - igT^a_{ij}A^{a\mu}, \qquad [T^a,T^b] = if^{abc}T^c \qquad (1.4)$$

T^a is the a^{th} generator of $SU(3)_c$ and g is the bare coupling.

The field strength tensor is

$$G^a_{\mu\nu} = \partial_\mu A^a_\nu - \partial_\nu A^a_\mu + gf^{abc}A^b_\mu A^c_\nu \qquad (1.5)$$

where f^{abc} are the structure constants of $SU(3)_c$. The QCD Lagrangian must be invariant under the local gauge transformation,

$$q_i(x) \to \exp(i\theta^a(x)T^a)q_i(x) \qquad (1.6)$$

which, for infinitesimal $\theta^a(x)$ lead to the following requirements,

$$A^a_\mu(x) \to A^a_\mu(x) - f^{abc}\theta^b(x)A^c_\mu(x) - (1/g)\partial_\mu\theta^a(x) \qquad (1.7)$$

This implies that the covariant derivative is a singlet. The gauge fields A^a_μ are in the adjoint representation so that they form a singlet in tensor products with the generators of the group T^a, which are also adjoint. Because of gauge invariance, a mass term $m^2A^a_\mu A^{a\mu}$ is not allowed

in the Lagrangian. For the same reason a massive photon field is forbidden in QED.

It seems at first sight that both QCD and QED are long range interactions because their gauge fields or vector bosons are massless. However the work of Politzer, Gross and Wilczek, showed that the coupling of QCD has a different energy behaviour from QED and offers a possible resolution to the observed confinement of quarks and gluons in hadrons [11]. The difference is attributed to their different quantum corrections in the two theories. Equipped with Feynman rules [7][12] quantum loop corrections to the bare quantities in the theory can be calculated perturbatively. The ultra-violet divergences in loop momentum integrals are removed by mass renormalization [13] (the infinite bare mass is made finite by cancelling with quadratic divergences) and rescaling of the fields (the logarithmic divergences can be written as a multiplicative factor) [14]. Because Green's functions are obtained from the time ordered product of the field operators, renormalized (finite) one particle irreducible (1PI) Green's functions are related to the bare 1PI Green's functions by multiplicative factors. As the bare Green's functions are independent of the momentum cut off in loop integrals, one obtains the familiar Stueckelberg-Peterman renormalization group equation RGE [15] for the renormalized Green's functions. The multiplicative renormalizability implies that divergences can be removed order by order by adding counterterms to the original Lagrangian. All these are valid only in the perturbative region where loop corrections are small. A natural

renormalization scheme is to impose that the effective mass and coupling at energy scale μ^2 be the same as those measured experimentally. The coupling α_s at a different energy Q is then given by

$$\alpha_s(Q^2) = \alpha_s(\mu^2) - \frac{\beta_0}{4\pi}\alpha_s(\mu^2)^2 \ln\frac{Q^2}{\mu^2} + (\frac{\beta_0}{4\pi})^2\alpha_s(\mu^2)^3\ln^2(\frac{Q^2}{\mu^2}) - \ldots\ldots \quad (1.8)$$

providing $\alpha_s(\mu^2)\ln(Q^2/\mu^2) << 1$, where

$$\alpha_s(Q^2) = \frac{g^2(Q^2)}{4\pi} \qquad , \qquad \beta_0 = 11 - \frac{2N_f}{3} \qquad \text{for SU(3)}$$

and is the 1 loop contribution to the β-function in the RGE.

The leading logarithm terms $\beta_0\alpha_s(\mu^2)\ln(Q^2/\mu^2)$ are resummed to give the running coupling constant

$$\alpha_s(Q^2) = \frac{4\pi}{\ln(Q^2/\Lambda^2)} \quad (1.9)$$

where Λ is to be determined experimentally. Therefore for $N_f < 17$

$$\beta = 4\pi \frac{\partial\alpha_s(Q^2)}{\partial \ln Q^2} \quad (1.10)$$

$$\simeq -\beta_0\alpha_s(Q^2)^2 < 0 \quad (1.11)$$

This leads to the phenomenon of asymptotic freedom; the coupling decreases as the momentum Q increases. QCD is therefore a renormalizable quantum theory [16] with asymptotic freedom. The asymptotically free nature of QCD is believed to be the theoretical justification for the success of the parton model.

1.2 INTRODUCTION TO THE PARTON MODEL

Deep inelastic scattering reveals that at large momentum ($Q > 3$ GeV) the charge of the target proton is concentrated in 'parton-like' free constituents [17]. These structureless particles, called partons [4][18], have the electromagnetic and weak interaction properties of the flavour quarks in the quark model. Each parton of flavour i carries a fraction x of the hadron momentum with probability $q_i(x)$. Measurement of the differential cross-section for deep inelastic electron scattering allows two structure functions to be determined in the standard way [4][10]. In terms of the charged parton distribution functions, these structure functions are simply

$$F_1(x) = \frac{1}{2}\Sigma\, e_i q_i(x) \qquad (1.12)$$

$$F_2(x) = x\Sigma\, e_i q_i(x) \qquad (1.13)$$

where e_i is the charge of the parton of flavour i and the Callan-Gross relation $F_2(x) = 2xF_1(x)$ [19] is a consequence of the spin-1/2 nature of quarks.

If this simple parton picture were the whole story, structure functions determined from experiment would be independent of the momentum Q of the probing virtual photon. For once the wavelength is short enough ($Q > 3$ GeV) to resolve the individual partons inside the hadron, making the wavelength still shorter would not reveal more structure. This is known as Bjorken scaling [20]. However, it is not

what experiment reveals. As Q increases we observe:

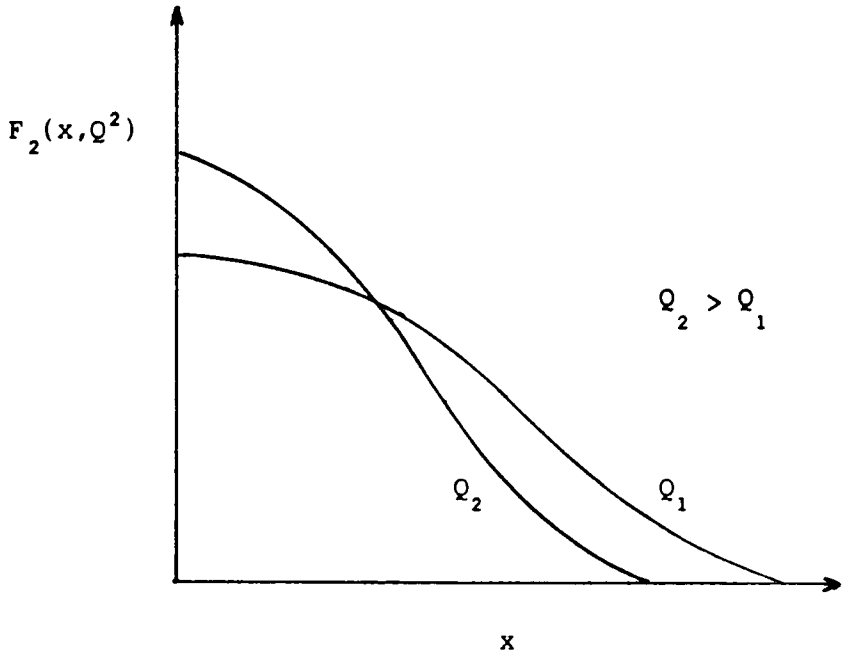

QCD naturally explains such deviations from Bjorken scaling, for gluons and $q\bar{q}$ pairs are created with ever increasing probability as the momentum of the probe increases, finding partons within partons. Because of the asymptotically free nature of QCD, perturbation theory can be used to compute the way in which this happens. This leads to the Altarelli-Parisi (A-P) evolution equations (see Section 2.2).

Intuitively,

$$q_i(x,Q^2) = q_i(x) + dq_i(x,Q^2) \tag{1.14}$$

$$g(x,Q^2) = g(x) + dg(x,Q^2) \tag{1.15}$$

where $g(x,Q^2)$ is the probability that a gluon carries a fraction x of the hadron momentum defined analogously to the quark probability distributions, $q_i(x,Q^2)$. The Q^2 dependence can be expressed in terms of

a set of splitting functions $P_{ba}(z)$, $z = x/y$, which are related to the probability of finding a daughter parton of type b with momentum fraction x in a parent parton of type a which has momentum fraction y. These splitting functions can be computed from the appropriate QCD Feynman diagrams which are the origin of the Q^2 dependence. The explicit form of these splitting functions will be discussed in Chapter 2 where we consider deep inelastic scattering on a glueball state.

1.3 GLUONIUM

1.3.1 Introduction

The non-Abelian nature of SU(3) of colour leads to the existence of terms $gf^{abc}\partial_\mu A_\nu{}^a A^b{}_\mu A^c{}_\nu$ and $(1/4)g^2 f^{abc} f^{adc} A_\mu{}^b A_\nu{}^c A^d{}_\mu A^e{}_\nu$ in the pure gauge sector from the TrG·G term of the QCD Lagrangian which involves self-coupling of the gauge bosons. The colour singlet excitations of these self-coupling gauge bosons form a particle spectrum called GLUEBALLS [21]. At first sight it seems that glueballs are simpler objects for study than quark mesons because they are present in pure QCD. If glueballs exist then it should be possible to generalize the constituent quark idea of hadrons to constituent gluons of glueballs. The glueball spectrum survives only if perturbations from the sea sector are small at modestly low energy. Perturbations from the sea quarks come as vacuum loops and are believed to be small in the perturbative regime because the quark loop coefficient is smaller than

that of gluon loop in β_0 for small N_f . This alone does not justify the notion of a constituent gluon and it is the object of Chapter 2 to study its viablity with a simple model.

Since glueballs are colourless objects the minimum number of constituent gluons is two. As gluons are neutral, charge conjugation is a good quantum number and is useful in classifying glueball decays. The photon field in QED is odd under charge conjugation C and this is generalised to gluon fields in QCD; $A_{\mu j}^{\ i} \xrightarrow{C} -A_{\mu i}^{\ j}$ with $A_{\mu j}^{\ i} = \sum_a (T^a)^i_{\ j} A^a_\mu$.

For a 2 gluon colour singlet, the colour configuration is

$$Tr(A_1A_2) \qquad \text{and has even C parity.}$$

For a 3 gluon colour singlet there are 2 possible colour configurations;

D state : $Tr(A_1A_2A_3) + Tr(A_1A_3A_2) \sim d^{abc}A_1A_2A_3$ is odd under C and,

F state : $Tr(A_1A_2A_3) - Tr(A_1A_3A_2) \sim f^{abc}A_1A_2A_3$ is even under C

where f^{abc} and d^{abc} are the antisymmetric and symmetric structure constants of SU(3). As gluons are vector particles the wavefunctions of glueballs must obey Bose symmetry and their quantum numbers can be worked out accordingly. Some excited gluonium states are called oddballs with J^{pc} not accessible to $q\bar{q}$ mesons. A neutral $q\bar{q}$ meson has parity $P = (-1)^{l+1}$ and $C = (-1)^{l+s}$. The J^{pc} of allowed and exotic quark mesons are listed in Table 1.

J^{pc}

	$q\bar{q}$	Exotic
S = 0	even^{-+}	even^{+-}
	odd^{+-}	odd^{-+}
S = 1	even^{++}	even^{--}
	odd^{--}	odd^{++}

Table 1

These exotic mesons would be a strong indication of the existence of glueballs but they have not yet been found.

Assuming the validity of constituent gluons, the gluonium spectrum has been obtained in many different models. There is much disagreement between the glueball spectra of various models but the one common feature is that the lightest glueball is a scalar and has mass in the 1 GeV region [22]. The following is an overview of the mass predictions of these models:

I. Bag Models:

Glueballs are constructed by putting massless gluon fields in a static spherical bag [23], with the confining boundary condition that no gluon flux passes through the surface. There are two families of gluon modes, transverse electric (TE) with parity $-(-1)^{\ell}$ and transverse magnetic (TM) with parity $(-1)^{\ell}$. The lowest state is the $\ell = 1$ TE mode

with $J^P = 1^+$. The corresponding TM mode $J^P = 1^-$ is rather higher in energy.

The lowest mass glueballs are formed from two TE gluons with $J^{PC} = 0^{++}, 2^{++}$. The first excited states have $J^{PC} = 0^{-+}, 2^{-+}$. The exotic 1^{-+} is absent because two massless transverse gluons cannot combine to give such quantum numbers because of Yang's theorem [24]. It has been shown that this corresponds to the absence of a 1^{-+} gauge invariant and Lorentz invariant interpolating glueball field formed from linear combinations of $G^a_{\mu\nu}G^a_{\mu\nu}$ [23][33]. The lowest three gluon bound states are formed by three 1^+ TE gluons which give a 0^{++} state with the colour factor f^{abc}, while with d^{abc} 1^{+-} and 3^{+-} are formed. The exotic 1^{-+} is among the first excited states and is believed to be heavy. Interactions split the glueball spectra. The QCD interactions between the valence gluons have been included perturbatively at the tree level [25]. The unknown self-energies of TE and TM can shift the overall mass scale and have been treated differently by different groups which is the major source of discrepancies. The resulting spectrum, in order of increasing mass, are $J^{PC} = 0^{++} < 0^{-+} < 0^{++} < 2^{++} < 2^{-+} \sim 1^{+-} \sim 2^{++}$.

II. Massive Constituent Gluons:

Glueballs in this model are thought to be bound states of massive gluons [26] interacting through a breakable string of the form

$$V(r) = 2m[1 - \exp(-r/r_0)] \qquad (1.16)$$

where m is the effective gluon mass, taken to be 500 MeV; with

r_0 = 0.6 fm. Although gluons appear as massless fields in the QCD Lagrangian, a gluon string breaks when sufficient energy (the potential energy at infinite distance) has been stored in it to materialize a gluon pair. The mass is generated dynamically through the strong gluon-binding forces. The bound states of massive gluons are investigated with a non-relativistic Schrodinger equation [26] and the calculated mass spectrum gives the following ordering of states: $0^{++} < 0^{-+} \leq 1^{-+} \leq 2^{++}$ with $0^{++} \sim 1.5$ GeV. The relatively light exotic 1^{-+} state in this model is formed by two massive gluons.

III. Lattice Gauge Theories:

Lattice gauge theories [27][28] offer the possibility of a non-perturbative QCD calculation of the glueball spectrum and gives potentially the most reliable results. Glueball masses are extracted by evaluating numerically two point correlation functions of operators, ϕ, with glueball quantum numbers. This idea is based on the observation that

$$\begin{aligned}
\langle v|\phi(t)\phi(0)|v\rangle &= \langle v|\phi(0)e^{-iHt}\phi(0)|v\rangle \\
(t \to -it) \quad &\to \langle v|\phi(0)e^{-Ht}\phi(0)|v\rangle \\
&= \sum_n \langle v|\phi(0)|n\rangle\langle n|e^{-Ht}|n\rangle\langle n|\phi(0)|v\rangle \\
&= \sum_n e^{-E_n t}|\langle v|\phi(0)|n\rangle|^2 \\
(t \to \infty) \quad &\to |\langle v|\phi(0)|0\rangle|^2 e^{-E_0 t}
\end{aligned}$$

V is the vacuum and ϕ is assumed to have zero vacuum expectation. The correlation function is dominated by the lowest excitation of the vacuum with energy E_0. In lattice gauge theories, correlation functions are evaluated by doing Feynman Path Integrals [29] on a finite

lattice with Monte Carlo [30] simulation. The glueball mass is obtained from the decay of the correlation over several temporal lattice spacings. An important problem is to find a sufficiently small lattice spacing so that the glueball mass calculated is that of the continuum limit. This requires that the lattice spacing ($\sim$ inverse of momentum) is sufficiently small that perturbation theory (up to 2 loops) is valid [28]. The QCD scale parameter Λ is then related to the lattice spacing through the RGE. Since glueball masses are expressed in terms of lattice spacing, a reference scale is needed to convert these masses into physical units. This would be a straightforward normalization if a glueball was experimentally established. In practice, glueball masses are expressed in units of Λ which is measured by comparing known quantities, such as m_ρ , string tension, the gluon condensate $\langle\alpha_s TrG\cdot G\rangle$ and the chiral condensate $\langle q\bar{q}\rangle$, with lattice calculations. The physical value of glueball masses are determined by what value of Λ is chosen. The value of $m(0^{++})$ is the most reliable [28] because 0^{++} shows good continuum behaviour (i.e. independent of coupling and satisfies $E^2 = p^2 + m^2$) and has small finite size effects. Masses of heavier glueballs are more difficult to extract because their correlation functions fall more steeply and disappear into statistical noise at smaller t than for the 0^{++}. In any case, the mass 0^{++} sets the scale of the glueball spectrum. A 1 GeV 0^{++} will put the low-lying glueball excitations in the 2-3 GeV range and a 800 MeV one will lower this range to 1-2 GeV. The above calculations are performed in the quenched approximation in which quark loops are ignored , the predicted spectrum is ordered as follows: $0^{++} < 0^{-+} < 2^{++} < 1^{-+} < 0^{--}$.

IV. Flux Tube Model:

This model is based on the strong coupling flux tube limit of QCD [31]. In strong coupling lattice QCD, quarks on lattice sites are connected by colour flux, the degrees of freedom are quark and gluon flux tubes rather than quarks and gluons. Glueballs are formed as glueloops by removing the quarks and joining the ends of the flux tube. The flux tube is assigned a constant mass per unit length and treated as a quantum string. The ground state 0^{++} has a mass of about 1.5 GeV. The spectrum is formed by rotational, vibrational and radial excitations. The resulting spectrum is ordered as: $0^{++} < 1^{+-} < 2^{++}$.

V. QCD Sum Rules:

Apart from lattice calculations, the QCD sum rules [32][33] have a better theoretical justification than other models. The basic idea of the sum rules is to extrapolate the two-point function, associated with a current J_μ carrying the same quantum numbers as the resonance being studied, from the asymptotic regime to large distances where resonances dominate and non-perturbative effects are at work. The non-perturbative effects arise as power corrections in $1/Q^2$ to the asymptotic freedom regime and are introduced through various vacuum expectation values such as the gluon condensate $\langle \alpha_s TrG \cdot G \rangle$ and the light quark condensate $\langle q\bar{q} \rangle$ which are phenomenological parameters. The time-ordered product $T(J_\mu(x)J_\nu(0))$ is expressed in terms of the operator product expansion (OPE) [34], which in some sense separates short and large distance effects. The short distance effects are contained in the Wilson coefficients of the various operators which can be calculated

perturbatively. The non perturbative effects are parameterized in the vacuum expectation values of the various operators in the OPE through dispersion relations (e.g. the Borel transformation) which relate the two point function to experimental measurements [32]. It is then speculated that the formation of resonances is a phenomenological manifestation of the interaction of the current quarks and/or gluons with fluctuations of vacuum fields. One phenomenological manifestation of non-perturbative fluctuations is the gluon vacuum condensate. The gluon vacuum fields, in turn, induce quark vacuum fields and the corresponding quark condensate is responsible for spontaneous breaking of chiral symmetry (see next section) [33].

The notion of current gluons is used instead of constituent gluons in sum rules. Unlike constituent gluons, current gluons are well defined objects which can be derived from the QCD Lagrangian. The lowest dimension currents for the 2^{++}, 0^{-+} and 0^{++} gluonia are:

$$J_{\mu\nu} = -G^a_{\mu\nu}G^a_{\mu\nu} + (1/4)g_{\mu\nu}G^a_{\alpha\beta}G^a_{\alpha\beta} \tag{1.17}$$

$$J_- = \frac{3\alpha_s}{4\pi}\,\mathrm{Tr}G\cdot\tilde{G} \qquad , \quad \tilde{G}_{\mu\nu} = \frac{1}{2}\,\varepsilon_{\mu\nu\alpha\beta}G_{\alpha\beta} \tag{1.18}$$

$$J_+ = \frac{\beta_0\alpha_s}{4\pi}\,\mathrm{Tr}G\cdot G \tag{1.19}$$

There are a set of low-energy theorems [33] which facilitate the evaluation of the current gluon two point functions at low Q^2 where non-perturbative effects are most essential. There is much disagreement on the mass spectrum according to whether it is believed that small size

instanton effects [35] should be included or not (see next section). The results without the these effects [36] agree with other estimates from Lattice and Bag models. With instanton effects [33][37] the scalar $0^{++} \sim 1.5$ GeV, and pseudoscalar $0^{-+} \gtrsim 2$ GeV are heavier than other predictions.

1.3.2 More on the QCD Lagrangian

This section serves as a brief introduction to some theoretical ideas that are relevant in previous and later discussions. It is profitable to hypothesize an ideal Lagrangian with perfect symmetries, some of which may be broken in the real world. A Lagrangian has a global internal symmetry G if it is invariant under the corresponding constant phase transformations. There always exists a charge conservation law for G by Noether's Theorem [38]. These charges are generators of G and obey the Lie Algebra of G even in the presence of symmetry breaking terms. One application of this is the current algebra in the SU(3) flavour quark model and is briefly discussed in Chapter 4. Although it is not physically interesting for field theories to have exact scale invariance since they cannot have finite mass particles, nevertheless the quark masses in the QCD lagrangian are free parameters and have particular values in physics, while QCD is assumed to be self-consistent for any values of these parameters. Putting all the masses to zero corresponds to the chiral limit and the resulting energy-momentum tensor is:

$$\theta_{\mu\nu} = -G^a_{\mu\nu}G^a_{\mu\nu} + (1/4)g_{\mu\nu}G^a_{\alpha\beta}G^a_{\alpha\beta} + \sum_k^{N_f} i\bar{q}_k\gamma_\mu D_\nu q_k \qquad (1.20)$$

Classically $\theta_{\mu\nu}$ is a traceless symmetric tensor and belongs to an irreducible representation of the Lorentz group. The generators of scale transformations and Lorentz transformations are:

$$D = \int_x D_0(x) \tag{1.21}$$

where $D_\mu = X_\nu \theta_{\mu\nu}$ is the conserved dilation current

and $J_{\mu\nu} = \int_x [X_\mu \theta_{\nu 0}(x) - X_\nu \theta_{\mu 0}(x)]$, respectively.

Given that $\theta_{\mu\nu}$ is traceless, symmetric, and conserved, these generators are also conserved. The massless QCD lagrangian also has a U(1) chiral symmetry with a conserved current

$$J^5_\mu = \sum_k^{N_f} \bar{q}_k \gamma_\mu \gamma_5 q_k \tag{1.22}$$

Both the classical U(1) chiral and scale invariance are broken at quantum level by the axial [39] and trace [40] anomalies,

U(1) axial:

$$\partial_\mu J^5_\mu = \frac{2N_f}{4}\alpha_s \, \mathrm{Tr} G \cdot \tilde{G} \qquad (+ 2i \sum_k^{N_f} m_k \bar{q}_k q_k) \tag{1.23}$$

Scale :

$$\partial_\mu D_\mu = \theta_{\mu\mu} = \frac{\beta_0 \alpha_s}{4\pi} \mathrm{Tr} F \cdot F \quad (-[1 + \gamma_m(\alpha_s)] \sum_k^{N_f} m_k \bar{q}_k q_k) \tag{1.24}$$

where $\gamma_m(\alpha_s)$ = mass anomalous dimension. For non-zero quark masses these anomalies are modified by adding explicit chiral symmetry breaking terms given in the brackets. Incidentally the gluon currents used in QCD sum rules are just the pure gauge part of $\theta_{\mu\nu}$, the U(1) axial and scale anomalies. Apart from these anomalies, the QCD vacuum also has field configurations called instantons [41] which correspond to

nontrivial minima of the Euclidean QCD action and are characterized by the topological quantum number,

$$n = \frac{g^2}{32\pi^2} \int_x \mathrm{Tr} G \cdot \tilde{G} \qquad \text{in Euclidean space.} \qquad (1.25)$$

These non-perturbative effects are expected to contribute to the vacuum condensates and are the source of disagreement mentioned earlier in QCD sum rules calculations.

For nearby glueballs and quark mesons with the same quantum numbers, mixing between them is inevitable. It is therefore particularly interesting to investigate the low lying isoscalar states where glueballs and/or mixed states are likely to be found. There are no definite predictions on the effects of including light quarks in glueball mass calculations and in the decay properties of glueballs. Meson-gluonium mixings have been studied in QCD sum rules by calculating the two-point correlation function of $T(J_{q\bar{q}}(x), J_{gb}(0))$ and in other phenomenological approaches like potential models (see chapter 3 for a brief discussion). An alternative approach is to use the effective Lagrangian of QCD. Because of confinement the fundamental fields, quarks and gluons, in the QCD Lagrangian do not appear as free particles. It is therefore useful to construct an effective Lagrangian for describing the properties of the observed particles, which at the same time possesses all the symmetry properties of the QCD Lagrangian (i.e. chiral symmetry in the massless limit). Such a low energy effective QCD lagrangian is a non-linear sigma model [42] and its

applications to glueball physics will be discussed in Chapter 3.

1.3.3 Hybrids

Apart from forming colour singlet hadrons from quarks and glueballs from gluons, there also exist other possible colourless systems called hybrids or meiktons or hermaphrodites [43]. These hybrid states contain both constituent quarks and gluons in the form of $q\bar{q}g$ and $qqqg$. The existence of constituent gluons can also be confirmed by establishing these hybrid states. In the framework of the Bag Model, the lightest hybrid states that can be formed are:

$$(q\bar{q})_{1^-,0^-} \times g_{TE} \rightarrow 0^{-+},\ 1^{-+},\ 2^{-+},\ 1^{--}.$$

The exotic 1^{-+} state can be as light as ~ 1.5 GeV in both the QCD sum rules [44] and the Bag Model [45][46] calculations. However, the mass spectrum can be shifted by an overall energy scale by the self-energies of gluons and quarks in the Bag Model [43][45]. These hybrids have their own characteristic decays and these will be discussed in the relevant context.

Finally, QCD has been remarkably successful in classifying the many hadron states so far discovered and has proved invaluable in studying hadron spectroscopy. However QCD could not be regarded as a complete theory for the strong interaction of hadronic matter if its predictions for the gluonic sector are not borne out by experiment. What follows in this thesis is an account of my efforts to validate QCD by establishing the existence of the ground state scalar glueball.

CHAPTER TWO

THE VALIDITY OF THE IDEA OF VALENCE GLUONS IN A GLUEBALL

2.1 MOTIVATION

Using the language of a constituent model, the simplest configuration of an even spin, even charge configuration and even parity glueball is a state composed of two hard gluons carrying most of the glueball's momentum. Of course, these gluons can, and will, continually emit gluons degrading their momenta so that the idea of valence gluons may became lost in a sea of soft gluons and $q\bar{q}$ pairs. The aim of this chapter is to check if, and how, this happens by considering a simple computation.

Let us begin with a prototype calculation. If we consider the static properties of a nucleon, it is essentially made of just three constituent quarks, which carry all the properties of the nucleon including all its momentum. However, when the nucleon is probed more closely, for example in deep inelastic scattering, this simple picture rapidly evolves to a situation where the three valence quarks carry less than 50% of the nucleon's momentum and gluons most of the remainder [4][47]. Probing still closer, these distributions evolve perturbatively till eventually at truly asymptotic energies, quarks and antiquarks in the nucleon equally share the momentum carried by charged partons. The rapid variation at low momentum is really

non-perturbative. However, this can be crudely mimicked by the lowest order Altarelli-Parisi equations [10][48] with Λ reasonably large $\sim$ 500 MeV (see Section 2.3). This then suggests a simple model, in which at $Q \sim 1$ GeV, all the nucleon's momentum is carried by just three quarks. So at $Q = Q_0$, the parton distribution functions satisfy:

$$\int_0^1 dx\ q(x,Q_0^2) = 3 \ ; \quad \int_0^1 dx\ xq(x,Q_0^2) = 1 \qquad (2.1)$$

where $q(x,Q^2)$ is the sum over quark distributions, while at $Q = Q_0$ the sum over antiquark probabilities, $\bar{q}(x,Q^2)$, and the gluon distribution, $g(x,Q^2)$, vanish. Moreover, we naively expect the momentum distribution $xq(x,Q_0^2)$ to peak close to $x = 1/3$ corresponding to each quark carrying 1/3 of the total momentum. We can then use the lowest-order Altarelli-Parisi equations to evolve these probabilities to $Q \sim 10$ GeV and see that the valence distribution, q_V , ($q_V = q - \bar{q}$, while $q_\Sigma = q + \bar{q}$) then peaks down at $x \sim 0.18$ and that the gluon's momentum fraction has grown from zero to 40% with a sea-quark component is generated at small x [Fig. 2.3], simply starting from a form for $q(x,Q_0^2) \sim x^{-\frac{1}{2}}(1-x)^3$ motivated by Regge behaviour [49] at small x and constituent interchange as $x \to 1$, as explained in the next section.

Armed with this simplified model of parton evolution, assumed governed by the equations of perturbation theory at all momenta, we go on in Section 2.4 to see how such distributions evolve for a state which is purely gluonic at $Q = 1$ GeV. There two gluons are pictured as carrying all its momentum, so that $xg(x,Q_0^2)$ peaks near $x = 1/2$ and

$$\int_0^1 dx\ g(x,Q_0^2) = 2 \ ; \quad \int_0^1 dx\ xg(x,Q_0^2) = 1 \qquad (2.2)$$

with $q(x,Q_0^2) = \bar{q}(x,Q_0^2) = 0$. A form for $g(x,Q_0^2)$ satisfying these conditions is $\sim x(1-x)$ which we will again explain in Section 2.4.

With these initial conditions we will discuss in Section 2.4 whether there is still a sense in which a hard gluon contribution can be separated, as soft gluon and sea quark components develop with increasing momentum of the probe. For a hadron whose 'static' constituents are quarks, the separation of hard and soft quark components is quite natural. The quark distribution is the sum of valence and sea contributions. Since baryon number conservation ensures the total number of quarks (i.e. quarks minus antiquarks) in the hadron remains unchanged, the sea distribution can be fixed by its equality with the antiquark distribution. For a glueball, the separation of hard and soft glue, not being aided by such a basic conservation rule, may appear more problematic. We therefore make the operational definition that all the glue with $x > x_0(Q^2)$ is hard, where x_0 is fixed by:

$$\int_{x_0}^{1} dx\ g(x,Q^2) = 2 \qquad (2.3)$$

the analogue of baryon number conservation, but where x is expected to grow steadily from $x_0 = 0$ at $Q = Q_0$. Of course, the fraction of momentum carried by this hard component is expected to decrease steadily as Q increases. However, the question is whether $xg(x,Q^2)$ for $x > x_0$ is really distinguishable in shape from that with $x < x_0$, or is there just a totally smooth distribution? The results, shown in Figure 2.8, as described in the Section 2.4, show that hard and soft components can be separated upto $Q \sim 10$ GeV, even though the gluon distribution is

monotonic.

2.2 THE EVOLUTION EQUATIONS AND THE MOMENTUM FRACTION

As discussed in Section 1.2, the momentum dependence of the structure functions measured in deep inelastic scattering can be computed in perturbative QCD in terms of corrections to the naive parton model with its natural Bjorken scaling.

Thus to $O(\alpha_s)$ and keeping only leading logs of momentum Q:

$$\frac{F_2(x,Q^2)}{x} =$$

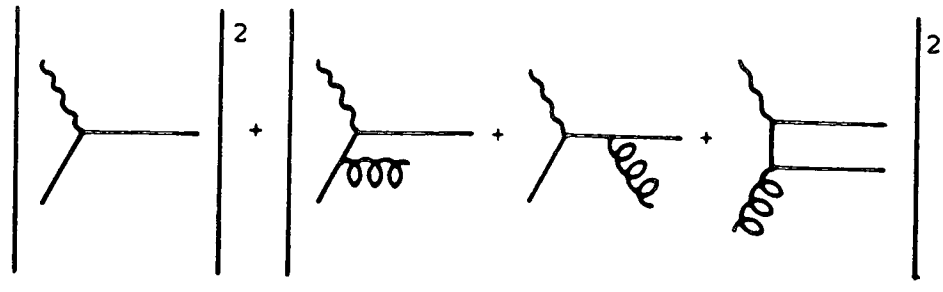

$$= \sum_i e_i^2 \int_0^1 dy \int_0^1 dz\; q_i(y,Q_0^2)\left[\delta(1-z) + \frac{\alpha_s(Q^2)}{2\pi} P_{qq}(z) \ln\frac{Q^2}{\mu^2}\right]\delta(x-zy)$$

$$+ \sum_i e_i^2 \int_0^1 dy \int_0^1 dz\; g(y,Q^2)\, \frac{\alpha_s(Q^2)}{2\pi}\, P_{qg}(z) \ln\frac{Q^2}{\mu^2}\, \delta(x-zy)$$

$$\equiv \sum_i e_i^2\, q_i(x,Q^2) \qquad (2.4)$$

The splitting function $P_{qq}(z)$ [48][10] depicted as

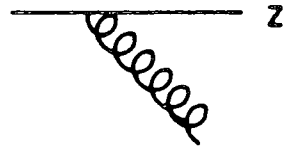

can be computed from the appropriate Feynman diagrams:

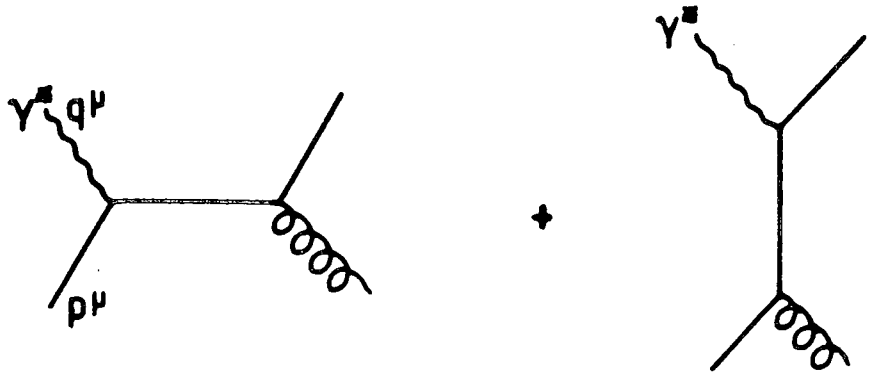

with s and t channel quark exchanges. With p_T the transverse momentum of the outgoing quark, the differential cross-section for $\gamma^* q \to qg$ is

$$\frac{d\sigma}{dp_T^2} = e_i^2 \frac{4\pi\alpha}{s} \cdot \frac{1}{p_T^2} \cdot \frac{\alpha_s}{2\pi} P_{qq}(z) \qquad (2.5)$$

with $z = \frac{Q^2}{2p\cdot q}$. For p_T^2 small (i.e. $s \gg |t|$)

$$P_{qq}(z) = C_2(F) \left(\frac{1+z^2}{1-z} \right) \qquad (2.6)$$

where $C_2(F)$ is the usual colour Casimir associated with quarks being in the fundamental representation of $SU(3)_c$. $P_{qq}(z)$ is singular at $z \to 1$. This infrared divergence is associated with the emission of soft or collinear massless gluons. This divergence is cancelled by the addition of virtual gluon contributions of the same order in α_s , so that we replace

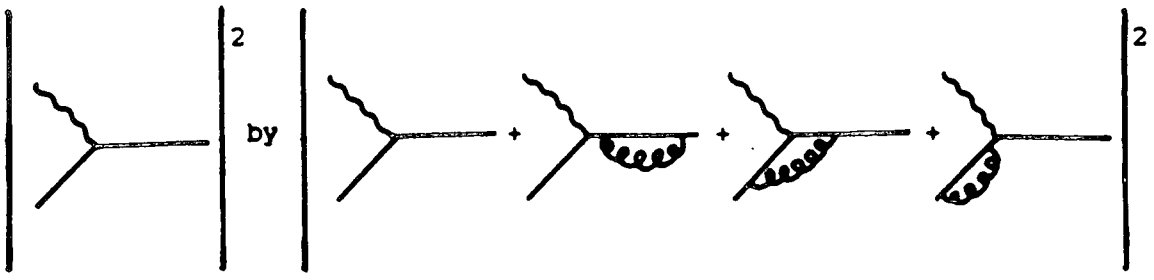

These virtual gluon contributions are of the form $\delta(1-z)$ and are absorbed into $P_{qq}(z)$ by the '+ prescription' [10] regularization in which $\frac{1}{1-z} \rightarrow \frac{1}{(1-z)_+}$ defined in terms of a non-singular weight function $\Phi(z)$ by

$$\int_0^1 dz \, \frac{\phi(z)}{(1-z)_+} \equiv \int_0^1 dz \, \frac{\phi(z)-\phi(1)}{1-z} \tag{2.7}$$

Calculation of the virtual contribution modifies $P_{qq}(z)$ to

$$P_{qq}(z) = C_2(F) \left[\frac{(1+z^2)}{(1-z)_+} + \frac{3}{2} \delta(1-z) \right] \tag{2.8}$$

or equivalently

$$P_{qq}(z) = C_2(F) \left[\frac{1+z^2}{1-z} \right]_+ \tag{2.9}$$

remembering that $f(z)_+ = f(z)$ for $z < 1$. The regularized form of $P_{qq}(z)$ ensures baryon number conservation as we will describe shortly.

The other splitting function $P_{qg}(z)$ in Eqn, 2.4 is depicted by

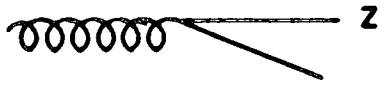

and can be similarily computed. It is obviously symmetric under $z \rightarrow 1 - z$ and is explicitly

$$P_{qg}(z) = T_2(F)\left[z^2 + (1-z)^2\right] \tag{2.10}$$

where $T_2(F)$ is the trace factor of the fermion representation, which is 1/2 with the conventional normalization of α_s. Differentiating Eqn. 2.4 with respect to Q^2 we have the lowest order Altarelli-Parisi equation for the evolution of the quark distribution of flavour i:

$$\frac{\partial q_i(x,Q^2)}{\partial \ln Q^2} = \frac{\alpha_s(Q^2)}{2\pi}\int_x^1 \frac{dy}{y}\left[q_i(y,Q^2)P_{qq}(\frac{x}{y}) + g(y,Q^2)P_{qg}(\frac{x}{y})\right] \tag{2.11}$$

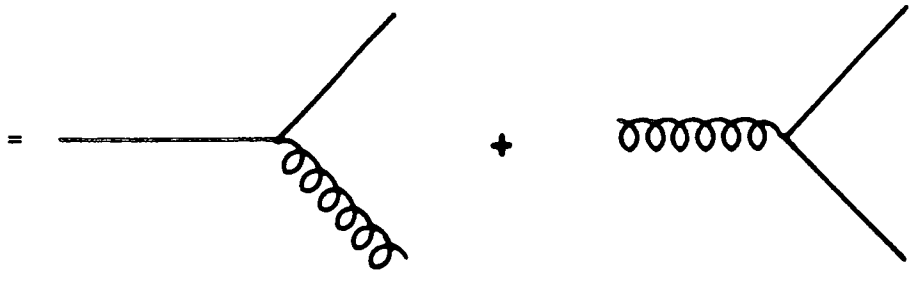

As seen in Eqn. 2.11 the evolution of each quark distribution depends on knowledge of the gluon probability too, any difference

$$q_{NS}(x,Q^2) = q_i(x,Q^2) - q_j(x,Q^2) \tag{2.12}$$

which is a non-singlet (NS) under flavour transformation, does not involve $g(y;Q^2)$, for we simply have

$$\frac{\partial q_{NS}(x,Q^2)}{\partial \ln Q^2} = \frac{\alpha_s(Q^2)}{2\pi}\int_x^1 \frac{dy}{y} q_{NS}(y,Q^2)P_{qq}(\frac{x}{y}) \tag{2.13}$$

Since clearly the number of quarks of any flavour must be conserved, since quarks and antiquarks can only be created in pairs,

$$\frac{\partial}{\partial \ln Q^2} \int_0^1 dx \, \{q_i(x,Q^2) - \bar{q}_i(x,Q^2)\} = 0 \qquad (2.14)$$

This is ensured by $\int_0^1 dz \, P_{qq}(z) = 0$, see Eqn 2.9.

The evolution of the gluon distribution is described in a similar way to Eqn. 2.11 by

$$\frac{\partial g(x,Q^2)}{\partial \ln Q^2} = \frac{\alpha_s(Q^2)}{2\pi} \int_x^1 \frac{dy}{y} \left[\sum_i^{2N_f} q_i(y,Q^2) P_{gq}\left(\frac{x}{y}\right) + g(y,Q^2) P_{gg}\left(\frac{x}{y}\right) \right] \qquad (2.15)$$

$=$ $\sum_{i=1}^{2N_f}$ 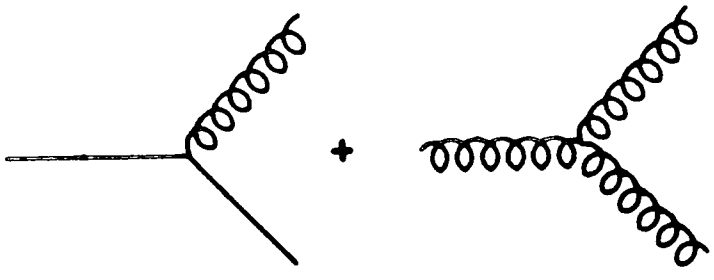 $+$

where the new splitting probabilities are given by:

$P_{gq}(z) =$  z $=$ 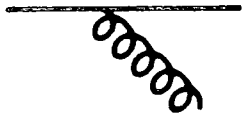 $1-z$ $= P_{qq}(1-z)$

$$= C_2(F) \left[\frac{1 + (1-z)^2}{z} \right] \qquad (2.16)$$

Since there is explicitly a gluon in the final state, this function is finite as $z \to 1$.

The gluon splitting function is clearly symmetric under $z \to 1 - z$ and has virtual contributions at $z = 1$ which regularizes it under an integral, cf. Eqn. 2.15 to be:

$$P_{gg}(z) = 2C_2(A)\left[\frac{z}{(1-z)_+} + \frac{1-z}{z} + z(1-z)\right] + \frac{\beta_0}{2}\delta(1-z) \qquad (2.17)$$

Since we have seen any non-singlet quark distribution evolves independently of the gluon distribution, it can only be the singlet function

$$q_\Sigma(x,Q^2) \equiv \sum_{i=1}^{2N_f} q_i(x,Q^2) = \sum_{i=1}^{N_f}\left[q_i(x,Q^2) + \bar{q}_i(x,Q^2)\right] \qquad (2.18)$$

that couples to $g(x,Q^2)$ to give

$$\frac{\partial}{\partial \ln Q^2}\begin{bmatrix} q_\Sigma(x,Q^2) \\ g(x,Q^2)\end{bmatrix} = \frac{\alpha_s(Q^2)}{2\pi}\int_x^1 \frac{dy}{y}\begin{bmatrix} P_{qq}(\frac{x}{y}) & 2N_f P_{qg}(\frac{x}{y}) \\ P_{gq}(\frac{x}{y}) & P_{gg}(\frac{x}{y})\end{bmatrix}\begin{bmatrix} q_\Sigma(y,Q^2) \\ g(y,Q^2)\end{bmatrix} \qquad (2.19)$$

All other quark distributions evolve according to Eqn. 2.13

Since in QCD all the momentum of the parent hadron must be shared by quarks, antiquarks and gluons:

$$\int_0^1 dx\, x\{\sum_{i=1}^{2N_f} q_i(x,Q^2) + g(x,Q^2)\} = 1 \qquad (2.20)$$

$$\text{i.e.} \qquad \frac{\partial}{\partial \ln Q^2}\int_0^1 dx\, x(q_\Sigma(x,Q^2) + g(x,Q^2)) = 0$$

at all momentum Q. This clearly requires

$$\int_0^1 dz\, z\{P_{qq}(z) + P_{gq}(z)\} = 0 \qquad (2.21)$$

and

$$\int_0^1 dz\, z\{2N_f P_{qg}(z) + P_{gg}(z)\} = 0 \qquad (2.22)$$

The forms given above for the splitting functions ensure these momentum conservation conditions are automatically satisfied. To see how the

momentum is shared between the partons in the hadron, consider the n = 2 moments, Eqn 2.20 of the distribution functions. With

$$M_2^{\Sigma}(Q^2) = \int_0^1 dx\ x q_{\Sigma}(x,Q^2) \quad ; \quad M_2^{g}(Q^2) = \int_0^1 dx\ x q_{g}(x,Q^2) \tag{2.23}$$

momentum conservation means $M_2^{\Sigma}(Q^2) + M_2^{g}(Q^2) = 1$.

Taking moments of the coupled evolution equations, Eqn. 2.19 gives

$$\frac{\partial}{\partial \ln Q^2}\begin{bmatrix} M_2^{\Sigma}(Q^2) \\ M_2^{g}(Q^2) \end{bmatrix} = \frac{\alpha_s(Q^2)}{2\pi}\begin{bmatrix} -16/9 & N_f/3 \\ 16/9 & -N_f/3 \end{bmatrix}\begin{bmatrix} M_2^{\Sigma}(Q^2) \\ M_2^{g}(Q^2) \end{bmatrix} \tag{2.24}$$

having used the forms of the splitting functions to deduce

$$\int_0^1 dz\ zP_{qq}(z) = -(4/3)C_2(F) = -\int_0^1 dz\ zP_{gq}(z) \tag{2.25}$$

$$2N_f \int_0^1 dz\ zP_{qg}(z) = (2/3)N_f T_2(F) = -\int_0^1 dz\ zP_{gg}(z) \tag{2.26}$$

We can readily see that

$$\frac{\partial}{\partial \ln Q^2}\{M_2^{\Sigma}(Q^2) + M_2^{g}(Q^2)\} = 0 \tag{2.27}$$

$$\frac{\partial}{\partial \ln Q^2} M_{sum} = \frac{\alpha_s(Q^2)}{2\pi}\left(\frac{16}{9} + \frac{N_f}{3}\right) M_{sum} \tag{2.28}$$

where $M_{sum} = (16M_2^{\Sigma}(Q^2) - 3N_f M_2^{g}(Q^2))$ from which we deduce:

$$M_2^{\Sigma}(Q^2) = \left[M_2^{\Sigma}(Q_0^2) - \frac{3N_f}{16+3N_f} \right]\left[\frac{\alpha_s(Q^2)}{\alpha_s(Q_0^2)} \right]^{d_2^+} + \frac{3N_f}{16+3N_f} \tag{2.29}$$

$$M_2^g(Q^2) = -\left[M_2^{\Sigma}(Q_0^2) - \frac{3N_f}{16+3N_f} \right]\left[\frac{\alpha_s(Q^2)}{\alpha_s(Q_0^2)} \right]^{d_2^+} + \frac{16}{16+3N_f} \qquad (2.30)$$

where $$d_2^+ = \frac{2(16 + 3N_f)}{3(33 - 2N_f)}$$

while for any non-singlet component, like that of valence quarks,

$$M_2^{NS}(Q^2) = M_2^{NS}(Q_0^2)\left[\frac{\alpha_s(Q^2)}{\alpha_s(Q_0^2)}\right]^{d_2^{NS}} \qquad (2.31)$$

with $$d_2^{NS} = \frac{32}{3(33 - 2N_f)}$$

In order to study the significance of non-perturbative dynamics, we naively extrapolate the lowest order evolution equations to low Q/Λ and compare the simulated proton structure function with experimental data and use this to gauge the reliability of the simulated glueball structure function. As a first step let us look at the behaviour of M_2^{Σ} and M_2^g for a proton and for a glueball using Eqn. (2.29,30) with the following initial conditions at $Q_0 = 1$ GeV with $N_f = 3$:

Proton $\quad M_2^{\Sigma}(Q_0^2) = 1 \quad , \quad M_2^g(Q_0^2) = 0$

Glueball $\quad M_2^{\Sigma}(Q_0^2) = 0 \quad , \quad M_2^g(Q_0^2) = 1$

The results with $\Lambda = 0.5$ GeV are shown in Figure 2.1.

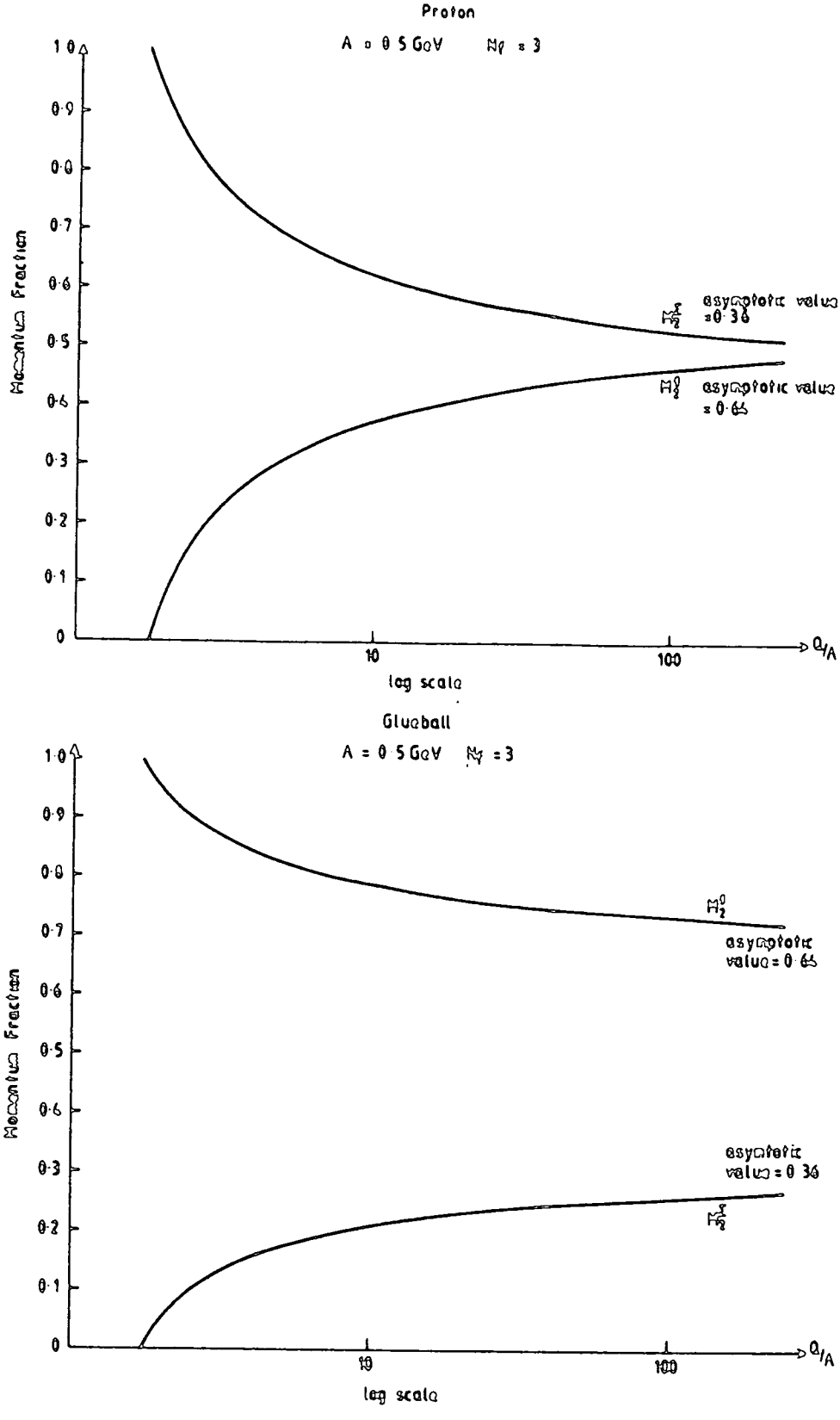

Figure 2.1 The evolutions of H_2^{Σ} and H_2^{g} in

(a) a proton,

(b) a gg Glueball.

2.2.1 The evolution of structure functions

Having seen that in this simple model of wholly perturbative evolution the momentum fraction of the proton is shared in rough agreement with experiment, we turn to the detailed evolution of the structure functions themselves. As a prototype we consider the flavour singlet component of a proton constrained to satisfy

$$\int_0^1 dx \quad q_\Sigma(x,Q_0^2) = 3 \ ; \text{ the number constraint} \tag{2.32}$$

$$\int_0^1 dx \ xq_\Sigma(x,Q_0^2) = 1 \ ; \text{ the momentum constraint} \tag{2.33}$$

$$xq_\Sigma(x,Q_0^2) \text{ ----- peaks roughly at } x = 1/3 \tag{2.34}$$

at $Q_0 = 1$ GeV. Before searching for suitable forms for $q_\Sigma(x,Q_0^2)$ there are a couple of points about the regularizing of the splitting functions we must first discuss.

In the previous section we only considered the regularization of integrals from $z = 0$ to 1 as that is what is involved in baryon number and momentum conservation. However, the evolution equations, Eqns 2.19, involve integrals from $z = x$ to 1. The '+ prescription' requires

$$\int_x^1 dz \ \phi(z)\left[f(z)\right]_+ = \phi(1)\left[-\int dz \ f(z)\right]_{z=x} + \int_x^1 dz\left[\phi(z)-\phi(1)\right]f(z) \tag{2.35}$$

where once again $\phi(z)$ is a non-singlular function and $f(z)$ is singular at $z = 1$. Then for instance

$$\int_x^1 \frac{dy}{y} P_{gg}(\tfrac{x}{y})\, g(y,Q^2)$$

$$= \int_x^1 \frac{dz}{z} \{2C_2(A)\left[\frac{z}{(1-z)_+} + \frac{1-z}{z} + z(1-z)\right] + \frac{\beta_0}{2}\delta(1-z)\}\, g(\tfrac{x}{z},Q^2)$$

$$= \frac{\beta_0}{2} g(x,Q^2) + 2C_2(A) g(x,Q^2)\ln(1-x)$$

$$+ 2C_2(A) \int_x^1 dz \frac{\{g(\frac{x}{z},Q^2) - g(x,Q^2)\}}{1-z}$$

$$+ 2C_2(A) \int_x^1 \frac{dz}{z} (1-z)(1+z^2) g(\tfrac{x}{z},Q^2) \qquad (2.36)$$

where $\lim_{z\to 1} \frac{g(\frac{x}{z},Q^2) - g(x,Q^2)}{1-z} = x\frac{\partial}{\partial x} g(x,Q^2)$

In an analogous way

$$\int_x^1 \frac{dy}{y} P_{qq}(\tfrac{x}{y})\, q(y,Q^2)$$

$$= \int_x^1 \frac{dz}{z} C_2(F)\left[\frac{1+z^2}{1-z}\right]_+ q(\tfrac{x}{z},Q^2)$$

$$= C_2(F)\{\frac{3}{2} q(x,Q^2) + 2\, q(x,Q^2)\ln(1-x)$$

$$+ \int_x^1 \frac{dz}{1-z}\left[\frac{1+z^2}{z} q(\tfrac{x}{z},Q^2) - 2q(x,Q^2)\right]\} \qquad (2.37)$$

where the integrand just becomes $2x\frac{\partial}{\partial x} g(x,Q^2)$ when $z \to 1$.

To begin our calculation we need to guess starting forms for q_Σ in the case of a proton and g in the case of a glueball. This we do with the guidance of the dimensional counting rules of the parton model.

2.2.2 Counting rules

It is well-known that the electric and magnetic form factors of the proton determined by elastic e^-p scattering using the Rosenbluth formula are empirically given by dipole forms $\sim 1/(Q^2 + 0.71)^2$. If one understands how such a Q^2 dependence arises for these elastic form-factors, one can hopefully generalize the idea to the structure functions of deep inelastic scattering.

A meson in the parton model has two valence quarks which are resolved by a virtual photon if $Q \gtrsim 3$ GeV. The valence quark, knocked off-shell by the probing γ^*, is called the active quark; the other is the spectator.

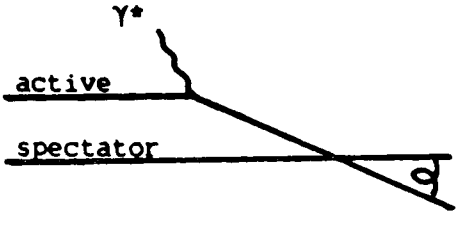

meson final state

After having been struck, the active quark must recombine with the unperturbed valence quark to form an exclusive meson final state. To do this, they must exchange a gluon with momentum Q. This gluon propagator behaves like $1/Q^2$ and so the meson form-factor must behave like $1/Q^2$ for $Q \gg 1$ GeV. Similar arguments, when applied to baryons, give form-factors a $(1/Q^2)^2$ dependence because at least two hard gluons must

be exchanged between the active quark and the two spectators.

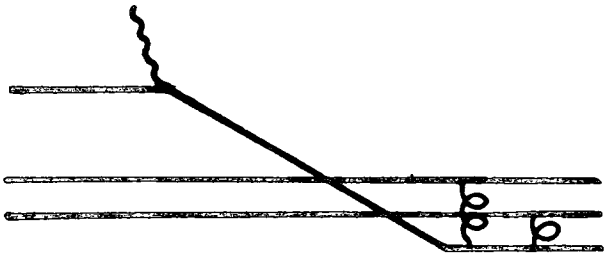

Thus the momentum dependence of the form-factors, $f(Q^2)$, can be summarized as

$$f(Q^2) \sim (\frac{1}{Q^2})^{n_s}$$

where n_s is the number spectators.

To see what such relations mean for parton structure functions, we need to express Q^2 in terms of x. When $x \to 1$, the hadron final state of mass W is no longer a continuum but passes a discrete set of exclusive states for which the above analysis applies. With

$$Q^2 = \frac{(W^2 - M^2)x}{1 - x} \qquad (2.38)$$

we see that the prediction of parton interchange becomes

$$f(x) \sim (1-x)^{n_s} \text{ for } x \to 1.$$

Writing the structure functions in the parton model in terms of these form-factors, we have for ep -> ep

$$F_2(x,Q^2) = \nu W_2 \sim Q^2 f(Q^2)^2 \sim (1-x)^{2n_s-1} \text{ as } x \to 1.$$

For an active valence quark in a proton $n_s = 2$ is the minimum number of

spectators, while for an active sea quark we have a minimum of 4 spectators, the 3 valence quarks and the brother antiquark in the sea, so that the valence quark distribution $q_v(x) \sim (1-x)^3$, while a sea quark distribution $q_s(x) \sim (1-x)^7$ in this model.

The contribution from the sea is then only important as $x \to 0$. This is hardly surprising if we view the sea of $q\bar{q}$ pairs as being created by gluons from Bremstrahlung radiation, they naturally occur with degraded momentum. The limit of $x \to 0$ with Q large is recognised to be a regime in which γ^*p scattering may be thought to be controlled by Regge pole exchange, the scattering off a valence quark being a non-diffractive process, while that of a sea quark is diffractive. Regge asymptotics then predicts for $x \to 0$ that the structure function

$$F_2(x) = \sum_i e_i^2 x q_i(x) \sim x^{1-\alpha(0)}$$

where $\alpha(0)$ is the intercept of the appropriate Regge exchange. For a sea quark, this is the exchange of vacuum quantum numbers, i.e. the pomeron, for which $\alpha_{IP}(0) = 1$, while for a valence quark, the exchange is that of a typical meson trajectory, for which $\alpha(0) \simeq 1/2$. Thus we expect for $x \to 0$,

$$q_v(x) \sim x^{-1/2} \quad , \quad q_s(x) \sim x^{-1}$$

2.3 THE PROTON STRUCTURE FUNCTIONS

As already explained in Section 2.1, we use the lowest order Altarelli-Parisi equations to evolve an initial proton structure function which satisfies Eqns. 2.32-34. The simplest form of $q(x,Q_0^2)$ is $\sim x^a(1-x)^b$ but this does not satisfy simultaneously Eqns. 2.32-34. A more complicated form is $\sim x^a(1-x)^b(1+Cx)$ with the ranges of a and b close to the values suggested by the counting rules i.e. -1/2 and 3. Although there are solutions of this form that satisfy the constraints but $q(x,Q_0^2)$ has negative values between $0 \leq x \leq 1$ in all these cases. Instead of adding more correction terms to this, we turn to counting rules for suggestion.

Let us first write down the general form

$$q(x,Q_0^2) = Ax^{-\frac{1}{2}}(1-x)^3\left[1+B(1-x)^2+C(1-x)^4+D(1-x)^6+E(1-x)^8\right] \qquad (2.39)$$

The simplest case with $B = C = D = E = 0$ does not satisfy all the initial constraints so it is ruled out and correction terms are needed. The correction terms in Eqn. 2.39 can be interpreted as hard exchanged gluons which contribute powers of $(1-x)^2$ to the structure function. The coefficients A,B and C are needed to satisfy the constraints but again $q(x,Q_0^2)$ has a negative region between $0 \leq x \leq 1$. The D term is required to make $q(x,Q_0^2)$ positive with the constraint $1 + B + C + D > 0$. The solution to Eqn. 2.32-33 is

$$A = 33.96 \qquad B = -1.55 \qquad C = 0.091 \qquad D = 0.45$$

and $xq(x,Q_0^2)$ peaks at $x = 0.38$ which is close to 1/3.

The evolutions of q_Σ , g and q_{NS} are governed by Eqns. 2.13 ,19 with initial values $q(x,Q_0^2) = q_\Sigma = q_{NS}$ and g = 0. These structure functions are all evoluted from Q_0 = 1 GeV upto Q = 10 GeV with Λ = 0.5 GeV. The structure functions of quarks $q(x,Q^2)$ and antiquark $\bar{q}(x,Q^2)$ are separated as

$$q = \Sigma\, q_i = \frac{1}{2}\,(q_\Sigma + q_{NS}) \qquad (2.40)$$

$$\bar{q} = \Sigma\, \bar{q}_i = \frac{1}{2}\,(q_\Sigma - q_{NS}) \qquad (2.41)$$

The results of xq and $x\bar{q}$ are shown together with experimental data [50] in Figure 2.2 for comparision.

The large discrepancy between the data and the predicted xq in Figure 2.2 indicates that the momentum fraction carried by the sea gluons has been underestimated. The naive starting form of $q(x,Q_0^2)$ can be improved by imposing that $xq(x,Q_0^2)$ must peak at x = 1/3. To achieve this we must use all the terms in Eqn. 2.39. The solution that satisfies all the constraints and the positivity condition 1 + B + C + D + E > 0 is

A = 68.81 B = -5.15 C = 12.0 D = -12.82 E = -4.98

The xq and $x\bar{q}$ distributions are evolved upto 10 GeV as before and the results are plotted in Figure 2.3. Experimentally the gluons are found to carry about 50% of the proton's momentum and the deficiency of our crude model is indicated by the low gluon momentum fraction of 36%. We extend this approach to test the validity of valence gluons in a glueball in the next section.

$Q = 10$ GeV $\Lambda = 0.5$ GeV

$$q(x,Q_0^2) = Ax^{-1/2}(1-x)^3\,[1+B(1-x)^2+C(1-x)^4+D(1-x)^6]$$

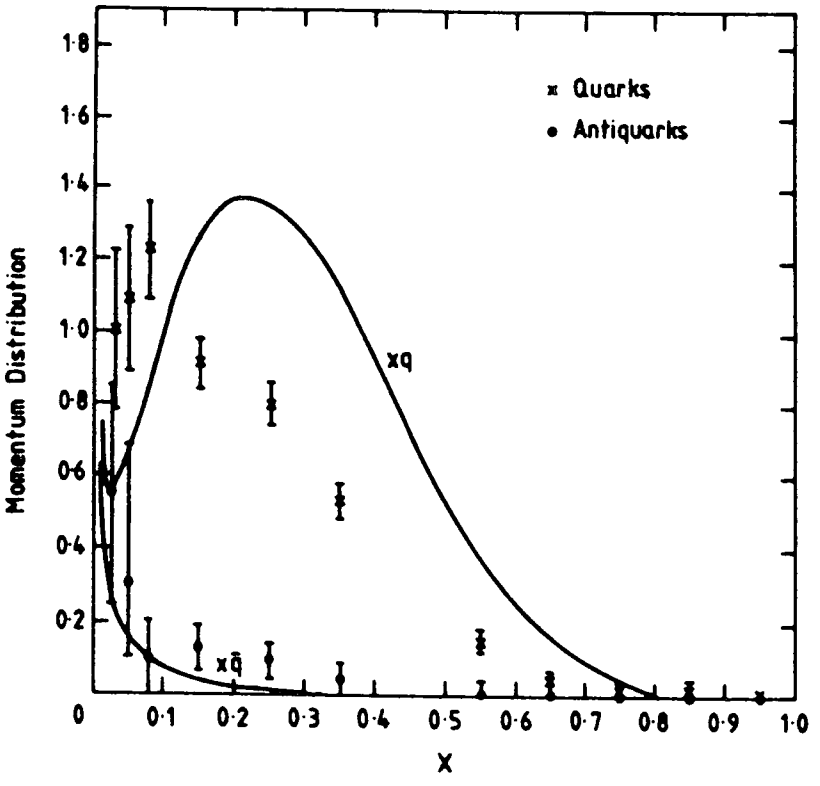

Figure 2.2

$$q(x,Q_0^2) = Ax^{-1/2}(1-x)^3\,[1+B(1-x)^2+C(1-x)^4+D(1-x)^6+E(1-x)^8]$$

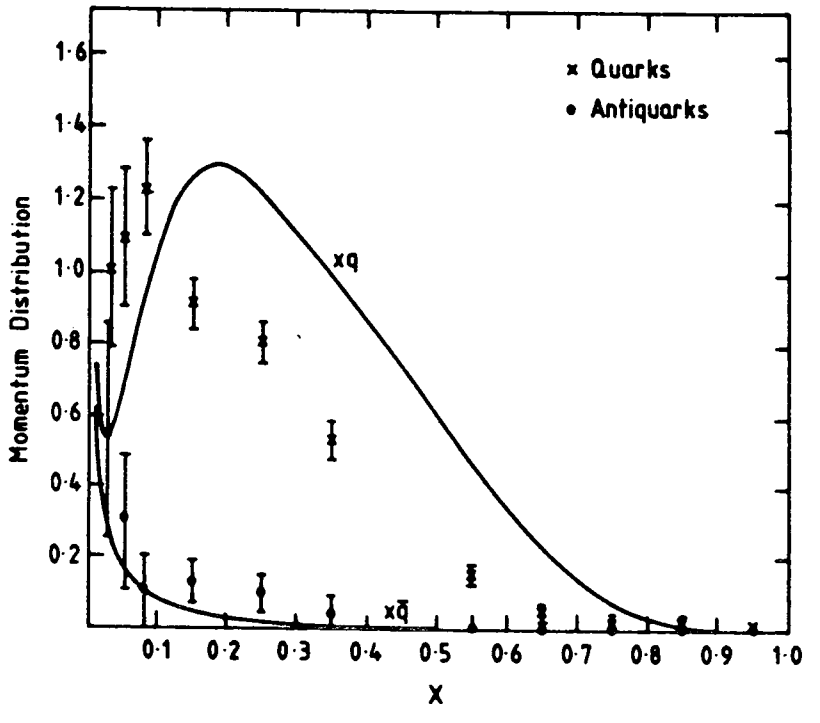

Figure 2.3

Figures 2.2-3 Comparisons between experimental data [50] and simulations of the Proton structure functions.

2.4 THE STRUCTURE FUNCTIONS OF A GLUEBALL

For simplicity, we consider only a glueball made up of two 'hard' gluons. The initial conditions for the gluon structure function are (similar to those of the proton):

$$\int_0^1 dx \; g(x,Q_0^2) = 2 \; ; \text{ the number constraint} \qquad (2.42)$$

$$\int_0^1 dx \; xg(x,Q_0^2) = 1 \; ; \text{ the momentum constraint} \qquad (2.43)$$

$$xg(x,Q_0^2) \text{ ----- peaks roughly at } x = 1/2 \qquad (2.44)$$

The simplest form is $\sim x^a(1-x)^b$ and Eqn. 2.42-43 require a = b. The counting rules this time do not offer much hint so we first test the rate of evolution by using 4 different sets of a = b.

1. $g(x,Q_0^2) = 5.10 \; x^{\frac{1}{2}}(1-x)^{\frac{1}{2}}$; $xg(x,Q_0^2)$ peaks at x = 0.75
2. $g(x,Q_0^2) = 12.0 \; x\,(1-x)$; $xg(x,Q_0^2)$ peaks at x = 0.67
3. $g(x,Q_0^2) = 60.0 \; x^2(1-x)^2$; $xg(x,Q_0^2)$ peaks at x = 0.60
4. $g(x,Q_0^2) = 280.0 \; x^3(1-x)^3$; $xg(x,Q_0^2)$ peaks at x = 0.57

The results of the evolution of these $g(x,Q_0^2)$ up to 3 GeV with $\Lambda = 0.5$ are shown in Figures 2.4-7. These graphs indicate that the momentum contribution from small x increases rapidly with increasing Q. The approximate valence gluon distribution functions are obtained by requiring that the area under each $g_v(x,Q^2)$ be equal to the number of valence gluons which is two. We have learnt from this exercise that the evolution of the small x region is so rapid that the initial value of a in x is irrelevant. Furthermore, we observe in Figure 2.7 that

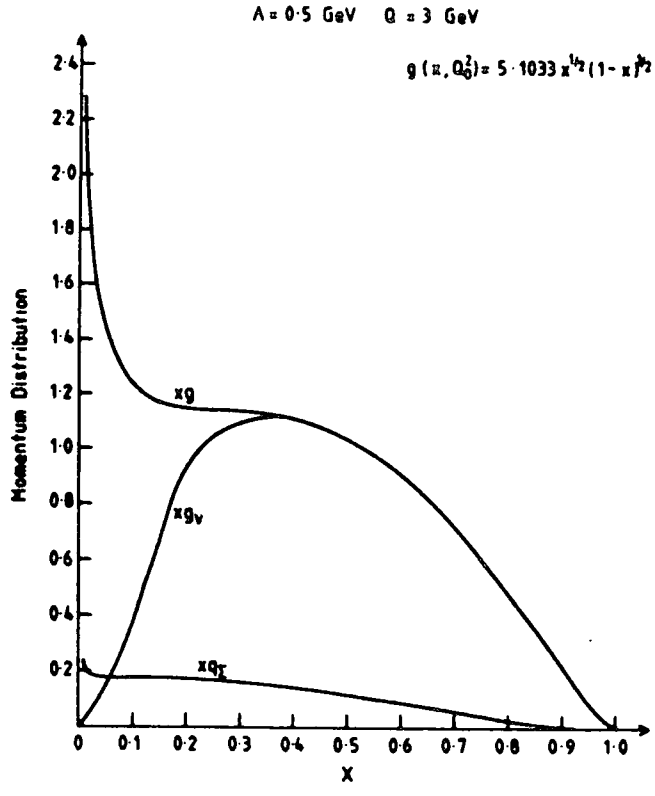

Figure 2.4

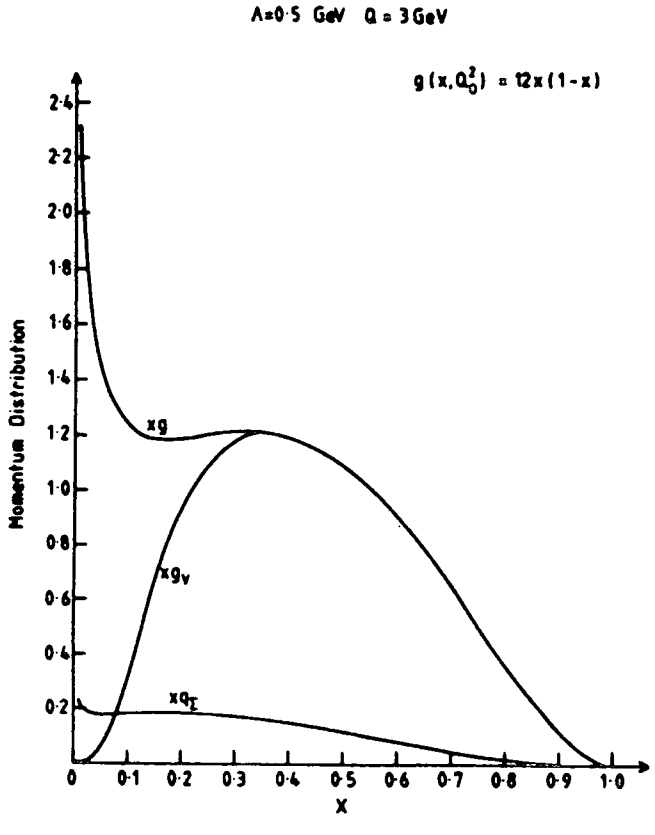

Figure 2.5

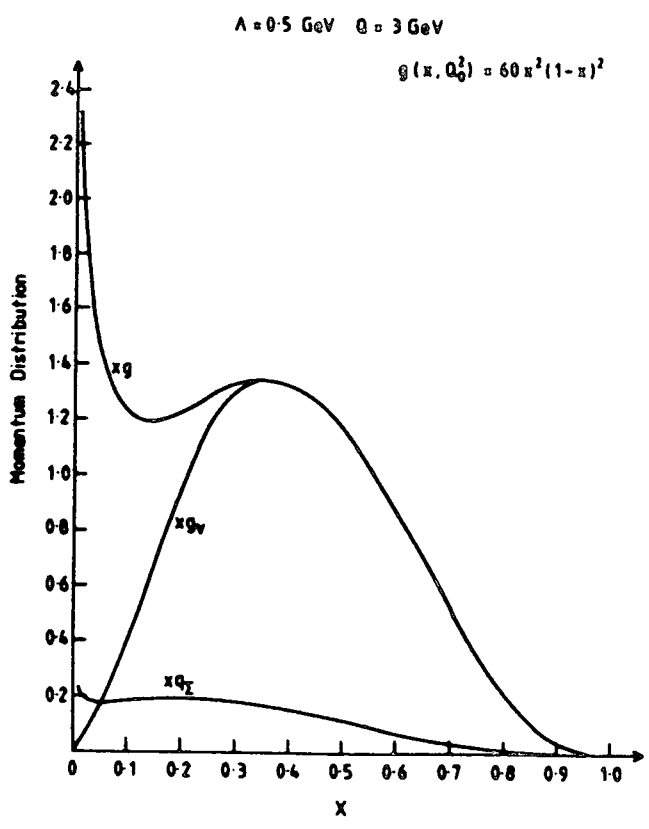

Figure 2.6

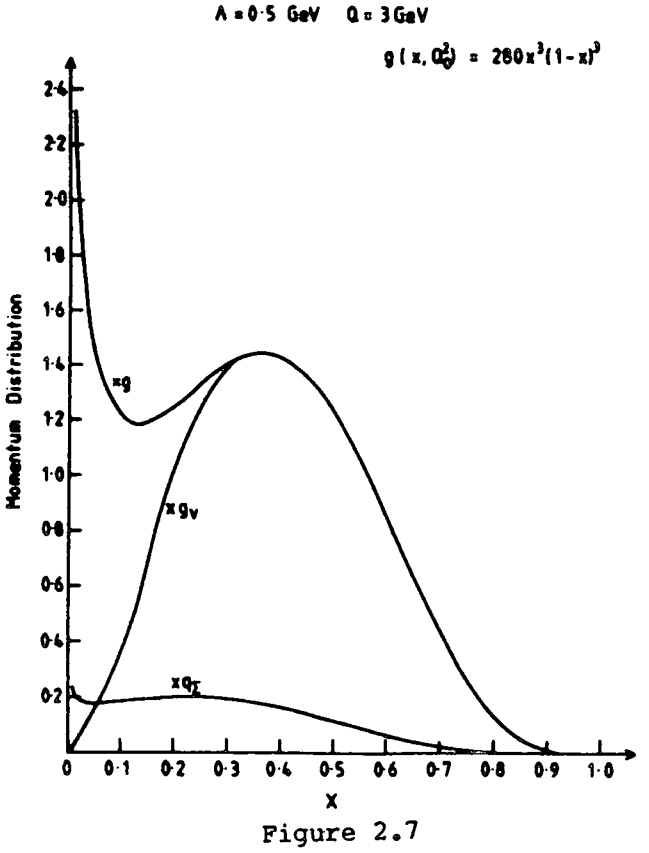

Figure 2.7

Figures 2.4-7 Simulations of the (gg) Glueball structure functions.

$g(x,Q_0^2) = 280x^3(1-x)^3$ has a distinct peak at $Q = 3$ GeV and this means an obvious separation of $g_v(x,Q_0^2)$. To study the validity of the valence gluon idea we chose the extreme case $\sim x(1-x)$, which does not have a distinct peak at $Q = 3$ GeV, as the basic form in our next discussion. We didn't choose $x^{\frac{1}{2}}(1-x)^{\frac{1}{2}}$ because it would mean overestimating the large x behaviour of $xg(x,Q^2)$ as it is indicated in Figure 2.4.

As in the case of the proton, correction terms are added to the basic form $x(1-x)$ to satisfy the initial constraints and the positivity condition. The form of $g(x,Q_0^2)$ required is

$$g(x,Q_0^2) = Ax(1-x)\left[1+B(1-x)^2+C(1-x)^4+D(1-x)^6+E(1-x)^8\right] \qquad (2.45)$$

with

$A = 10.90$ $B = -3.79$ $C = 40.0$ $E = -91.01$ $E = 57.0$

The shapes of various momentum distribution functions at $Q = 10$ GeV with $\Lambda = 0.5$ GeV are depicted in Figure 2.8. The momentum distribution $xg_v(x,Q^2)$ for so-called valence gluons is separable down to about $x = 0.09$. Hence the idea of valence gluons in light mass glueballs appears to be a valid one, at least as far as a perturbative treatment of the problem is concerned. The implication is that such low mass states would retain their glueball nature with an essential hard gluon content even when probed closely and would not dissolve into a sea of $q\bar{q}$ pairs and soft gluons until much higher momenta.

Finally, the evolution of the momentum distributions for the proton and the glueball are summarized in Figure 2.9, which are in good agreement with Figure 2.1. We next describe the experimental searches

for glueballs and our analyses of the data on the ground state scalar glueball.

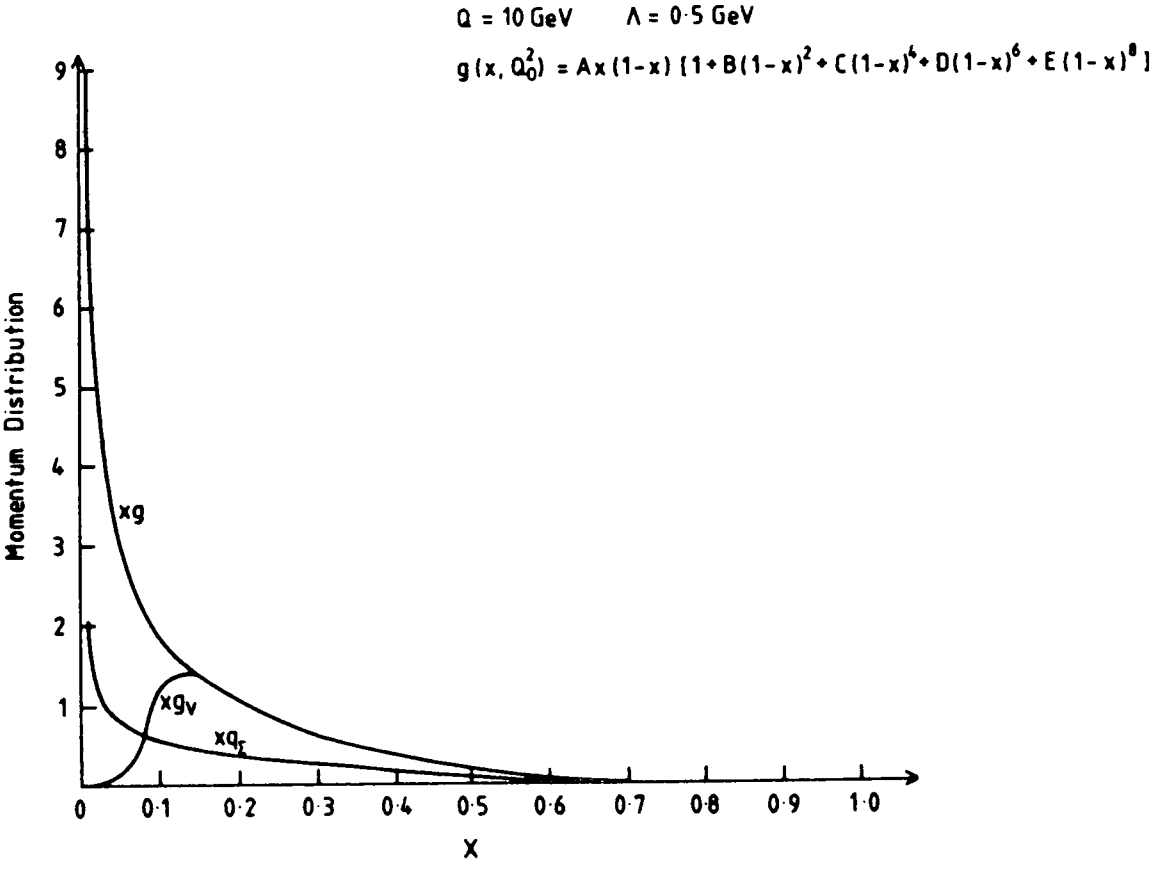

Figure 2.8 The structure functions of a (gg) Glueball with an initial form of $g(x,Q^2)$ given by Eqn. 2.45.

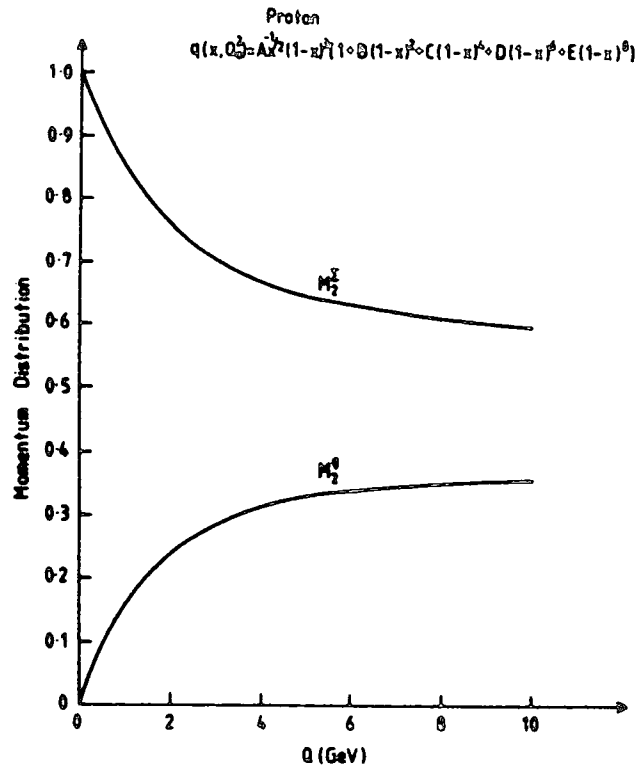

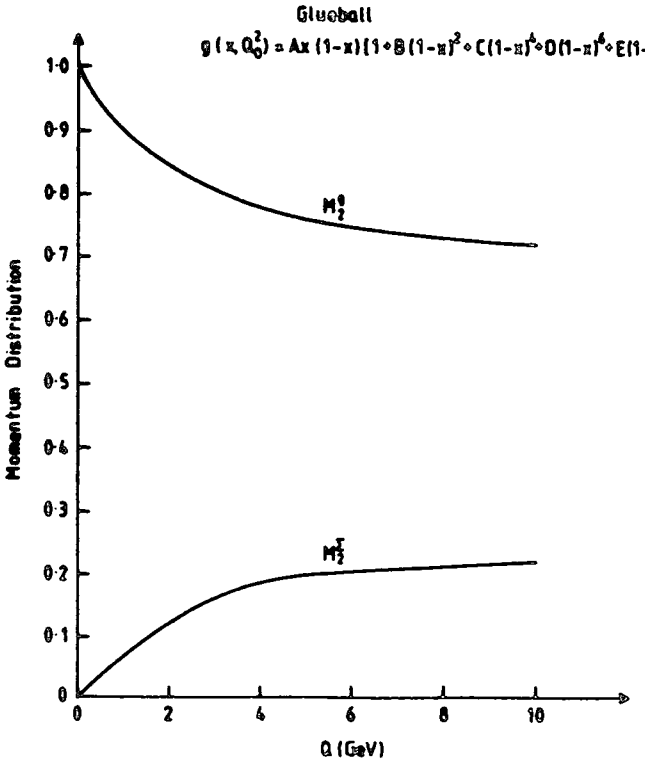

Figure 2.9 The evolutions of M_2^Σ and M_2^g in

(a) a proton with $q(x,Q_0^2)$ given by Eqn. 2.39,

(b) a gg Glueball with $g(x,Q_0^2)$ given by Eqn. 2.45.

CHAPTER THREE

EXPERIMENTAL SEARCHES FOR GLUEBALLS

3.1 INTRODUCTION

This chapter serves as a brief review of the current status of theoretical and experimental aspects of glueball spectroscopy. The current theoretical criteria for identifying glueballs are examined and applied to the possible candidates found up till now [51][52]. The discovery in 1980 of a large signal in $J/\psi \rightarrow \gamma(K\bar{K}\pi)$, at 1440 MeV (see Section 3.4.1), sparked off the current interest in the search for gluonic degrees of freedom in the hadron spectrum. This is because for J/ψ to decay into non-charm quarks, gluon intermediate states must be involved. However, the search is made difficult by the problem of gluonic states having no uniquely clear signatures [53]; they must be disentangled from a complex, densely spaced spectrum of $q\bar{q}$ mesons. This is hindered further by our poor understanding of the radially excited meson spectra. Because of this no definite conclusions have been reached on the glueball candidates that have emerged since 1980. The situation can only be improved by high quality data with largely increased statistics such that the necessary partial wave analyses can be performed with greater confidence.

The potential glueball candidates have been identified using a number of different criteria. Some of these are not stringent enough to be

taken literally. Moreover alternative explanations to the gluonium interpretation have been suggested for all these potential candidates. There are already many reviews [54][55][56] on glueballs with emphasis on comparing predictions from various models of explanation with experimental data. However, the creditability of these models depends very much on the assumptions involved. The selection criteria and ingredients of individual models are examined in the following sections.

3.2 GLUONIUM SELECTION CRITERIA

Although we have not yet fully understood the properties of glueballs, largely because of the lack of any convincing glueball candidates, there are some general features of glueballs which can be used as pointers in glueball searches. The followings are criteria based on such features for identifying potential glueball candidates.

3.2.1 Flavour symmetric couplings

Pure glueball states are by nature SU(3) flavour singlets and in principle will have no preferential coupling to particular quark flavours or charges. According to this, glueballs must decay to isospin, flavour singlets.

Another useful selection mechanism is to use the conservation of charge conjugation together with SU(3) symmetry. The isospin, flavour singlet is just the 1_S in the tensor products of two octets,

$$8 \times 8 = 1_s + 8_s + 8_a + 10_a + \overline{10}_a + 27_s$$

and is a linear combination of charge conjugated pairs like $K\bar{K}$ [57].

The selection rules are (without kinematics):

1. by SU(3)

   g $\not\rightarrow$ non flavour singlets i.e. $\not\rightarrow$ $K_L K_S$, $\eta\eta'$

2. by SU(3) and conservation of charge conjugation with $C = \pm 1$

   $g^+ \not\rightarrow$ VP, VT etc i.e. $\not\rightarrow$ $K_V\bar{K}$, $K_V\bar{K}_T$

   $g^- \not\rightarrow$ PP, VV, TP etc i.e. $\not\rightarrow$ $K\bar{K}$, $K_V\bar{K}_V$, $K_T\bar{K}$

   where V, P and T stand for vector, pseudoscalar and tensor respectively.

For octets in the tensor product both even and odd C can be constructed depending on the symmetry of the combination. As a quarkonium $q\bar{q}$ can decay into flavour non singlets hence

$$(q\bar{q}) \rightarrow PP, PV, PT, VV, VT \text{ etc.}$$

Therefore a glueball can be identified by checking the decay channels.

The last two selection rules are stable against $SU(3)_f$ symmetry breaking, as quark masses only create splittings between different iso-multiplets within flavour multiplets. Nevertheless, such breaking will change the relative decay rates between allowed states. They are also expected to hold even if by some mechanism some particular flavour channels are prefered as this again will only change relative decay rates. $SU(3)_f$ symmetry breaking effects of both dynamical and kinematical origin are discussed in the context of $\iota(1440)$ and $\theta(1690)$ decays. The first selection rule may be broken by mixing between isoscalars. There is an alternative derivation of the above selection

rules which generalizes the G_I-parity of isospin to G_U and G_V parities of U, V spin that relate s, d and u, s quarks [58].

3.2.2 Suppression of radiative decays

Since photons do not couple directly to gluons, glueballs can only decay radiatively via a virtual quark loop. From Figure 3.1 , the amplitude is suppressed by a factor α_s compared to the two photon decays of quark mesons. The suppression breaks down if there is substantial mixing between quark and gluon states. Such mixing can happen if the states are almost degenerate. However, the suppression can still be broken for the scalar and pseudoscalar channels without mixings. This is because of the trace and axial anomalies, which afflict the scalar and pseudoscalar channels respectively [33]. The total anomalies in chiral limit which include QED contributions are:

$$\theta_{\mu\mu}^{tot} = \frac{\beta(\alpha_s)}{4\alpha_s} \mathrm{Tr} G\cdot G + N_c\left(\sum_i^{N_f} e_i^2\right) \frac{\beta(\alpha_s)}{4} F\cdot F \qquad (3.1)$$

$$\partial_\mu J_\mu^5 = \frac{2N_f}{4} \mathrm{Tr} G\cdot\tilde{G} + N_c\left(\sum_i^{N_f} e_i^2\right) \frac{\alpha}{4\pi} F\cdot\tilde{F} \qquad (3.2)$$

where $\beta(\alpha)$ = QED beta function

$$= \frac{2\alpha}{3\pi} + \frac{\alpha^2}{2\pi^2} + \cdots\cdots$$

and e_i = electric charge of ith quark.

From these anomaly equations, the low energy theorems [33] for two photon matrix elements can be derived.

$$\langle 0 | \frac{\beta(\alpha_s)}{4\alpha_s} \mathrm{Tr} G\cdot G \, | \gamma(k_1)\gamma(k_2)\rangle = \frac{\alpha}{3\pi} N_c\left(\sum_i^{N_f} e_i^2\right) F^1F^2 + O\left[(k_1k_2)^2\right] \qquad (3.3)$$

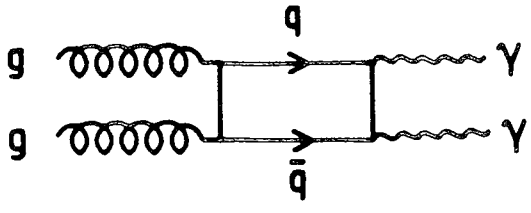

Figure 3.1 The lowest order QCD diagram for gg -> γγ.

$$\langle 0| \frac{\alpha_s}{4\pi} \mathrm{Tr} G.\tilde{G} |\gamma(k_1)\gamma(k_2)\rangle = \frac{\alpha N_c}{\pi N_f}\left(\sum_i^{N_f} e_i^2\right)F^1F^2 + O\left[(k_1k_2)^2\right] \quad (3.4)$$

where $F^i_{\mu\nu} = k^i_\mu \varepsilon^i_\nu - k^i_\nu \varepsilon^i_\mu \qquad (i = 1, 2)$

The important feature of these equations is that the right hand sides do not have the expected suppression factor α_s^2. Thus the scalar and pseudoscalar glueballs may well have substantial two photon widths. Furthermore the photon widths can be converted into radiative decay widths using vector dominance [59] arguments. Hence their radiative widths may also be significant.

3.2.3 Exotic quantum numbers and state counting

There are gluonic states with quantum numbers not accessible to $q\bar{q}$ mesons in the quark model such as $J^{pc} = 1^{-+}$ in the spectrum of pure glueballs and hybrids. The discovery of such a state would provide strong evidence for the existence of gluonic states. However, even this would not be definitive, since such exotic quantum numbers might also be carried by quark states not describable in the non-relativistic quark model. As there will be no mixing for odd glueballs, radiative decay modes can be used to distinguish odd glueballs from exotic quark states. Other glueballs that do not have exotic quantum numbers are difficult to separate from singlets of meson nonets. A clear signature of these glueballs is the presence of an extra singlet, one more than required by the non-relativistic quark mode. The counting of the number of states ($I = 0$) with given quantum numbers is the only reliable way to establish the intrusion of extra dynamics regardless of the strong possibility of mixing or hybrids. This is the solid criterion that we use in our

search for the ground state glueball to be described in Chapter 4.

3.2.4 OZI selection rule

OZI rule [60] applies to ideally mixed quarkonium decays in which final states without the initial quarks are suppressed. Together with the criteria in Section 3.2.1 the following selection rules can be obtained (without kinematics):

$(u\bar{u}, d\bar{d}) \not\rightarrow \phi\phi, \phi\eta$

$(s\bar{s}) \not\rightarrow \omega\omega, \omega\eta, \rho\rho, \rho\pi, \pi\pi$

$g^+ \rightarrow \omega\omega, \phi\phi, \rho\rho, \pi\pi$

$g^- \rightarrow \omega\eta, \phi\eta, \rho\pi$

Potential glueball candidates would decay into both OZI allowed and forbidden channels. However these rules may not be exact because of symmetry breakings in which some particular flavour channels are favoured. A glueball may then be misidentified as an ideally mixed meson as a result. In any case, the breakdown of the OZI rule has been used as an indication for glueball formation [61] and examples of such identification will be discussed in the next Section. It is generally taken that the glueball widths should be the geometric mean of OZI allowed and forbidden decays [62]. This is based on the observation that in perturbative QCD, OZI suppressed amplitudes are mediated by intermediate gluons. Figure 3.2 shows that initial state quarks in the process annihilate into gluons which then create the final state quarks. Only the R.H.S of the diagram occurs in glueball decay so we expect a suppression which is the square-root of full OZI suppression given by

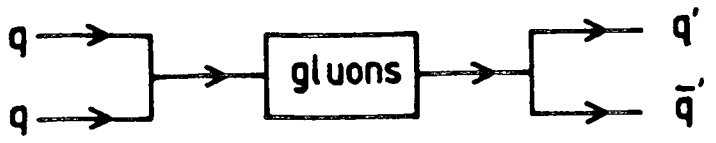

Figure 3.2 OZI disconnected diagram - the number of intermediate gluons depends on the quantum numbers of the initial $q\bar{q}$ pair.

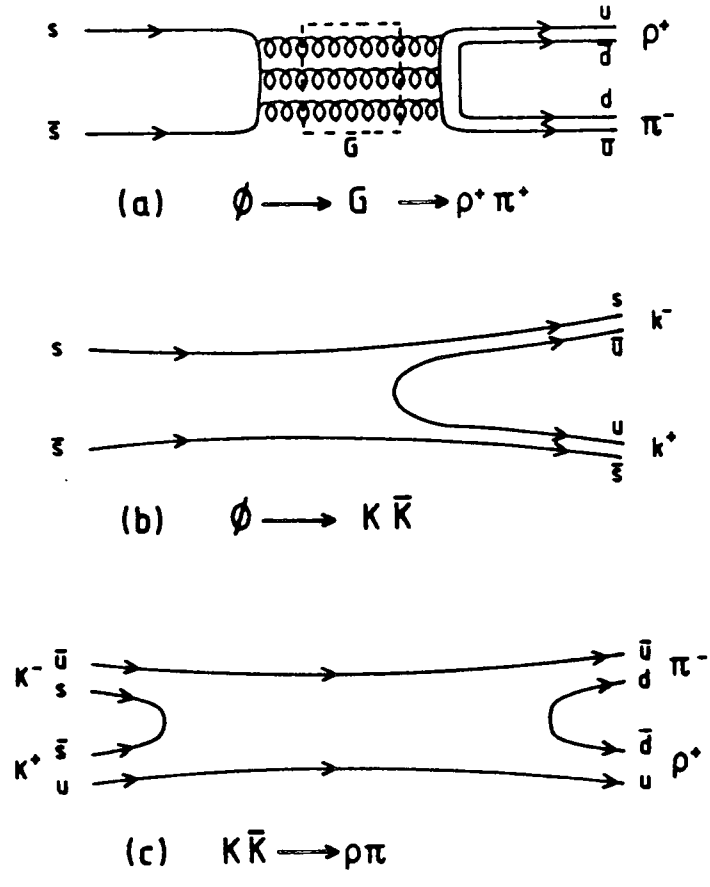

Figure 3.3 (a) The OZI quark line diagram for the reaction $\phi \rightarrow \rho^+\pi^-$, which is disconnected and OZI forbidden.

(b)&(c) The OZI allowed diagrams for $\phi \rightarrow K\bar{K}$ and $K\bar{K} \rightarrow \rho\pi$.

$\Gamma^2_{\text{OZI forbidden}}$. However this estimate ignores the distinction between the two and three gluon channels which depends on the quantum numbers of the initial state. As is well known the light pseudoscalars show large deviations from ideal mixing (see Section 3.4.1.5) which implies that the phenomenological OZI rule exhibited by the vector nonet is not honoured in the $J^{PC} = 0^{-+}$ two gluon channel at ~ 1 GeV.

The width of a glueball Γ_G is usually estimated on the assumption that OZI suppressed amplitude like Fig. 3.2 are dominated by glueballs as intermediate state. A simple example of this assumption is the reaction $\phi \rightarrow G \rightarrow \rho\pi$ in which a glueball G appears as the dominant pole, such that the width Γ of $\phi \rightarrow \rho\pi$ is roughly equal to the square of Γ_G. Γ is obtained by giving the OZI allowed width $\Gamma_{\text{OZI allowed}}$ a suppression factor $\Gamma_{\text{OZI forbidden}}$, yielding the estimate $\Gamma_G \sim \sqrt{(\Gamma_{\text{OZI allowed}} \cdot \Gamma_{\text{OZI forbidden}})}$. This assumption rests entirely on the empirical OZI rule which is not of itself consistent with unitarity (see Section 4.2). This can be illustrated by the unitarity equation for $\phi \rightarrow \rho\pi$,

$$\text{Im}\langle\phi|\rho\pi\rangle = \langle\phi|K\bar{K}\rangle\langle K\bar{K}|\rho\pi\rangle + \text{OZI forbidden terms} \qquad (3.5)$$

$\phi \rightarrow K\bar{K}$ and $K\bar{K} \rightarrow \rho\pi$ are both OZI allowed as shown in Figure 3.3. The L.H.S of the unitarity equation is OZI suppressed, though the term with $K\bar{K}$ intermediate state is OZI allowed. There should be no cancellation between the allowed and disallowed terms so $\langle K\bar{K}|\rho\pi\rangle$ must be small even though it is OZI allowed. The glueball couplings in this case depend on the contribution from the OZI allowed channel $K\bar{K}$ to the real part of

$\langle\phi|\rho\pi\rangle$. Γ_G would be smaller than the simple estimate if $Re\langle\phi|\rho\pi\rangle$ is saturated by the $K\bar{K}$ contribution or much bigger if there are big cancellations. This discussion becomes complicated if quark resonances occur close to the relevant glueball poles. In general, the widths of glueballs may not be simply characteristized by hadronic widths through simple estimates based on OZI rule.

3.2.5 Production in hard gluon channels

If the gluonic states are made of valence gluons then they will be copiously produced in hard gluon channels. A good example is the radiative decays of vector mesons, in particular the radiative decays of J/ψ [63][64]. There are four main energetically allowed decay modes of the $J/\psi \to \gamma + X$ that require c and $\bar{c}$ quarks to annihilate. They are those in Figure 3.4. This 'classic' method is attractive because the estimate $\Gamma(J/\psi \to \gamma gg)/\Gamma(J/\psi \to ggg) = 16\alpha/5\alpha_s$ gives $B(J/\psi \to \gamma gg) \simeq 10\%$ [65]. In perturbation theory $J/\psi \to \gamma gg$ is the dominant radiative decay mode of $J/\psi \to \gamma + X$ where the two gluons are in a net colour singlet. Hence this is an excellent channel to search for glueballs with positive C-parity. The $\iota(1440)$, the $\theta(1690)$ and possibly the $\xi(2200)$ were found as glueball candidates in the study of this channel [64]. The validity of these claims will be discussed later in the Chapter.

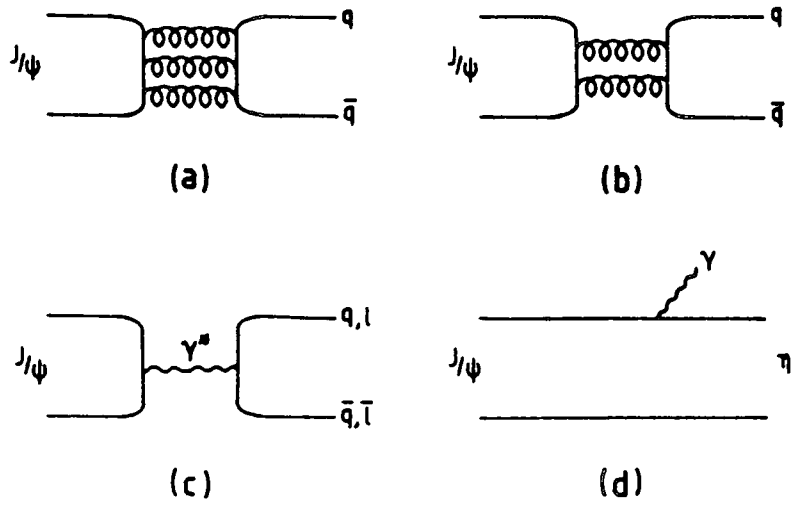

Figure 3.4 Leading order Feynman diagrams for radiative J/ψ decay.

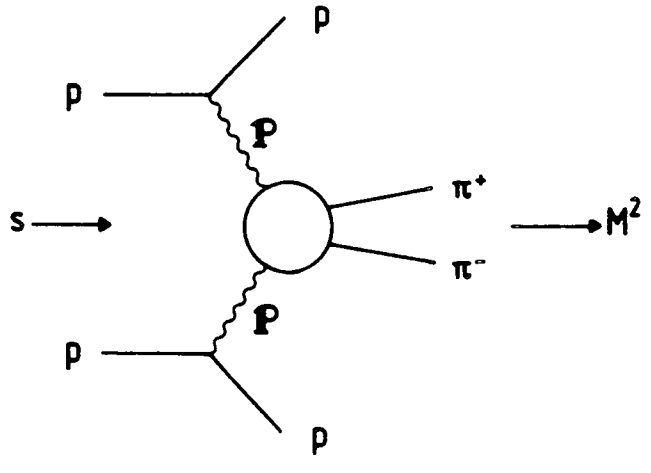

Figure 3.5 Diagram for P P -> ππ.

3.2.6 Double diffractive processes

An attractive possibility available at very high energies for glueball searches is the special nature of double diffractive processes [66]. Just as single diffraction can be viewed as gluons surrounding one proton being transferred in the glancing interaction to the other through a gluonic intermediate state, known as the pomeron, double diffraction can be pictured as gluons from each proton fusing to make new meson states [Fig. 3.5]. This double pomeron exchange process yields final states with the quantum numbers of glueballs. Such was the motivation for a series of experiments at the ISR [67][68][69]. The first showed double pomeron events could be isolated, while the Axial Field Spectrometer (AFS) Collaboration experiment [69] on exclusive central meson production in $pp \rightarrow pp\pi\pi$, $pp4\pi$, $pp K\bar{K}$, etc., allowed for better resolution and increased statistics. In such a process, the quantum numbers are restricted to $I = Y = 0$, $C = P = +1$ and even spins. The studies of meson states produced in such diffractive reactions constitute the main core of this thesis and the details of their analysis are presented in the following Chapters.

3.3 THE TENSOR GLUEBALL CANDIDATES FROM BNL

Three tensor glueball candidates $g_T(2050)$, $g_T'(2300)$ and $g_T''(2350)$ were found in the BNL/CCNY π^-p experiment [61] through the OZI forbidden $\phi\phi n$ channel shown in Figure 3.6. The background to the experiment are the two OZI allowed transitions
(a) $\pi^-p \to K^+K^-K^+K^-n$ and (b) $\pi^-p \to \phi K^+K^-n$, shown in Figure 3.7. The breakdown of OZI rule is indicated by the enormous enhancement in the $\phi\phi$ production cross section. It is found that after corrections the enhancement is many times the density of the backgrounds. The three resonances with $J^{Pc} = 2^{++}$ correspond to the three K-matrix poles (see Appendix A.III & Section 7.1) in the best fit to the data found in a partial wave analysis. According to BNL the mixing of S- and D-waves is substantial in these three tensor states. Nevertheless, the interpretation of K-matrix poles as being the actual resonances requires more thought. The topic of pole interpretation will be discussed in Chapters 6 and 7.

3.3.1 Two poles model

In terms of a fit with Breit-Wigner poles, the BNL first reported a two resonance solutions to their $\phi\phi$ enhancement [70]. Let us first look at this. Figure 3.6 can be re-expressed in terms of particle exchanges as shown in Figure 3.8 . With the aid of Figure 3.8 , the amplitude for $\pi^-p \to \phi\phi n$ can be written as a product of three terms summing over the number of glueball states [71],

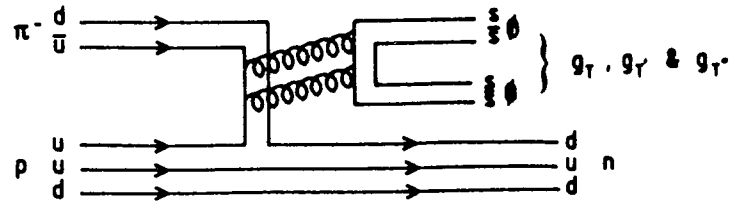

Figure 3.6 The OZI disconnected diagram for the reaction $\pi^- p \rightarrow \phi\phi n$. For the g_Ts, $J^{PC} = 2^{++}$, only two intermediate gluons are required.

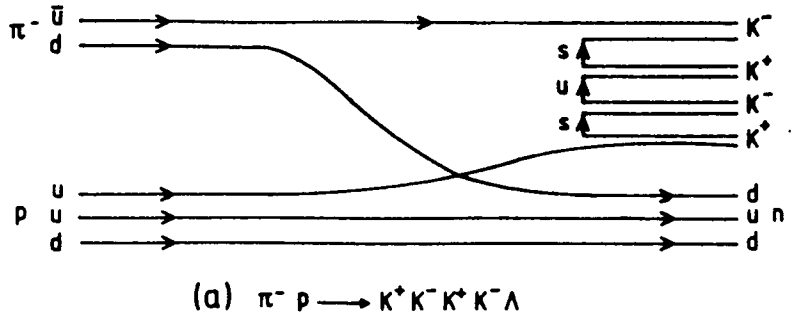

(a) $\pi^- p \longrightarrow K^+ K^- K^+ K^- \Lambda$

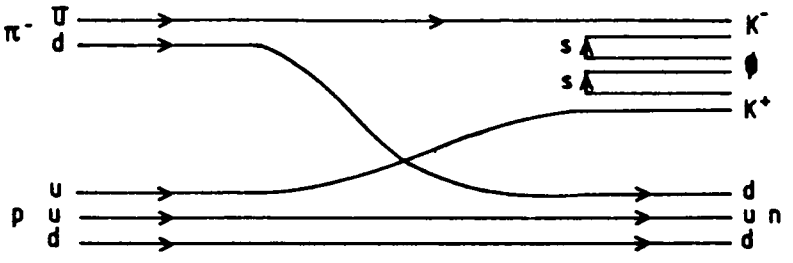

(b) $\pi^- p \longrightarrow \phi K^+ K^- n$

Figure 3.7 Backgrounds (OZI allowed) of the OZI forbidden $\pi^- p \rightarrow \phi\phi n$.

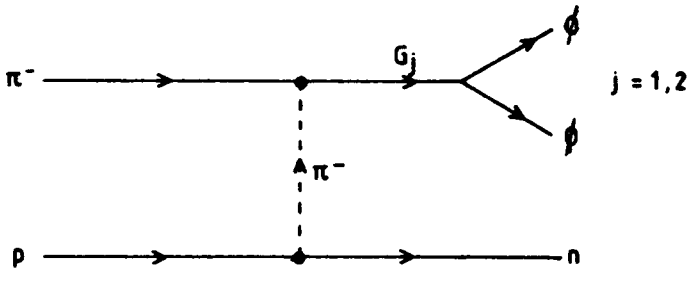

Figure 3.8 The reaction $\pi^- p \rightarrow \phi\phi n$ with a π exchange and two possible glueballs $G_{1,2}$ as resonance propagators.

$$\text{i.e.} \quad A(\pi^- p \to \phi\phi n) = \sum_{j=1}^{2} R(\pi^- p \to G_j n)\Phi_j T(G_j \to \phi\phi).$$

where R is the production amplitude given by a standard Reggeized expression,

Φ is the usual resonance propagator,

T represents the decay amplitude for $G_j \to \phi\phi$.

The glueball pole G_1 is the average of g_T and g_T' while G_2 is identical to g_T''. These are the positions of the 2 resonances first reported by BNL [70]. The glueballs are treated as ordinary hadrons in that their couplings to $\phi\phi$ are comparable to other hadronic couplings. This assumption is the simplest explanation for the OZI violation in glueball production channels. With the flavour independent decays of glueballs as a further assumption this model is able to explain the main features of the BNL data. The same may not be true for a three pole analysis as there are no obvious cancellations in this model. The success of this analysis raises the question of where the glueball Regge trajectory is.

3.3.2 Quarkonium Explanation

Having briefy discussed the glueball option of the g_Ts. We now consider the possibility of quarkonium. A tensor isoscalar resonance ε has been seen in partial wave analysis of $p\bar{p} \to \pi\pi$ at 2150 MeV [72]. If the tensor nonet is ideally mixed as it is believed to be (c.f. Section 3.4) , then ε can be thought of as a second radial excitation of the nonstrange f(1270). The isoscalar partner of the ε would then be entirely made up of strange quarks and decay strongly to $\phi\phi$ as the g_Ts do in $\pi^- p$. However, this does not match the number of

resonances observed, even if a glueball is included. Either this simple minded picture is completely wrong or the BNL interpretation is at risk. Since the radially excited tensor nonet is not well understood, this makes the discussion of quarkonium-glueball mixing impossible. In any case it is important to look for other decay channels as an $s\bar{s}$ meson at 2160 MeV would decay to $\phi\phi$, $K^*\bar{K}^*$ and $K\bar{K}$ in the ratios 1 : 4 : 0.37 [73].

3.3.3 Hybrids

The $\phi\phi$ enhancement can also be a hybrid $q\bar{q}g$. These hybrid states are likely to decay by formation of a $q\bar{q}$ colour-octet pair from the gluon, $g \rightarrow (q\bar{q})_8$, followed by disassociation of the resultant $q\bar{q}q\bar{q}$ state into two $q\bar{q}$ mesons [Fig. 3.9], $q_1\bar{q}_2 g \rightarrow (q_1\bar{q}_2)_8(q_3\bar{q}_4)_8 \rightarrow (q_1\bar{q}_4)_1(q_3\bar{q}_2)_1$. As will be discussed later in Section 3.4.1.1, the TM mode of gluons in the Bag Model has strong s-channel coupling to $s\bar{s}$ while the TE mode has flavour symmetric coupling. A ϕ-like hybrid with a TM mode gluon, $s\bar{s}g_{TM}$, therefore decays to final states with four kaons including $\phi\phi$. The mass of such hybrid has been estimated to lie within the enhancement region and can be identified with one of the $\phi\phi$ candidates [54]. Another $\phi\phi$ candidate might also be identified with a 2^{++} TM-TM glueball which, like the $s\bar{s}g_{TM}$ hybrid, decays chiefly to the $\phi\phi$ in a relative S-wave. However the g_Ts are known to have both S- and D-waves. The last candidate would have to be either a 2^{++} TE-TE glueball or its radial excitation. Because of parity conservation arguments, the TE gluon does not couple to an S-wave pair $(q\bar{q})_8$, these 2^{++} TE glueballs decay to two vector mesons with two units of angular momentum. If this

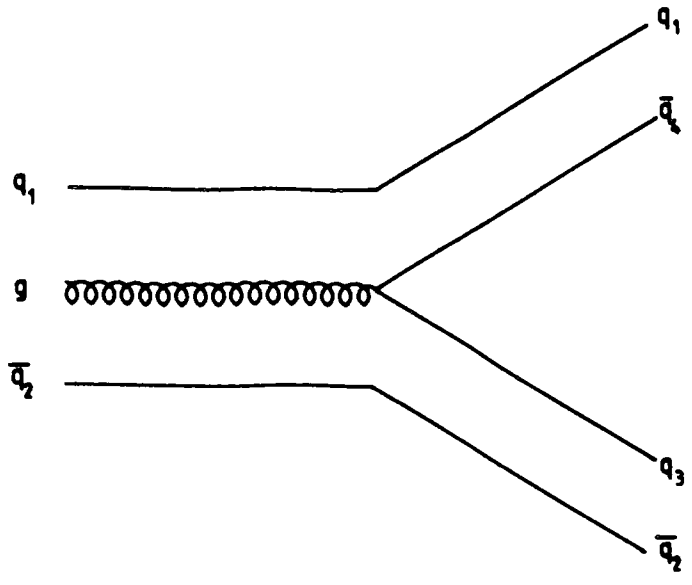

Figure 3.9 The dominant two-body decay diagram for a $q\bar{q}g$ hybrid.

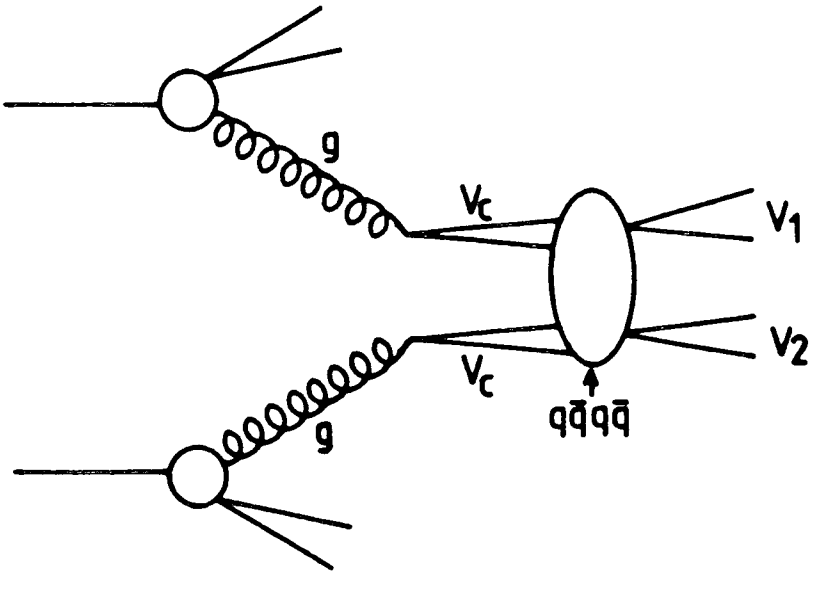

Figure 3.10 Drell-Yan type mechanism for the production of two vector mesons with a four-quark intermediate state.

is the case then other final states such as ρρ and K*K* should also have been seen, because of the flavour symmetric couplings of the TE gluon.

3.3.4 Four-Quark scenario

An attempt to identify the enhancement in φφ as a four-quark state resonance has been made [74]. An S-wave four-quark state in bag and potential models has the following salient features:

I.

The wavefunctions of $q\bar{q}q\bar{q}$ states consist of two parts; in one, the $q\bar{q}$ pairs are in the colour singlet representations and in the other part, the $q\bar{q}$ pairs are in the colour octet representations.

II.

Their decays obey the OZI rule; most of the $q\bar{q}q\bar{q}$ can be split into two constituent colour singlet $q\bar{q}$ mesons, making them difficult to distinguish from a continuum. However, there are $q\bar{q}q\bar{q}$ states which mainly decay through a pair of vector mesons (VV). They have widths narrow enough to be observed as resonances [75]. What is attractive is that a 2^{++} $s\bar{s}s\bar{s}$ four quark state at 2.25 GeV has been predicted to exist in the Bag Model [76]. This predominantly decays to φφ with a width of 360 MeV.

The production of narrow four quark states is by a Drell-Yan [77] type process in which the glue partons originating from the colliding hadrons couple to the colour octet (V_c) of the $q\bar{q}q\bar{q}$ states which in turn decay into two vector mesons. This mechanism is depicted in

Figure 3.10 . The coupling between gluon and colour octet vector $q\bar{q}$ is evaluated using the QCD version of the Vector Dominance Model in QED. The calculated $\phi\phi$ production cross section for a 2^{++} state at 2160 MeV is in agreement with experiment, when a K factor correction is taken into account. One of the remaining $\phi\phi$ resonances seen at BNL could be assigned as an excited $s\bar{s}s\bar{s}$ four quark state with an orbital angular momentum L = 2 which decays to $\phi\phi$ through a D-wave. Another possibility for $J^{PC} = 2^{++}$ is an excited $s\bar{s}s\bar{s}$ with S = 2, L = 2, which should be much heavier than the S = 0, L = 2 state at 2160 MeV. A tensor glueball can be included to make up the required number. However, it is believed that only the 0^{++} sector of the four-quark states can exist as observable bound states [78]. Nevertheless this approach provides an alternative explanation of the data.

3.3.5 Sequential Pair model

The identification of the g_Ts as glueballs at BNL soley rests on the validity of OZI rule. However, it is possible that the gluons which convert into di-mesons do themselves favour some particular mass value through the semi-classical sequential pair creation mechanism [79]. The mesons are produced in the following sequence:

$$J^{PC} = 2^{++} \qquad gg \rightarrow \bar{q}_1 q_1 \rightarrow \bar{q}_1 (q_2 \bar{q}_2) q_1 \rightarrow (\bar{q}_1 q_2)(\bar{q}_2 q_1)$$

The gluon system is supposed to convert rapidly to a light $q_1\bar{q}_1$ which then breaks apart, maintaining a gluonic field ('string') between them. Eventually a second pair $q_2\bar{q}_2$ is produced along the 'string' and this leads to the two vector mesons $\phi\phi$ in this particular case. The decay

rate of $\bar{q}_1 q_1 \rightarrow (\bar{q}_1 q_2)(\bar{q}_2 q_1)$ is proportional to the square of the overlap integral of the radial wavefunctions of $\bar{q}_1 q_1$ and two mesons. The integral is an oscillating function of the mass of the system and leads to broad mass bumps which are not resonances but an interference effect reflecting the sequential mechanism of pair creation. The oscillations are governed by the zeros of the spherical Bessel function in the partial waves of $\bar{q}_1 q_1$. Successive mass bumps are generated by this mechanism in the region of the BNL enhancement. Although there is no prohibition for a genuine resonance to occur on top of such a bump. It is unlikely that this should happen several times as is implied by the three resonance claim.

3.3.6 Phenomenological argument

Apart from the above argument, the threshold enhancement can also be explained with phenomenlogical reasoning [80]. Instead of going through the process in Figure 3.6, the reaction $\pi^- p \rightarrow \phi\phi n$ can proceed by the emission of two hard gluons as depicted in Figure 3.11 . The two hard gluons are supposed to be collinear and independent. They also behave like the gluons in Drell-Yan and other hard-scattering processes. Since hard gluons in these processes decay into lepton pairs with $\langle p_\perp \rangle \simeq 0.6$ GeV [81] thus for the S-wave, the threshold enhancement is

$$m_{\phi\phi} \simeq \sqrt{[(2m_\phi)^2 + 2 \times (0.6 \text{ GeV})^2]} \simeq 2.2 \text{ GeV}.$$

The angular momentum barrier for the D-wave is approximately given by

$$\frac{2\ell + 1}{r} \simeq 1 \text{ GeV}$$

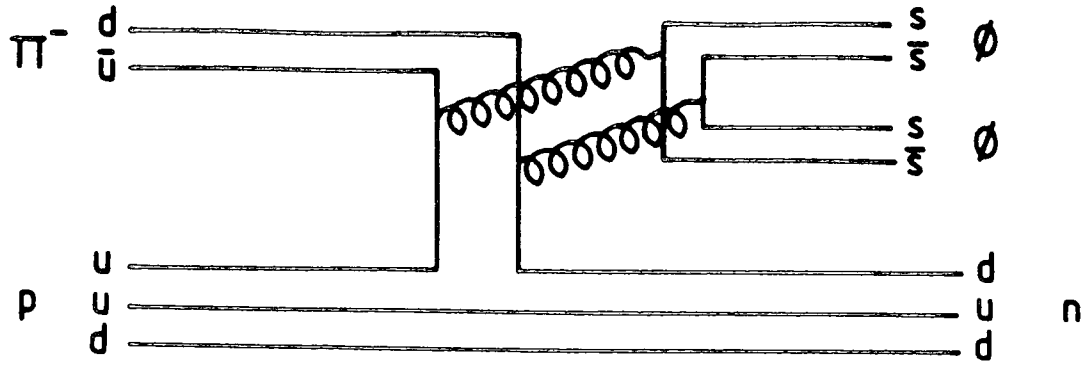

Figure 3.11 $\pi^- p \rightarrow \phi\phi n$ with hard gluon emissions.

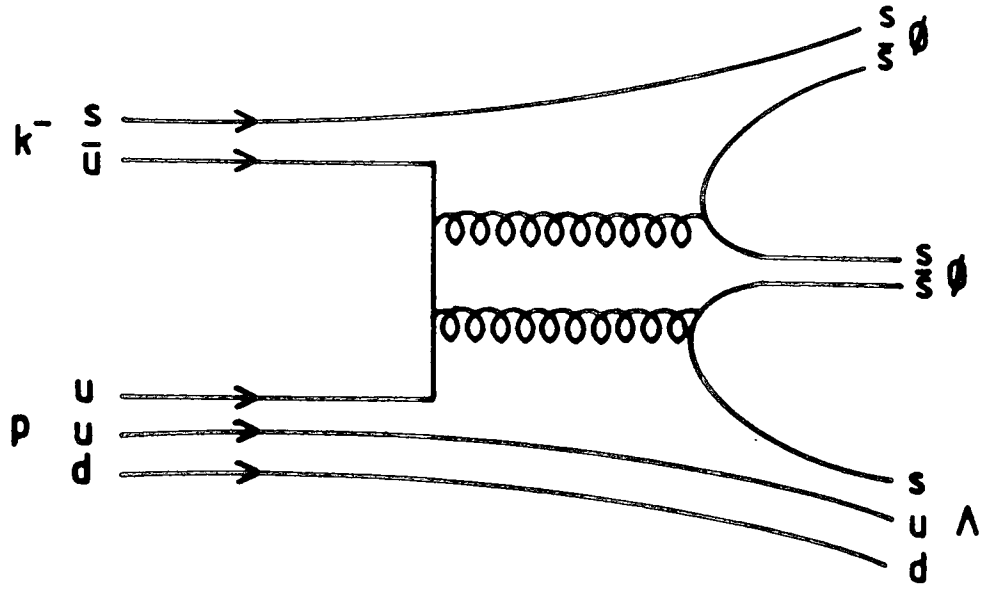

Figure 3.12 $K^- p \rightarrow \phi\phi\Lambda$ as an OZI forbidden process.

for $\ell = 2$ and $r = 1$ fm.

Thus for D-wave

$$m_{\phi\phi} \simeq \sqrt{[(2m_{\phi})^2 + 2 \times (0.6\ \text{GeV})^2 + (1\ \text{GeV})^2]} \simeq 2.4\ \text{GeV}.$$

This is in general agreement with the data. The same reasoning does not apply to $K^-p \rightarrow \phi\phi\Lambda$ in which two of the quarks created hadronize with the fragments of the original particles and these tend to move in opposite directions [Fig. 3.12]. It is therefore crucial to search for g_Ts in K^-p scattering to consolidate the glueball claim. However, the $K^-p \rightarrow \phi\phi\Lambda$ channel is viewed as an OZI allowed process [Fig. 3.13] by some fraction of the physics community [61]. To them the absence of g_Ts in K^-p is not a problem.

3.4 GLUONIUM CANDIDATES IN J/ψ RADIATIVE DECAYS

As already mentioned in Section 3.2.5 that $J/\psi \rightarrow \gamma + X$ is a hard gluon process which is thought to be an ideal place for glueball hunting [82]. Two more glueball candidates $\theta(1690)$ [83] and $\xi(2200)$ [84] have been found in this channel after the discovery of the first candidate, the $\iota(1440)$ [85]. The radiative J/ψ decays have been studied in experiments DM2 [86], MARK II [87], MARK III [88] and CRYSTAL BALL [89] operating at the storage rings DCI and SPEAR. Although lots of data have been assembled no definite conclusions about their glueball status can be made. What follows is an attempt to give a concise review of the various interpretations of the ι, θ and ξ.

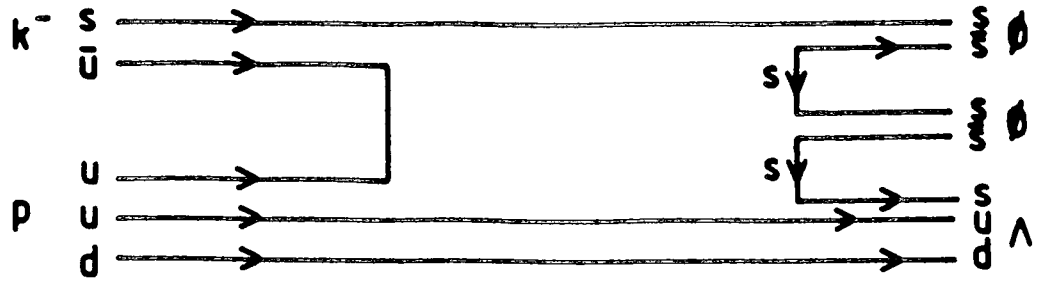

Figure 3.13 $K^-p \rightarrow \phi\phi\Lambda$ as an OZI allowed process.

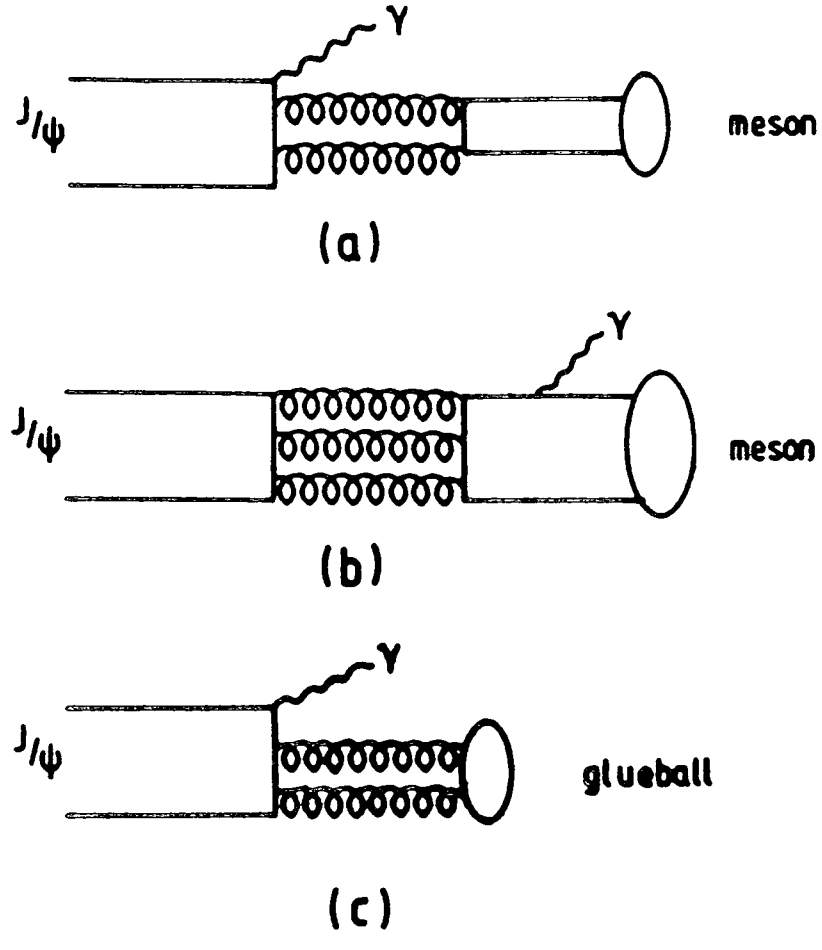

Figure 3.14 Radiative decay of the J/ψ into mesons or glueballs.

3.4.1 The Pseudoscalar Glueball Candidate Iota(1440)

The Iota was seen in $J/\psi \rightarrow \gamma K\bar{K}\pi$ [85]. The $K\bar{K}$ system was produced preferentially with low mass as though the decay $\iota \rightarrow \delta\pi$, $\delta \rightarrow K\bar{K}$ were the dominant decay mode of Iota. These data overwhelmingly favours the 0^{-+} channel in a partial wave analysis allowing both the 0^- and 1^+ partial waves [90]. The possibility of spin 2 has yet to be tested.

The suppression of $J^P = 1^+$ is thought to be due to Yang's theorem [24] and its p-wave decay to $\delta\pi$. There are four low lying 0^{-+} isoscalars namely the established $\eta(548)$, $\eta'(958)$ and $\iota(1440)$ together with a possible $\eta(1275)$. It is not clear whether the ι is a radial excitation of η'. The situation is made worse by the presence of a nearby isoscalar E(1420) observed in hadronic reactions. The E itself is a mystery. It was first seen in $p\bar{p}$ annihilations at rest [91] and in the more recent π^-p [92] experiments as a 0^{-+} resonance in $\delta\pi$, just as found for the Iota. This E can be identified with the Iota. However, the E has also been observed as a $J^{PC} = 1^{++}$ with dominant decay mode $K*\bar{K}$ and $K\bar{K}*$ [93].

The gluonium interpretation of $\iota(1440)$ is based on the following arguments:

I.

The Iota is produced in a hard gluon channel with the largest branching ratio of its kind for reasons transparent from Figure 3.14 , and its mass is consistent with Bag model [94][95] and lattice [96][97] calculations for a 0^{-+} glueball.

II.

The $B(J/\psi \to \gamma\iota)$ is too large for the ι to be a member of radially excited 0^{-+} nonet with the η,η' and $\eta(1275)$ [98]. This is based on two observations

1. $\eta(1275) \to \eta\pi\pi$ is strongly present in $\pi^- p$ scattering and there is no significant signal for $\iota \to \eta\pi\pi$.
2. In $J/\psi \to \gamma\iota$, is strongly present in $K\bar{K}\pi$ and indicated in $\eta\pi\pi$ but there is no $\eta(1275)$ signal in both channels, i.e. $\Gamma(J/\psi \to \gamma\iota) \gg \Gamma(J/\psi \to \gamma\eta(1275))$.

If the $\eta(1275)$ and ι are radially excitations of η and η' with the same singlet mixing then

$$\frac{\sigma(\pi^- p \to n\iota)}{\sigma(\pi^- p \to n\eta(1275))} \simeq \frac{\sigma(\pi^- p \to n\eta')}{\sigma(\pi^- p \to n\eta)}$$

This is badly violated by experimental observations, i.e. R.H.S $\gg$ L.H.S [99]. If ι and $\eta(1275)$ are ideally mixed with $\iota \simeq s\bar{s}$ then $\Gamma(J/\psi \to \gamma\eta(1275) \to \gamma\eta\pi\pi) \gg \Gamma(J/\psi \to \gamma\iota \to \gamma\eta\pi\pi)$, since $\eta\pi\pi$ would be a OZI suppressed decay of ι. But this is violated by (2) therefore ι is unlikely to be the $I = 0$ partner of $\eta(1275)$. This naive argument is sensitive to how the SU(3) flavour symmetry is broken so it can only serve as a guide. To consolidate the glueball claim one must confirm the $\eta(1275)$ and find an acceptable $I = 0$ radial excitation, η^*, for $\eta(1275)$ to exclude ι from the nonet. The members of radially excited pseudoscalar nonet, 2^1S_0 , seen so far are the $I = 1$ $\pi(1300)$, $I = (1/2)$ $K(1400)$ and $I = 0$ $\eta(1275)$. Phenomenologically the approximate degeneracy of $\pi(1300)$ and $\eta(1275)$ suggests ideal mixing between η^* and $\eta(1275)$, as in the ideally mixed vector nonet where ρ and ω are almost

degenerate in mass. Generalising the rough equality $m_\phi \simeq 2m_{K*} - m_\rho$ to the radially excited pseudoscalar gives $m(\eta^{*\prime}) \simeq 1600$ MeV. However mixing between glueball and isoscalars may shift the masses of $\eta(1275)$ and η^*, making the mass degeneracy of $\pi(1300)$ and $\eta(1275)$ accidental. Hence again high statistics data are needed to allow a partial wave analysis in channels like $\pi^- p \to (K\bar{K}\pi)n$, $(\eta\pi\pi)n$ and $(\eta'\pi\pi)n$, and $pp \to (K\bar{K}\pi)\pi\pi$, $(\eta\pi\pi)\pi\pi$, $(\eta'\pi\pi)\pi\pi$ to search for η^*. This is the way in which $\eta(1275)$ was discovered.

III

The width of the ι is more than an order of magnitude greater than the η' so the ι decays too fast to be a radial excitation of the η' or a quarkonium state.

There are also objections to the gluonium interpretation of the Iota.

I.

The criterion of flavour symmetric decays is the strongest argument against the glueball interpretation as $B(\iota \to \eta\pi\pi)/B(\iota \to K\bar{K}\pi) < 0.26$ according to MARK III [100].

However as already mentioned in Section 3.2.1 there are flavour symmetry breaking mechanisms which may produce non-flavour symmetric decays and such mechanisms are discussed in the next section.

II.

The Iota may have been seen in the $\gamma\rho^0$ channel, but the experimental results are confusing. With the present statistics, it is not possible to unambiguously identify the enhancement in $\gamma\rho^0$ as being due to the ι. Assuming the ι to decay mainly into $K\bar{K}\pi$ then this corresponds to a

sizable radiative decay width of 2 MeV which looks surprisingly large for a glueball and seems to rule out the pure gluonium claim [98].

Although glueballs are not normally expected to have large radiative decay widths, a hybrid or a mixed state may have radiative widths comparable to ordinary quark mesons. As in the case of the g_Ts, the properties of the $\iota(1440)$ can be explained by various models and these models are examined in the following sections.

3.4.1.1 Models for a pure ι glueball

In this section we discuss ways of producing non-flavour symmetric decays for a glueball which may then overcome the strongest objection to the glueball identification of the iota.

I.

There are ways of breaking SU(3) flavour symmetry. The lowest order diagrams for the decay of a two gluon glueball are shown in Figure 3.15. The flavour symmetry is broken kinematically in Figure 3.15(a) because for a $J^P = 0^-$ initial state the corresponding amplitude is proportional to m_q [101][102]. The situation is the same as that of the helicity argument responsible for the leptonic decays of pion having $\Gamma(\pi \to \mu\bar{\nu}) \gg \Gamma(\pi \to e\bar{\nu})$ despite the existence of μ-e universality. This then produces an enhancement of the final states containing strange quarks or kaons. Another breaking mechanism is due to Bag Model dynamics [94] which enhances final states rich in kaons and is applicable to both diagrams in Figure 3.15 . In cavity perturbation

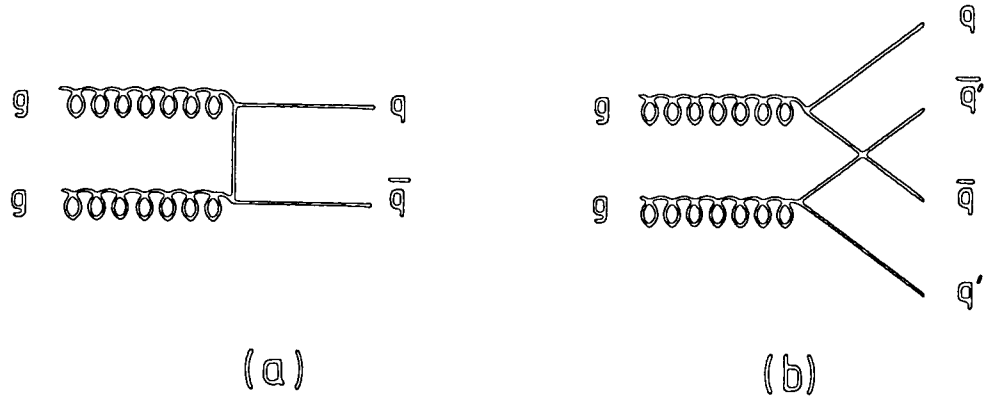

Figure 3.15 The lowest order diagrams which contribute to a 2-gluon glueball decay.

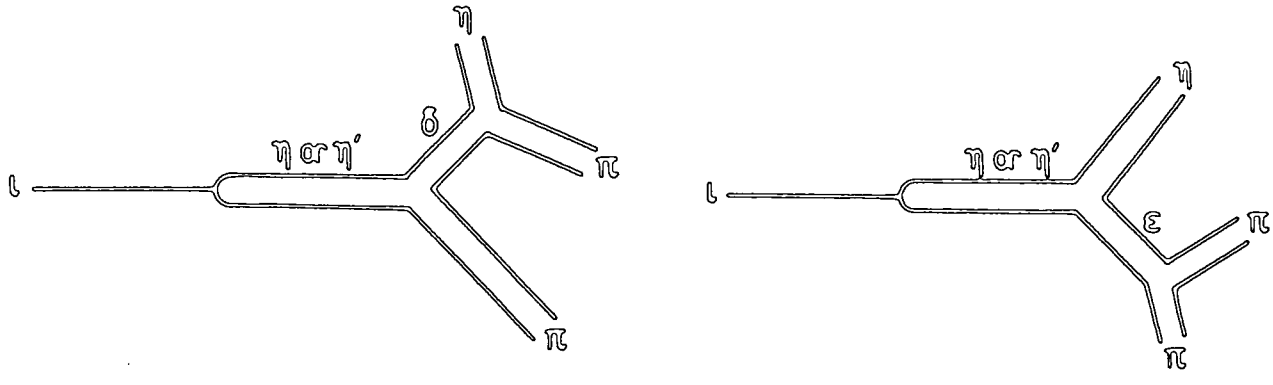

Figure 3.16 Pole diagrams for the decay ι -> ηππ.

theory the vertices are proportional to the overlap integrals of the cavity mode eigenfunctions. When the self energies of a quark and gluon, determined empirically, are included, the TE gluon mode is found to have flavour symmetric s-channel couplings, while on the other hand the TM mode couples strongly to $s\bar{s}$ [94]. A pseudoscalar glueball made of TE-TM modes therefore decays predominantly to final states with kaons just as the Iota does. Although these counter arguments are based on perturbation theory, they highlight the point that it is perilous to use flavour symmetry as a criterion for glueball spotting.

II.

The dominance of $\delta\pi$, $\delta \rightarrow K\bar{K}$ and the absence of $\eta\pi\pi$ in ι decays can also be explained with a simple pole model [103] with the ι taken as a glueball pole. The suppression of $\iota \rightarrow \eta\pi\pi$ is due to the cancellation of the two diagrams in Figure 3.16 . Furthermore, an estimate of the radiative decay width $\Gamma(\iota \rightarrow \gamma\gamma)$ for a gluonium Iota which makes use of the matrix element of Eqn. 3.4 is as large as 1 MeV [104].

3.4.1.2 Iota as a $K\bar{K}$ molecule

The dominance of $\iota \rightarrow \delta\pi$, $\delta \rightarrow K\bar{K}$ can also be explained if the ι is not a $q\bar{q}$ meson but rather a $K\bar{K}$ molecule [105]. It has been claimed that contrary to the findings in both potential and bag models, four-quark bound states can only exist in the form of a weakly bound state of two colour singlet mesons [78]. The Hamiltonian used in this analysis is of the simplest form in which only the harmonic confinement potential and the colour hyperfine interaction are included. For three flavours, the

qq pair may reside in a 3 or 6 of $SU(3)_f$ and vice versa for $\bar{q}\bar{q}$. Two scalar nonets can be obtained from combining qq and $\bar{q}\bar{q}$ pairs together using spin assignments consistent with the exclusion principle. The low mass scalar nonet is the cryptoexotic sector [6]. Four-quark bound states can be searched for by solving the four-particle Schrodinger equation. It was found that with the phenomenological SU(3) constituent quark masses only the cryptoexotic sector with $K\bar{K}$ quantum numbers can exist [78]. In this model, the $\delta(980)$ is a $K\bar{K}$ molecule bound via the residual colour interaction analogous to those binding two nucleons into the deuteron. The existence of such $K\bar{K}$ four-quark bound state also affects the interpretation of the well known scalar S*, a topic to which we will return later on (see Chapter 7).

There are two ways in which the $K\bar{K}$ residual interaction, $V_{K\bar{K}}$, can create the δ produced in ι decay. The first is a direct decay of the ι to $K\bar{K}\pi$, as shown in Figure 3.17 The observed δ is simply an effect of the enhanced $K\bar{K}$ wave function at the origin and is derived by approximating $V_{K\bar{K}}$ with a square well.

The second case involves the isobar decay of the ι[Fig. 3.18]. The presence of $V_{K\bar{K}}$ smears the $K\bar{K}^* + \bar{K}K^*$ into a much weaker and wider signal and causes an enhancement at low $K\bar{K}$ mass. Since a C = +1 glueball cannot decay to $K\bar{K}^* + \bar{K}K^*$. If this $K\bar{K}$ molecule scenario is correct for the δ then a detailed analysis of the effective mass distributions will give a definite answer to the glueball interpretation of the ι.

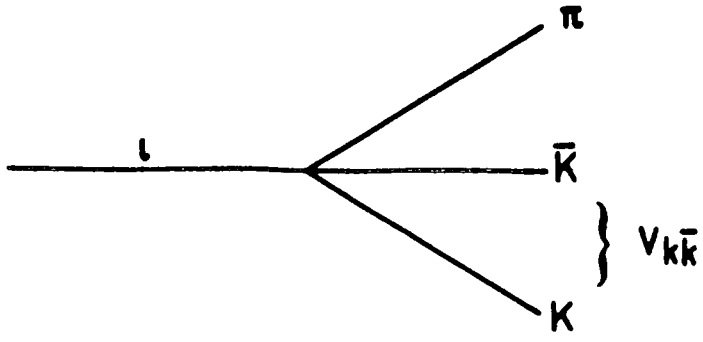

Figure 3.17 ι -> KK̄ with $V_{K\bar{K}}$.

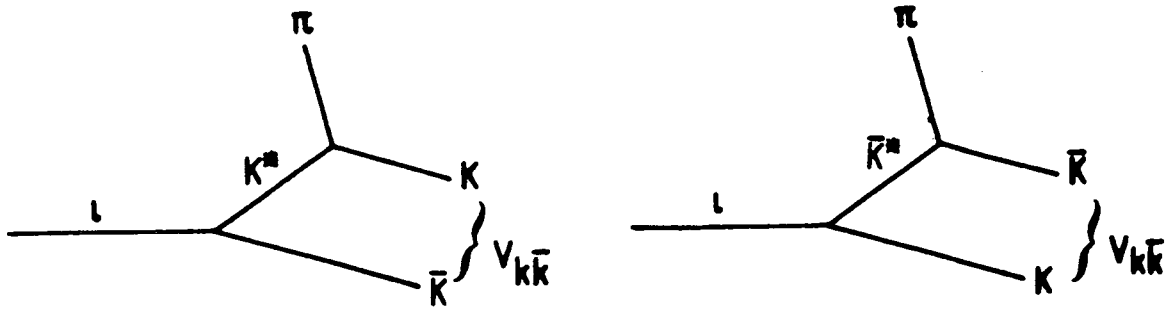

Figure 3.18 ι -> KK̄* + K̄K* -> KK̄π with $V_{K\bar{K}}$.

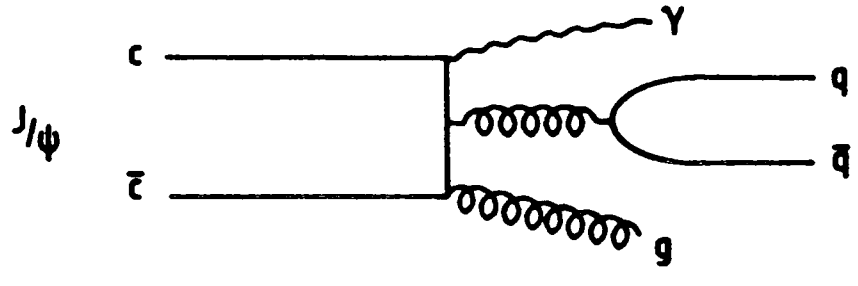

Figure 3.19 The lowest order diagram for J/ψ -> γqq̄g.

3.4.1.3 Iota as a Hybrid

The ι may also be a hybrid meson [45][106] because QCD predicts that the branching ratio of $J/\psi \rightarrow \gamma q\bar{q}g$ [Fig. 3.19] is the same order as that of $J/\psi \rightarrow \gamma gg$. For low lying hybrid mesons the $q\bar{q}$ pair is a $^3S_1$ colour octet. The quantum numbers of hybrids with a TM mode gluon are 0^{++}, 1^{++}, 2^{++} and with a TE mode are 0^{-+}, 1^{-+}, 2^{-+} where spin one states may be produced with off shell gluons. A hybrid state decays into two ordinary mesons with an amplitude proportional to the overlap integral of the wave functions of the mesons [106]. An estimate for the decay width of a 0^{-+} hybrid of the mass of the Iota can be made using non-relativistic wavefunctions given by the harmonic oscillator potential model. Such a non-relativistic calculation gives a width of 15 MeV which is much smaller than the experimental value of $70\pm^{20}_{30}$ MeV. Unfortunately the magnitude of relativistic corrections is not known and the possibility of a hybrid Iota remains. It is possible to identify the ι as the 0^{-+} ωg. But this would mean a 0^{-+} ϕg state at 1650 MeV with half the production rate of the ι in J/ψ radiative decays, which is inconsistent with observation [45]. Since the 0^{-+} glueball is predicted to have a mass within the mass region of the low-lying 0^{-+} hybrids, mixing between them is also a possibility which may change the above picture.

3.4.1.4 Iota as a Mixed state

The sizable width of the magnetic dipole transition $\iota \rightarrow \gamma\rho^0$ remains an obstacle to identifying the ι as a pure glueball even though the simple pole model offers an explanation of this. Fine tuning is needed to achieve the required cancellation in the model. There are other alternative explanations in which the ι is treated as a mixed state, such alternative models are discussed below.

I. Mixing in the Bag Model:

To explain the radiative decay width of the ι, mixings between a 0^{-+} glueball and $q\bar{q}$ isosinglet pseudoscalars (both the ground state and the first radial excitation) are found to be large in the Bag model [107][108]. The photon couplings of a glueball are generated by mixing $q\bar{q}$ components into its wavefunction. A large electromagnetic width of the ι (taken to be a mixed glueball) can be obtained in this framework for two reasons:

1. Phase space increases strongly with the mass of the ι.
2. Mixings with the ground states are sizable.

Apart from these, contributions from higher order diagrams are also significant. These features enable mixed glueballs to have a larger magnetic dipole radiative width than radially excited $q\bar{q}$ mesons. However, the above model relies on the assumption that all particles have the same radius, and that mixing amplitudes was very sensitive to shifts in quark masses and other parameters in the model. Another approach in the Bag model [109] with η-η'-glueball mixing gives similar

qualitative conclusions.

II. Mixing in the Non-Relativistic Quark model:

An alternative way of estimating the mixing is the non relativistic quark model in which constituent quark masses, harmonic-oscillator confining potential and the hyperfine (Fermi-Breit) spin-spin interaction are used. The hyperfine interaction is responsible for the mass splittings of the pseudoscalar and vector meson masses. In the following, different approaches will be discussed in order of increasing complexity.

(i)

The simplest model is to consider mixings between the η, η' and ι. Physical states are expressed as a linear combination of non-strange, strange and gg wavefunctions [110]. The content of a state is simply given by the corresponding coefficients of the base states. A constant mass matrix with orthogonal mixing and linear mass formulae are used in this. Using this simple idea, an investigation of J/ψ decays to pseudoscalar-vector final states suggests that a sizable gluon component ($\sim$ 30%) may be present in the η'. Indeed, long ago N.Isgur [111] proposed that the mass splitting between the η and η' may be due to a sizable mixing with glueballs.

(ii)

A more sophisticated model [112] involves η, η', $\eta(1275)$, ι and a new hypothetical high mass pseudoscalar state between 1600 and 1900 MeV, labelled NS. In this model either ι or NS could be a mixed quarkonium $s\bar{s}$ or a mixed glueball. Mixings only occurs between the glueball and

isoscalars, there is no direct mixing between ground and radial excitations. Data on production and decays like $\iota \to \gamma\rho^0$, $\eta' \to \gamma\rho^0$ are needed to distinguish between the two possibilities. Physical masses are taken as constraints. Bare masses and glueball-isoscalar mixings are free parameters. The quark or gluon content of the physical states are determined by the eigenvectors of the mass matrix using the MARK III results on J/ψ radiative decays [82]. The solution with $\iota \simeq 68\%$ glueball and $NS(\sim 1700) \simeq s\bar{s}$ is strongly preferred.

(iii)

In a more complicated version [113], the physical states are a mixture of harmonic-oscillator basis states with mixing generated by the hyperfine interaction. The ground state, the first two radially excited states and a glueball with basis state $|gg\rangle$ mix together in this model. Known radiative decay widths are needed to constrain the parameters in this approach. The ι is taken as the mixed glueball and the calculated $\Gamma(\iota \to \gamma\rho^0)$ is about 4 MeV. Apart from giving a reasonable $\Gamma(\iota \to \gamma\rho^0)$ width, this also gives an explanation for the suppression of $\iota \to \eta\pi\pi$ in terms of its composition. An unsatisfactory point is that masses of the radially excited η' are heavy. But these states have not been seen and this disadvantage may later turn in its favour.

(iv)

Another model that mixes the ground state with the first two radial excitations, but without a glueball, is called the giant resonance model [114]. The mass splittings in this model are fixed phenomenologically by comparing the charmonium and low lying hadron spectra. The Iota is not interpreted as a mixed glueball but a mixture

of different degrees of radial excitation with collective coherent effects analogous to the giant resonant states observed in nuclear and condensed matter physics. The predictive power of this model is very limited as it is very sensitive to details of the radial wave functions and exact values of some of the parameters. This and the previous model both suffer from the fact that if radial excitations are allowed to mix with ground states then this should not just be confined to the isoscalars. The consequences of such mixings to occur at low energies would spell disaster for conventional meson spectroscopy.

A final comment on mixing models is that genuine radially excited states will have a reduced magnetic dipole transition amplitude. In a non-relativistic model, the excited state wavefunction is orthogonal to the ground state wave function. If the magnetic dipole transition was a simple spin flip, as in non-relativistic model, the overall amplitude would vanish because of the wavefunction orthogonality. Although this orthogonality is not exact in relativistic cases, at least an order of magnitude suppression for the radiative decay rates of radially excited mesons compared to the ground state is expected [108]. Judging from the present data, the Iota is therefore unlikely to be a radial excitation of the η'.

III. Mixing through the Axial Anomaly:

A completely different approach is to mix the pseudoscalar glueball with the η and η' through their anomalous couplings [Fig. 3.20]. These gluonic or anomalous couplings of the η and η' are given by

$$\langle 0|\frac{\alpha_s}{4\pi} \mathrm{Tr} G\cdot\tilde{G} |\eta\ ,\ \eta'\rangle \qquad (3.6)$$

Identifying $\mathrm{Tr}G\cdot\tilde{G}$ as the interpolating pseudoscalar glueball field, the η-η'-glueball mixing [115] is determined through the Partial Conservation of the U(1) current hypothesis [116]. Experimental data on electromagnetic decays of the isoscalars are used to relate the parameters in the model. The mixing between the ι and η' is found to be much bigger than that of the ι with the η because the amount of mixing depends on the square of the masses. The results on the decays of the ι agree qualitatively with experiments and favour the ι as a mixed glueball.

The above strong anomaly plays a more important role in the pseudoscalar nonet then just mixing η-η'-glueball. It has been shown that the η-η' mass splitting and the deviation from ideal mixing can be understood if there exists a substantial annihilation amplitude of positive sign [111]. Such a contribution is small in the vector and tensor nonets, where ideal mixing is a consequence of the $SU(3)_f$ breaking induced by quark masses. The perturbative contribution to the annihilation amplitude in the pseudoscalar nonet is dominated by the 'diamond' diagram of Figure 3.21 through this anomalous coupling. Such a $q\bar{q}$ annihilation diagram is relatively suppressed in the scalar nonet because the two gluons are in a P-wave. The isoscalar scalar will be discussed later in Chapter Seven. Incorporating the positivity of the q-$\bar{q}$ annihilation amplitude in the previous mixing model, R.Sinha [117] finds solutions for the η-η'-ι mixing that are consistent with present experimental data. Although the ι in these solutions has a substantial

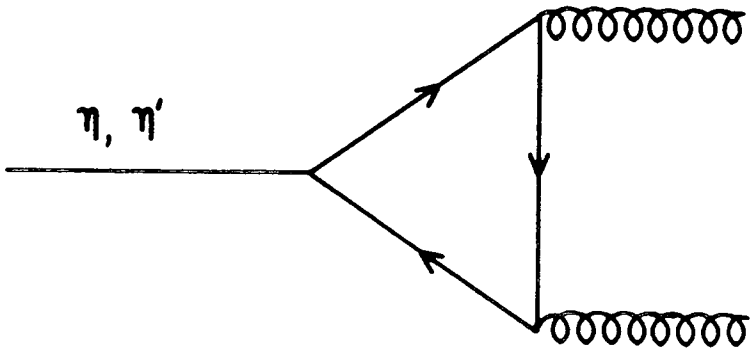

Figure 3.20 Diagram for the anomalous couplings of η, η'.

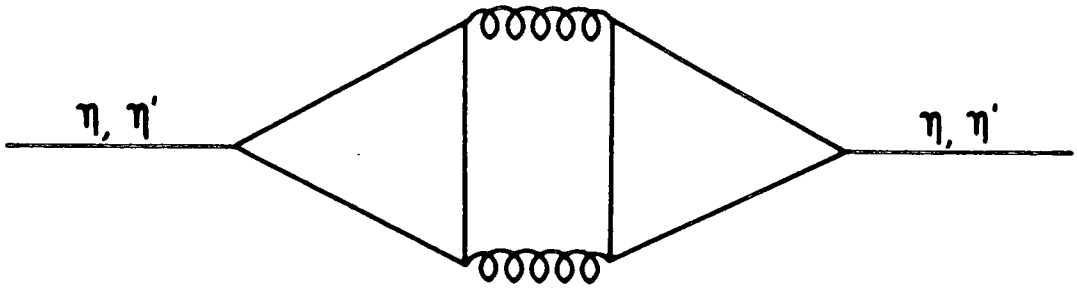

Figure 3.21 Quark diamond diagram for isosclar pseudoscalar $q\bar{q}$ mesons (η,η') with only two gluons exchanged.

amount of gluonium content, the overall picture of mixing is different from all previous mixing models. The anomalous coupling has to be put in by hand in this mixing approach and a better alternative is to use the effective QCD Lagrangian which we now discuss.

3.4.1.5 Effective Lagrangian approach to the Iota

Because of confinement the fundamental fields (quarks and gluons) in the QCD Lagrangian do not appear as free particles. It is therefore useful to construct an effective Lagrangian for describing the properties of the observed particles and at the same time possesses all the symmetry properties of the QCD Lagrangian (i.e. chiral symmetry in the massless limit). The old U(1) or the η-mass problem can be solved by including a pseudoscalar field in an effective chiral Lagrangian [118] which automatically gives the correct anomalous conservation law for the axial U(1) current. The required effective Lagrangian which reproduces the axial anomaly has been written down some time ago [119] and the mixing of η-η'-0^{-+} glueball is discussed within such a Lagrangian with the massless axial anomaly term [Eqn. 1.23] identified as the pseudoscalar glueball field [120][121]. The Lagrangian contains a kinetic energy term and an interaction term with matter fields for the 0^{-+} gluonic field. The anomaly term can be split into two distinct glueball fields. One of these is responsible for the annihilation contribution in the η' as in Figure 3.21 while the other could correspond to the physical glueball state. This already implies

mixing between η' and 0^{-+} glueball. The amount of mixing between the η, η' and ι is obtained by fitting experimental data on the production and decays of the particles. It turns out in this picture [120] that the ι is almost a pure gluonium with 92% glue content and the η is a quarkonium. The overall result is in qualitative agreement with data.

3.4.1.6 Remarks on the Iota

There are signs of the ι in other radiative decay channels of the J/ψ . At least three pseudoscalar states below 2 GeV have been seen in $J/\psi \rightarrow \gamma\{K\bar{K}\pi\ ,\ \gamma\rho^0\ ,\ \rho\rho\ ,\ \omega\omega\}$ [122]. In addition, a large radiative rate to $\eta\pi\pi$ suggests the existence of at least one other state in the region but its spin-parity has not been determined. It is difficult to say whether all these enhancements are due to the ι or there are more new states to be discovered. The data on $\rho\rho$ and $\omega\omega$ mass distribution can be explained if a new resonance X(1800) is allowed to interfere with the ι [122]. However such a scheme does not agree with the $\gamma\rho^0$ spectrum. The $\eta(1275)$ has now been confirmed and it may have some contribution to the above processes.

As a concluding remark, the ι is the oldest of the glueball candidates and yet both the present experimental and theoretical situation is still confusing. If both $\eta(1275)$ and ι are radially excited pseudoscalars then their mass pattern and production rates in J/ψ radiative decays are hard to understand. It seems that the ι must have a substantial gluon content even if it is not pure gluonium. The

next glueball candidate to be considered is the θ.

3.4.2 The Tensor Glueball Candidate $\theta(1690)$

The θ was first observed in the channel $J/\psi \rightarrow \gamma\eta\eta$ and later in $J/\psi \rightarrow \gamma\theta$, $\theta \rightarrow K\bar{K}$, $\pi\pi$ [64]. No other decay modes have been found and overall ratios of the decays is

$$K\bar{K} : \eta\eta : \pi\pi \simeq 3 : 1 : 0.8 \qquad (3.7)$$

Since the θ does not seem to have $\gamma\gamma$ decay channels this makes it more acceptable as a pure gluonium candidate.

The gluonium interpretation of the $\theta(1690)$ is based on arguments similar to those of the ι :

I.

The production rate of the θ in radiative J/ψ decay, along with its mass and width agreeing with calculations [46][95][97], qualify the θ as a glueball candidate.

II.

The θ is not likely to be a member of the radially excited tensor nonet because;

1. The mass splitting between the θ and f'(1525) is far too small for the quarkonium scenario to be tenable.
2. The production rate of the θ in J/ψ decay is too large.

f(1270) and f'(1525) are the two established isoscalars of the ideally mixed tensor nonets. The $\theta(1690)$ does not seem to fit into this tensor

nonet and its preferred decay to $K\bar{K}$ would point to an $s\bar{s}$ content, so it would have to be the radial excitation of f' for a quarkonium assignment. Indeed, a study of the θ as an excited nonstrange meson fails to explain the observed decay rates completely [73]. The $B(J/\psi \rightarrow \gamma\theta)$ is about two times larger than $B(J/\psi \rightarrow \gamma f')$ which is in contradiction with what is expected of a radial excitation.

If $\Gamma(\gamma\gamma \rightarrow f') \gg \Gamma(\gamma\gamma \rightarrow \theta)$ then the θ would almost definitely be a glueball but the present experimental limit is not yet sensitive enough for the comparision to be made. The main problem for the gluonium hypothesis is again the decay pattern. The decay rates for a tensor flavour singlet should be related by SU(3) to

$$K\bar{K} : \eta\eta : \pi\pi \simeq 3 : 0.5 : 6$$

after taking into account the D-wave phase space effects [73]. There are again models to explain this observation and we now discuss these models in turn.

3.4.2.7 Models for a pure θ glueball

It is possible to argue that the suppression of the $\theta \rightarrow \pi\pi$ decay mode (cf. Eqn. 3.7) is due to competition of phase space. A flavour symmetric $q\bar{q}$ pair, given by $(u\bar{u} + d\bar{d} + s\bar{s})/\sqrt{3}$, would be created by a gluon or flavour symmetric annihilation of gluons. The quark pairs then subsequently hadronize to form the observed final states. The $u\bar{u} + d\bar{d}$ pairs can form the following final states with pions:

$\pi\pi$, $\rho\rho \rightarrow 4\pi$ $\omega\omega \rightarrow 6\pi$ etc.

However because of the mass of the θ, the $s\bar{s}$ pairs can only materialize to one $K\bar{K}$ pair, other heavier strange states like ηη are penalized by phase space. But the multi-pion channels can proceed without inhibition through the quasi two body S-wave channels ρρ and ωω. Therefore a much larger fraction of the $s\bar{s}$ decays to $K\bar{K}$ than $u\bar{u}$ + $d\bar{d}$ to ππ simply because of phase space effects. Although the initial decays of the gluons are flavour symmetric, the symmetry is broken in the observed final states. This is to be compared with the flavour symmetry breaking mechanisms mentioned for Iota decays (Section 3.4.1.1). Hence the θ with its mass at 1690 MeV can be identified as the 2^{++} TE-TE glueball in a Bag Model where the Iota is taken as a gluonium [46][54].

The possiblity of a mixed state can not be ruled out with the present experimental data and we consider such a possiblity in the next section.

3.4.2.8 θ as a Mixed state

A mixed θ offers an alternative to the flavour symmetry breaking mechanisms used in the previous discussion in explaining the large decay rates of the θ to final states with strange quarks with the θ taken to be a gluon rich state.

I. Mixing in Non-Relativistic Quark Model:

An analysis of the mixing of the f, f' and θ in the simplest approach (see Section 3.4.1.4) can explain the decay characteristics of the particles if and only if [73][123]

$$f \simeq 90\%\ (u\bar{u} + d\bar{d})/\sqrt{2} + 10\%\ \text{glue}$$

$$f' \simeq 99\%\ s\bar{s} + 1\%\ \text{glue}$$

$$\theta \simeq 90\%\ \text{glue} + 10\%\ (u\bar{u} + d\bar{d})/\sqrt{2}.$$

This is good phenomenologically but the ad hoc requirement that f' should be left out of the mixing is not understood. Other versions requiring larger amount of mixings have not been very successful [124]. It may simply be that the θ is almost pure gluonium and mixes very little with $q\bar{q}$ states.

II. Mixing in Effective Lagrangian:

The effective Lagrangian approach described earlier can be generalised to encompass the tensor glueball. This is to be compared with the strong gravity model which describes the gravitational, scalar and electromagnetic fields. In such a model an ad hoc dilaton field is required to make the theory conformal invariant. In the effective QCD Lagrangian the scalar glueball field naturally acts like the dilaton. The QCD trace anomaly (in the massless limit) is identified as the scalar glueball field since the term TrG•G has quantum numbers of a scalar. A conformal invariant Lagrangian describing a massive spin 2 field, the tensor glueball, has been derived [125]. The main feature of the Lagrangian is that there exists multi-glueball interaction terms [126]. The decay of an unmixed tensor glueball $\theta_0 \to \eta\eta$ then has contributions from the diagrams of Figure 3.22 . These contributions have been neglected in the previous mixing models but are important in this approach. The θ_0 is assumed to mix only with the $f'(\simeq s\bar{s})$ and the above contributions are required to explain the large $\theta \to \eta\eta$ decay

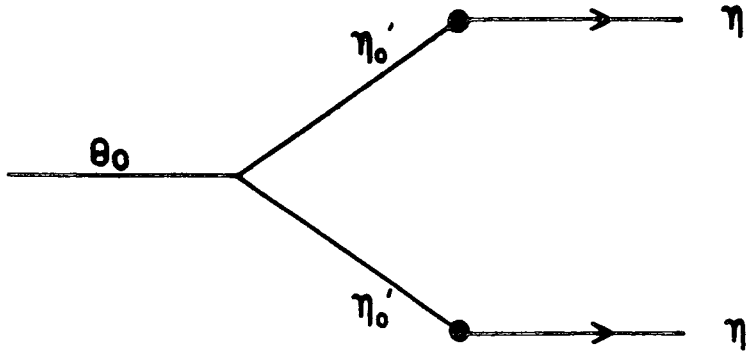

(a)

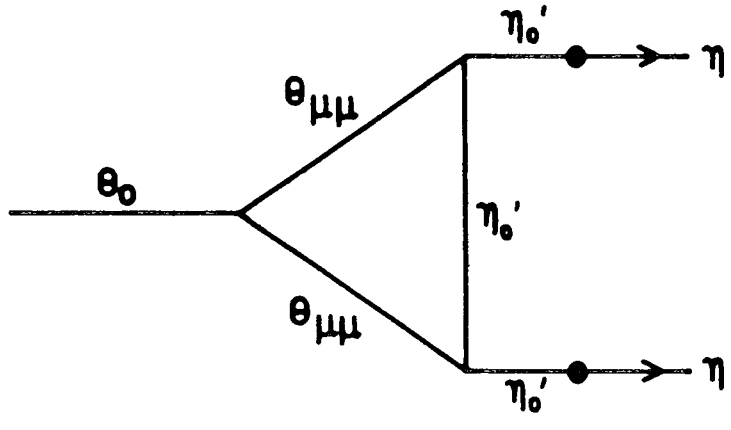

(b)

Figure 3.22 (a) θ_0 decays into $\eta\eta$ through the SU(3) singlet.
(b) A possible unitarity correction to (a).

rate. Although the effective Lagrangian approach works reasonably well for the ι, it fails to explain the total width of the θ. This makes the previous mixing in which θ and f are mixed more difficult to understand as the f' and θ are closer in terms of mass. Having discussed the possiblities of a pure and mixed glueball we now turn to other alternatives.

3.4.2.9 θ as a Hybrid

The possibility of the θ being a hybrid is small as the lowest lying 2^{++} are predicted to be in the mass range of 1.9 - 2.3 GeV [54][94] which are too heavy for $\theta(1690)$. In radiative J/ψ decays the $q\bar{q}$ pairs in low lying hybrids are in the $^3S_1$ state. Hence tensor hybrids are made of $q\bar{q}g_{TM}$ and because of the s-channel coupling of g_{TM} they are expected to decay predominantly into two vector mesons containing strange quarks. Furthermore constituent quark masses are usually used in the calculation of decays to include some of the final state interactions associated with confinement. As a consequence of this approximation tensor hybrids are forbidden by the spin operator σ, responsible for the transition, to decay into two meson final states with a pseudoscalar. The hybrid interpretation therefore fails to explain the decay pattern of the $\theta(1690)$ [106].

3.4.2.10 θ as a Four Quark State

Alternatively the θ could be a four quark state. These states are generally expected to be very broad, except may be for the 0^{++}. But the tensor $(u\bar{u} + d\bar{d})s\bar{s}$ state would have a mass below the fall apart threshold and might be observed as a narrow resonance. However, it is expected that $\Gamma(\theta \rightarrow K\bar{K}) \simeq \Gamma(\theta \rightarrow \eta\eta)$ and this is in slight disagreement with the data. It is puzzling that given the large production rate of the θ , no other potential four quark candidates especially the S*(975) have been seen in J/ψ radiative decays (see Section 5.4.1).

3.4.2.11 Remarks on the θ

Nothing definite can be said about the θ at present, but it is most likely to be a gluon rich or four-quark state. Data on other decay channels are much needed, especially the radiative decays which may provide us with a firm footing for assigning θ as a gluonic state.

3.4.3 A possible Glueball Candidate ξ(2200)

This is the last glueball candidate observed in radiative J/ψ decays. It has been seen in K^+K^- and $K_S^0K_S^0$ channels in the ratio of 1.3 ± 0.9 [127]. This is consistent with the value 2 expected for an isoscalar meson. Although it is known from observation that the ξ has a narrow width, partial wave analysis has failed to determine its spin. Since the ξ decays to $K_S^0K_S^0$ its spin, parity, and charge conjugation must

be $J^P = (2n)^{++}$, n = 0, 1 , 2 , 3..... Even though the spin of the ξ is not known, one can still speculate on its nature with its known properties.

I. ξ as a Quarkonium:

If the ξ is a quarkonium then the observed $K\bar{K}$ decay requires it to be made of strange quarks. Such a candidate in the relativistic potential model is the L = 3 $^5F_2$ $s\bar{s}$ meson, an excitation of the f'(1525) [128]. It is expected to decay to $K^*\bar{K} + \bar{K}^*K$ with a branching ratio approximately equal to $K\bar{K}$. This is an important decay mode as it is forbidden to a C = +1 glueball. The absence of such a decay is hard to explain even when mixing with other states is allowed.

II. ξ as a Gluonium:

Although the ξ is too heavy for the low lying 0^{++} and 2^{++} two gluon glueballs in Bag models with massless constituent gluons, it is possible to identify them with the ξ if mass is given to the gluons. The gluon mass is supposed to represent a large distance effect and is taken to be 0.8 GeV [129]. The ξ is taken as a TM-TM glueball in this approach. According to the production rate both scalar and tensor glueballs are possible candidates, but they are predicted to decay substantially into final states of $K\bar{K} + \pi s$. Although the suppression of the $\pi\pi$ mode is a direct consequence of this scenario the failure to observe other predicted decay modes [129] is a serious problem.

III. ξ as a Hybrid:

The preferential decays of the ξ to final states with strange quarks qualify it as a possible $s\bar{s}g_{TM}$ hybrid. However only a $\ell_{q\bar{q}} = 2$, 2^{++} hybrid meson at the mass of the ξ would be narrow enough to be compatible with the observed width [106][130]. The calculation of its decay rates is basically the same as those described in previous hybrid models. It turns out that the production rate to $K\bar{K}$ is too small in comparison with experiment. Other decay channels like $\phi\phi$ and $\phi\eta$ are also expected to be seen. The hybrid interpretation seems to be unlikely with the present experimental information.

IV. ξ as a Four Quark state:

For a four quark interpretation, the ξ mass seems too high for it to be observable. As mentioned earlier [131], only light four quark states are expected to survive as observable resonances.

Finally, it seems that ξ does not fit into any of the above scenarios as they all predict other decay channels that are not seen in present experiments. Searching for other decay modes of the ξ is therefore important in identifying the ξ.

3.4.4 The Lightest Scalar Glueball ε_g

The existence of the scalar glueball is very important in

- establishing the valence gluon hypothesis,
- calibrating the glueball mass spectrum, which is crucial in glueball

physics,

- and to provide hints for better model construction.

The resonance G(1590) seen in $\pi^- p \rightarrow G+n$ [132] has been considered as a candidate for the scalar glueball [133] or as it's radial excitation [134]. Its dominant decay mode is $\eta\eta'$ which is possible for a scalar glueball if flavour symmetry breaking is taken into account. The $\eta\eta'$ decay is thought to go via a gluon analogue of the ordinary planar diagrams in the quark sector [Fig. 3.23b] which is also assumed to be the dominant contribution to $\eta\eta$. This is motivated by the success of Ref. 135 in explaining the large decay rate of the η' in the radiative decays of the J/ψ, which assumes a strong coupling of the η' to gluons. The assumption that the process of Figure 3.23(b) dominates those with an intermediate $q\bar{q}$ pair of Figure 3.23(a) in scalar glueball decays is questionable. A naive counter argument is that the valence gluons must first be stretched out far enough for a virtual gluon pair to be created to screen the colour, and there is no a priori reason to favour such a process. A complete breakdown of the flavour selection rule is also more than expected. Furthermore, if the G(1590) is the scalar glueball then the Iota cannot be a pseudoscalar glueball candidate as it is lighter than the G(1590) and θ would be too light for a tensor glueball. If this is the case then why have both the non gluonium states, the lighter $\iota(1440)$ and the heavier $\theta(1690)$, been seen in the gluonic J/ψ radiative decays but not the G(1590). G(1590) is also not likely to be a four-quark state $(u\bar{u}+d\bar{d})s\bar{s}/\sqrt{2}$ as the ratio $BR(G \rightarrow K\bar{K})/BR(G \rightarrow \eta\eta)$ is too small for such an interpretation.

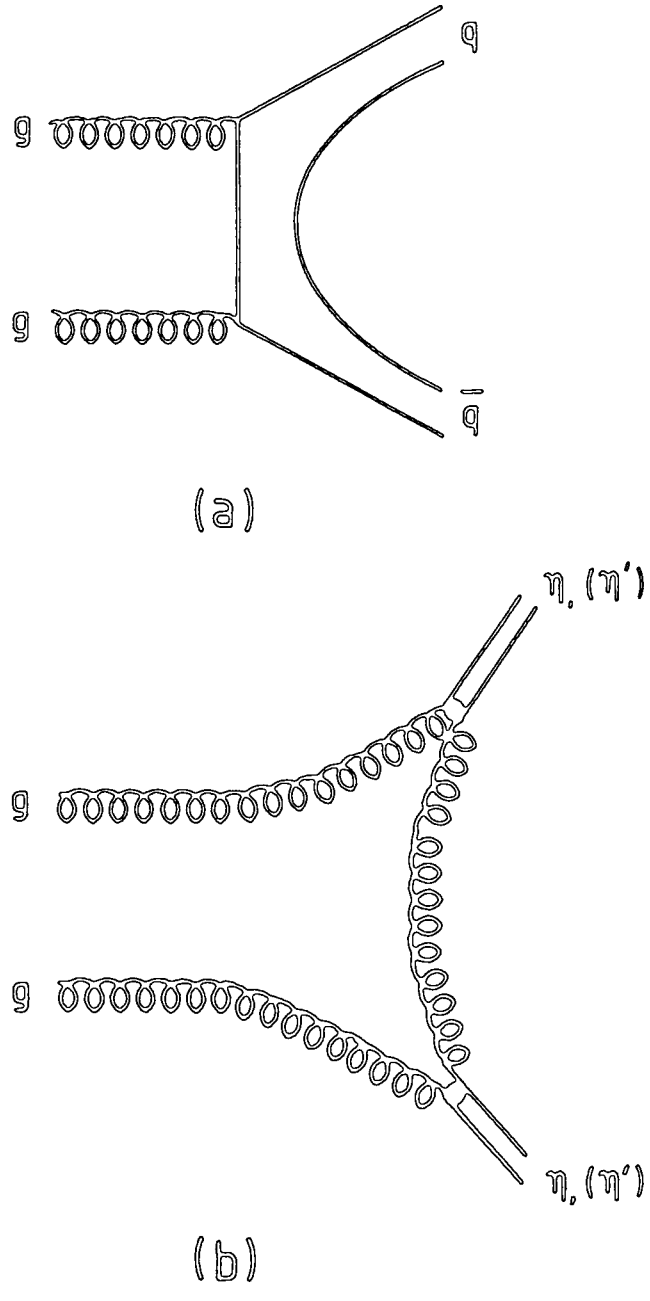

Figure 3.23 (a) Diagram for the (gg) glueball decay through an intermediate $q\bar{q}$ pair.

(b) Diagram for the (gg) glueball decay to $\eta\eta$ ($\eta'\eta'$) without an intermediate $q\bar{q}$ pair (i.e. through anomalous couplings).

Phenomenologically, the G(1590) is more likely to be the first radial excitation of the isosinglet in the scalar octet. The G(1590) is not generally regarded as a scalar glueball candidate.

Having found candidates for the lowest 0^{-+} and 2^{++} glueballs, the absence of any plausible candidate for the scalar glueball subsequently prompts a lot of speculations. There are mainly two schools of thought. One advocates a broad scalar gluonium [136], its width so wide that it ceases to be an observable resonance. Others prefer the opposite extreme for a very narrow scalar glueball [137] which escapes detection. As the mass of the scalar gluonium is predicted to be in the neighbourhood of 1 GeV [138], its properties depend on whether it is above, below or on top of the $K\bar{K}$ threshold.

If $m(\varepsilon_g) < m(K\bar{K})$, ε_g can decay into two or four pions. But from previous studies on $\pi\pi$ scattering, the four pion channel is found to open only well above 1 GeV. Thus a ε_g resonance is hard to hide in $\pi\pi$ scattering below $K\bar{K}$ threshold, which is virtually elastic. As a Breit-Wigner resonance usually occurs with a phase shift δ at 90^0 (see Section 4.2.1), one hopes to understand more about ε_g by studying the $\pi\pi$ phase shift. There are several measurements on the isosinglet S-wave $\pi\pi$ phase shift δ which do not agree on details, but the general features are quite well established [Fig. 5.3]. The phase shift shows no rapid energy variation below $K\bar{K}$ threshold, it rises slowly from $\pi\pi$ threshold and passes through 90^0 on its way up to the $K\bar{K}$ threshold where it is rapidly rising. Although δ passes through 90^0, it clearly is not the result of a traditional resonance described by a Breit-Wigner form. The

generally accepted explanation is for a narrow resonance S*(975) near $K\bar{K}$ threshold to sit on a rising background of a very broad $\varepsilon(1300)$. There are alternative explanations of the structure either in terms of a very broad S-matrix pole ε at 700 MeV with a 1 GeV width [139], or a $q\bar{q}q\bar{q}$ state at 650 MeV [140], or in terms of the unitarized quark model [141]. If the widths of glueballs are believed not to be much broader than ordinary hadronic states than it is unlikely to associate the entire phase structure below 1 GeV with a scalar glueball. It has been pointed out by the authors of Ref. 137 that there are two possible ways of hiding a glueball. The most obvious solution is to assign a very narrow width to ε_g so as to escape detection due to binning of the data and the finite experimental resolution. Such a narrow state can only have local effects on the data and it is found that after smearing the local effects, a glueball with a width less than 1-2 MeV can be hidden in the data. The second scenario is for a glueball to mix via unitarity effects with a $q\bar{q}q\bar{q}$ state at 650 MeV. Both states can have widths of the order of 100 MeV providing their masses and widths are fine tunned to reproduce the global behaviour of δ and a very narrow structure which again is hidden in the data.

If $m(\varepsilon_g) > m(K\bar{K})$, $K\bar{K}$ channel then becomes available and since S-wave data can be confidently separated up to 1.5 GeV a glueball with mass less than 1.5 GeV can be investigated with a coupled channel analysis. For a heavier scalar glueball, multichannel analyses are needed and the experimental situation becomes more complicated. The possiblity of a narrow ε_g heavier than 1 GeV has been examined in the framework of the

effective QCD Lagrangian [136]. The QCD trace anomaly is reproduced by introducing a scalar field in the effective Lagrangian which is identified as the scalar glueball field. The couplings of this pure gluonium to quark states and two photons can be estimated using the appropriate low energy theorems. It is concluded that the width of a scalar gluonium with mass greater than 1 GeV is unobservably wide, and a gluonium with mass between 400 to 1000 MeV would have detectable widths but are ruled out by the $\pi\pi$ scattering data. Such a result comes as a surprise, as already pointed out in Section 3.2.2. The scalar glueball can have a substantial two photon width through the trace anomaly. Indeed using the matrix element in Section 3.2.2, the estimated two photon width of a scalar glueball with mass greater than 1 GeV is comparable to that of conventional $q\bar{q}$ resonances [22][104].

Apart from mixing the scalar gluonium with a four-quark state, ε_g can also be mixed with the isosinglet of the scalar quark multiplet [138]. The apparent solution to this mixing is the $S^* + \varepsilon$ scenario which explains the $\pi\pi$ phase shift. This scenario has been studied in QCD sum rules which make use of the low-energy theorem [142] derived from the trace anomaly (in chiral limit):

$$\langle 0 | \theta_{\mu\mu} | \pi\pi \rangle = q^2 + O(q^4) \qquad (3.8)$$

where q is the $\pi\pi$ invariant mass.

Again the disappearance of the α_s^2 factor on the right hand side indicate that a scalar glueball can have a strong $\pi\pi$ coupling, much stronger than the meson one. The scalar glueball may therefore have a broad width

with or without mixing. The ε is thought to be such a broad mixed state with a large gluon component and the S* is mainly a $u\bar{u}+d\bar{d}$ like quark state with a small amount of gluon mixture [134]. It is then argued that the S* should be absent [134] in the double pomeron exchange pp -> pp ππ process. However the AFS group has found evidence for the S* in their data [69] which contradicts this expectation. Others who favour a mixing scenario with a significant gluonic content in S* [137][138] receive support from such a finding. However, the lack of evidence for the S* in J/ψ radiative decays (see Section 5.4.1) [43] seems to favour the scheme with small mixing. The whole picture seems confusing as our understanding of the scalar multiplet is poor. To make the situation more bizarre the S* has been nominated as the most probable candidate for both a four quark state [6] and a $K\bar{K}$ molecule [78][143]. The mysterious nature of S* qualifies us to call it the S* puzzle.

Clearly a detailed study of the isosinglet scalar channel below 2 GeV is urgently needed both in glueball physics and in hadron spectroscopy. The rest of this thesis describes such an endeavour made in collaboration with Michael Pennington and David Morgan. [144]

CHAPTER FOUR

QUEST FOR THE LIGHTEST SCALAR GLUONIUM

4.1 INTRODUCTION

The dilemma faced in the search for the scalar glueball is that it is either very narrow or very wide compared with normal $q\bar{q}$ hadrons. In either case a systematic study of 'hard gluon' channels like $J/\psi \to \gamma\pi\pi$, $J/\psi \to \phi\pi\pi$, $\psi' \to J/\psi\pi\pi$, $T' \to T\pi\pi$ and in particular the AFS double pomeron exchange experiment is needed. The AFS experiment $pp \to pp\ \pi\pi\ ,(K\bar{K})$ are specially designed to search for the scalar glueball and provides the highest statistics data on the $\pi\pi$ spectrum at low $\pi\pi$ masses which is quite different from that of $\pi\pi$ scattering itself. However, any scalar meson in the 1 GeV mass region can only decay to $\pi\pi$ and/or $K\bar{K}$ channels, and the fact that strong interaction processes must conserve probability tightly correlates these processes to the elastic reactions $\pi\pi \to \pi\pi$ and $\pi\pi \to K\bar{K}$ and so severely limits the scope for new effects. As we shall see, the difference between the $\pi\pi$ mass spectra is caused by final state interactions that can shape and colour the actual spectra we observe. Nevertheless, so tight is the relationship required by unitarity between channels with essentially just $\pi\pi$ and $K\bar{K}$ final states, that any new experimental information can add greatly to our understanding of the I = 0 J = 0 sector. Another way of expressing the unitarity constraint is that any extra low mass state should already have been seen in $\pi\pi$ scattering without any need for a

special production mechanism. Though the AFS experiment can of itself provide no new excitations, it can shed valuable light on states already there. For this it is ideally suited, because unlike classic processes like $\pi^- p \rightarrow \pi^- \pi^+ n$, the S-wave $\pi\pi$ final state in $pp \rightarrow pp\,\pi\pi$ is not swamped by a dominant I = 1 (ρ) signal. Thus the AFS data is a major addition, supplementing experimental information on meson-meson scattering. This allows us to perform a new coupled channel analysis of essentially all $\pi\pi$, $K\bar{K}$ information and obtain more detailed conclusions than previously possible. Such analysis relies crucially on our understanding of the interplay of production mechanisms and final state interactions, which form the basis for the extraction of meson scattering information.

4.1.1 Production mechanisms and final state interactions

The nature of glueballs suggests the way to look for them is to consider processes with an initial state rich in glue. We then look at the meson final state of such reactions, for example the $\pi\pi$ mass spectrum. From this we learn about a process we like to regard as 'gluon' $\rightarrow \pi\pi$. It is natural then to compare and contrast this with the $\pi\pi$ mass spectrum from a reaction initiated by quarks. Let us recall how we learn about meson states in such channels as this will introduce many ideas relevant to gluonium searches.

In contrast to our very detailed access to baryons, essentially the only states of zero baryon number we can form in the laboratory are

those found in e^+e^- annihilation. Consequently, our knowledge of the spectroscopy of mesons comes about almost entirely from production processes. There in pN or NN scattering, we analyse some sub-channel of the final state. For example, we learn about the ρ from studying the $\pi\pi$ final state in $\pi^-p \to \pi^-\pi^+n$. Such processes are often thought of in a factorised way, wherein we regard the ρ as being first produced by the particular mechanism involved and then decaying in a universal fashion. This is the basis of the isobar picture.

In general, the production process is complex, depending on a multitude of kinematic variables and sub-reactions. Consequently, the 2 or multi-body final states may have a quite different appearance in differing kinematic situations and, in particular, a 'resonance' may appear to have a variable shape. An example is the S* puzzle, the S* production is believed by some group to be suppressed in the $pp \to pp\,\pi\pi$ double pomeron exchange process due to the absence of the S* peak in the data [134]. But a partial wave analysis of the data has shown a strong presence of S* in this process [69]. Thus unless we have a detailed understanding of the production mechanism and the properties it must satisfy we may not know whether a short-lived state appearing in one channel is the same or different from that in some other. It is therefore essential to have an accurate description of production to be able to distinguish new from old effects. Thus in the investigation of final states interactions to be described later, it will be necessary to outline for each reaction what the production mechanism is and how we are to describe it.

In general, production mechanisms cannot be accurately modelled. We therefore seek situations where these mechanisms simplify: at high energies and small momentum transfers, for example. There processes become dominated by exchanges in the t-channel, which carry well-defined quantum numbers and for which the Regge model provides an excellent phenomenological description. Thus the high energy production of the ρ in $\pi^-p \to \pi^-\pi^+n$ may be factorised in the t-channel to give information about $\pi"\pi" \to \rho \to \pi\pi$, where the "initial" state π is off-shell with a negative mass-squared. As recognised long ago by Chew and Low [145], and independently by Goebel [146], the pion has such a tiny mass that its pole at $t=0.02\ (GeV)^2$ is appreciably felt in the scattering region of $t<0$. In reactions like $\pi^-p \to \pi^-\pi^+n$ or $\pi^-p \to K^-K^+n$, which are controlled by the exchange of pion quantum numbers in the t-channel, we can therefore factor off the nucleon vertex and extrapolate the residual meson vertex to the pion pole. We thus obtain information on physical $\pi\pi \to \pi\pi$, $\to K\bar{K}$ scattering. For the channels in question these have hitherto been the only purely mesonic processes, for which there has been sufficient experimental information to allow the extraction of amplitudes, thus our only source of information on what in the naive parton description we may regard as quark interactions initiated by meson.

It is possible that information on what we may think to be gluon interactions can be extracted by special mechanisms in a similar way. Such a mechanism is believed to be the 'hard gluon' double pomeron exchange which yields final states with quantum number accessible to

glueballs. Experiments on both 'quark' and 'gluon' channels reveal that up to roughly 1.4-1.5 GeV in mass, 4π, 6π etc, production are small enough (in a sense to be quantified later) to be neglected in comparison with the dominant $\pi\pi$ and $K\bar{K}$ channels. What is more, below $\sim$ 1 GeV, $\pi\pi$ scattering is purely elastic and unitarity is a particularly powerful constraint [147]. When the $K\bar{K}$ channel opens up, it is known to couple strongly, so that a coupled channel analysis is essential and with detailed experimental information on both channels, this becomes feasible. The formalism which allows us to take into account the constraint of two channel unitarity so important for such an analysis is explained in Section 4.2. With this apparatus, we will be able to investigate simultaneously the way the I = 0 S-wave appears in the seemingly quark initiated $\pi\pi \to \pi\pi$ ($K\bar{K}$) channels (Section 4.2.2) and as well as the supposedly glue-rich reactions $pp \to pp\ \pi\pi$ ($K\bar{K}$) of Section 5.2 and $\psi' \to J/\psi\pi\pi$, $J/\psi \to \phi\pi\pi$ of Section 5.4.1 .

4.2 MULTI-CHANNEL UNITARITY AND FINAL STATE INTERACTIONS

4.2.1 Unitarity

The conservation of probability requires that the scattering matrix $\underset{\sim}{S}(s,t,u)$ be unitary: $\underset{\sim}{S}^{\dagger}\underset{\sim}{S} = \underset{\sim}{I}$. In terms of the transition matrix $\underset{\sim}{T}$ and the phase space matrix $\underset{\sim}{\rho}$, $\underset{\sim}{S} = \underset{\sim}{I}+i2\underset{\sim}{\rho}^{\frac{1}{2}}\underset{\sim}{T}\underset{\sim}{\rho}^{\frac{1}{2}}$, the unitarity condition becomes

$$\underset{\sim}{T} - \underset{\sim}{T}^{\dagger} = 2i\underset{\sim}{\rho}\,\underset{\sim}{T}^{\dagger}\underset{\sim}{T} \qquad (4.1)$$

This is the most powerful condition in hadronic physics and provides a

number of useful constraints on any model of hadronic interactions. A brief introduction to the usefuless of unitarity is first given here with a simple one channel elastic process a + b -> a + b as an example, then follows by its application to coupled channel. The threshold factor or the density of final states ρ takes the form $\rho = \sqrt{(s-m^2)/s}$ where $m^2 = (m_a+m_b)^2$. Since a resonance has definite spin and parity, it is therefore natural to expand the transition amplitude $\mathcal{T}$ in terms of partial waves

$$\mathcal{T}(s,t) = \sum_{l=0}^{\infty} (2l+1)\mathcal{T}_l(s)P_l(\cos\theta) \tag{4.2}$$

where $\mathcal{T}_l(s)$ is the l^{th} partial wave amplitude and $P_l(\cos\theta)$ are the Legendre polynomial. The unitarity condition of Eqn. 4.1 implies that

$$\mathrm{Im}\,\mathcal{T}_l(s) = \rho|\mathcal{T}_l(s)|^2 \tag{4.3}$$

For simplicity and later relevance we only consider the low energy domain where interactions are purely S-wave. This reduces to $\mathcal{T}(s,t) = \mathcal{T}_{l=0}(s)$ and a parametrization that satisfies the unitarity condition are equivalently:

$$\mathcal{T}(s) = \sin\delta\, e^{i\delta}/\rho \tag{4.4}$$

$$= (e^{2i\delta} - 1)/2i\rho \tag{4.5}$$

$$= 1/[\rho(\cot\delta - i)] \tag{4.6}$$

Cross sections are proportional to $|\rho\mathcal{T}|^2$. The energy dependence of ρ can be obtained with a simple radioactive decay argument [148] which

gives the well known Breit-Wigner form

$$\rho\mathcal{T} = \frac{\Gamma/2}{(E_R - E) - i\Gamma/2} \qquad (4.7)$$

where Γ is the total width of the resonance at E_R . But from Eqn. 4.4, $|\rho\mathcal{T}|$ attains its maximum value when $\delta = \frac{\pi}{2}$. A simple Breit-Wigner resonance with mass E_R therefore has a 90^0 phase shift. We can now go back to the conventional understanding of the low energy $\pi\pi$ phase shift in which the S*(975) sits on a rising background from $\varepsilon(1300)$. This is illustrated in Figure 4.1 as the superposition of phase shifts from a narrow and a very wide Breit-Wigner resonances. The shape of the $|\rho\mathcal{T}|^2$ or cross section corresponds to the solid line in Figure 4.1 is drawn in Figure 4.2 which shows the characteristic dip of S* near 1 GeV. We now turn to the next section for coupled unitarity.

4.2.2 Coupled channel unitarity and its generalization

As we are only concerned with the scalar sector, all the formalism in this section are for the I = 0 S-wave. When the $K\bar{K}$ channel becomes accessible there are three different transition amplitudes $\mathcal{T}_{ij}$ which are the elements of the coupled hadronic $\mathcal{T}$-matrix. The i and j of $\mathcal{T}_{ij}$ denotes the initial and final state of the transition. The elements $\mathcal{T}_{ij}$ are

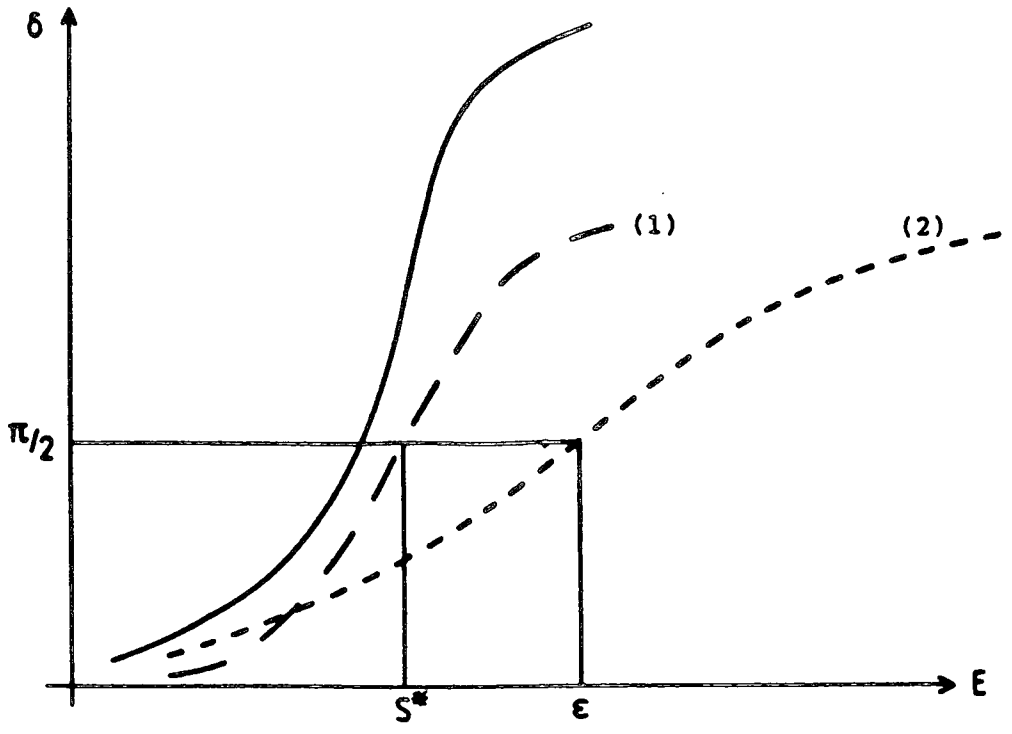

Figure 4.1 The dotted lines (1) and (2) are the phase shifts of two pure Breit-Wigner resonances S* and ε. The solid line is the combined effect of these two pure resonances (one narrow and one wide) that produces the classic S* signal (see Figure 4.2).

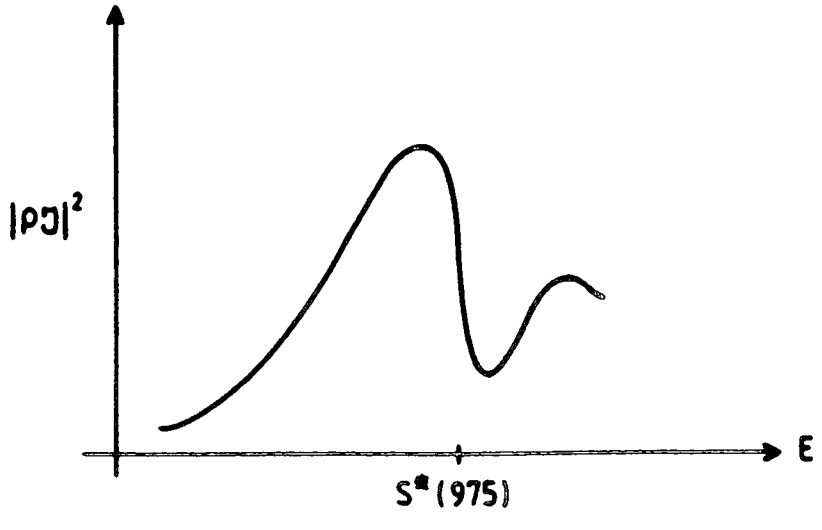

Figure 4.2 The shape of the cross-section corresponds to the solid line in Figure 4.1.

$$\mathcal{J}_{11} = \mathcal{J}(\pi\pi \to \pi\pi) \tag{4.8}$$

$$\mathcal{J}_{12} = \mathcal{J}(\pi\pi \to K\bar{K}) \tag{4.9}$$

$$\mathcal{J}_{22} = \mathcal{J}(K\bar{K} \to K\bar{K}) \tag{4.10}$$

and $\mathcal{J}_{12} = \mathcal{J}_{21}$ by the CPT invariance of strong interactions. Inelastic effects can be accounted for by introducing the elastic factor η ($0 < \eta < 1$) into Eqn. 4.5 which becomes

$$\mathcal{J}_{11} = (\eta e^{2i\delta_{11}} - 1)/2i\rho_1 \tag{4.11}$$

ρ_1 stands for the effective threshold factor for the $\pi\pi$ channel with effective pion mass m_1 defined by

$$4m_1^2 = (4(m_1^n)^2 + 8(m_1^c)^2)/3 \tag{4.12}$$

$$= 0.076132 \text{ GeV}^2$$

where n and c denote neutral and charged respectively. We also define an effective threshold factor ρ_1 for the $K\bar{K}$ channel as

$$\rho_2 = (\rho_2^n + \rho_2^c)/2 \tag{4.13}$$

with $\rho_2^k = \sqrt{[s - 4(m_2^k)^2]/s}$, k = n and c

These threshold factors ρ_1 and ρ_2 form the elements of the digonal matrix $\underset{\sim}{\rho}$ with $\rho_{ii} = \rho_i$, i = 1, 2.

The single channel elastic unitarity for $\pi\pi \to \pi\pi$ in the language of bubble diagrams is

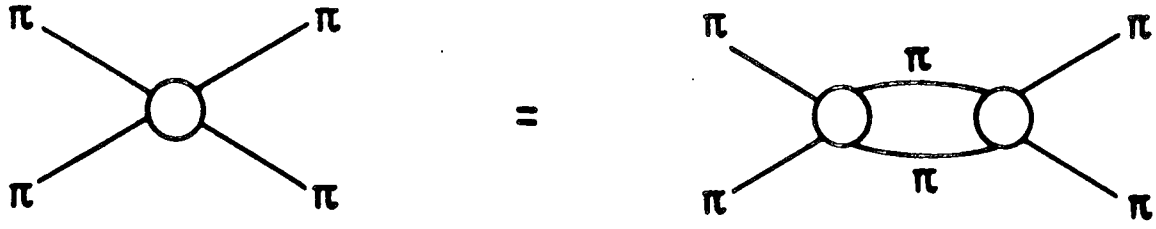

$$\mathrm{Im}\,\mathcal{J} = \rho|\mathcal{J}|^2$$

The coupled channel unitarity can be written as generalization of the single channel unitarity bubble diagram:

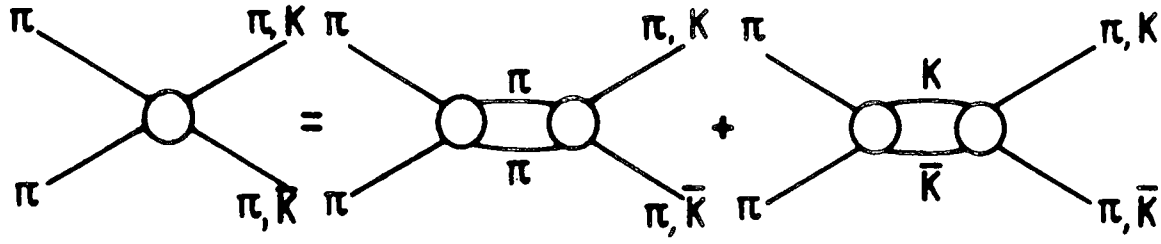

$\pi\pi \to \pi\pi$ $\qquad \mathrm{Im}\,\mathcal{J}_{11} = \rho_1|\mathcal{J}_{11}|^2 + \rho_2|\mathcal{J}_{12}|^2$

$\pi\pi \to K\bar{K}$ $\qquad \mathrm{Im}\,\mathcal{J}_{12} = \rho_1\mathcal{J}_{11}^*\mathcal{J}_{12} + \rho_2\mathcal{J}_{12}^*\mathcal{J}_{22}$

$$\mathrm{Im}\,\mathcal{J}_{ij} = \sum_k \rho_k \mathcal{J}_{ik}^* \mathcal{J}_{kj} \qquad (4.14)$$

Having obtained the coupled channel unitarity we can analyse the $\pi\pi \to \pi\pi$, $K\bar{K}$ data and in principle find all the possible resonances in these channels. However all existing data have relatively poor statistics in the crucial 1 GeV mass region where the scalar glueball is predicted to be and may have a very narrow width. The reason for this can be seen in Figure 4.2 where the S-wave is at a minimum in the 1 GeV region. In order to make use of data from other processes with the same final states, such as the AFS data, we need to relate the amplitudes $\mathcal{J}_{ij}$ to the amplitudes of these processes.

We use the term '<u>production processes</u>' to denote any mechanisms, like $\gamma\gamma$ -> hadrons or $I\!P\,I\!P$ -> hadrons, where the incoming particles do not participate as intermediate states in the unitarity bubble diagram.

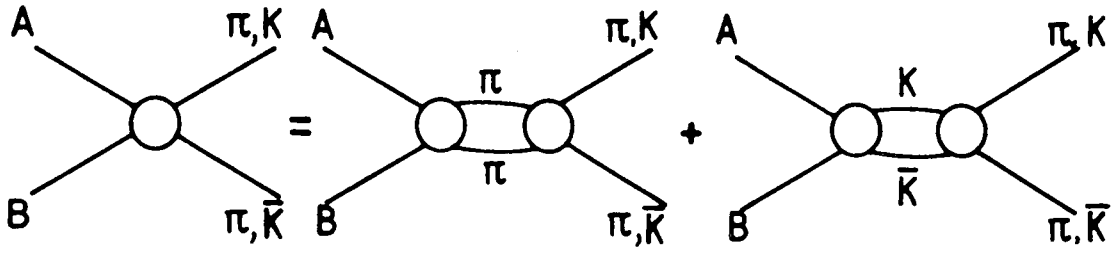

where A and B are not pions nor kaons

$$AB \to \pi\pi \qquad \mathrm{Im}\,\mathcal{J}_1^{(c)} = \rho_1 \mathcal{J}_1^{(c)*} \mathcal{J}_{11} + \rho_2 \mathcal{J}_2^{(c)*} \mathcal{J}_{21}$$

$$AB \to K\bar{K} \qquad \mathrm{Im}\,\mathcal{J}_2^{(c)} = \rho_1 \mathcal{J}_1^{(c)*} \mathcal{J}_{12} \quad \rho_2 \mathcal{J}_2^{(c)*} \mathcal{J}_{22}$$

The production amplitudes are denoted by $\mathcal{J}_i^{(c)}$. The unitarity condition for the coupled production channel is

$$\mathrm{Im}\,\mathcal{J}_i^{(c)} = \sum_j \rho_j \mathcal{J}_j^{(c)*} \mathcal{J}_{ji} = \sum_j \rho_j \mathcal{J}_j^{(c)} \mathcal{J}_{ji}^* \qquad (4.15)$$

which is a generalization of Eqn. 4.14. Note that Eqn. 4.15 in contrast to Eqn. 4.14 is a linear constraint, a consequence of the assumed non-strongly interacting character of the incoming particles. Where just one final state is available, Eqns. 4.14-15 require that (modulo π's) the phase of the hadronic and all production processes should be the same - the familiar Watson's final interaction theorem [149]. We are concerned with its multi-channel generalization [150]. To this end, we can immediately write down an expression for $\mathcal{J}_i^{(c)}$, which embodies the above constraints,

$$\mathcal{J}_i^{(c)} = \sum_j \tilde{\alpha}_j^{(c)} \mathcal{J}_{ji} \qquad (4.16)$$

with the $\tilde{\alpha}_j^{(c)}$ real. Such a form obviously satisfies Eqn, 4.15 given

Eqn 4.14. Finally, the production amplitudes $\mathcal{T}_i^{(c)}$ are related to the corresponding cross section $\sigma_i^{(c)}$ by

$$\sigma_i^{(c)} = f^{(c)} \rho_i |\mathcal{T}_i^{(c)}|^2 \qquad (4.17)$$

where $f^{(c)}$ is the initial flux

and ρ_i is the appropriate density of final states.

4.2.3 Analyticity and Adler zero condition

To give a sensible parametrization of our formalism we must take into account all the properties of the amplitudes. We consider the $\pi\pi$ scattering as an example to illustrate analyticity and to derive the Adler zero condition [151][152]. The right hand side of the unitarity sum of Eqn. 4.14 for $\pi\pi$ scattering, $\mathcal{T}_{11} = \Sigma \rho_k \mathcal{T}^*_{1k} \mathcal{T}_{k1}$, sums over all the kinematically accessible channels. The opening of a new channel may therefore change the sum drastically and there must be a singularity in $\mathcal{T}_{11}$ at each reaction threshold $s > 4m_\pi^2$. Furthermore, the s-plane is complex with resonances as poles on the complex s-plane i.e. a simple Breit-Wigner resonance with mass m_R and width Γ corresponds to a pole $s = m_R^2 - i m_R \Gamma$ in the complex s-plane. The complex s-plane can be divided into different sheets, known as Riemann sheets, according to the signs of $\mathrm{Im}\ \rho_k$. In perturbation theory the singularities in $\mathcal{T}_{11}$ take the form of cuts with branch points at the thresholds on the real s-axis and extending to $s = \infty$, known as Right hand cuts, with possible values of s extending over many Riemann sheets. The sheet containing the real axis below the branch point is called the physical sheet. As s and u

are directly related by the expression $s = \sum_i m_i^2 - t - u$ with t fixed, then branch points in the u-channel reaction must appear on the negative real s-axis, with cuts extending to $s = -\infty$. These are the Left hand cuts of the complex s-plane.

Furthermore, if there exists a particle with mass $m_0 < 2m_\pi$ and the quantum number of $\pi + \pi$, then there is a corresponding pole on the real axis at $s = s_0 = m_0^2$. The contribution of such pole at $\mathcal{J}_{11}$ is called the Born term. In $\pi\pi$ scatterings there is no Born term (no particle exists with mass < 280 MeV that can couple to two pions). Moreover, low energy scattering is known to be suppressed as a consequence of the soft pion theorems we now describe.

As already pointed out in Section 1.3 the symmetry of the Lagrangian is always reflected in the algebra of currents. The QCD Lagrangian with three quark flavours has the chiral symmetry $SU(3)_L \times SU(3)_R$ in the massless quark limit but the symmetry is spontaneously broken down to $SU(3)_V$ required by the observation that the vector nonet is heavier than the pseudoscalar nonet. The light masses of the pions indicate that the $SU(2)_L \times SU(2)_R$ chiral symmetry is only softly broken by the u and d quark masses and the breaking of the symmetry is reflected in the non-conservation of the axial current. The partially conserved axial current (PCAC) hypothesis [152][153] then assumes that the divergence of this non-conserved axial current is dominated by the pion field.

e.g. $$\partial_\mu A_\mu^+(x) = f_\pi m_\pi^2 \phi_\pi^+(x) \qquad (4.18)$$

where ϕ_π^+ creates a π^+ and f_π is the pion decay constant, with

$$A_\mu^+ = A_\mu^1 + iA_\mu^2 .$$

To investigate low energy $\pi\pi$ scattering we consider on-shell scattering

$$\pi^\alpha(p_1) + \pi^\beta(p_2) \to \pi^\gamma(p_3) + \pi^\delta(p_4),$$

with amplitude

$$\langle \gamma , \delta \mid \mathcal{T} \mid \beta , \alpha \rangle .$$

Assuming one of the πs is off shell, say α, as in $\pi^- p \to \pi^-\pi^+ n$ then from PCAC we have

$$\int \langle \gamma, \delta \mid \partial_\mu A_\mu^\alpha(y) \mid \beta \rangle e^{ip_2 y}\, dy = \int f_\pi m_\pi^2 \langle \gamma , \delta \mid \phi^\alpha \mid \beta \rangle e^{ip_2 y}\, dy$$

$$\propto \frac{f_\pi m_\pi^2}{p_\alpha^2 - m_\pi^2} \langle \gamma , \delta \mid \mathcal{T} \mid \alpha , \beta \rangle \qquad (4.19)$$

But $\langle \gamma , \delta \mid \partial_\mu A_\mu^\alpha \mid \beta \rangle = -ip_\mu^\alpha \langle \gamma , \delta \mid A_\mu^\alpha \mid \beta \rangle$

Hence $\langle \gamma , \delta \mid \mathcal{T} \mid \alpha , \beta \rangle \propto (p_\alpha^2 - m_\pi^2) p_\mu^\alpha \int \langle \gamma , \delta \mid A \mid \beta \rangle e^{ip_2 y}\, dy$

Thus in the limit $p_\mu \to 0$ or $s = t = u = m_\pi^2$ the amplitude vanishes because the matrix element of the axial current between a single-pion and a two-pion state has no pole in this limit. This is known as the Adler zero. Indeed experiment shows that S-wave $\pi\pi$ scattering is suppressed at threshold for on-shell pions. This is to be contrasted with a process like $\gamma\gamma \to \pi\pi$ or $I\!P\,I\!P \to \pi\pi$ for which there is a pion exchange Born term and the Adler condition implies no zero [Fig. 4.3].

Having briefy discussed the theoretical background for our formalism to describe the final state interactions for both meson scatterings and production processes, we now turn to the parametrization of the amplitudes.

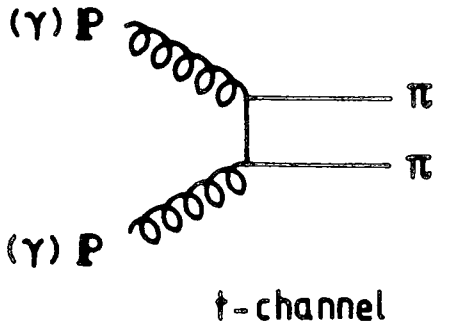

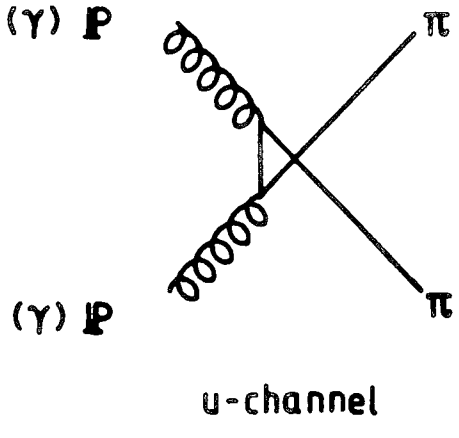

Figure 4.3 Born Diagrams for P P (γγ) -> ππ.

4.2.4 Analyticity and unitarity

We believe, the coupled channel unitarity of Eqn. 4.14 and its generalization Eqn. 4.15 with the particular form of $\mathfrak{I}_i^{(c)}$ in Eqn. 4.16, provide a full description for all the S-wave $\pi\pi$ and $K\bar{K}$ final state interactions below 1.7 GeV. Before describing the specific parametrizations used in our formalism. We first consider some general features.

The assumed real and smooth forms of the $\tilde{\alpha}$'s in Eqn. 4.16 is implied by all the right hand cut structure of $\mathfrak{I}_i^{(c)}$ being explicitly included in the sum over $\mathfrak{I}_{ji}$. Moreover, in the case of interest with $\pi\pi$ final states, we must allow appropriately for the occurrence of Adler zeros near threshold. The actual position of the zero is process-dependent; in particular, the zero for the elastic amplitude $\mathfrak{I}_{11}$ is shifted, or in some cases removed, when one turns to the associated production process. We can cater for this in the above formalism by dividing through by the zero of the elastic channel at $s = s_0$. Thus defining

$$T_{11} \equiv \frac{\mathfrak{I}_{11}}{s-s_0} \tag{4.20}$$

we can allow for zeros in the production process in question by requiring them to enter in the $\alpha^{(c)}$'s. For simplicity of discussion, we set the closely related zeros in $\mathfrak{I}_{12}$ and $\mathfrak{I}_{22}$ at the same position, since the data are only sensitive to the zero of $\mathfrak{I}_{11}$. Thus

$$T_{ij} \equiv \frac{\mathcal{J}_{ij}}{s-s_o} \tag{4.21}$$

enabling us to write

$$\mathcal{J}_i^{(c)} = \sum_j \alpha_j^{(c)} T_{ji} \tag{4.22}$$

with the tilde over the α's removed to signify that they are coefficients of the 'reduced' T's. The $\alpha_j^{(c)}$ may be viewed as intrinsic couplings, which control the propensity of process (c) to initiate production in channel j, the final outcome being determined by the final state interactions supplied by the T_{ji} factors [154].

It is interesting to compare the resulting expression for $\mathcal{J}_i^{(c)}$ with that resulting from a one-channel analysis [147], where an application of unitarity and analyticity yields the form

$$\mathcal{J}_1^{(c)} = P^{(c)} \Omega^{(c)} \tag{4.23}$$

Here $P^{(c)}$ is, in general, slowly varying, incorporating any zero factors, and $\Omega^{(c)}$, the Omnès function [155], is given by

$$\Omega^{(c)} = \exp\left[\frac{s}{\pi} \int_{4m_\pi^2}^{\infty} ds' \frac{\phi^{(c)}(s')}{s'(s'-s)} \right] \tag{4.24}$$

with $\phi^{(c)}$ the phase of $\mathcal{J}_1^{(c)}$. the corresponding expression for the reduced elastic amplitude T_{11} takes the form

$$T_{11} = n \Omega^{(el)} \tag{4.25}$$

where $\Omega^{(el)}$ is the analogue of Eqn. 4.24 with the appropriate phase $\phi^{(el)}$

substituted for $\phi^{(c)}$. Below the second threshold ($s=4m_K^2$), all the phases in question are equal by Watson's theorem. This has the consequence, for the actual phases that pertain in practice, that the Ω's are effectively universal below the vicinity of the $K\bar{K}$ threshold. As previously discussed, this virtually eliminates any possibility of new processes uncovering new effects in the single channel region [147]. However, very close to $K\bar{K}$ threshold the signal may be individual to that reaction.

To see how this translates into the two-channel formalism, we need only compare the rival formulae for $\mathfrak{Z}_1^{(c)}$:

$$\begin{aligned}\mathfrak{Z}_1^{(c)} &= P^{(c)}\,\Omega^{(c)} \\ &= \alpha_1^{(c)}\,T_{11} + \alpha_2^{(c)}\,T_{21} \\ &= (\alpha_1^{(c)} + \alpha_2^{(c)}\,\frac{T_{21}}{T_{11}})\;n\;\Omega^{(el)}\end{aligned} \tag{4.26}$$

The quantity to compare with $P^{(c)}$ is $\tilde{P}^{(c)}$ defined by

$$\tilde{P}^{(c)} = (\alpha_1^{(c)}\,T_{11} + \alpha_2^{(c)}\,T_{21})/\Omega^{(el)} \tag{4.27}$$

which is real over the region of interest, since $\arg(T_{21}) = \arg(T_{11}) = \arg(\mathfrak{Z}_1^{(c)}) = \phi^{(el)}$ by Watson's theorem. For the practical analysis to be described in Chapter 5, the resulting $\tilde{P}^{(c)}$ compares well with the corresponding $P^{(c)}$[Fig. 5.11], indicating the near universality of the Ω's below $K\bar{K}$ threshold.

A simple reaction which illustrates this intimate relationship between processes with the same final state imposed by unitarity and analyticity is $e^+e^- \to \pi^+\pi^-$. Here the production mechanism is explicitly controlled by one virtual photon to a high degree of accuracy and consequently the quantum numbers of the $\pi\pi$ final state are forced to be those of the photon and have isospin one. Through Eqns 4.14-17 & 4.23-25, the ρ signal in the elastic process is closely related to that in e^+e^-, the Omnès function being almost identical. The small difference in the line shape of the ρ in these two channels is a result of the difference between n (recall Eqn.4.25) and $P^{(ee)}$ expected form their differing left hand cut structures - $P^{(ee)}$ in particular, having no cut, is just a simple polynomial. This relationship has been extensively investigated in studies of the pion's electromagnetic form-factor [156].

As we shall see the situation in the I = 0 J = 0 channel with strongly overlapping resonances and a nearby threshold greatly complicates this simplicity. Indeed, the I = 0 S-wave constitutes the most significant non-trivial mesonic example of coupled channel unitarity amenable to detailed analysis. It is to this we now turn.

4.3 PARAMETRIZATIONS OF THE K- AND M-MATRICES

After outlining the formalism for relating production and scattering information on the I = 0 $\pi\pi$ and $K\bar{K}$ S-waves. We need a parametrization to describe the energy behaviour of the $\mathcal{J}$-matrix and at the same time account for the unitarity properties and threshold singularities of the $\mathcal{J}$-matrix. A form of such parametrization is suggested by Eqn. 4.6 from which we can write the single-channel amplitude in the form

$$\mathcal{J}_{11} = \frac{1}{\frac{1}{K_{11}} - i\rho_1} \tag{4.28}$$

where K_{11} is a real function of s. The generalization of this to multi-channel situation is known as the K-matrix formalism and that

$$\underset{\sim}{\mathcal{J}} = \underset{\sim}{K}\,[\,\underset{\sim}{1} - i\underset{\sim}{\rho}\,\underset{\sim}{K}]^{-1} \tag{4.29}$$

$$= [\underset{\sim}{M} - i\underset{\sim}{\rho}]^{-1} \tag{4.30}$$

Here, $\underset{\sim}{\rho}$ is the diagonal matrix with diagonal elements ρ_1, ρ_2 . $\underset{\sim}{K}$ is a real symmetric matrix and $\underset{\sim}{M}$ its inverse. The associated S-matrix is defined by

$$\underset{\sim}{\mathcal{S}} = \underset{\sim}{1} + 2i\underset{\sim}{\rho}^{\frac{1}{2}}\,\underset{\sim}{\mathcal{J}}\,\underset{\sim}{\rho}^{\frac{1}{2}} \tag{4.31}$$

$$= [\,\underset{\sim}{1} + i\underset{\sim}{\rho}^{\frac{1}{2}}\,\underset{\sim}{K}\,\underset{\sim}{\rho}^{\frac{1}{2}}][\,\underset{\sim}{1} - i\underset{\sim}{\rho}^{\frac{1}{2}}\,\underset{\sim}{K}\,\underset{\sim}{\rho}^{\frac{1}{2}}]^{-1} \tag{4.32}$$

In the fits reported in Section 5.3, we take $\underset{\sim}{K}$, which is now 2x2, of the form [157] with $s = M^2$

$$K_{ij} = \frac{(s-s_o)}{4m_K^2} \sum_p \frac{f_i^p f_j^p}{(s_p-s)(s_p-s_o)} + \sum_{n=0} c_{ij}^n \left[\frac{s}{4m_K^2} - 1\right]^n \qquad (4.33)$$

$$\equiv (s-s_o)\hat{K}_{ij}$$

Our 'reduced' T-matrix elements (cf. Eqns.4.20-22) are then given by

$$\underset{\sim}{T} = \hat{\underset{\sim}{K}} \left[\underset{\sim}{1} - i\rho \underset{\sim}{K} \right]^{-1} \qquad (4.34)$$

Note, importantly, the single appearance of $\hat{\underset{\sim}{K}}$ in this formula.

Alternatively, we parametrize the $\underset{\sim}{M}$-matrix, Eqn. 4.30, as

$$M_{ij} = \frac{a_{ij}}{s-s_o} + \sum_p \frac{f_i'^p f_j'^p}{s_p' - s} + \sum_{n=0} c_{ij}'^n \left[\frac{s}{4m_K^2} - 1\right]^n \qquad (4.35)$$

In Eqns. 4.33,35, $s = s_0$ represents the Adler zero of the T-matrix, Eqns. 4.20-21. The number of poles and order of the polynomial in Eqns. 4.33,35 required to fit the data will be detailed in Chapter 5.

Finally, for the α_i's we take the simple power expression

$$\alpha_i = \sum_{n=0} \alpha_i^n \left[\frac{s}{4m_K^2}\right]^n \qquad (4.36)$$

(Note that we have now ceased to label the initiating reaction and use the superfix label to identify terms in this Taylor expansion). The number of terms we take in such an expansion will depend upon the range of energies over which we are fitting data. For example for the $\psi' \to \psi\pi\pi$ decay, for which phase space is limited to $279 \lesssim M \lesssim 589$ MeV, a linear form is adequate, while for the $\bar{p}p$ reaction, we fit S-wave information up to 1700 MeV and use quadratic forms.

In order to determine the parameters in our K- and M-matrix expressions, we need to fit data on the classic hadronic phase-shift data on δ_{11} and δ_{12}. We shall see later that in fact a combined fit to the $\mathbb{P}\mathbb{P}$ production results is even more constraining, since we can profit from the additional statistical weight and the distinct and efficient partial wave separation these new data allow. As is customary, the $K\bar{K}$ channel is assumed to dominate the inelasticity from $\pi\pi$, rendering a two channel analysis a good approximation. We will comment in detail later when and where this assumption breaks down and the likely effect of this.

CHAPTER FIVE

DATA ANALYSIS

5.1 DATA SELECTION

Given the framework described in Chapter 4, one is looking for information on just 3 parameters at each energy δ_{11}, η_{11} and ϕ_{12}. These fix $\mathcal{I}_{11}$ and $\mathcal{I}_{12}$, through the usual relations (cf. Appendix B)

$$\mathcal{I}_{11} = [\eta_{11} e^{2i\delta_{11}} - 1]/2i\rho_1 \tag{5.1}$$

$$\mathcal{I}_{12} = [1-\eta_{11}^2]^{\frac{1}{2}} e^{i\phi_{12}}/2(\rho_1\rho_2)^{\frac{1}{2}} \tag{5.2}$$

The quantities η_{11} and δ_{11} have been determined in numerous analyses of di-pion production experiments. Of these, we select as input to the present fit, the classic energy independent analysis by the CERN-Munich group of their high statistics expeiment on $\pi^-p \rightarrow \pi^+\pi^-n$ at 17 GeV/c [158][159]. These results are strongly supported by earlier experiments, in particular by the LBL $\pi^+\pi^-$ experiment of Protopopescu et al [160]. Above $K\bar{K}$ threshold, we supplement this $\pi^+\pi^-$ information with the phase shifts derived by Cason et al from an analysis of their 8 GeV/c experiment on $\pi^-p \rightarrow \Delta^{++}\pi^0\pi^0$ [161]. However, below 1 GeV, the S-wave solutions of Cason et al are controversial being in total disagreement with the $\pi^+\pi^-$ results of LBL and CERN-Munich. We therefore exclude their results at lower $\pi\pi$ masses. Above 1 GeV, when many waves become important particularly in $\pi^+\pi^-$ scattering, a multitude

of partial wave solutions is possible. These are constrained by fixed t-dispersion relations to essentially two solutions [162]. Of the $\pi^+\pi^-$ solutions found in the energy independent analysis of Martin and Pennington, the $\pi^+\pi^-$ results of Cason et al [161] and the polarized target data of the ACCMOR collaboration [163] favour the so-called β' solution. We therefore input this solution together with the phase shift solutions of Ochs [159] and of Cason et al [161]. The reason for including as independent data sets the results of both the Ochs and the Martin and Pennington analyses of the same $\pi\pi$ data is that these analyses have differing constraints and the resulting S-wave, being the lowest wave in data dominated by higher waves up to spin 3, is poorly determined, and has sizeable error ellipses (shown on representative data points in Fig. 5.6). Our aim is to pick out a smooth track through this error corridor.

Under the two-channel assumptions, additional and perhaps more reliable information on η_{11} [Eqns. 5.1-2], comes from the analogous $K\bar{K}$ production experiments with incoming pion beams. There have been a number of experiments both on K^+K^- and $K^0_SK^0_S$ production [164][165][166]. Besides fixing the magnitude of η_{12}, these also provide information on its phase, ϕ_{12}, relative to one of the other participating waves, in practice the D-wave. On the magnitude, $|\eta_{12}|$, the various experiments concur fairly well; however, there is a significant disagreement as to the phase behaviour of $\phi_{SD} = |\phi_{12} - \phi_D|$ below 1150 MeV. According to the K^+K^- experiments of Ref. 164, ϕ_{SD} is flat over this energy domain whilst the other $K\bar{K}$ experiments find a steep rise

[Fig. 5.8], at the lowest energy, the discrepancy is some 70^0 [167]. Since 'a priori' we do not know which, if either, is correct, we input the results of the amplitude analyses of two representative high statistics experiments:

1. by Cohen et al [164] of their $\pi^-p \to K^+K^-n$ and $\pi^+n \to K^+K^-p$ 6 GeV/c data, and
2. by Etkin et al [165] of their $\pi^-p \to K^0_SK^0_Sn$ 23 GeV/c data.

These appear to span the range of experimental possibilities.

In order to extract ϕ_{12} from the published information on ϕ_{SD}, we need to know the behaviour of the D-wave phase in $\pi\pi \to K\bar{K}$. Below roughly 1.4 GeV, this is dominated by the f-resonance and accordingly assumed to be given by

$$\tan \phi_D = \frac{\sum_i m_f \Gamma^i_f \beta^i_2(s)\ \theta(s-s_i)}{m^2_f - s} \qquad (5.3)$$

where i runs over all contributing channels $\pi\pi$, $\eta\eta$, $K\bar{K}$, ... each with threshold at $s = s_i$. We input the barrier factor β_2 suggested by duality [168] from the nearest crossed-channel singularity to be

$$\beta^i_2(s) = \left[\frac{s-s_i}{m^2_f - s_i}\right]^{\frac{1}{2}} \frac{P_2(1+2m^2_\rho/(m^2_f-s_i))}{P_2(1+2m^2_\rho/(s-s_i))} \qquad (5.4)$$

where we take the standard PDG values for the f-resonance mass and width, and their uncertainties [169].

Such a form for ϕ_D we believe more plausible than that modelled by Etkin et al [166] below 1.2 GeV and this is the form we take to extract

ϕ_{12} , appropriately folding in the uncertainties in ϕ_D given by those on m_f and Γ_f^i , which are typically 1^0 - 4^0. Since the D-wave phase given by Eqn. 5.3 accords well with D-wave modelled by Cohen et al [164] below 1.4 GeV, where it is f-dominated, we take their plotted values of ϕ_{12} directly as input. The resulting phases are shown in Figure 5.8, while the magnitude of $|\Im_{12}|$ is plotted Figure. 5.7.

A priori we have no reason to favour one experiment over the other (and in fact the analysis by Görlich et al [170] of their polarized target results disagrees with all of them). It is however worth noting that other experiments on $K\bar{K}$ production from Wetzel et al, Costa et al, Polychronakos et al [165], while all agreeing on the magnitude of the cross-section, tend to support the phase of Etkin et al, Figure 5.8. On the other hand, Cohen et al would justifiably argue that their analysis is the only one amenable to the necessary I = 0, 1 separation. In face of this, we shall henceforth assume that the results of Cohen et al and of Etkin et al span the range of current knowledge of ϕ_{12} . Their sizeable disagreement means that our input on the $\pi\pi \rightarrow K\bar{K}$ channel is far from homogeneous and we will describe in Section 5.3 the effect this has. Lastly, the uncertainties in ϕ_{12} within each experiment are very similar, reflecting their comparable statistics. Only the second data point of Etkin et al with a quoted $\pm 6^0$ on ϕ_{SD} is acutely out of line and its error has been increased to $\pm 20^0$ in our global fit to all these data, see Figure 5.8.

A guide to where our two channel saturation of unitarity breaks down can be seen by comparing the S-wave inelastic cross-section, viz

$(1 - \eta_{11}^2)/4$, as determined from the analyses of the CERN-Munich $\pi\pi$ scattering data [158] and the better defined $K\bar{K}$ contribution to this given by the actual $\pi\pi \rightarrow K\bar{K}$ cross-sction on which essentially all experiments agree [164][165][166]. We see in Figure 5.7 this comparison suggests the importance of other final states above 1.4 GeV. There already exists experimental evidence of a by no means negligible $\eta\eta$ S-wave signal in the f-region [171] and 4π production is beginning to take off [172]. Rather than attempt to fit obviously inconsistent data, in which the better determined $K\bar{K}$ cross-section would dominate this aspect of the fit, when clearly the total inelastic cross-section is more likely to be that of the CERN-Munich results of Figure 5.7, if other channels were included, we have determined solutions in which the $\pi\pi \rightarrow K\bar{K}$ data above 1.4 GeV are switched in and out. The results we describe in Section 5.3 will for the most part be those with it out and we will discuss later the rather small effect that neglecting other inelastic channels has on our results.

5.2 DOUBLE POMERON MECHANISM

The AFS experiment [69] was designed to study central dimeson production in $pp \rightarrow pp(MM)$. The triggering is such that though this experiment was performed at the CERN ISR, where the square of the c.m. energy, s_{tot}, is almost 4000 GeV^2, most of this momentum continues along the direction of the two beams. The protons scatter at tiny angles and only a small amount of momentum is transferred from each: $-0.015 \gtrsim t \gtrsim -0.045$ $(GeV/c)^2$. Importantly, this is a far smaller range

than any other experiment [67][68]. Moreover, the two mesons produced are well-separated in rapidity from the on-going protons, so that the mechanism for their production is naturally factorised from the scattering of the protons. The Regge model provides a phenomenologically well-tested description for this [173]. The satisfactory factorisation of the dimeson production from the forward going protons means that this reaction can be regarded as $(p\bar{p})(p\bar{p}) \rightarrow \pi\pi$ and the formalism of Section 4.2.2 is applicable to its analysis.

The quantum numbers of the 'reggeons' coupling to the protons [Fig, 5.1] are those appropriate to pp elastic scattering. At such high energies, these exchanges are dominated by vacuum quanum numbers carried by the 'pomeron'. Though the motivation for this experiment, as discussed in Section 3.2.6, is predicated on the specific idea that the pomeron is a colour singlet configuration of glue, so that the central production of mesons is generated by the fusing of glue, rather than quarks [66], knowledge of the exact nature of the production mechanism is inessential for our analysis which only needs an accurate phenomenological description.

The pomeron, having vacuum quantum numbers, fixes the quantum numbers of the dimeson final state to have I = 0 and even spin. Contamination from lower lying Regge exchanges like the ρ shows up in the dimeson angular distribution having odd angular momentum components in addition to a ρ peak in the $\pi\pi$ mass spectrum. This signal allows such extraneous effects from non-vacuum quantum numbers to be removed, as discussed extensively in Refs. 69 and 176. With such a tiny range of t in this

particular experiment, such contamination from non-pomeron exchanges is believed to be under control and readily separated.

The Mueller-Regge approach gives us a description for the contribution for the pp -> pp(MM) process. With s_{tot} the total c.m. energy squared, M the mass of the meson pair, t_1 and t_2 the square of the momentum transferred at each pp vertex [Fig. 5.1] and y the rapidity, such a Regge analysis allows us to factorise off the pp vertices and pomeron propagators to give what we may regard as a pomeron-pomeron cross-section (much like the $\gamma\gamma$ process studied in e^+e^- -> e^+e^-X - see Section 5.4.2) defined by

$$\frac{d^4\sigma}{dt_1 dt_2 dy dM^2/s_{tot}} = \alpha'^2\, \beta_{pp\,IP}(t_1)^2\, \beta_{pp\,IP}(t_2)^2\, |\xi_{IP}(t_1)|^2 \xi_{IP}(t_2)|^2 \left[\frac{\alpha(s_{tot})}{\alpha(M^2)}\right]^{\alpha_{IP}(t_1)+\alpha_{IP}(t_2)} \frac{M^2}{s_{tot}}\, \sigma_{IP\,IP}(M) \quad (5.5)$$

where $\xi_{IP}(t)$ is the 'signature' factor for the reggeon, normalised so that $Im\xi = 1$, and α' is the Regge slope of 0.9 GeV^{-2} introduced to make all the couplings β dimensionless. With such a normalization the pomeron contribution to the pp total cross-section is then

$$\sigma_{pp}^{tot} = \alpha'\, \beta_{pp\,IP}(0)^2 \quad (5.6)$$

The explicit M^2/s_{tot} in Eqn. 5.5 is a flux factor, which is to be distinguished form the $\alpha(s_{tot})/\alpha(M^2)$ factor. Though when $s_{tot} >> M^2 >> 1\ GeV^2$, this also becomes s_{tot}/M^2. In general

$\alpha(M^2) = 1/2 + \alpha' M^2$ is expected from the f-dominance of the pomeron; such a form provides an extrapolation to low dimeson masses of this Regge behaviour [174]. As s_{tot} is so enormous, $\alpha(s_{tot})$ can be replaced by $\alpha' s_{tot}$, leading to the expression

$$\frac{\alpha(s_{tot})}{\alpha(M^2)} = \frac{\alpha' s_{tot}}{\frac{1}{2} + \alpha' M^2} = \frac{s_{tot}}{M_\rho^2 + M^2} \qquad (5.7)$$

In the AFS experiment, t_1 and t_2 cover such a tiny range near the forward direction that we can take $t_1 = t_2 = 0.03\ GeV^2 = t$ and $\alpha_{I\!P}(t) = 1$. Then we simply have

$$\sigma_{I\!P\,I\!P}(M) = \frac{1}{2\alpha'^2\, \beta_{pp\,I\!P}(t)^4} \frac{(m_\rho^2+M^2)^2}{M^3} \frac{d^4\sigma}{dt_1 dt_2 dy dM} \qquad (5.8)$$

5.2.1 Overall mass dependence of the cross-section

Though this is inessential to our spectroscopic analysis of these data, it is interesting to see if we can understand the mass dependence of this corss-section over the whole region studied. Expressing the cross-section in terms of the $I\!P\,I\!P$ amplitude $\mathfrak{F}(M^2,z)$ where z is the cosine of the scattering angle of the mesons in the pomeron-pomeron c.m. for dipion production, this amplitude can be crudely modelled by one pion exchange. That the $I\!P\,I\!P \to MM$ process has such a one meson exchange Born term means that the Adler condition requires no vanishing of such amplitudes close to threshold [182], in contrast to $\pi\pi$ scattering itself. This will be important later on. This $I\!P\,I\!P$ reaction is in many ways similar to the $\gamma\gamma$ process [175]. Though both have such one meson

exchange Born terms (whether reggeised or not is almost irrelevant), their phenomenology requires this contribution to have low partial wave components that are strongly absorbed. Exactly how is not well understood [175]. Nevertheless, we can use such a model to illustrate the overall trend of the dipion mass spectrum. To confront the data we have to fold in the experimental angular acceptance function. From Cecil's thesis [176] we learn that this is

$$A(M,z) = \sum_{L \text{ even}} (2L+1)\, H_L(M)\, P_L(z) \qquad (5.9)$$

with z the cosine of the scattering angle in dimeson rest frame and where the coefficients $H_L(M)$ are given by Cecil for $L \leqslant 8$ up to 2.5 GeV - the acceptance function is roughly like $(1 - z^2)^2$. With a free overall normalization, we see from Figure 5.2, where (M^4) times the experimental cross-section is plotted, such a model can crudely describe the fall of the data. Of course, this amplitude, has no explicit M^2 - channel dynamics. From old ideas on the duality, we may expect pion exchange to average this in some sense, which it approximately does. However, such duality was never a well-defined concept for pomeron processes [177], as discussed again in Section 5.2.3, so perhaps we should not expect any better agreement. We would expect such an approximation to model the trend of the earlier data of Waddi et al [67], if we knew the relative acceptance and included the effects of the larger range in t_1 ,t_2 in Eqn. 5.5.

5.2.2 S-wave dimeson production

Let us now turn to our main purpose which is to analyse S-wave dimeson production. Decomposing this $I\!P\,I\!P$ cross-section into components for which the dimeson final state has definite spin J, the contribution a partial wave $\mathfrak{T}^J(M)$ makes is

$$\sigma^J_{I\!P\,I\!P}(M) = 16\pi \frac{\sqrt{M^2-4\mu^2}}{M^3} (2J+1) \left|\mathfrak{T}^J(M)\right|^2 \qquad (5.10)$$

where μ is the mass of each of the final state mesons, π or K as appropriate. Detailed analysis of the dimeson angular distribution shows that the cross-section is overwhelmingly S-wave to well beyond 1 GeV. The AFS collaboration have separated out this S-wave component up to 2.3 GeV and it is this we shall study in both the $\pi\pi$ and $K\bar{K}$ channels. From the tables of Ref. 69, we can deduce these S-wave cross-sections in 50 MeV bins by folding in the appropriate acceptance function, or more readily we can read off the full-corrected S-wave corss-section from Cecil's thesis [176] Figure 7.11, our Figure 5.9, in 25 MeV bins. The corresponding S-wave amplitudes are then given by combining Eqns. 5.8,10 to give

$$\left|\mathfrak{T}^{J=0}(M)\right|^2 = N \frac{(m_\rho^2+M^2)^2}{\sqrt{M^2-4\mu^2}} \frac{d^4\sigma^{J=0}}{dt_1 dt_2 dy dM} \qquad (5.11)$$

where

$$N = \left[32\pi\ \alpha'^2\ \beta_{pp\,I\!P}(t)^4\right]^{-1}$$

The circumstance that the $\pi\pi$ and $K\bar{K}$ channels both couple strongly must be allowed for in the formalism. From Section 4.2.2 we have for

$I\!P\,I\!P \to \pi^+\pi^-$

$$\mathfrak{I}_1^{I\!P\,I\!P} = \sqrt{\frac{2}{3}}\left[\alpha_1^{I\!P\,I\!P}\ T_{11} + \alpha_2^{I\!P\,I\!P}\ T_{21}\right] \qquad (5.12)$$

where the $\sqrt{2/3}$ is the appropriate isospin Clebsch-Gordon coefficient, and for $I\!P\,I\!P \to K^+K^-$

$$\mathfrak{I}_2^{I\!P\,I\!P} = \frac{1}{\sqrt{2}}\left[\alpha_1^{I\!P\,I\!P}\ T_{12} + \alpha_2^{I\!P\,I\!P}\ T_{22}\right] \qquad (5.13)$$

where again $1/\sqrt{2}$ is an isospin factor. The functions α_1 and α_2 contain the left hand cut singularities of the $I\!P\,I\!P$ amplitude which differ from those of $\pi\pi$ scattering being in principle complicated by additional singularities of the six point function $pp \to pp\pi\pi$ as studied by Halliday [178]. Nevertheless, with such a small range in t_i, the major difference along the right hand cut is, as we have already remarked, the fact that the Adler condition requries no near threshold zero in the $I\!P\,I\!P$ channel, in contrast to most other pion processes we consider. So though we parametrize α_1, α_2 by simple polynomials in M^2 suitable to describe their smooth behaviour along the right hand cut, they are not expected to vanish close to threshold.

In principle, knowing $\mathfrak{I}_{11}$, $\mathfrak{I}_{12}$ and $\mathfrak{I}_{22}$ from fitting the $\pi\pi \to \pi\pi$, and $\to K\bar{K}$ channels, the ISR data just determine α_1, α_2. However, the AFS results provide significant extra information on the hadronic $\mathfrak{I}_{ij}$ in the 1 GeV region to add to the traditional meson scattering processes, largely because the $\pi\pi$ S-wave is small there and the angular distribution in $\pi\pi \to \pi\pi$ scattering controlled by S-P interference

effects. In contrast, the $\mathbb{P}\mathbb{P}$ reaction is overwhelmingly S-wave even at 1 GeV and a more accurate signal is obtained. Thus the AFS data acts as a severe constraint on the determination of even $\mathfrak{J}_{11}$ and $\mathfrak{J}_{12}$, partiuclarly through the crucial $K\bar{K}$ threshold region. In Section 5.3 we describe fits to the data selected in Section 5.1, together with the AFS S-wave dimeson results [69][176].

5.2.3 Note on the D-wave cross section

Using notions of duality one can also estimate the expected cross-section for f-resonance production in this double pomeron process. Assuming the triple Regge coupling of the f to two pomerons determined in pp -> pX with the f-exchange having zero mass extrapolates on shell in the same way as the f coupling to $\pi\pi$ does, one predicts from the triple Regge analysis of Inami and Roberts [179] that the f-signal in the reaction pp -> pp$\pi\pi$ in the kinematic regime of the AFS experiment should be at least 5 μb GeV^{-4} for $d^4\sigma/dt_1 dt_2 dy\, dM$ integrated over the f-width [180]. The partial wave analysis [69][176] gives the 'observed' cross-section to be merely (0.5 ± 0.3) μb GeV^{-4}. This discrepancy, discussed in more detail in Ref. 180, could be ascribed either to a failure of simplistic duality ideas for pomeron couplings or an incorrect modelling of the relative D-wave acceptance in this experiment or both. Even if the experimental D-wave acceptance is at fault, this has little bearing on the predominantly S-wave cross-section we use, since such correction factors will inevitably be smooth functions of dimeson mass and so, as discussed in the previous section, absorbable in

the coupling functions $\alpha_i(s)$. It is for this reason that the previous simpler analysis [147] using earlier data with no acceptance corrections or partial wave separation at all is quite consistent with the present treatment Section 5.3.1.

Neverthless, the fact that the f-signal is so small in the AFS results, while clearly seen in other ISR experiments with larger t_1 , t_2 ranges [Fig. 5.1] may indicate that the f $I\!P$ $I\!P$ coupling has a more complicated t-dependence than we have naively assumed. Only by comparing the relative t-dependence of the S- and D-waves at both large and small momentum transfers will we understand this dramatic difference between the 3% D-wave in the AFS experiment in the f-region and 47% in that with the SFM.

5.3 THE FITS

In Section 4.2 we introduced a formalism to implement two channel unitarity. This is readily expressed in terms of either the K-matrix, or its inverse the M-matrix, Eqns. 4.29-30. Their real matrix elements we parametrize by sums of poles plus simple polynomials in s, the square of the dimeson mass, Eqns. 4.33,35. These forms determine the $\mathcal{J}$-matrix elements $\mathcal{J}_{ij}$, Eqns. 4.29-30 and, through the channel dependent functions α_i , the amplitudes for each production process, Eqn. 4.22. In this section we describe the outcome of an extensive global fit of these forms to the I = 0 S-wave data on $\pi\pi \to \pi\pi$, $\pi\pi \to K\bar{K}$ selected in Section 5.1 and the cross-section for $\pi\pi$, $K\bar{K}$ production in the AFS

experiment discussed above.

To summarize Section 5.1, the data sets used in our global analysis are:

$\pi\pi \rightarrow \pi\pi$; Cern-Munich [158][159], Cason et al [161] and the β' solution of Martin and Pennington [162].

$\pi\pi \rightarrow K\bar{K}$; Etkin [166] and Cohen [164]

$I\!P\,I\!P \rightarrow \pi\pi, K\bar{K}$; AFS [69]

We observe from Figure 5.8 that Etkin and Cohen provide two conflicting data sets for ϕ_{12} (cf. Section 5.1). To obtain a good starting point for our global analysis we first ignored the data of Cohen et al in our initial fits. As explained in Section 5.1, the S-wave ϕ_{12} has only been separated up to 1.4 GeV, we therefore fit Etkin from $K\bar{K}$ threshold up to 1.4 GeV. All data on $\pi\pi \rightarrow \pi\pi$ are fitted from the $\pi\pi$ threshold up to 1.7 GeV. Our initial strategy is to avoid all fine tuning and unnecessary complications, so effective pion and kaon masses given by $4m_1^2 = 0.07613$ GeV^2 and $4m_2^2 = 0.98277$ GeV^2 have been used in ρ_1 and ρ_2 (cf. Appendix A.V) to obtain the fits we now describe.

We first employed the K-matrix formalism with just one pole (cf. Eqn. 4.33 and Appendix A.III & IV). As a starting point, we tried out an illuminating exercise leaving out the AFS data. The outcome of this is that we obtained numerous good fits all with χ^2/d.f. ~ 1 for the rest of the data. When the AFS data was included the parameter space was found to be greatly constrained and tightly restricting the $\mathcal{T}$-matrix amplitudes. These restrictions mean that only by painstaking work were the best fits (to be described later) obtained. The best way I found of

fitting data with rapid variations, like the sharp rise in δ_0^0 [Fig. 5.3] and the shoulder of the AFS data [Fig. 5.9], is to fit the data point by point (or in small groups) in the region of rich structures. To see how best to deal with this we performed an exercise, in which the data in the region of rapid variation ($0.9 \leqslant E \leqslant 1.1$ GeV) were switched off and we were able to find solutions without a K-matrix pole. However, when the 0.9 - 1.1 GeV region was switched back on we found that the polynomial alone (with a reasonable number of terms i.e. < 10) could not do the job and the total number of parameters was dramatically reduced with the introduction of a K-matrix pole (see Appendix A.III). In fact one does not need to go very far with the polynomial to find out that it alone is not adequate. When one introduces an extra parameter to a fit one expects a decrease in χ^2 by a sensible amount. We illustrate this technical aside by introducing the concept of χ^2/d.f. used for measuring the quality of fits. Let's denote the number of data points by N_{data} and the number of parameters by N_{par}. The degree of freedom d.f. is defined to be $N_{data} - N_{par}$. When one increases N_{par} to N'_{par} one expects the quality of the fit to improve, i.e.

$$\left(\frac{\chi^2}{\text{d.f.}}\right) > \left(\frac{\chi^2}{\text{d.f.}}\right)'$$

From this we can justify the number of parameters required in our fits. Furthermore, one can also look at the correlations between the parameters to find out if any of them is redundant, i.e. with tiny correlation coefficients. (The minimizer employed in our analysis is the MINUIT (Cern) programme which has the facility for working out

correlation coefficients). Based on the above reasoning we only use one common Adler zero in all our fits [157].

Having briefly explained the philosophy of our fitting approach we now describe the various fitting procedures that lead to the final representative fits given in Table 5.1 (with K and M for K- and M-matrix fits; the subscripts are for the number of poles in the parameterizations). We shall leave all the fine details like resonance assignments to Chapter Six and only concentrate on giving an account of the fitting procedures here.

A representative one K-matrix pole global fit without Cohen et al described earlier has a χ^2/d.f. of 1.24 for 224 data and 24 parameters. When we searched for the $\mathcal{J}$-matrix poles (Appendix A.VI) of all the one K-pole solutions we always found among other poles one (to be explained later) on sheet II at 0.988 GeV which we call the B pole (See Chapter 6 for details). The pole pattern of all the solutions were extremely similar and deserved more investigation. Here, I would like to point out that the K-matrix pole in this parametrization must be near 1 GeV as required by the rise of δ_0^0 in the region (see Appendix A.III). Therefore to make sure that the B pole is not an artefact of the K-matrix parameterization we look for variations in the nearby K-matrix pole by performing multi-pole K-matrix fits, an example being the 3-pole K-matrix fit. A typical three pole fit has a χ^2/d.f. of 223/196. With two additional poles in the K-matrix the polynomial background is consequently simpler (cf. Eqn. 4.33). The main feature of the three pole fits is that one of the K-matrix pole is always near 1 GeV as

expected, while the other two are dispersed, so that compared with the one pole solutions the effect of these extra poles is just to reparametrize the smooth background - one pole occurs below $\pi\pi$ threshold reparametrizing left hand cut effects and the other above the region we fit reparametrizing the high energy continuum (cf. see K_3 in Table 5.1). The quality of the one pole and three poles K-matrix fits is remarkably similar, as is the pole pattern of these different amplitudes. While the position of the $\sim$ 1 GeV K-matrix pole varies slightly from fits to fits, the position of the B pole remains unchanged. To confirm our believe that the B pole is not an artefact of the parameterization and the pole pattern in general, we have obtained distinct solutions with an M-matrix parameterization, Eqn. 4.35.

The first M-matrix parametrization we used had one M-matrix pole (excluding the Adler zero pole, Appendix A.IV). A typical fit has a χ^2/d.f. of 217/196 = 1.11. We found again the B pole at exactly the same position as in all the previous K-matrix fits. An interesing observation is that the M-matrix pole is always close to 1 GeV which I believe is the reflection of its companion the $\sim$ 1 GeV K-matrix pole (cf. K_1 and M in Table 5.1 and Eqn. A.19). To convince myself that this is indeed the case, I have tried a two poles M-matrix fit and the χ^2/d.f. is 213/193 = 1.10. One of the two M-matrix pole is again near 1 GeV and the other one turns out to be above 2 GeV which is just the reflection of the far distance K-matrix pole in our previous three pole K-matrix fits (cf. K_3 in Table 5.1). The $\mathcal{J}$-matrix pole pattern is again found to be unchanged and proves the existence of the B pole

beyond doubt (see Section 6.1). However, the nature of B is not clear from these fits and we will study the role of B in more details later (see Section 6.2).

Having understood the nature of the poles in the parameterizations and established the pattern of the $\mathfrak{J}$-matrix poles, we went on to complete our global analysis by including Cohen et al up to 1.4 GeV (cf. Section 5.1). Furthermore, in obtaining the final representative fits [Table 5.1] we have used the ρ_2 defined in Eqn. 4.13 (Appendix A.V). This is just a fine tuning procedure because we had reproduced all the trial fits using this averaged ρ_2 instead of the old ρ_2 (with $4m_2^2 = 0.98277$). In general, we have not concerned ourselves with the fact that the experimental results are binned. In fitting, we have treated each datum as though it represented the value of the experiment at the bin's mean energy value. This is appropriate for smoothly varying amplitudes. However, from our trial fits described earlier we know that the B pole is on the real energy axis and is close to 1 GeV. Hence in the case of the AFS results in the neighbourhood of 1 GeV, for both $\pi\pi$ and $K\bar{K}$ channels [69], we have actually averaged the parametrizations over the bin widths, using Simpson's rule, when comparing with these data. This correctly allows for any rapid variation in the $\mathfrak{J}$-, and consequently $\mathfrak{F}$-, matrix elements in this region caused by the B pole. We have found that the K- and M- matrix parametrizations we have discussed give equally good fits to all the 258 data in the mass range from $\pi\pi$ threshold up to 1.7 GeV, their parameters are listed in Table 5.1. A typical one pole solution, K_1 ,

is shown in Figures 5.3-10. Apart from the revised error on one datum discussed in Section 5.1, no attempt has been made to weight particular sets of data in their contribution to χ^2 by anything other than the errors quoted in the relevant analysis of each data set [181]. The χ^2/d.f. is then roughly 1.3. As seen from Figures 5.3-10 the major contribution to χ^2 comes from the conflicting data sets on ϕ_{12}, Figure 5.8 . Leaving out either of these, i.e. exercising a prejudice as to which is correct, decreases the χ^2/d.f. in our otherwise global fit. (The strategy employed in the trial fits described earlier). This exercise favours Etkin et al over Cohen et al with a χ^2/d.f. of only 1.09 compared with 1.23. The parameters of the solution, K_1(Etkin), fitting the $\pi\pi \rightarrow K\bar{K}$ results of just Etkin et al are listed in table 5.1 too (i.e. one of the previous one pole trial fits). However, we find our amplitudes change so little between such alternatives that for the most part we quote those of the compromise global fit [181], Figures 5.3-10. We will comment later on this stability. Apart from the troublesome $\pi\pi \rightarrow K\bar{K}$ results, the data are very well fitted as illustrated in Figures 5.3-10, even, for example, the 3 data set on the $\pi\pi$ phase, δ_{11}, above 1 GeV from CERN-Munich as analysed by Ochs [159] and by Martin and Pennington [162] and from the $\pi^0\pi^0$ results of Cason et al [163]. Though these are not exactly consistent, the fit has found a very satisfactory smooth track through these data, see Figures 5.4,6.

As already remarked in Section 5.2, the input of the AFS double pomeron results is a severe constraint on the solution, not just on the

couplings α_i , for which quadratic forms have been used (Eqns. 4.22,36), but on the strong interaction amplitudes $\mathcal{T}_{11}$ and $\mathcal{T}_{12}$. As pointed out earlier in the philosophy of our fitting, the tight constraint imposed by the AFS on the amplitudes is borne out by the fact that the data set in the 1 GeV region could only be fitted with patient and delicate variation in the parameters. The AFS data tightly restrict how the amplitudes develop through the $K\bar{K}$ threshold region. This is reflected in the much more striking and stringent conclusions we will be able to deduce from this analysis than was previously possible using just elastic hadronic reactions. Notice in Figure 5.9 , the shoulder at $M \sim 0.9$ GeV before the steep fall. This is an important feature of both the AFS data [69] and all our fits as will be discussed in Chapter Six. Such a structure is also seen in the $\gamma\gamma$ data discussed in Section 5.4.2.

It is important to note that the rapid variations in $\mathcal{T}$-matrix elements required by experiment in the crucial $K\bar{K}$ threshold region, Figures 5.3-10, are not wholly generated by the nearby K-matrix pole. Rather they are due to the interplay between this pole and the 'background' polynomial. Because of the structures required near $K\bar{K}$ threshold, we have not been able to find solutions without a K-matrix pole with less than 40 parameters, though with more parameters we believe this may be possible (see earlier discussion and Appendix A.III). We have on the other hand been able to find further solutions with additional poles in the K-matrix and a consequently simpler polynomial background (cf. Eqn. 4.33). The parameters of a typical three pole solution, K_3 , are tabulated in table 5.1 . As

expected from the similarity of the previous one pole and three poles K-matrix trial fits, the introduction of more poles does out not change the global description of the data and the fits are almost indistinguishable from K_1 of Figure 5.3-10. We shall describe the detailed features of these different amplitudes in Chapter Six.

We have also obtained fits with a one-pole M-matrix parameterization. The parameters of a typical M-fit are listed in Table 5.1. Again the quality of the fit is excellent and the resulting physical amplitude is almost identical to solutions K_1 and K_3 - see Chapter Six. The small differences between these amplitudes is highlighted by looking at the Argand plot of the $\pi\pi \rightarrow \pi\pi$ S-wave, $\rho_1 T_{11}$. In Figure 5.5 the solutions K_1 , K_1(Etkin), K_3 and M are compared. They are essentially identical except for the energy range of 960 to 1100 MeV, and then only K_1(Etkin) differs above 1040 MeV. In this region of $K\bar{K}$ threshold, the amplitudes are varying most rapidly and so differences become exaggerated. Focussing on K^+K^- threshold where each solution leaves the circle and remembering that unitarity requires $\phi_{11} = \phi_{12}$ up to this energy, we see how changes in this point can bring a sizable difference in ϕ_{12} with only a small change in the corresponding amplitudes and their consequent pole structure (See Chapter 6). From Figure 5.5 ,the phase ϕ_{11} [$\phi_{11} = \delta_{11} + \tan^{-1}((1-\eta)/(1+\eta)\tan\delta_{11})$] is seen to fall quickly above K^+K^- threshold by almost 90^0 before rising again. It seems rather natural that ϕ_{11} and ϕ_{12} having been equal up to K^+K^- threshold should tend to keep together in the 8 MeV upto $K^0\bar{K}^0$ threshold (the reason for using the average ρ_2 in the global fits is for such purpose - to

distinguish the difference between Etkin et al, Cohen et al and AFS, cf. Appendix A.V). It is a feature of all our solutions that ϕ_{12} does indeed fall initially just as implied by the $\pi\pi \rightarrow K\bar{K}$ results of Etkin et al.

Our fitting procedure is predicated on the assumption that the $\pi\pi$ and $K\bar{K}$ channels exhaust the content of unitarity in the energy range for which we fit, namely up to 1.7 GeV. We know, of course, that this is a far too strong an assumption even above 1.2 GeV. Results on the $\eta\eta$ final state [171] suggest that this may contribute 2% to the inelastic cross-section even in the f-region [Fig. 5.7]. Such an additional channel would in fact have only a small effect on our amplitudes. More serious is the appreciable onset of 4π channels near ρ-ρ threshold [172] as mentioned in Section 5.1. Furthermore, we do not have precise information on the amplitude η_{12} above 1.4 GeV (see Figure 5.7). In all the fits reported so far (including the trial fits), the $K\bar{K}$ data are only fitted up to 1.4 GeV and beyond that η_{12} is determined by the inelastic $\pi\pi$ cross-section as determined from the elastic channel by CERN-Munich [158] (the magnitude $(1 - \eta_{11}^2)/4$ of η_{12} is obtained by measuring η_{11}). Another way to obtain information on η_{12} is to follow the $K\bar{K}$ contribution of Cohen et al [164] and Etkin et al [166]. We have obtained such a fit, K_1' , in which the inelastic cross-section is required to resemble more the above $K\bar{K}$ contribution (i.e. the Etkin et al and Cohen et al are fitted up to 1.7 GeV but the $\pi\pi$ inelastic data are only included up to 1.4 GeV). The truth presumably lies somewhere between the two extreme, Figure 5.7. In obtaining the K_1'

solution no phase input on ϕ_{12} has been imposed above 1.4 GeV, just its magnitude. This is because the strict imposition of the $K\bar{K}$ phase (as determined by Cohen et al, for example) is surely over-restrictive in the presence of other appreciable open channels. Nevertheless, by introducing more parameters a satisfactory fit to the phase information on ϕ_{12} (form Cohen et al) can be obtained giving a solution with a similar pole content to K_1' . As expected, the differences between K_1 and K_1' only occur above 1.4 GeV and then largely in their couplings to $K\bar{K}$. In Chapter Six we will exhibit these differences, which are again small.

5.3.1 Consistency checks

Here we perform two consistency checks on our solution and how they fit the AFS double pomeron results. The first is to consider how this much more sophisticated and complete treatment is related to the earlier single channel Omnès analysis by D.Morgan and M.R.Pennington [147] using 40% of the AFS statistics with their preliminary treatment of their acceptance. As detailed in Section 4.2.4, this can be done by comparing the two channel function $\tilde{P}$ of Eqn. 4.27 with the single channel P [Eqns. 4.23,26], which in Ref. [147] was taken to be a constant. The $\tilde{P}$ from our fits is plotted in Figure 5.11 and is seen to remain remarkably flat, emphasising the universality of the Omnès function below $K\bar{K}$ threshold and indicating no dramatic difference in the way the $\pi\pi$ final state couples to $\mathbb{P}\mathbb{P}$ than to $\pi\pi$ itself. This is to be contrasted with our discussions of the $\gamma\gamma$ process in Sections 5.4.2 and

7.4.

In fitting the AFS data we have only considered the S-wave cross-section, Eqn. 5.11, with no reference to its phase. However, there does exist phase information on this channel as analysed by Cecil [176]. Our second check is therefore to compare the prediction for the S-D wave interference predicted by our solutions with that given by experiment. With the D-wave phase assumed dominated by just the f-contribution and so given again by Eqn. 5.3 and its normalisation chosen to reproduce the reported height of the D-wave cross-section, we obtain the prediction shown in Fig. 5.12 in excellent agreement with AFS's experimental interference [69]. Deviations at higher $\pi\pi$ masses are to be expected as the D-wave phase is no longer f-dominated. The ability of our solutions to predict results not fitted make this a very satisfactory test of our amplitudes.

Apart from the elastic and inelastic channels of $\pi\pi$ scatterings which we have used to obtain our amplitudes, there are other sources of dimeson final states like heavy flavour decays and the two photon channel. These are all related through unitarity to the $\pi\pi$ and $K\bar{K}$ hadronic amplitudes, $\mathcal{J}_{ij}$ (cf. Eqn. 4.16), we have determined up to 1.7 GeV. In the next section, we have used one of our fits, K_1, to represent these amplitudes and consequently determined the $\pi\pi$ and $K\bar{K}$ couplings (the α_i) of these other processes.

5.4 OTHER SOURCES OF DIMESON FINAL STATES

5.4.1 Heavy flavour decays

The dipion mass spectrum observed in the decay of $\psi' \to J/\psi\pi\pi$ is seen to peak at high $\pi\pi$ masses ($\sim$ 600 MeV). This is often spoken of as reflecting some low mass epsilon-like structure in the I = 0 S-wave $\pi\pi$ system. This is to forget that $\pi\pi$ and $K\bar{K}$ decays of the states of hidden charm and hidden beauty are subject to exactly the same constraints as all other hadronic decays by virtue of their common final states. The amplitudes for these S-wave decays are also given by the formulae of Sections 4.2,3. [182].

Let us first consider the decays $\psi' \to J/\psi\pi\pi$ and $\Upsilon' \to \Upsilon\pi\pi$ (generically $V' \to V\pi\pi$). The phase space for the $\pi\pi$ final state is limited by the V' - V mass differences of less than 600 MeV. The experimental spectrum for the decay A -> B(MM) can be expresssed in terms of the appropriate S-wave amplitude $\mathfrak{Z}(M)$ by

$$\frac{d\Gamma}{dM} = \frac{\pi^2}{2M_A^3} \{[(M_A+M_B)^2-M^2][(M_A-M_B)^2-M^2][M^2-4\mu^2]\}^{\frac{1}{2}} |\mathfrak{Z}(M)|^2 \quad (5.14)$$

where M is the dimeson mass and once again μ is the mass of the individual mesons in this pair. The amplitude $\mathfrak{Z}$ will be given by an equation of the form of Eqn. 4.22. In the following fits we now describe, the 'reduced' amplitudes T_{ij} are obtained from the $\mathfrak{I}_{ij}$ amplitudes of the K_1 fit through Eqn. 4.20. The functions α_1 and α_2 are expected to contain an Adler zero, as PCAC requires such a zero close to

threshold for these ψ' and Υ' decays, there being no Born term. Otherwise we expect these functions α_1 and α_2 to be simple as these channels have a suppressed left hand cut, since the OZI rule 'forbids' $J/\psi\pi$ and $\Upsilon\pi$ intermediate states, Figure 5.13. We therefore parametrize them by a linear function of M^2. The position of the on-shell zero is to be determined by the data. It turns out that the experimental results are well-described by such forms which incorporate the crucial twin ingredients of PCAC and final state interactions required by unitarity [183]. Others [184] have fitted these, and earlier data on the same channels [185][186][187][188][189][190] with just the constraint of PCAC and a single channel analysis, i.e. in our language setting T_{11} in Eqn. 4.22 to be a constant and α_2 to zero. In the small mass region explored in these decays, it happens to be true that T_{11} is slowly varying. However, the advantages of this fuller treatment are:

1. no such fortuitous accidents are needed; nevertheless, a peaking at larger $\pi\pi$ masses is generated by the low mass suppression provided by the Adler zero rather than a localized ε enhancement.
2. by performing a coupled channel analysis we can determine the relative couplings to $\pi\pi$ and $K\bar{K}$.

In Table 5.2 we give the position of the zero, s_0, and the ratio of α_1 to α_2 for the fit to each data set shown in Figures 5.14-15. Note from Figure 5.15 that the quality of the fits to the Υ' data, whether of the ARGUS group at DORIS [187] with over 5000 acceptance-corrected events or the CESR groups [188][189] with over 4000 such events, is excellent. In contrast, the ψ' data, Figure 5.14 , with merely a

thousand acceptance-corrected events from each of Mark II [185] and Crystal Ball [190] are considerably poorer. This suggests that the statistical errors on the Crystal Ball $\pi^0\pi^0$ results [190] in particular, which are all that are shown in Ref. 186, are far from the total uncertainties on these data.

The one surprise among these decays is when we turn to $\Upsilon' \rightarrow \Upsilon\pi\pi$, which with a larger mass difference allows $\pi\pi$ masses up to 900 MeV. Even though the statistics are poor with only fifty or so events from both CLEO [191] and CUSB [192], Figure 5.16 , we see the data are consistent with unadorned phase space. In our terminology, α_1 and α_2 appear constant and show no sign of vanishing near threshold. Why the Adler zero does not occur in this channel is a mystery. No Born term in the $\Upsilon'' \rightarrow \Upsilon\pi\pi$ channel is known, but these data do suggest some unexpected dynamics, which more data would hopefully illuminate.

A particularly fortunate situation would arise if one of these narrow states, below heavy flavour threshold, would allow $\pi\pi$ masses beyond $K\bar{K}$ threshold. This, together with explicit information on the $K\bar{K}$ channel, would allow another look into the S* region, which at present only the AFS data explores fully. Several such channels are possible but all have complications. First, there is $J/\psi \rightarrow \phi(MM)$, where the ϕ is isolated by its $K\bar{K}$ decay mode. This channel allows dimson masses up to 2 GeV, again has suppressed left hand cut effects (we know of no $J/\psi\pi$ or $J/\psi K$ states in keeping with the OZI rule, Fig. 5.17) and can have quite different couplings to $\pi\pi$ and $K\bar{K}$ from any of the channels previously discussed. Unlike the AFS data, the 'S*' shows as a peak near $K\bar{K}$

threshold [Figs. 5.18-19]. This is a sign that the $K\bar{K}$ couplings are dominant, as the presumed $s\bar{s}$ structure of the ϕ would imply [Fig. 5.17(b)]. The only published data from Mark II at Spear [193] are far too poor to be very precise. However, a dramatic improvement is expected in the near future with results from Mark III at PEP and DM2 at DCI on both the $\pi\pi$ and $K\bar{K}$ channels. Preliminary results have been presented at the 1986 Rencontre de Moriand [194][195] to which we apply our analysis. Knowing Υ_{11} and Υ_{21}, these data can be fitted to determine the coupling functions α_1 and α_2. These each contain the Adler zero for this channel, but with the present uncertainties we merely put s_0, Eqns. 4.33-35, equal to its $\pi\pi$ position, Table 5.1. As an indication of what can be achieved, we have fitted quadratic forms for the α_i's simultaneously to the published Mark II [193] and preliminary Mark III data [194]. The parameters are listed in Table 5.2 and the fits shown in Figures 5.18-20. Though the fits are shown as continuous curves they are in fact averaged over the same bins as the data shown, just as for the AFS results [Section 5.3]. This is essential in the $K\bar{K}$ threshold region, where our amplitudes have local structure, caused by the B pole (See Section 6.1), resulting in the shoulder and fall in the $I\!P\,I\!P \to \pi\pi$ spectrum [Fig. 5.9], while giving a peak in the present $J/\psi \to \phi\pi\pi$ distributions [Figs. 5.18-20]. Data with sufficient statistics to allow finer binning may usefully check our amplitudes in the 1 GeV region. Indeed, we eagerly await the final Mark III and DM2 [196] results, which, once acceptance corrected, the dimeson mass accurately calibrated and the S-wave separated, could be added to the data sets of Section 5.1 to constrain the determination of

our basic hadronic amplitudes $\mathcal{T}_{ij}$ of Section 5.3.

Another reaction with far higher statistics, for which data have been available for a number of years is $J/\psi \to \omega\pi\pi$ [197]. This channel exposes a large $\pi\pi$ mass region and is known to have a sizable D-wave signal as the f-resonance is clearly seen. However, an analysis of this decay is complicated by crossed channel effects [198]. The $\pi\pi$ spectrum, even if it were angular separated, could not be discussed without regard to strong reflections from the $\omega\pi$ channel which, again because of final state interaction effects, has a sizable B-signal. To arrive at any conclusions from this channel, a full Dalitz plot analysis is necessary together with a complete treatment of the $\omega\pi$ as well as coupled $\pi\pi$ channel.

5.4.2 Two photon channel

We have already drawn an analogy in Section 5.2 between the $\mathbb{P}\mathbb{P} \to MM$ and the two photon process accessible in $e^+e^- \to e^+e^-(MM)$. Unfortunately only relatively poor statistics results exist for this in principle cleaner channel [175]. Data on dipion production have been published by PLUTO at Petra [199] and DM1 at DCI [200], Figure 5.19, the shape of which has been recently corraborated by preliminary results from DM2 at DCI [201]. In the absence of angular separation, we naively assume that all the data below 1 GeV is S-wave. Having determined $\mathcal{T}_{11}$ and $\mathcal{T}_{12}$ from our global fits (K_1 is used), we can fit these $\gamma\gamma$ data using the analogue of the $\mathbb{P}\mathbb{P}$ scattering formula Eqn. 5.10:

$$\sigma_{\gamma\gamma}^{J=0}(M) = \frac{\sqrt{M^2-4\mu^2}}{M^3} \left| \mathcal{T}^{J=0}(M) \right|^2 \qquad (5.15)$$

and so determine α_1 , α_2 for the $\gamma\gamma$ process. Just as for the $I\!P\,I\!P$ reaction, there is a non-zero pion exchange Born contribution [Fig. 4.3] and the αs are not expected to have an Adler zero. The results of a fit to the PLUTO [199] and DM1 [200] data are shown in Figure 5.21, with the corresponding parameters listed in Table 5.2. We would predict that the DM2 [201] data when finalised should have the same form as this.

To investigate the intrinsic difference between the $\gamma\gamma$ and $I\!P\,I\!P$ processes, we compare their couplings by plotting the relevant funtion $\tilde{P}$ of Eqn. 4.27 in Figure 5.22 to be contrasted with Figure 5.11. The effective coupling to the $I\!P\,I\!P$ channel is flat showing no mass dependence compared with $\pi\pi$ itself, but the $\gamma\gamma$ couplings increase towards 1 GeV. Such sharp contrast between the two couplings can have a significant implication which we will discuss in Chapter Seven. A crude extrapolation of the S-wave couplings of Figure 5.22 up to 1.4 GeV (unconstrained by any data in that region!) does suggest however that there is a large S-wave signal under the f and emphasises the importance of a partial wave separation before results on the size of the f signal can be believed. Moreover, after this analysis was completed, new results from the TPC $\gamma\gamma$ collaboration have been published [202], which do not agree with the PLUTO data of Figure. 5.21 (and hence Fig. 5.22) and so no firm conclusions can be drawn until this discrepancy is resolved. Nevertheless, the formalism outlined in Section 4.2-3 should apply as previously discussed for instance by Lyth [203] and by Mennessier [204].

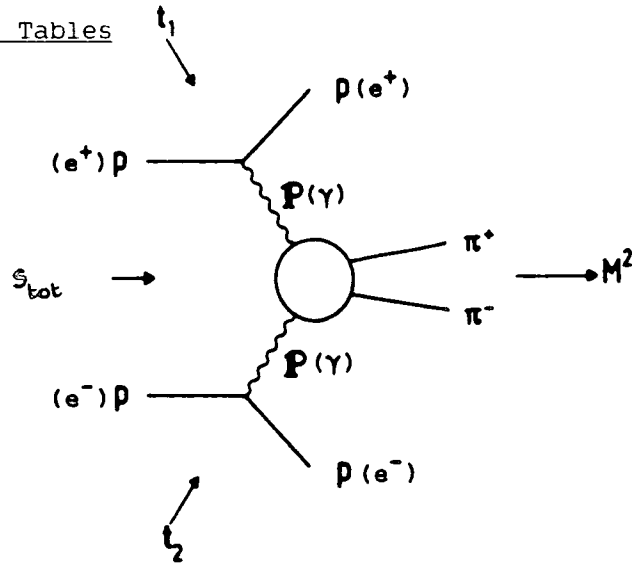

Figure 5.1 The double Pomeron exchange graph controlling central dimeson production in pp -> pp(MM). Its analogue e^+e^- -> e^+e^-(MM) is shown in brackets.

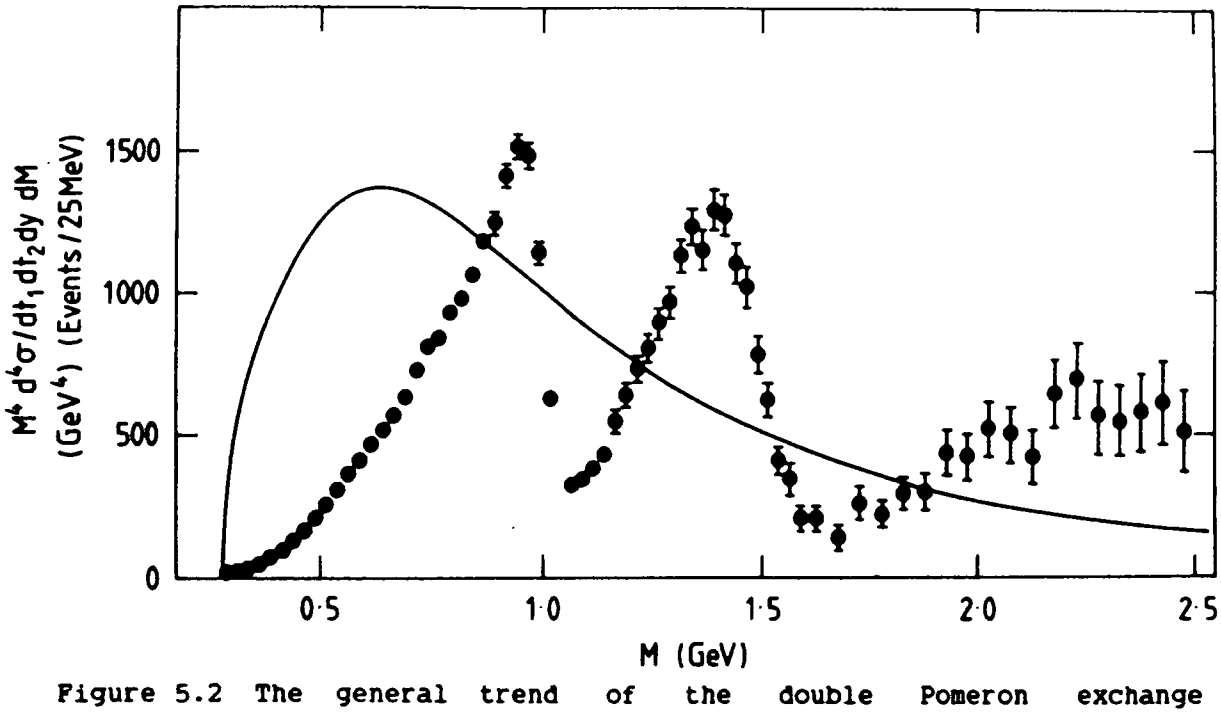

Figure 5.2 The general trend of the double Pomeron exchange cross-section for dipion production may be attributed to pion exchange. Normalised to the AFS data [69] and folding in their acceptance, this 'duality average' is plotted together with the AFS results on $M^4 \times d^4\sigma/dt_1\, dt_2\, dy\, dM$ as a function of dipion mass M. For ease of plotting, the factor M^4 has been included as this conveniently reduces the scale of the M-dependence.

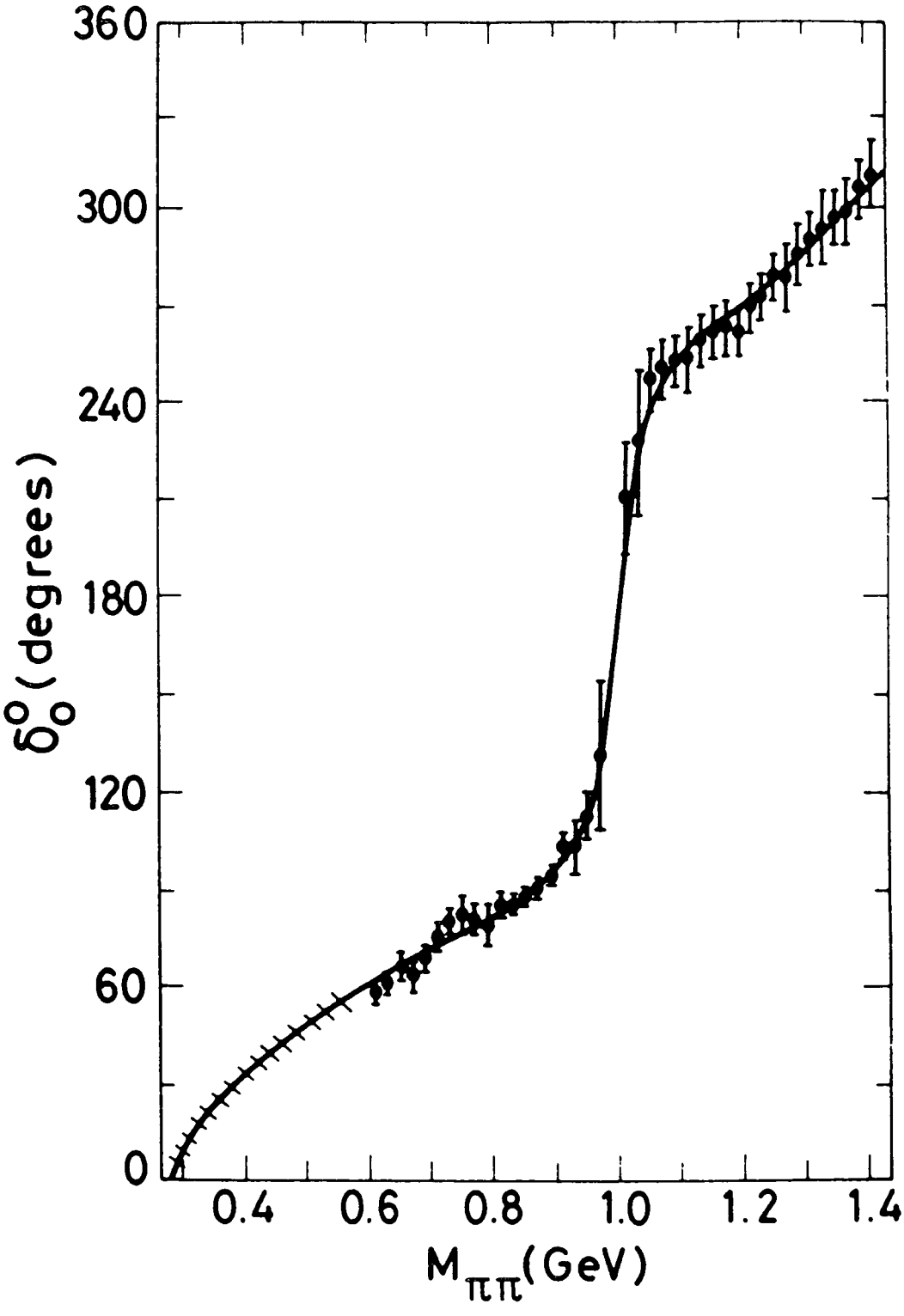

Figure 5.3 The I = 0 S-wave phase shift, δ_0^0, for $\pi\pi$ scattering (denoted δ_{11} in the text) from the CERN-Munich group [158]. The hatched band represents the continuation down to threshold provided by the Roy equations [162]. The curve shows a fit typical of all the solutions.

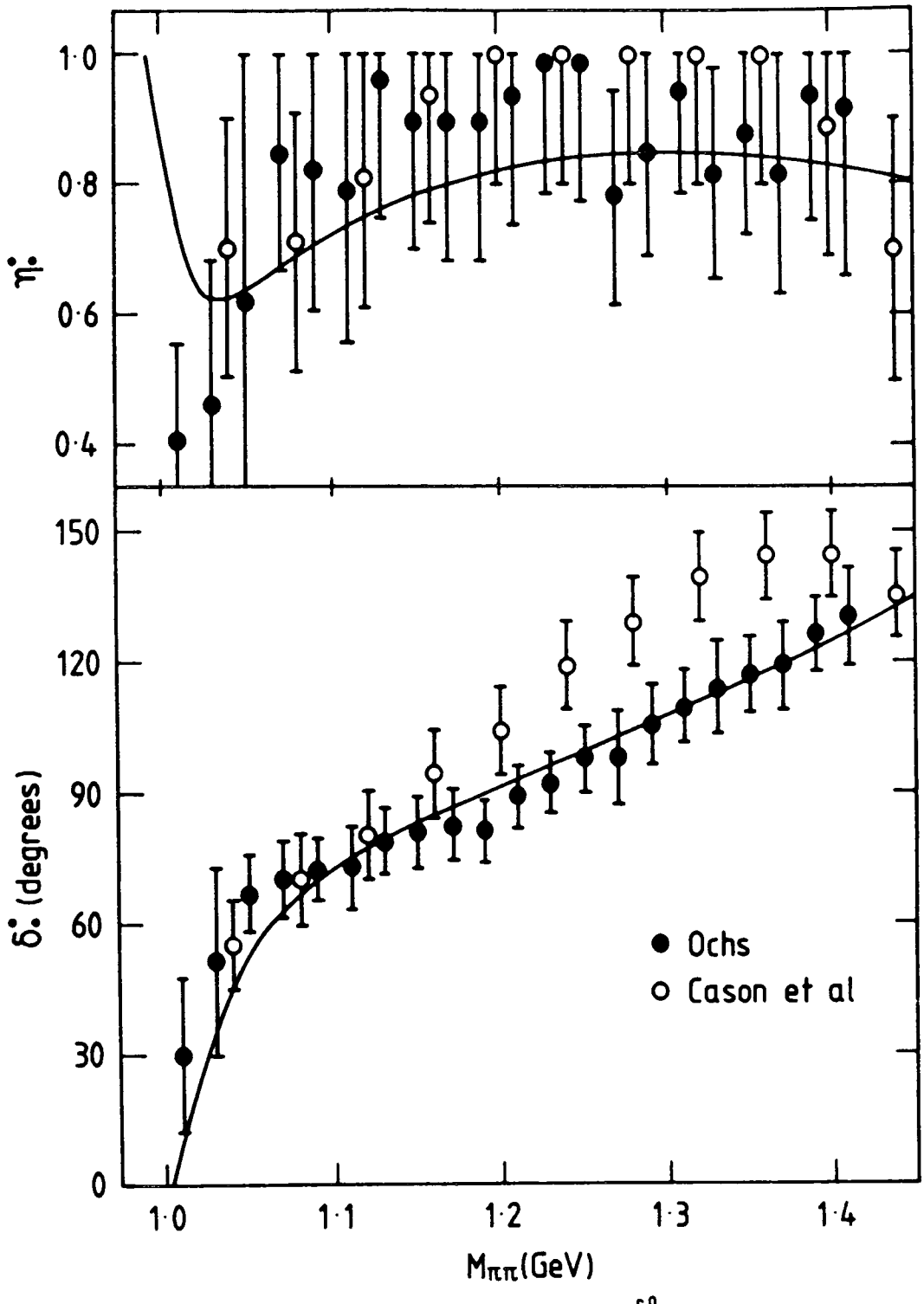

Figure 5.4 The $\pi\pi$ I = 0 S-wave phase-shift, δ_0^0 , and inelasticity η_0^0 (denoted by δ_{11} , η_{11} in the text) above $K\bar{K}$ threshold showing the CERN-Munich results as analysed by Ochs [159] and the preferred B solution of Cason et al [161]. Again the curves show a typical fit given by the solutions.

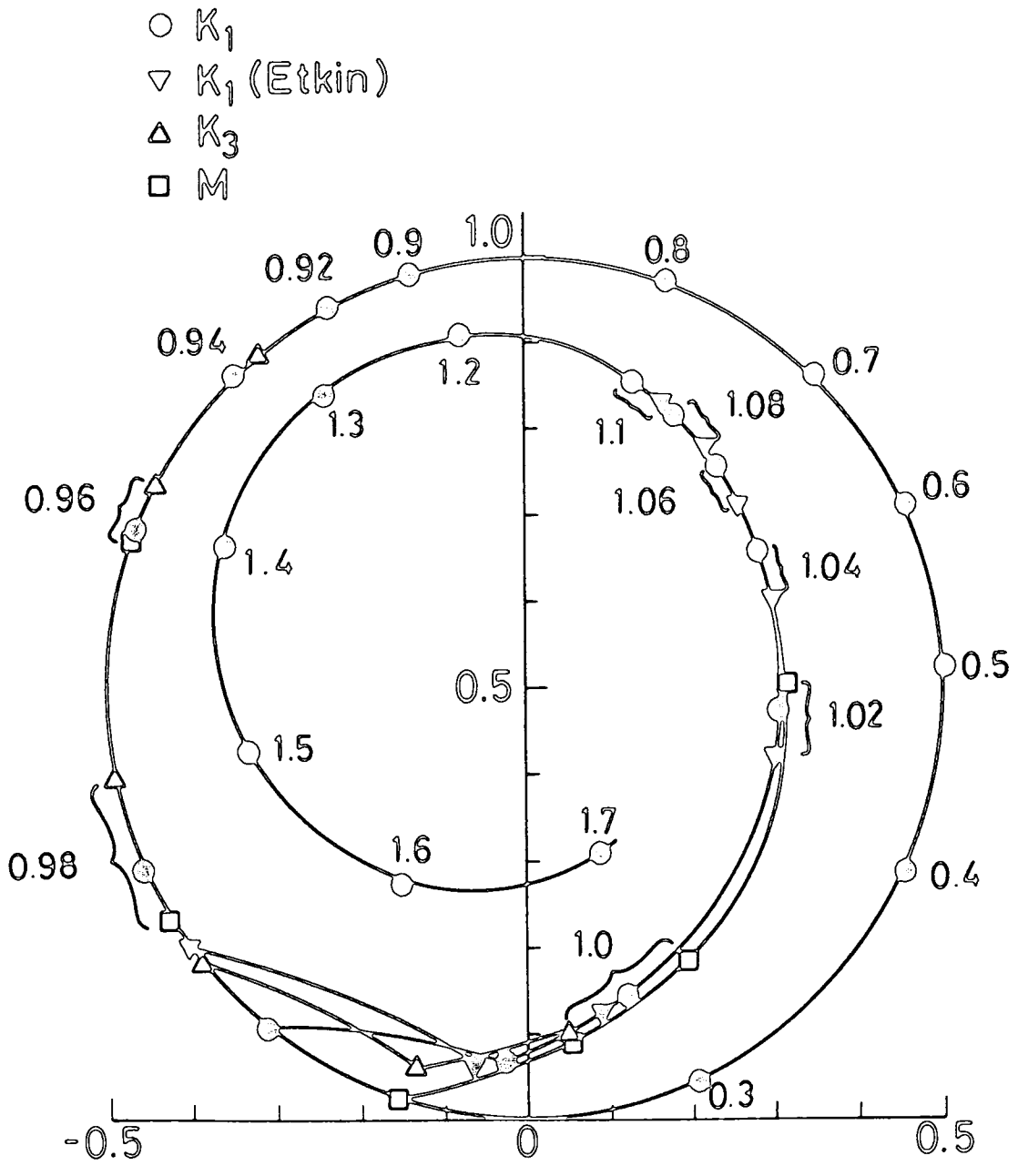

Figure 5.5 The MM I = 0 S-wave amplitude $\rho_1 T_{11}$ shown in an Argand plot comparing the solutions K_1 (○), K_1(Etkin)(▽), K_3(△) and M(□). The last three are only shown where they differ from solution K_1 .

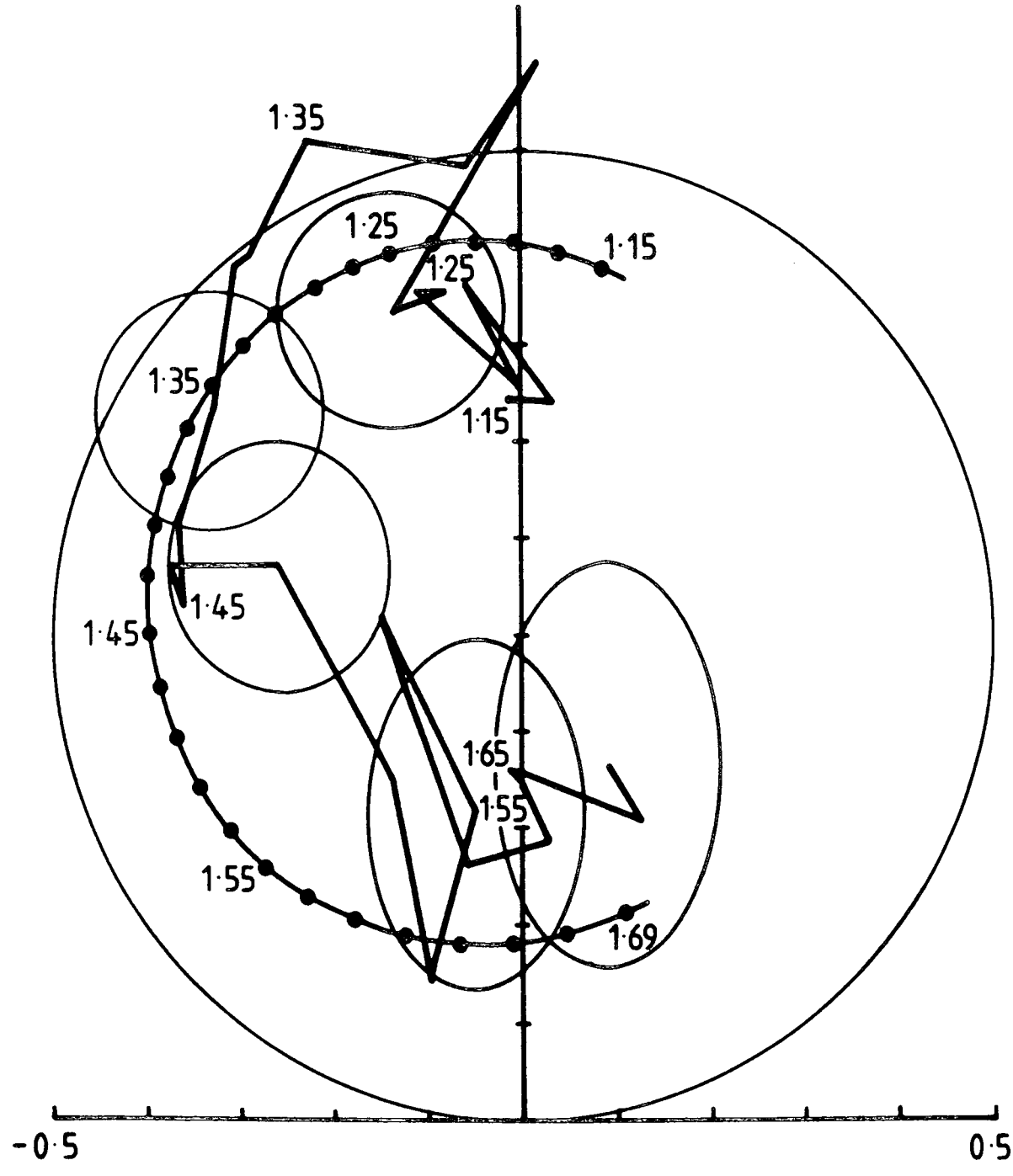

Figure 5.6 The I = 0 S-wave amplitude $\rho_1 T_{11}$ shown in an Argand plot with solution K_1 compared with the CERN-Munich results from the energy-independent analysis of Martin and Pennington [162] from 1.15 to 1.69 GeV in 20 MeV bins. Error ellipses have been drawn at representative energies.

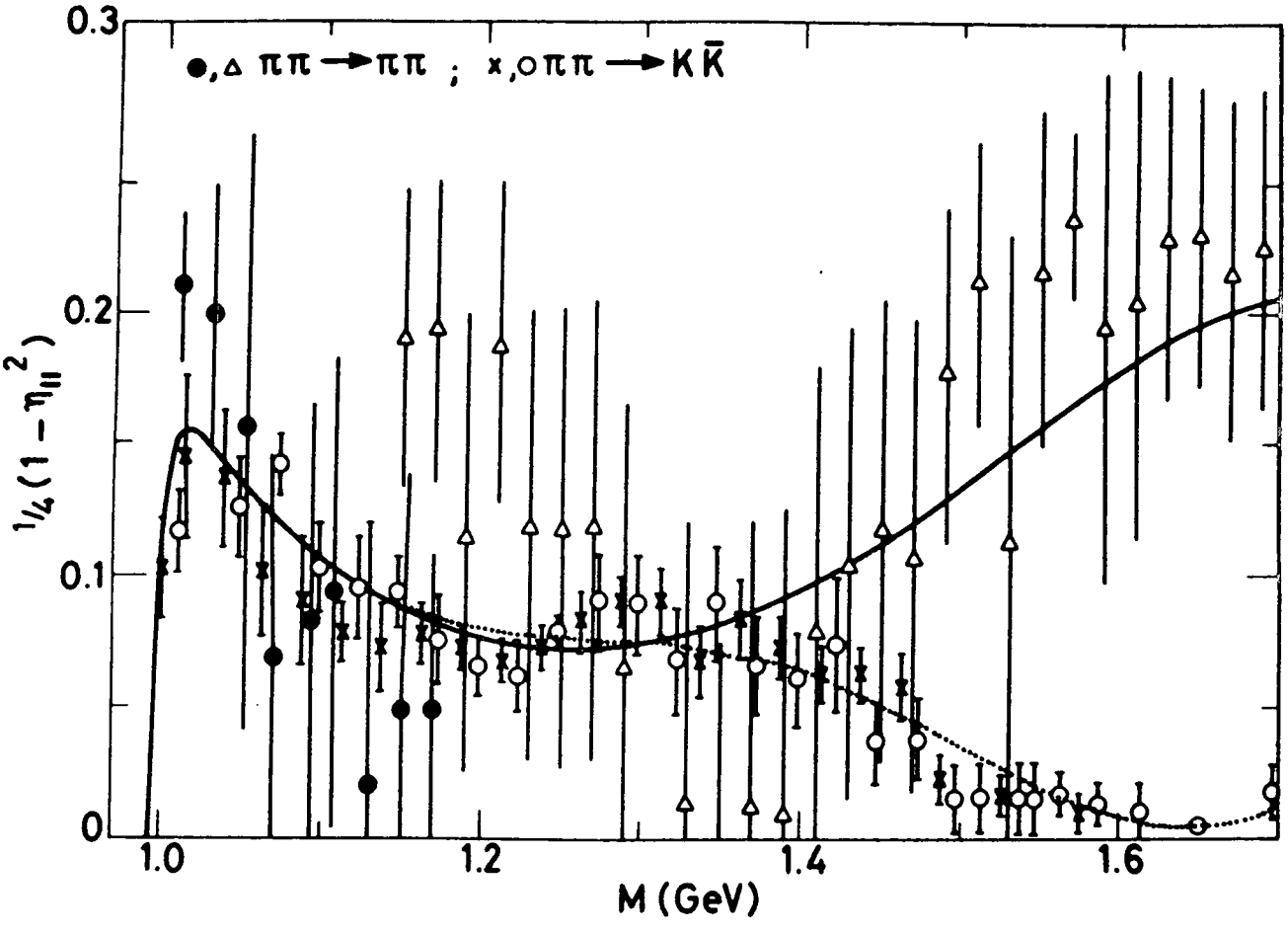

Figure 5.7 The cross-section for inelastic I = 0 S-wave ππ scattering. This cross-section is proportional to $(1/4)(1-\eta_{11}^2)$, where η_{11} is the ππ inelasticity, and it is this that is plotted from the analyses of the CERN-Munich ππ results by Ochs [159](●) and by Martin and Pennington [162](Δ). The I = 0 S-wave ππ -> $K\bar{K}$ contribution to this inelastic cross-section is plotted from the results of Cohen et al [164](x) and Etkin et al [166](o). Some of the data points have been displaced for easier presentation. The full curve corresponds to solution K_1 and the dotted one to K_1' as described in the text.

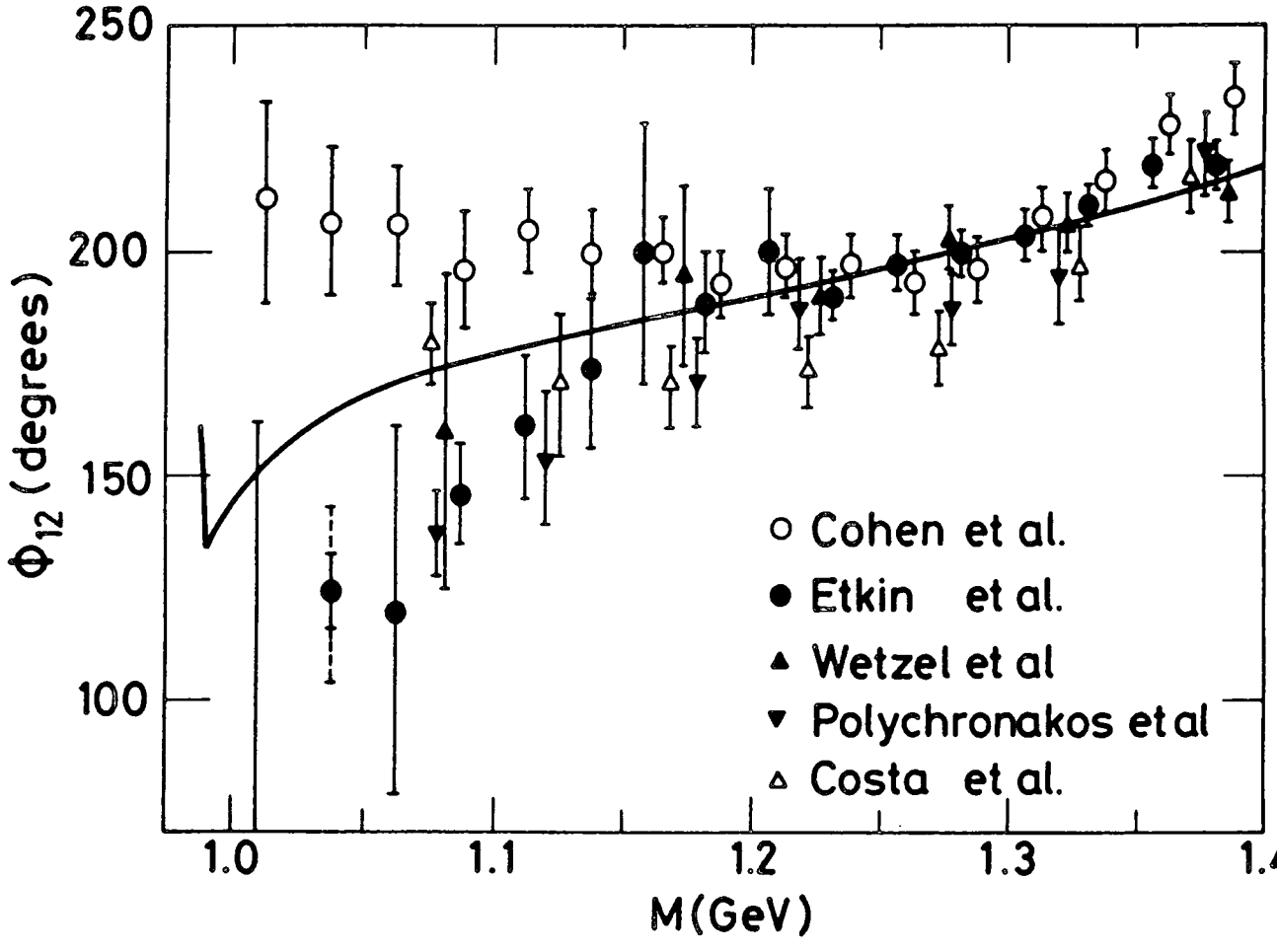

Figure 5.8 The phase of I = 0 S-wave $\pi\pi \rightarrow K\bar{K}$ scattering from Cohen et al [164>](o), Etkin et al [166](●), and from Wetzel et al (▲), Polychronakos et al (▼) and Costa et al (Δ)[165]. Experiment determines the phase of this S-wave relative to the D-wave. Modelling that by resonance dominated forms gives the S-wave phase, ϕ_{12}, shown.

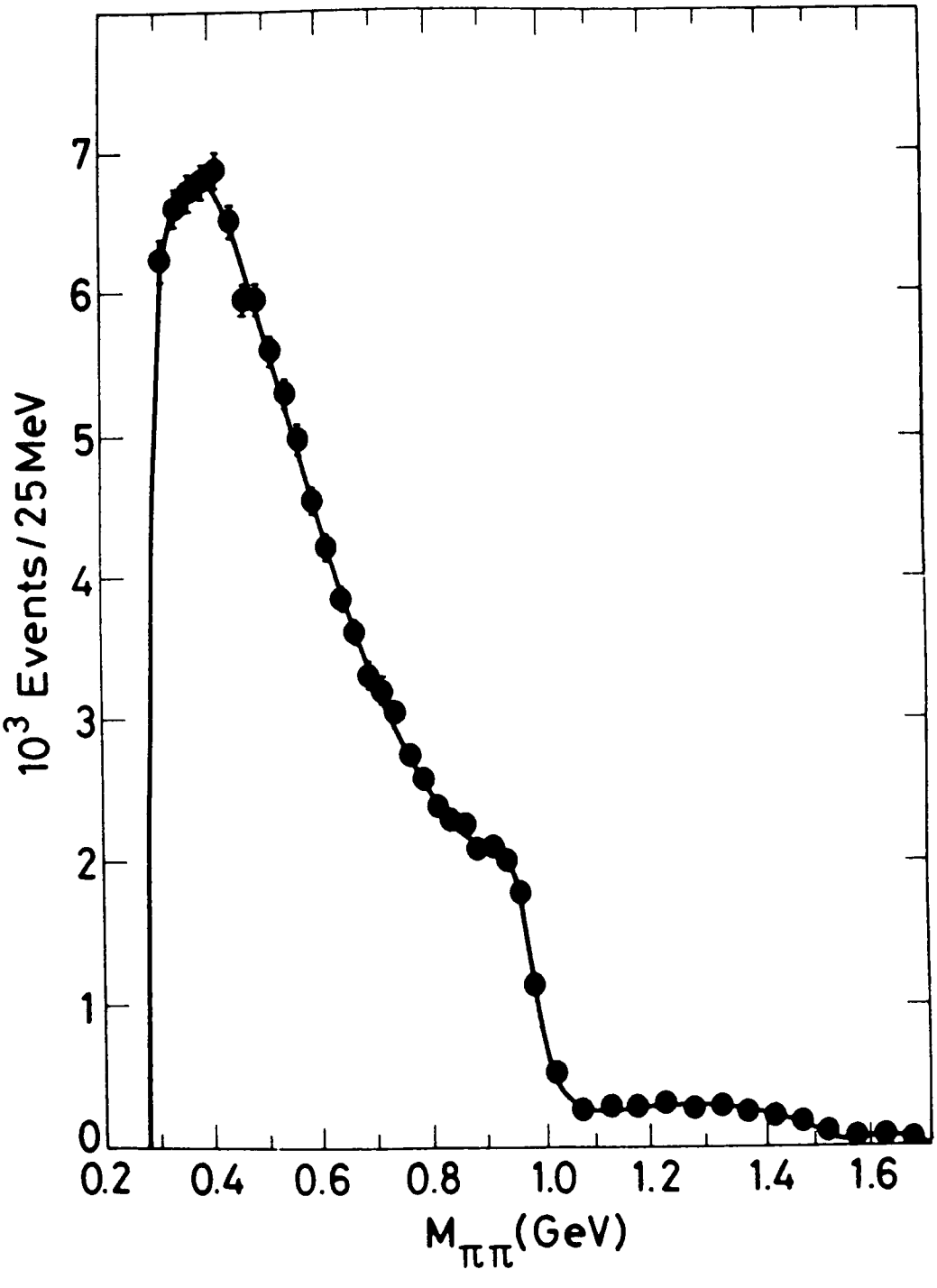

Figure 5.9 Mass spectrum of centrally produced S-wave ππ events in pp -> ppππ from the AFS Collaboration [69] are shown above 1 GeV. These data have been corrected for acceptance [176]. The curves show a typical fit given by solution K_1 .

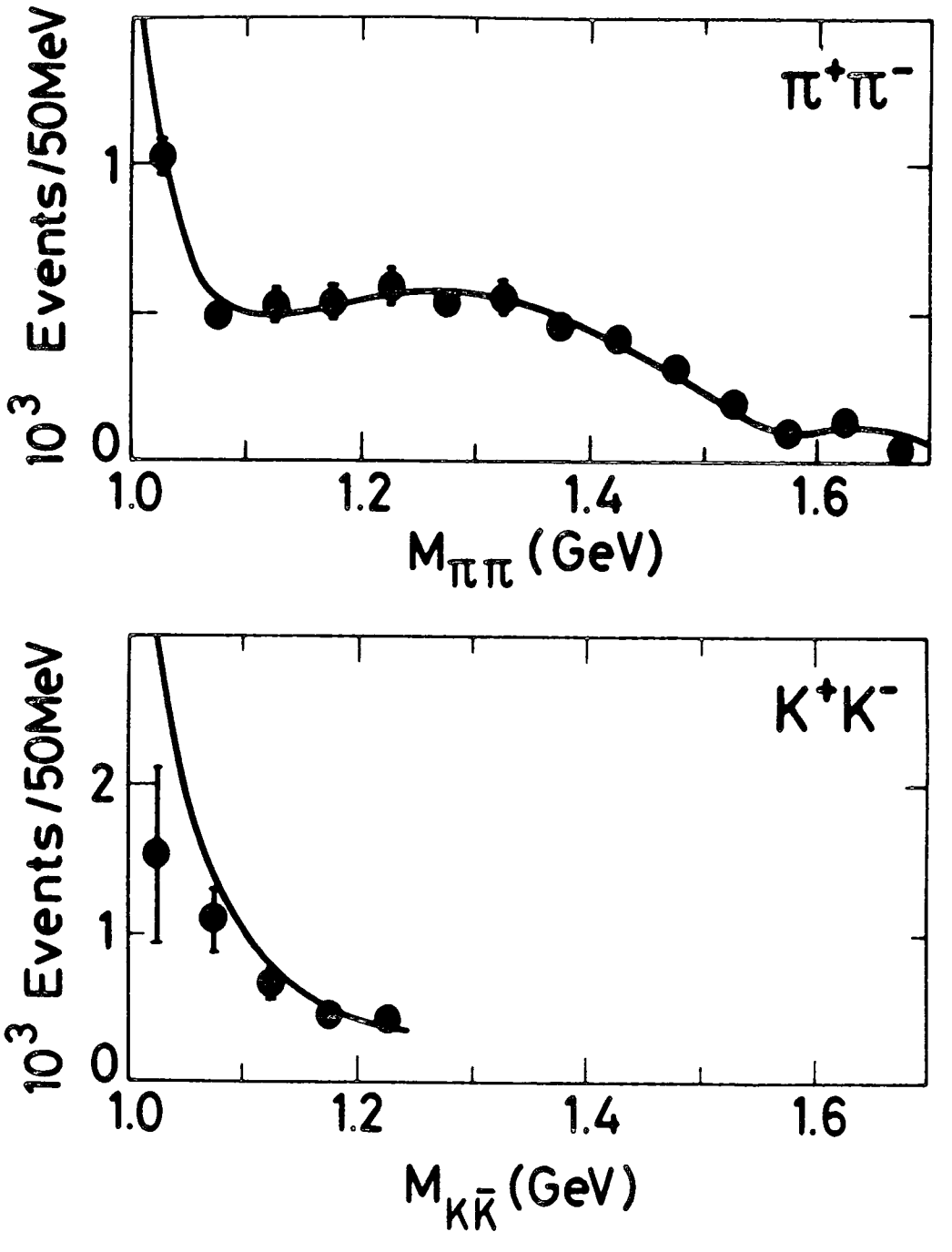

Figure 5.10 Mass spectrum of centrally produced S-wave $\pi\pi$ and $K\bar{K}$ events in pp -> pp(MM) from the AFS Collobration [69] are shown above 1 GeV. These data have been corrected for acceptance [176]. The curves show a typical fit given by solution K_1 .

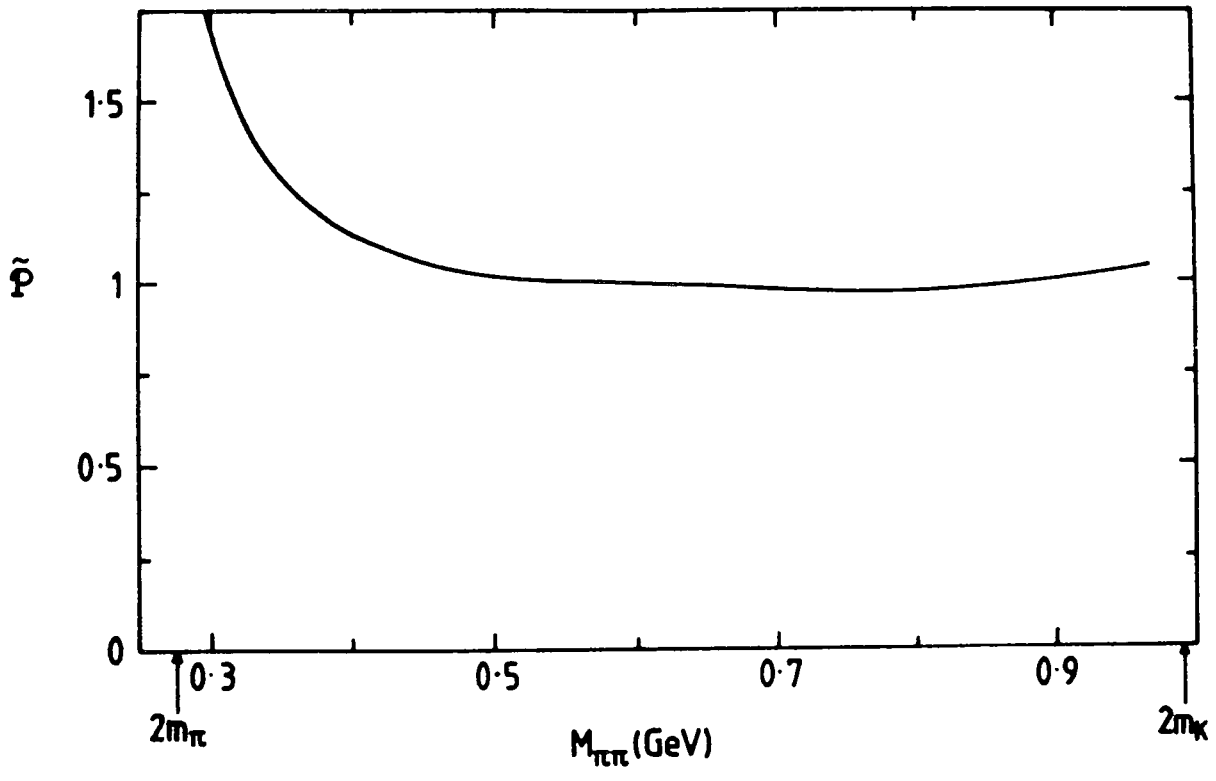

Figure 5.11 A plot of the effective two-channel coefficient function of the Omnes representation, Eqn. 4.27, for the production process pp -> pp$\pi\pi$ as a function of dipion mass, M for a representative solution, K_1 . The flatness indicates the near equality of the Omnes function for this process and $\pi\pi$ scattering itself, Eqns. 4.26-27.

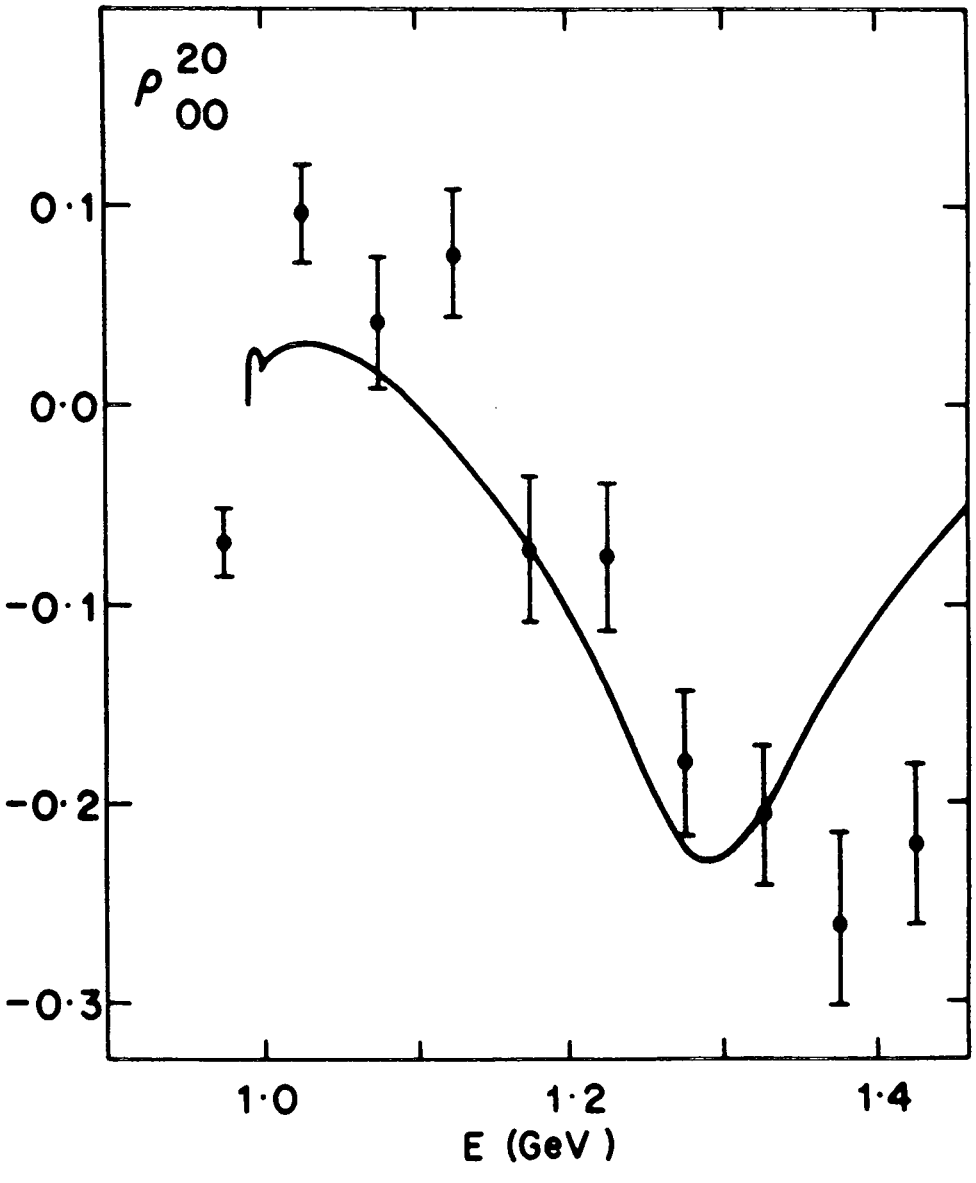

Figure 5.12 The AFS results on S-D wave interference in pp -> pp$\pi\pi$ [69] are compared to the prediction from the analysis with the solutions determining the S-wave and the D-wave assumed dominated by the f-resonance below 1.4 GeV. (At higher masses, this simple model of the D-wave becomes inadequate).

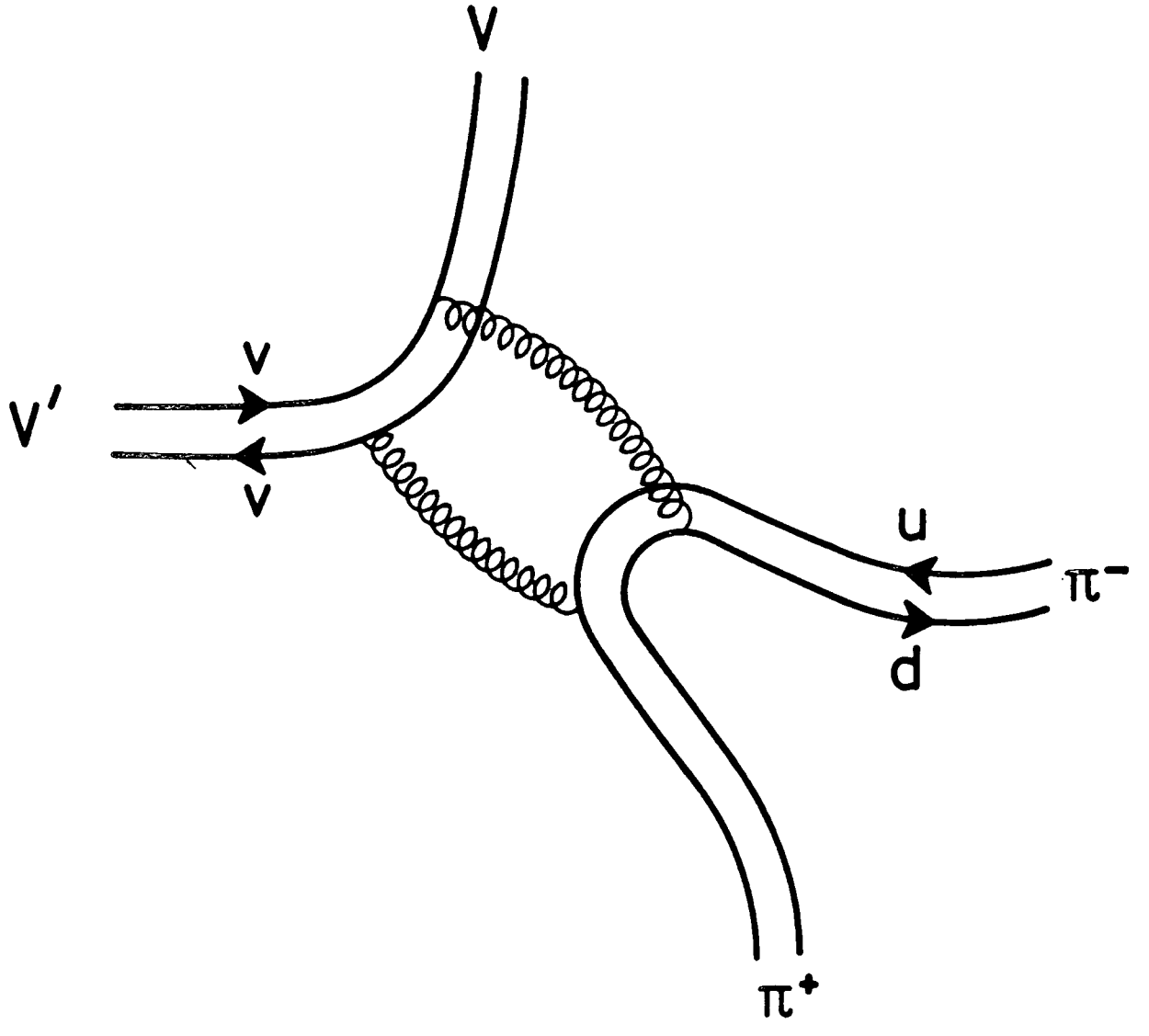

Figure 5.13 Parton diagram of the decay V' -> Vππ, with V made of heavy quarks v, so that v = c, b means V = ψ or ϒ, emphasising the gluonic nature of the intermediate state expected in this picture.

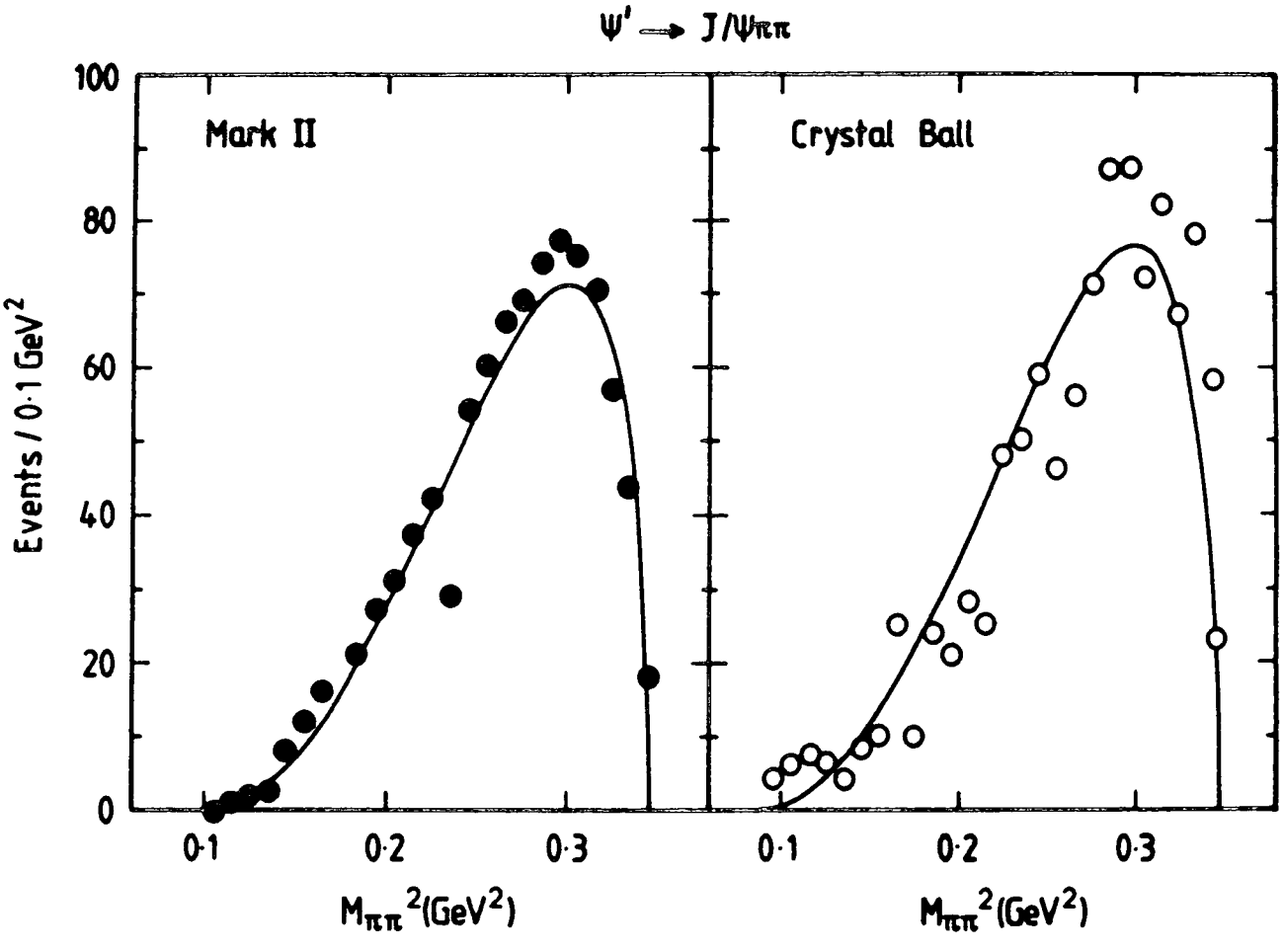

Figure 5.14 The ππ mass spectrum for the decay $\psi' \rightarrow J/\psi\pi^+\pi^-$ as a function of M^2 for

(a) $\pi^+\pi^-$ from Mark II [185],

(b) $\pi^0\pi^0$ from Crystal Ball [186].

The curves show the results of a combined fit typically given by the S-wave solutions.

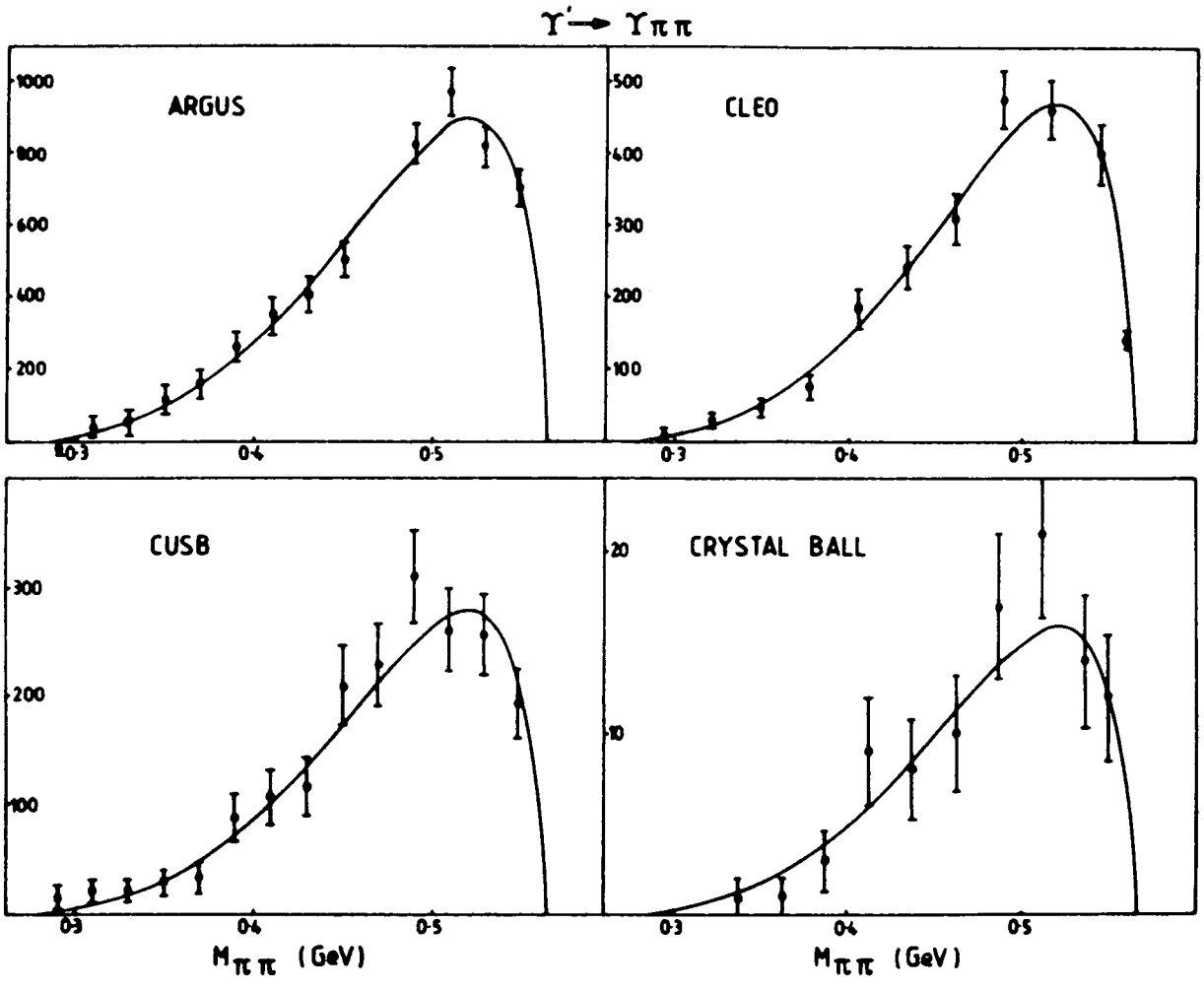

Figure 5.15 The $\pi\pi$ mass spectrum for the decay $\Upsilon' \rightarrow \Upsilon\pi\pi$ as a function of M for:

(a) $\pi^+\pi^-$ from Argus [187],

(b) $\pi^+\pi^-$ from CLEO [188],

(c) $\pi^+\pi^-$ from CUSB [189],

(d) $\pi^0\pi^0$ from Crystal Ball [190].

The curves show the results of a combined fit typically given by the S-wave solutions.

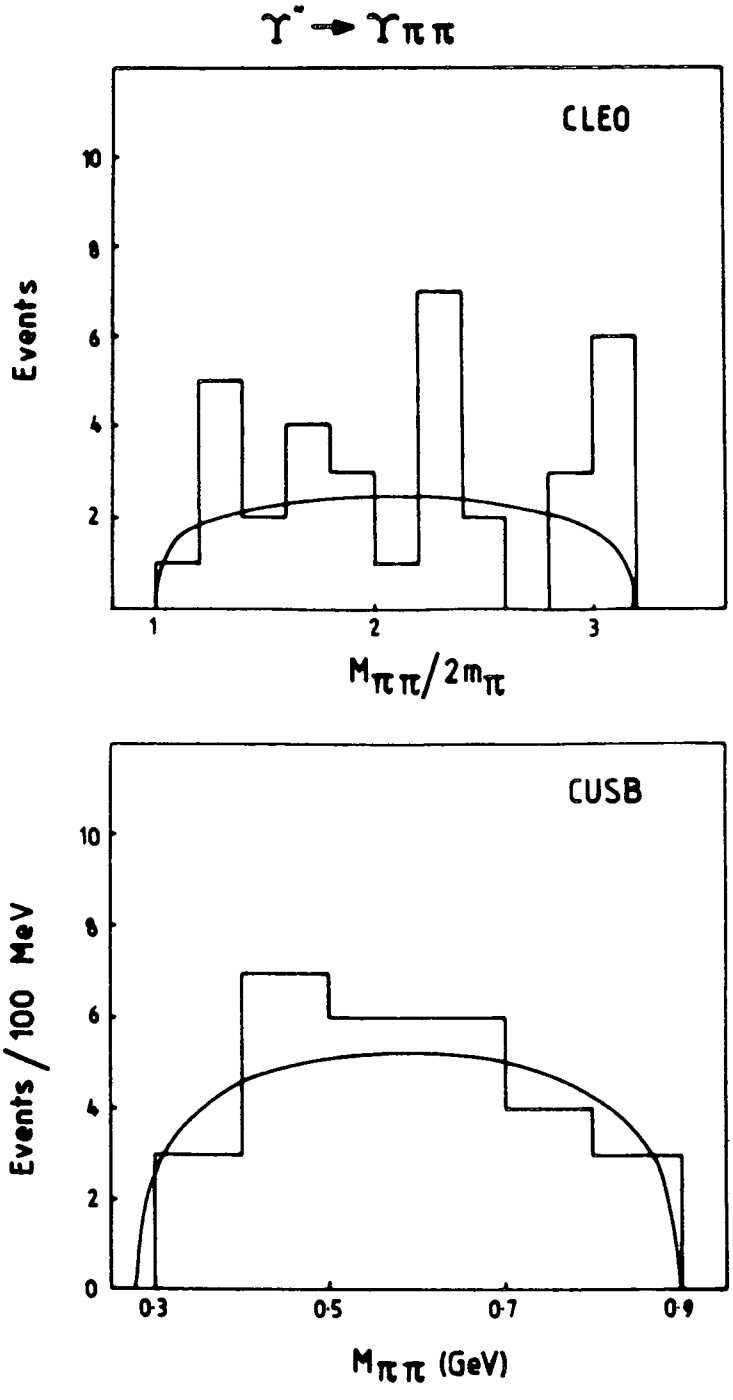

Figure 5.16 The ππ mass spectrum for Υ'' -> Υππ as a function of M from

(a) CLEO [191],

(b) CUSB [192].

The curves show the data are essentially consistent with phase space with no low mass Adler suppression.

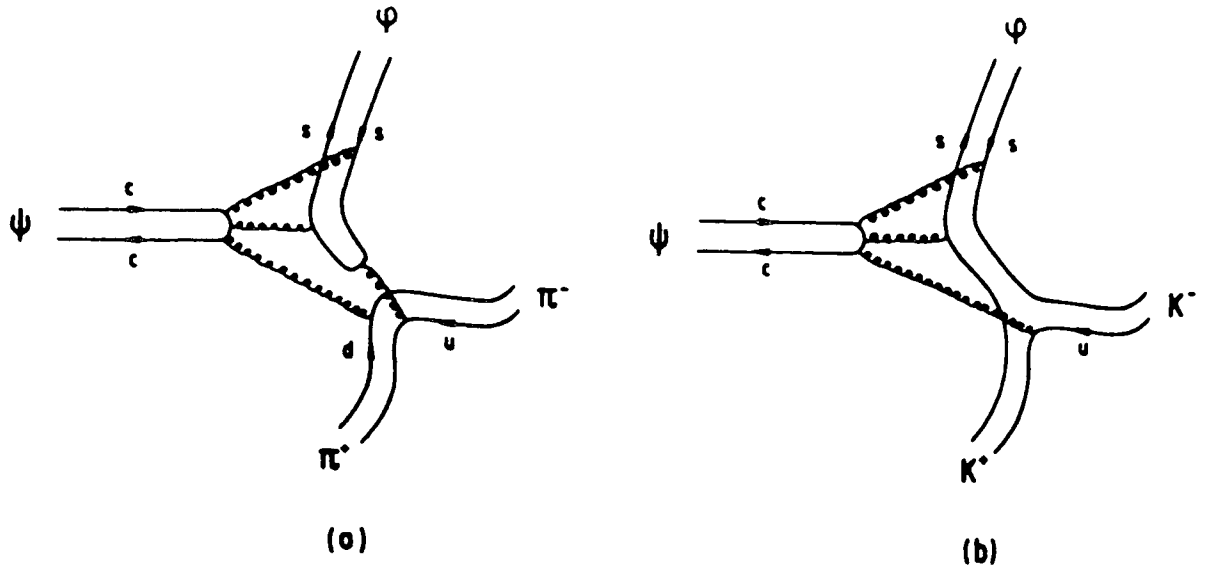

Figure 5.17 Parton line diagrams of the processed

(a) $J/\psi \to \phi\pi\pi$, (b) $J/\psi \to \phi K\bar{K}$.

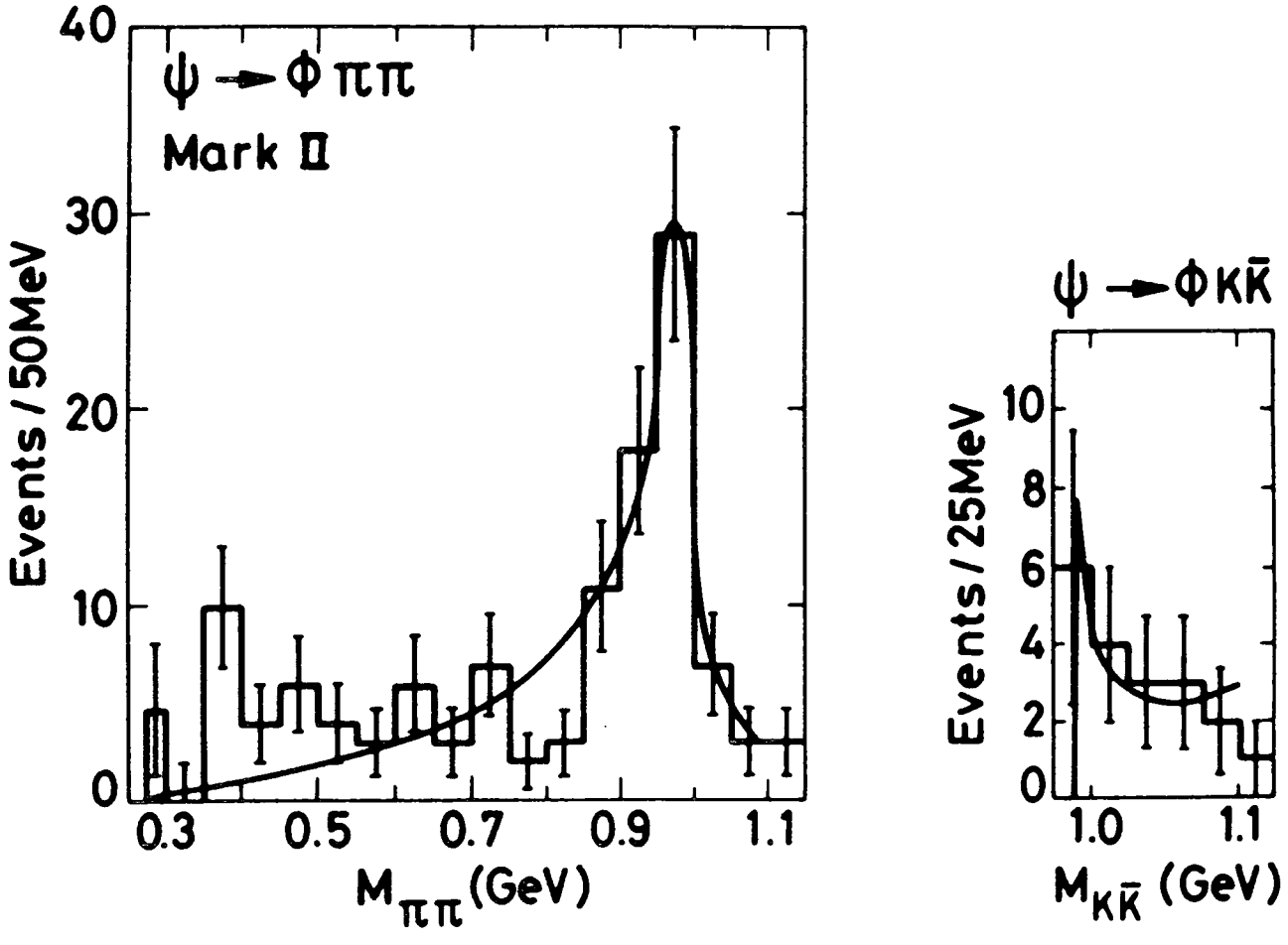

Figure 5.18 The $\pi\pi$ and $K\bar{K}$ mass spectra for the decays $J/\psi \to \phi(MM)$ from Mark II [193]. Our solutions typically give the curves shown which in fact represent the average over each bin width, assuming pure S-wave.

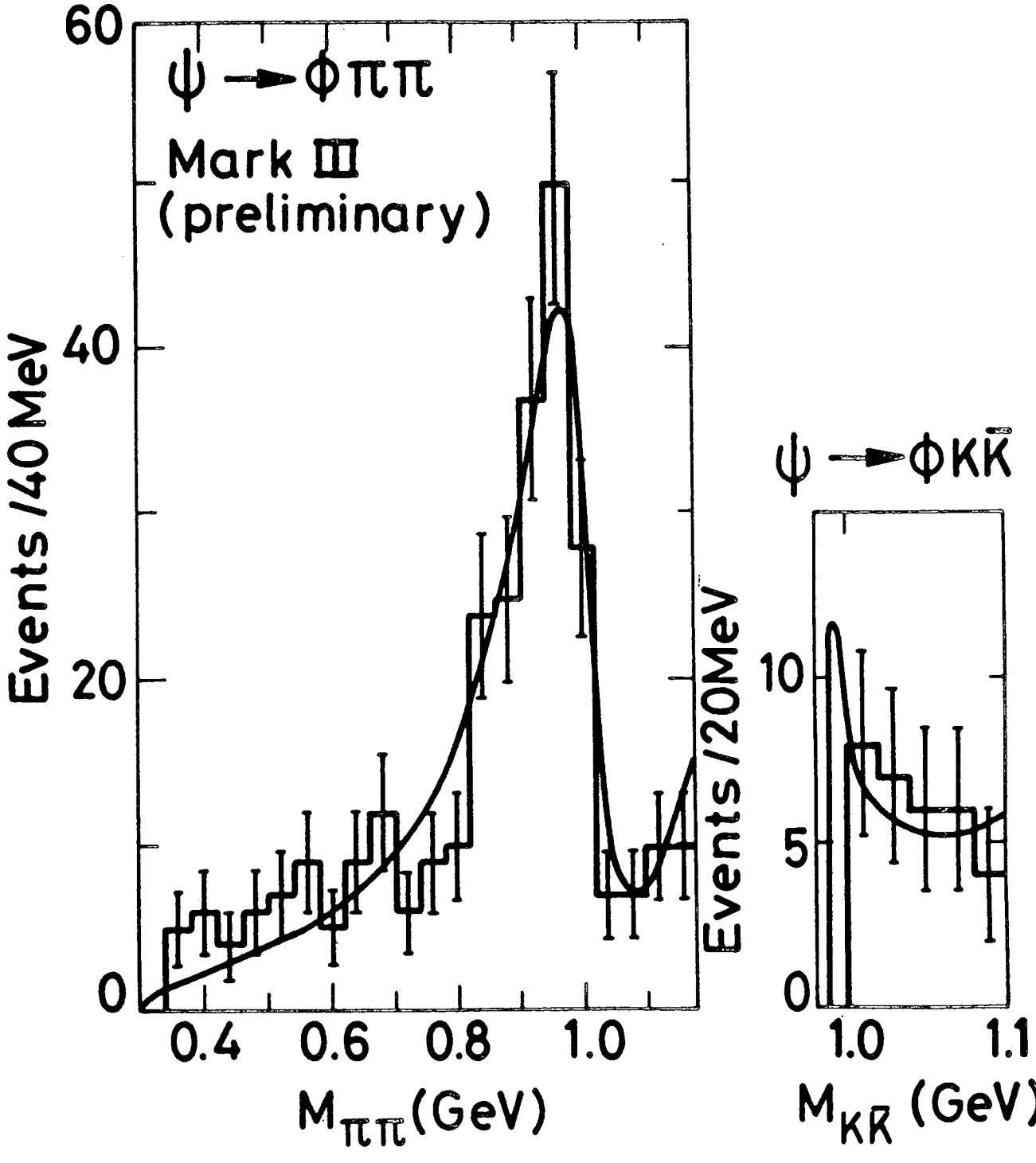

Figure 5.19 The preliminary ππ and KK̄ mass spectra for the decays J/ψ -> φ(MM) from Mark III presented by Mallik [194]. Our solutions are exemplified by the curves shown; these represent the average over each bin width, assuming pure S-wave.

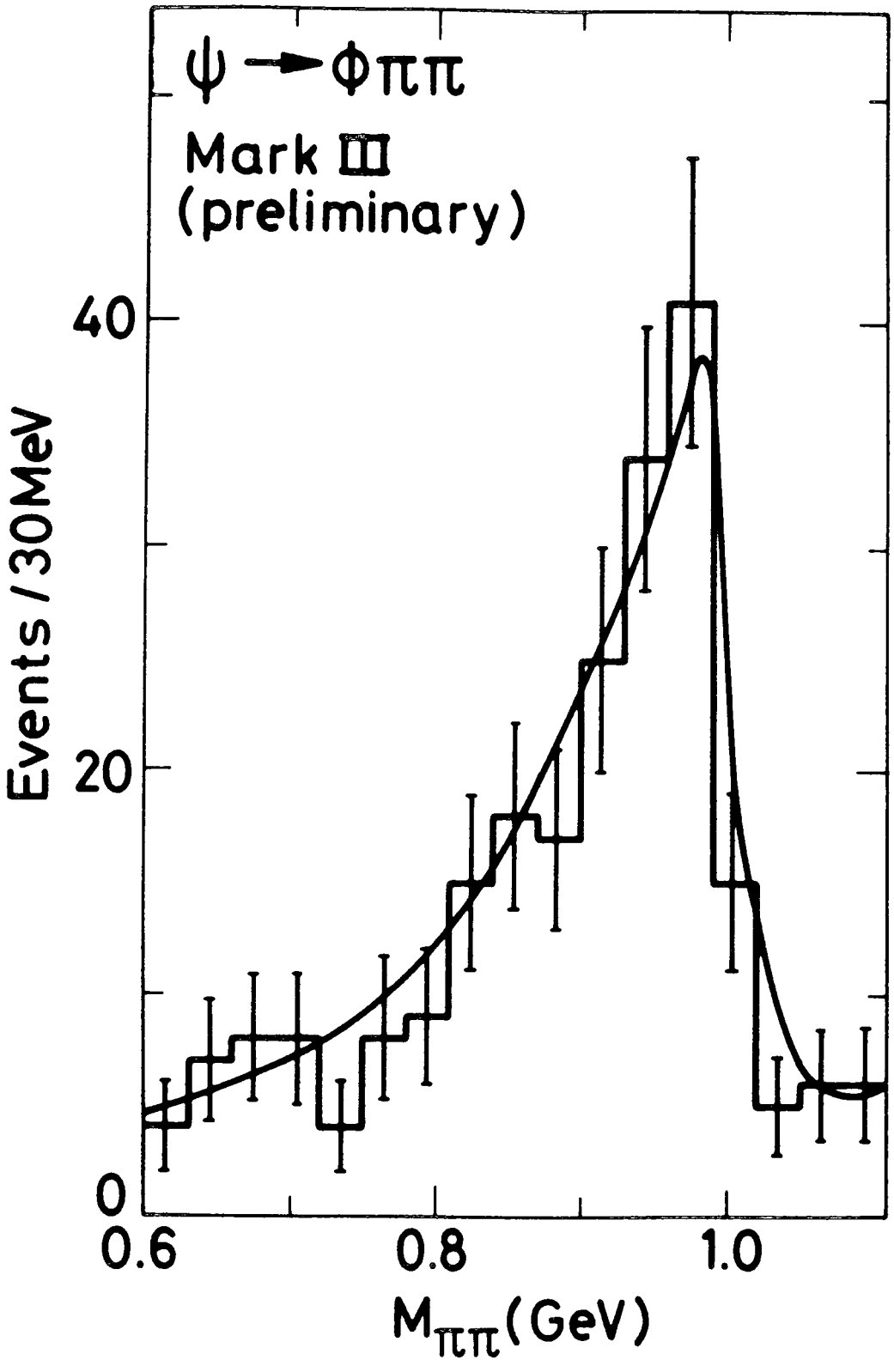

Figure 5.20 As for Figure 5.19 with the ππ data above 600 MeV in 30 MeV bins.

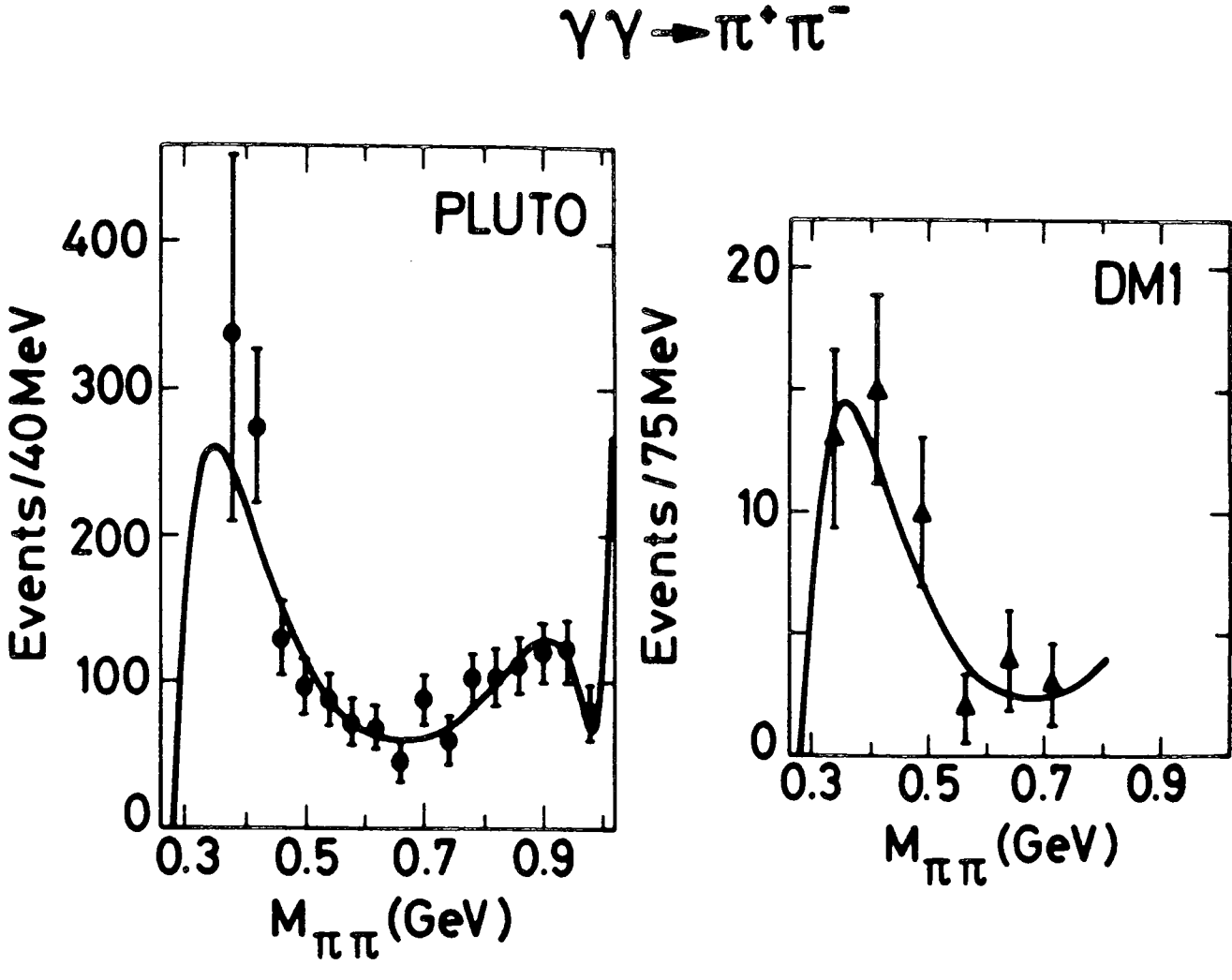

Figure 5.21 The ππ mass spectrum for the process $\gamma\gamma \rightarrow \pi^+\pi^-$ from

(a) the PLUTO Collaboration [199],

(b) DM1 [200].

Note that in plot (b) the purely leptonic contribution to the detected final state has been folded in to allow comparision with the DM1 results [200]. Assuming the data is S-wave dominated, the solutions readily accord with these spectra as shown by the curves.

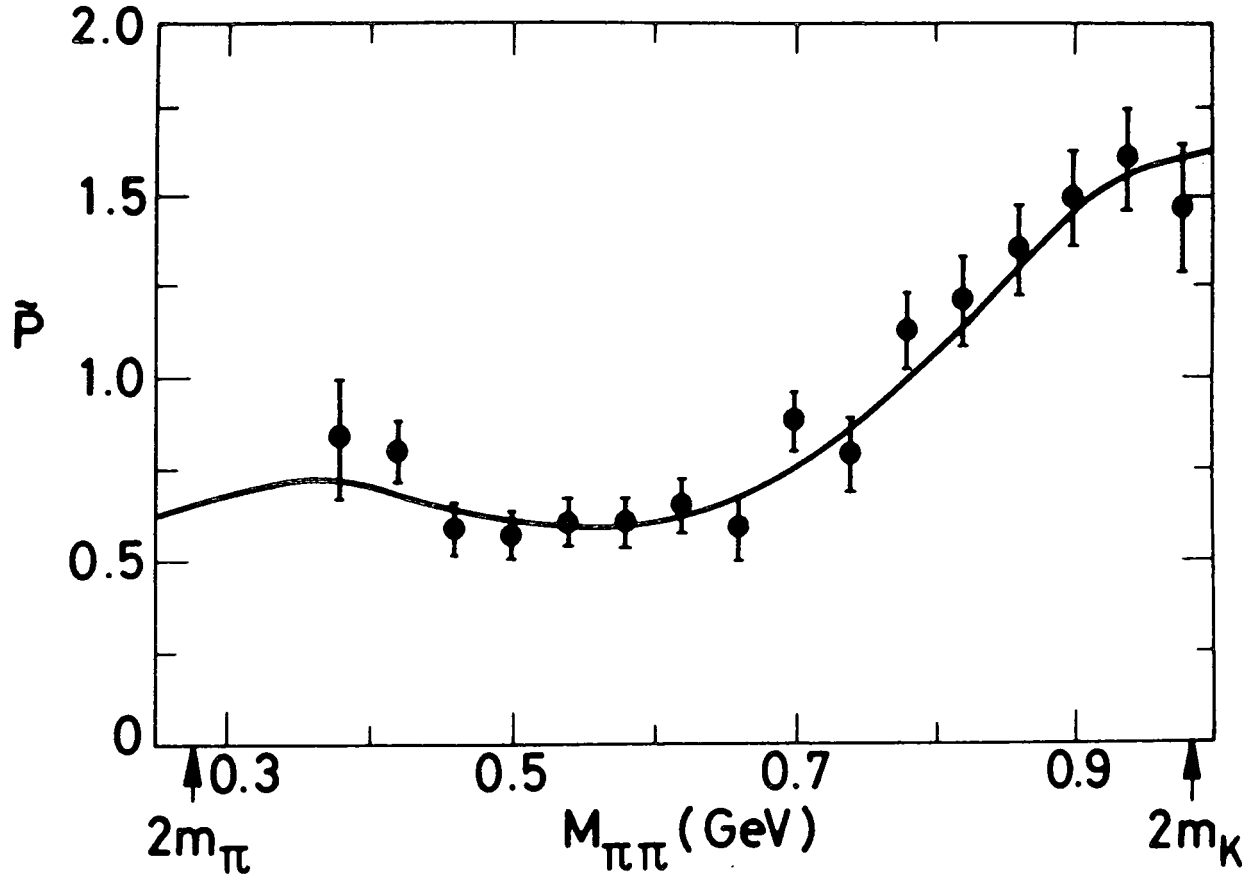

Figure 5.22 Effective two channel coefficient function for an Omnes representation of the process $\gamma\gamma \to \pi\pi$. The data are from PLUTO [199] and the curve corresponds to the fit shown in Figure 5.20. This is to be contrasted with the flat function of Figure 5.11 for $\mathbb{P}\mathbb{P} \to \pi\pi$ indicating that the S-wave states have from 0.3 to 1 GeV an increasing coupling to $\gamma\gamma$ with increasing mass compared to $\pi\pi$ and $\mathbb{P}\mathbb{P}$. However, these conclusions are not definitive without partial wave separation, information on the $K\bar{K}$ channel and a resolution of the experimental inconsistency between different $\gamma\gamma$ data sets.

Parameter	K_1	K_1 (Etkin)	K_1'	K_3	H	
s_o	-0.0110	-0.0162	-0.0141	0.0220	-0.0074	
s_1	0.9247	0.9383	0.9226	0.0544	0.9828	
s_2				0.9547		
s_3				2.2815		
f_1^1	-0.2242	-0.1659	-0.2334	0.0870	0.1968	
f_2^1	0.5829	0.5852	0.5969	0.3800	-0.0154	
f_1^2				-0.1298		
f_2^2				0.6011	0.1131	a_{11}
f_1^3				-2.1130	0.0150	a_{12}
f_2^3				4.1900	-0.3216	a_{22}
c_{11}^0	0.7347	0.4247	0.7871	-0.9527	0.0337	
c_{11}^1	-0.5266	-0.5822	-0.5610	-0.6893	-0.3185	
c_{11}^2	2.6151	2.5478	1.6987	1.1313	-0.0942	
c_{11}^3	-1.7747	-1.7387	-2.0451	-2.1052	-0.5927	
c_{11}^4	0.8031	0.8308	0.6361		0.1957	
c_{12}^0	-3.2762	-3.1401	-3.3270	0.6619	-0.2826	
c_{12}^1	-0.6662	-0.1359	-0.4788	1.9239	0.0918	
c_{12}^2	0.8778	1.0286	1.1362	0.3866	0.1669	
c_{12}^3	-2.1190	-2.3029	-1.0623	1.5638	-0.2082	
c_{12}^4	0.2319	0.1944	0.6290		-0.1386	
c_{22}^0	-2.6785	-2.8447	-2.7914	-3.4567	0.3010	
c_{22}^1	7.9951	6.9164	7.5952	-1.8117	-0.5140	
c_{22}^2	5.5763	5.2846	4.5612	2.4379	0.1176	
c_{22}^3	-1.4956	-0.9646	-0.9356	-2.7982	0.5204	
c_{22}^4					-0.3977	
a_1^0	-0.4012	-0.5711	-0.4700	-0.2368	0.1393	
a_1^1	0.5468	0.7800	0.6593	0.3183	-0.0278	
a_1^2	0.2440	0.1622	0.2036	0.3131	0.3952	
a_2^0	3.273	3.310	3.542	3.328	3.241	
a_2^1	-3.483	-3.533	-3.824	-3.763	-3.432	
a_2^2	1.183	1.193	1.284	1.340	1.147	
N_{Data}	258	224	244	258	258	
N_{Parm}	24	24	24	28	24	
χ^2	303	219	307	305	303	
χ^2/df	1.29	1.09	1.40	1.31	1.29	

Table 5.1 Parameters of global fits. The four significant figures are to allow an accurate reproduction of the fit rather than an indication of their accuracy. All dimensional parameters in appropriate powers of GeV.

Process	Experiment	s_o/m_π^2	$\alpha_1(s)$	$\alpha_2(s)$	χ^2/data
$\psi' \to \psi\pi\pi$	Mark II Crystal Ball	5.4	-0.176	1.0	28/23 97/26
$T' \to T\pi\pi$	Argus CLEO CUSB Crystal Ball	3.4	-0.176	1.0	9/13 7/11 10/14 5/10
$T'' \to T\pi\pi$	CLEO CUSB	∞	-0.176 (fixed)	1.0	13/11 1/6
$\psi \to \phi\pi\pi$	Mark II				39/18
$\psi \to \phi K\bar{K}$	Mark II	-0.5	$\alpha_1^0 = 0.53$	$\alpha_2^0 = 0.08$	1/4
$\psi \to \phi\pi\pi$	Mark III	(fixed)	$\alpha_1^1 = -1.58$	$\alpha_2^1 = 3.64$	50/38
$\psi \to \phi K\bar{K}$	Mark III		$\alpha_1^2 = 1.23$	$\alpha_2^2 = -2.72$	1/5
$\gamma\gamma \to \pi\pi$	PLUTO DM1	∞	$\alpha_1^0 = -0.44$ $\alpha_1^1 = -2.46$ $\alpha_1^2 = 0$	$\alpha_2^0 = 1.11$ $\alpha_2^1 = 7.99$ $\alpha_2^2 = -8.10$	12/17 4/6

Table 5.2 Parameters of fits to heavy decays and $\gamma\gamma \to \pi\pi$ with s_0 the position of the process-dependent Adler zero and the coupling functions $\alpha_i(s)$ of Eqn. 4.36 normalised so the $\alpha_2(4m_K^2) = 1$.

CHAPTER SIX

RESULTS AND SUMMARY

6.1 POLES OF THE S-MATRIX

In this Chapter, we resume our main theme addressing the question: What $I = 0$ scalar dynamics is entailed by our global fit? When people discuss the pseudoscalars or tensors, there is no question that the $\iota(1440)$ or $\theta(1690)$ are resonances or what the other 0^{-+} and 2^{++} states are; speculative interpretation starts from that point (cf. Chapter 3). For the scalars, especially in the $I = 0$ sector, it is a major and subtle enterprise to establish what the resonances are, still more to assign meaningful parameters. The difficulty stems from all the classic complications of the resonance concept occurring simultaneously: resonances are variously broad and overlapping with substantial coupling to strongly opening channels (see the S* puzzle in Section 3.4.4). We are going to proceed in rather slow careful stages in the following discussions and this is inevitable given the complexity of the phenomena.

In the present section, we list and discuss the pole content of our solutions pointing out how our rather elaborate pole scenario is tied to the phenomena it explains and to general requirements on possible structures of the S-matrix. The ensuing list of poles and residues is the objective outcome of our analysis. As we shall show in this

chapter, in all our solutions, we always find seven poles of the S-matrix below 1.7 GeV. In Section 6.2 , we attribute these to four resonances, two broad objects $\varepsilon(900)$ and $\varepsilon'(1420)$ [205] and two narrow resonances $S_1(993)$ and $S_2(988)$, which together reproduce the S* phenomenon. Couplings to $\pi\pi$ and $K\bar{K}$ reveal the $\varepsilon(900)$ and $\varepsilon'(1420)$ to be consistent with a $(u\bar{u} + d\bar{d})$ composition within an ideally mixed nonet; likewise the $S_2(988)$ could have an $(s\bar{s})$ composition and the $S_1(993)$ appears like an SU(3) singlet, compatible with a glueball make-up.

Having sketched our destination, we now proceed to detail and justify this pole content of our solutions. This entails specifying not only positions and residues (couplings), but also on which sheet of the energy plane (see Appendix A.VI) poles are located [Fig. 6.1]. This latter is only an issue when dynamical activity coincides with the opening of a new threshold - precisely, the present case. Normally, all but one of the unphysical sheets of the energy plane is remote and resonances are unambiguously identified with poles on the adjacent sheet, e.g. for $\rho(770)$ sheet II and $f(1270)$ sheet III. A new threshold temporarily multiplies possibilities (see Appendix A.VI), since three unphysical sheets adjoin the physical region and can be the seat of physically significant resonance poles. The resulting structure is conveniently displayed in a k_2-plane [Fig. 6.2a], which explicitly distinguishes the two alternatives $k_2 = \pm\sqrt{E^2/4 - m_2^2}$ corresponding to a given complex energy E. In fact, k_2 is the c.m. 3-momenta of the $K\bar{K}$ in $\pi\pi \rightarrow K\bar{K}$.

As mentioned in Section 4.2.3, reaction thresholds appear as singularities in $\mathfrak{J}$ which take the form of cuts with branching points at the thresholds and extending to $s = \infty$. Furthermore, there is no fundamental difference between a resonance and a stable hadron besides the mass (assuming all other quantum numbers to be the same). One therefore expects the exchange of a resonance to result in a pole in the complex s plane near the real axis, but above the first branch point. For a simple Breit-Wigner resonance, the pole can neither be on the real axis nor on the physical sheet, so hermitian analyticity demands that there be in fact two poles, placed symmetrically on opposite sides of the real axis and on an unphysical sheet. Only the one which is below the real axis is close to the physical sheet, since the unphysical sheet is reached from the physical sheet by crossing the real axis from above (i.e. from I to II as in Figure 6.1). Hence, resonance poles usually have images on related sheets, for example, the physical f-pole has a counterpart on sheet II and that of the ρ on sheet III. In the K_2-plane, these images occur at approximately the mirror position $k_2^{II} \simeq -k_2^{III}$ (we will return to this for more details in Section 6.2), as follows directly from the Breit-Wigner description of these resonances. Normally, this phenomenon of pairing is of no physical importance. It is only where resonances occur close to the corresponding threshold that both members of such a duo get the chance to affect the physics. As we shall see, the present solutions illustrate this possibility in rather a complex fashion.

We first amplify the statement that resonance poles usually have images and to explain how exceptions come about. The general idea is as follows: let $\underset{\sim}{T}^{II}$ denote the scattering matrix on Sheet II and $\underset{\sim}{T}^{III}$ its counterpart on Sheet III. The analytic continuation from one to the other is specified by the relation [206]

$$[\underset{\sim}{T}^{III}]^{-1} = [\underset{\sim}{T}^{II}]^{-1} + 2i\underset{\sim}{\rho}_2 \qquad (6.1)$$

and resonances are associated with zeros of det $(\underset{\sim}{T}^{-1})$. Normally, the variation with energy that produces such zeros is already present in the corresponding inverse K-matrix elements (cf. Eqn. 4.30). A resonance pole in T^{II} then readily induces an image pole in T^{III} and vice versa; this is what usually occurs. However, it can happen that the K-matrix elements are essentially constant. Then, it is the phase space factors, in particular the rapidly varying ρ_2, which feeds the resonant variation. In this case, the image pole does not occur (or has 'moved off to infinity') and one has the situation referred to as a virtual bound state (an odd pole in the sense that it does not have a mirror image). The pole configuration that our solutions generate combine both possibilities. Despite appearances this corresponds to quite a simple structure of the K-matrix.

As already described in Section 5.3, we have performed fits using both K-matrix and M-matrix forms. The former yielded solutions for 1 explicit K-matrix pole, denoted K_1, a variant K_1', and a solution for 3 explicit K-matrix poles, labelled K_3; corresponding to the latter we obtained a single fit which we term M (we have not extended the 2-pole

M-matrix trial fit reported in Section 5.3 to a global fit because the number of poles in the K- and M- matrix do not affect the pole content of the $\mathcal{J}$-matrix and we only use the 1-pole M-matrix global fit here to study the stability of the poles). The pole pattern that emerges from each of these types of solution is remarkably stable. The details are displayed in Tables 6.1-2, and Figures 6.2-3. Each solution is seen to have seven 'nearby' poles, denoted A - G. Though S-matrix poles are not demanded by the forms with which we fit, they are the most important outcome of our solutions. Table 6.1 gives their positions for our representative solutions K_1 , K_1' , K_3 and M, while Figure 6.2a, b displays these in the k_2 and energy planes respectively, the latter illustrating how sheet II and sheet III poles form pairs, viz D - E and G - F. In Figure 6.3 are plotted the complex residues of these poles (Appendix A.VI), defined by:

$$\gamma_i \gamma_j = \lim_{s \to s_R} (s_R - s)\, \mathcal{J}_{ij} \qquad (6.2)$$

In fact, to make the plot intelligible we show γ_1 and $\bar{\gamma}_2 = -\gamma_2$. The average value of these couplings for each of our seven poles are tabulated in Table 6.2. Such residues are a important ingredient in our parton (spectral) assignments of the associated resonances as discussed in Section 6.2.1.

We must remark that the foregoing are not the only structures in our amplitudes. Forms which fit data along a limited region of the real axis in the energy plane inevitably also have distant poles which are mere artefacts of the parametrization and consequently are unstable.

Such poles occur for all our solutions on the physical sheet I. Though such poles violate causality, they always occur at least 500 MeV into the complex plane and so have no effect on the nearby structures reliably determined by the data.

To gain a mental picture of the complex pole scheme that has emerged, it is helpful to flip between the plot in terms of the k_2-plane [Fig. 6.2a] and that in the energy plane [Fig. 6.2b]. Read together, these display a short range system comprising the triplet A, B, C governing the $K\bar{K}$ threshold region, and long range structure dominated by the pole-pairs D - E and G - F (long range because they are far away from the real energy axis, Figure 6.2a). It is the former that constitutes the principal novelty of our solutions. The poles revealed by many previous analyses (using subsets of the data we consider) are illustrated in Figure 6.4 [207]. As will be seen [207], analyses of the S* have quite a long history [208] with one pole [209][210] and two pole scenarios [158][159][211][212] having early exemplars. For discussions in a similar spirit to the present one (although leading to quite different conclusions owing to different input) see especially Fujii and Fukugita [212]; Martin, Ozmultu and E.J.Squires [212],[213]; and Irving, Martin and Done[214]. (The last of these focusses very much on the $K\bar{K}$ data of Cohen et al [164] and only uses $\pi\pi$ information over the very resticted mass range 0.91 to 1.05 GeV). The PDG average [169] (in our terms for the position of pole A) is dominated by the result of fitting the low statistics data on $J/\psi \rightarrow \phi\pi^+\pi^-$ of Gidal et al [193]. This we believe to be quite unjustified as evidenced by the ease with which we

fit the same data [Fig. 5.1] using our own $\mathcal{J}$-matrix solutions with their appreciably different pole positions (see Figure 6.4b). These various analyses [207] have commonly reported just one pole (similar to A), or sometimes two, to describe the S* effect whilst we find three. What are the differences between these fits and what is the role of all our poles in achieving the reported fits?

As a step to answering the above questions, we examine what types of energy variation alternative pole configurations can achieve. Suppose just one pole controlled the $K\bar{K}$ threshold region, say at a position $K_2 = K_A$. There will in general be a background phase, δ_b . Allowing for this, a minimal representation (see Appendix C.II for derivation) for the $\pi\pi$ S-matrix element S_{11} is simply:

$$S_{11} = \frac{-(k_2 + k_A^*)}{(k_2 - k_A)} e^{2i\delta_b} \qquad (6.3)$$

This illustrates the rule that a pole at $k_2 = k_A$ automatically entails an associated zero of S_{11} at the mirror point $k_2 = -k_A^*$. This is a general result and follows from analytically continuing unitarity to the pole. The pole A of our fit (on sheet II) together with the background (D-E) produces the familiar sharp rise of the $\pi\pi$ phase shift just below $K\bar{K}$ threshold seen in Figure 5.3 (cf. Section 4.2.1). This is the classic signal for the S* resonance and, for that reason, some version of A has featured in all analyses of the past 13 years [207], (cf. Figure 6.4). The associated zero of S_{11} required by unitarity of itself produces a deep dip in the inelasticity, η_{11} , just above threshold, Figure 5.4. Such a feature is qualitatively in agreement with

experiment. It is for achieving quantitative agreement that other poles come into play [215].

It has long been noted [158][159][211][212][152] that a one-pole description of the S*-effect gives too blunt a signal in $\sigma(\pi\pi \rightarrow K\bar{K})$ (or, equivalently in the behaviour of η_{11}) as compared to the data. The qualitative effect is easily understood, either in terms of the poles and zeros picture sketched above, or by remarking that having just a sheet II pole with no corresponding sheet III image is, in a sense, to have half a resonance. Away from the resonance, the corresponding amplitude falls like $|E - E_{res}|^{-\frac{1}{2}}$, rather than as $|E - E_{res}|^{-1}$. Already for fitting the CERN-Munich $\pi\pi$ phase-shift data [158] (part of the input to the present fit), two-pole ansatzes yield much better fits to the S* region than do one pole formulae, such as arise from the complex scattering length descritpion. The contrast is very clearly exposed in Fujii and Fukugita [212] (see especially their Fig. 2) wherein a two-pole description is seen to be far superior for following the long range trends of both δ_{11} and η_{11}. How does our 3-poles solution compares with this? It turns out that the phase shift prediction hardly differs, but the inelasticity profile has a less pronounced and broader minimum [Fig. 5.4], consonant with the actual $\pi\pi \rightarrow K\bar{K}$ cross-section information used in the present fit and the assumption that the $K\bar{K}$ channel saturates inelasticity. The way our fit has responded to this requirment is to move pole C upwards towards the real axis [Fig. 6.4] as compared to Fujii and Fukugita [212]'s version of this feature. We shall demonstrate this in the next Section. Finally, all this readily

provides an excellent fit to the $\mathbb{P}\,\mathbb{P} \to \pi\pi$ production spectrum including the shoulder just below 1 GeV.

The primary role of the pole B in a χ^2 sense is to enable the locations for A and C, required by the data, to co-exist within the general constraints of unitarity. As we shall see in the next Section, removal of pole B dramatically worsens the global fits (of course, all the classic $\pi\pi$ data could be reproduced by a 2 pole fit). There are, of course, potentially, much more direct signals for B. The expected sharp peak in $\sigma(\mathbb{P}\,\mathbb{P} \to K\bar{K})$ just above threshold is to an extent borne out by the data [Fig. 5.10]. (As it stands this is not a convincing statement because the strong opening of the $K\bar{K}$ channel in Figure 5.7 could be described by the conventional 2-pole scenario [Fig. 6.6]. However, as we shall see, the peak in $\sigma(\mathbb{P}\,\mathbb{P} \to K\bar{K})$ can only be fitted with a 3-pole solution). With the pole B so close to threshold very striking differences should appear between spectra for K^+K^- and $K_S^0K_S^0$. The latter channel should also register a very sharp peak (uncontaminated by a $\phi(1020)$ signal) in $K^-p \to \Lambda(\Sigma)K_S^0K_S^0$. Another consequence of B should be a very sharp downward blip in $\phi_{12} = \arg \mathfrak{J}_{12}$ just above threshold and indeed there are hints of such behaviour in the data [Fig. 5.8]. We have previously [144] suggested that this feature of the input plays a significant role in selecting the 3-pole option. We now know this not to be the case (see the following section).

Our long range pole pairs D - E and G - F are certainly the most economic solution for describing the presently available data. An important goal for future experiments is to establish whether it is also

sufficient. Already, there are claims for additional structure from Etkin et al [216] on the basis of $\pi\pi \rightarrow K\bar{K}$ information and an amplitude analysis of $\eta\eta$ production [171]. As always, it will be difficult to tie down detailed pole parameters closely; indeed their very existence is deduced from long rang phase movements (cf. discussion of the analogous but much less complicated $\kappa(1350)$ effect in $K\pi$ scattering [217]). Nevertheless, the pairing D - E successfully unites the source of the slow rise of δ_{11} from $\pi\pi$ threshold (the old $\varepsilon(900)$ effect) principally given by D with the description of phase movements above 1 GeV via E. (We shall return to this in Section 7.2). This forms the background on which the pair A-C sits to give rise the classic S* signal. Our resonance assignments (Section 6.2) are based on the foregoing pattern of short range and long distance poles.

6.1.1 The role of pole B

The principal new feature of our analysis is that we find 3 poles, A, B, C in the region of $K\bar{K}$ threshold rather than the one or two of previous treatments, which only considered subsets of the data we have used. Remember that our parametrizations do not 'a priori' have any particular number of poles of the S-matrix, yet all our solutions have this same A, B, C structure. Our extensive analysis with fits of different forms (i.e. K_1 , K_3 and M) illustrates the well-known fact that resonances are given by the poles of the S-matrix and not by the poles in the parametrizations (cf. the g_Ts in BNL and see Chapter 7).

When resonances are narrow and non-overlapping and a single channel predominates, it is relatively easy to investigate the effect of adding in or taking out particular resonances. In the present situation with strongly coupled channels, this is non-trivial to implement because of the over-riding need to ensure that unitarity remains satisfied. Nevertheless, we present here a way to discuss why our analysis finds 3 poles in the neighbourhood of $K\bar{K}$ threshold whilst previous treatments did not.

To allow the number of S-matrix poles to be fixed 'a priori', consider the Jost function (or determinant [218] , see Appendix C), which up to some real function $d(K_2^2)$ is the denominator of the S-matrix, so that

$$\phi(k_2) = d(k_2^2)\,[1 - i\rho_1 K_{11} - i\rho_2 K_{22} - \rho_1\rho_2 \det K] \qquad (6.4)$$

The zeros of ϕ, which correspond to poles of $\underset{\sim}{S}$ or $\underset{\sim}{\eta}$ and thus to resonances, are its sole source of variation apart from distant effects from the $\pi\pi$ threshold and from left hand cuts. The function $\phi(k_2^2)$ thus provides a highly useful method for exploring possible pole scernarios for the $K\bar{K}$ threshold region. Indeed, it enables one to parametrize amplitudes explicitly in terms of poles by representing the Jost function by a simple product of zeros (one for each pole) and an entire function (see Appendix C.II). Thus, we write for example

$$\phi(k_2) = \left[1 - \frac{k_2}{k_{2A}}\right]\left[1 - \frac{k_2}{k_{2B}}\right]\left[1 - \frac{k_2}{k_{2C}}\right] \exp\left[\sum_{n=0} \gamma_n k_2^n\right] \qquad (6.5)$$

where the γ_n are complex numbers and $k_2 = k_{2j}$ (j = A, B, C) are the

three poles A, B and C. Comparing Eqns. 6.4-5 above $\pi\pi$ threshold, we can read off K_{11} , K_{22} and det $\underset{\sim}{K}$ and consequently relate the $\mathcal{J}$-matrix elements to the parameters of Eqn. 6.5. Unitarity, of course, requires K_{12} real (Appendix A.I and II), i.e. $\eta_{11} \leqslant 1$. Unfortunately, here this condition is not automatic requiring $K_{11}K_{22} \geqslant \det \underset{\sim}{K}$ [Eqn. C.8] which, though trivially fulfilled by a K- or M- matrix parametrization, is easily lost writing $\phi(k_2^2)$ as a product of zeros. The positivity condition, $K_{11}K_{22} - \det \underset{\sim}{K} \geqslant 0$, must be checked at every stage and is found in practice to greatly restrict the acceptable region of the γ_n parameter.

As shown in Appendix C.I, the arbitrary function $d(k_2^2)$ cancels out in physical quantities, viz the $\mathcal{J}_{ij}$, as does any arbitrary real function in Eqn. 6.5. Thus we can set Re $\gamma_{2n} = 0$ for all n because $k_2^{2n} = [(1/4)E^2 - m_2^2]^n$ is real, so are the products $\mathrm{Re}\gamma_{2n}k_2^{2n}$. Such a form as Eqn. 6.5 with only 3 poles (and not the 7 of Fig. 6.2) can only be expected to represent experiment in a limited region of the k_2-plane. Specifically, from Figure 6.2a, we see that we can expect the poles D - G to provide just a smooth background for $|k_2| \leqslant 0.24$, say, i.e. $0.87 \leqslant E \leqslant 1.10$ GeV. Our aim is first to show that a fit of all the data in this limited energy regime with a 3 zero form like Eqn. 6.5 is possible and then to compare this with a similar fit using a two zero form (i.e. to remove the B pole). Because of the condensed ranges of the parameters that allow unitarity to be fulfilled, we must choose the starting parameters with care. In the case of the 3 pole scenario, these are readily found by first fitting the form Eqn. 6.5 , to any of

the amplitudes we already found with 3 poles. (We use the effective kaon mass in ρ_2 and again Simpson's rule in the AFS fit in the 1 GeV region to allow for the rapid variation caused by the B pole). We then refit the experimental data within a $|k_2| < 0.24$ GeV radius of $K\bar{K}$ threshold. The parameters and result for all the classic $\pi\pi$, $K\bar{K}$ and AFS double pomeron data are listed in Table 6.3b. In this narrow energy range, the discrepant results on ϕ_{12} , Figure 5.8 , play a dominant role. Hence, the compromise fit has a χ^2/d.f. of 2.2, while selecting Etkin et al [166] very satisfactorily reduces this to 1.1 for the 3-pole fit. The parameters of these fits are also displayed in Table 6.3b. The success of such a fit illustrates that a parametrization in which poles of the S-matrix simply enter as a product of zeros in the Jost function is viable (confirming the factorization of the Jost function described in Appendix C.II). The limited 3-pole global fits to the inelastic $\pi\pi \rightarrow \pi\pi$, $\pi\pi \rightarrow K\bar{K}$ channels and the AFS data are illustrated in Figures 6.5-7 (solid lines).

Our next step is to compare the above 3-pole fit with one with only two poles. To obtain good starting parameters without the B-pole, we choose a form with the positions of A anc C as found by Fujii and Fukugita [212] fitted just to the CERN-Munich $\pi\pi$ data [158]. A perfectly adequate fit can be retained not only when the $\pi\pi$ results of Cason et al [161] are added, but when we include one of the $\pi\pi \rightarrow K\bar{K}$ data sets. This shows that a two pole scenario is equally possible for all the classic dimeson channels, Figures 6.5-6 (dotted lines). It is when the AFS results on $\pi\pi$ and $K\bar{K}$ channels [69] are introduced that the

2-pole form fails dramatically even in this limited energy regime as illustrated in Figure 6.7 (dotted lines). With many random starts, the best χ^2's we have achieved, together with the corresponding parameters, are listed in Table 6.3a. All these 2-pole fits are considerably worse than the corresponding 3-pole solutions. The fits are no longer able to reconcile the AFS data with any of the results on $\pi\pi \rightarrow K\bar{K}$. Furthermore, the 2-pole fit to the inelastic δ_{11}[Figure 6.5] is also worse than that of the 3-pole fit. Even to achieve these limited successes, the poles A, C both move very close to the axis from the Fujii-Fukugita positions [212] (Figures. 6.2b, 6.4 and the pole positions in Table 6.2a) to compensate for the lack of the B pole.

This analysis unambiguously favours our solutions with 3 poles in the neighbourhood of $K\bar{K}$ threshold. The confidence level for this is some 30%, while that for just 2 poles, when the AFS information is included, is less than 0.01%! This has demonstrated directly the tight constraint provided by the AFS data through unitarity (Section 4.2).

6.2 RESONANCE ASSIGNMENTS AND INTERPRETATION

Here we summarize the pole structure reported in the previous section and convert them to a resonance spectrum. As already emphasized at the beginning of this chapter, most resonance poles have replicas on associated sheets. This is usually true but not so here in our solutions. I shall use here a crude scheme for pairing up the associated resonances. A much more rigorous and systematic scheme is

the 'λ-tracking' method of David Morgan which is presented in Ref.[219]. As it turns out the conclusions of these two schemes are almost exactly identical. This further strengthens our claim that there are three poles in the S* region. In any case, no matter how the poles are paired we have extra dynamics responsible for the intrusion of a third pole, the B, in our solutions.

We now consider the convention for our resonance assignments. The convention for extracting couplings has already introduced earlier, Eqn 6.2, and we simply follow the same recipe for extracting masses and widths. To be more precise, we assume that each resonance be describable in the neighbourhood of the pole by a factorisable form:

$$\mathcal{J}^R_{ij} = \frac{g_i q_j}{s_R - s} e^{i(\delta^b_i + \delta^b_j)} \qquad (6.6)$$

This will have complex residues at the pole owing principally to the background phases; however one conventionally uses the corresponding moduli, $|\gamma_i|$, as effective coupling constants (cf. Eqn. 6.2 and Appendix A.VI). For the resonance position or mass one normally takes the real part of the complex pole position

$$m_R = \mathrm{Re}(E_R) \qquad (6.7)$$

where $E_R^2 = \mathrm{Re}(s_R)$. The corresponding width is given by

$$\Gamma = 2\ \mathrm{Im}(E_R) \qquad (6.8)$$

where $E_R\Gamma = -\mathrm{Im}(s_R)$. The crude resonance assignments given in this section adhere closely to this simple recipe.

We now consider the pairing procedure. As already argued in Section 6.1 that the respective pole pairs (D,E) and (G.F) should be associated simply from their nearness in the energy plane (Table 6.2 and Fig. 6.2b). To put this on a firm basis we need to understand (at least crudely) how sheet II and sheet III poles might be associated. As explained in Appendix A.I the $\mathcal{J}$-matrix elements have a common denominator which in terms of M-matrix can be written in the form

$$\Delta \equiv \det M - i\rho_1 M_{22} - i\rho_2 M_{11} - \rho_1\rho_2 \qquad (6.9)$$

The poles of $\mathcal{J}$ correspond to zeros of Δ; the relevant sheet structure arises from the factors of $\rho_2 (\equiv 2k_2/E)$ in Eqn. 6.9 (see Appendix A.VI). The fact that there exist pole pairs (X - Y) with X on sheet II and Y on sheet III means that switching ρ_2 to $-\rho_2$ in Eqn. 6.9 only slightly disturbs the zeros of Δ. To assign the resonance position to the pole pairs (X - Y) we simply take the average of their values. This naive assignment can be justified if the above statement on the stability of the zeros under the switch $\rho_2 \rightarrow -\rho_2$ is true (i.e. the zeros of Δ for ρ_2 and $-\rho_2$ are very similar). The 'λ-tracking' method of David Morgan [219] addresses this problem in much more details and the conclusion agrees with the above naive approach for the resonance assignments. This then justifies the crude pairing of poles (D,E) and (G,F) on the ground that they are close to their partners in the energy plane (Table 6.2). Furthermore, this simple scheme also implies that A and C should be paired and B as the odd man out - B does not have a imaginary part (it is in fact very tiny $\sim 10^{-5}$ GeV) but that of A and C are very close. The supporting evidence comes from the previous 2- and

3- pole Jost function fits in the S* region. There we observe that the positions of the poles in the 2-pole Jost fit are always close to those of A and C in the k_2-plane (compare Tables 6.3a and b). This again leaves the B pole out and suggests that in the absence of B, A and C combine together to reproduce the classic S* effects, i.e A and C should be paired up. A more theoretical argument follows from the stability of zeros of Δ. We know from Table 6.2 that the (untwinned) B almost sits on top of the $K\bar{K}$ threshold giving $|\rho_2| \to 0$. Therefore changing $\rho_2 \to -\rho_2$ in Eqn. 6.9 does not disturb the zero (the position of B) of Δ at all, leaving B without a mirror image. The zero imaginary part of B is crucial in such a phenomenon as even a small imaginary component would mean two distinct solutions to the quadratic (in energy) expression of Eqn. 6.9, the pole pair (A-C) being the best example. The pole B has all the features of a a virtual $K\bar{K}$ bound state, having no mirror image and sitting close to $K\bar{K}$ threshold. The above assignments are confirmed by the more rigorous 'λ-tracking' approach [219].

Finally, we summarize the pole positions of our solutions (Table 6.1-2) with the above assignments in Table 6.4. The variations of the pole positions from solution to solution are small except for the D-pole parameters according to solution M (given in brackets in Table 6.1) which are not included in the average values in Table 6.1. We next look for particle identifications of the resonances in Table 6.4

6.2.1 Parton composition of our states

In this section we consider the quark model assignments of our spectrum and the types of new dynamics responsible for the presence of our odd B pole.

Conventional quark model classification looks to find meson families arranged in ideally mixed nonets, generically [S(I = 0), V(I = 1), K(I = 1/2), S'(I = 0)][220] with a standard pattern of masses and decay couplings given by the presumed quark content and the OZI rule. This is the benchmark against which we have to discern novelties and abberations. This idealized pattern is not always realized in practice and various mechanisms are invoked to explain the departures (eg. see Section 3.4.1.4(III) for the non-ideal mixing of the 0^- nonet). In principle, the I = 0 sector should consist of two standard ground-state $q\bar{q}$ compounds which will be ideally mixed if no special mechanism operates. Additions can come either from radial excitations or from non-standard configurations such as glueballs, hybrids and multiquark compounds. Examples of these are the various interpretations of the $\iota(1440)$ and $\theta(1690)$ described in Chapter 3. As we will explain in Chapter 7, the most likely candidate among non-standard configurations for the B pole is the ground state scalar glueball $\varepsilon_g(0^{++})$ which according to various models (Section 1.3) is the lightest glueball. If $\iota(1440)$ is identified with the pseudoscalar glueball η_g , than ε_g should lie well within our energy range (Section 3.4.4). In the absence of mixing it should be a pure SU(3) singlet (Section 1.3). The other

non-standard configurations, like hybrids, etc, all entail the existence of $I \neq 0$ companions (extra δ's and κ's). We shall provisionally ignore these other possibilities because the existing information on the relevant decay channels (which could be improved) does not provide any clear signals for such additions (see Section 7.4 for more discussions). Another possible type of intrusion is from what we shall call 'molecular' or 'bootstrap' resonances such as can occur in multihadron systems from explicit hadron exchanges (see Section 3.4.1.2).

In our case, very broad states are involved making precise mass values of the resonances ambiguous. The only information available for spectroscopic assignments is the pattern of branching ratios and that only as between $\pi\pi$ and $K\bar{K}$. The empirically determined $|g_\pi/g_K|$ ratios are listed in Table 6.4 (these values are similar to those obtained by the 'λ-tracking' method in Ref. 219). We now compare these empirical ratios with those of the simple idealized SU(3) configurations (Table 6.5 and Appendix D). We use the labels ε_1 for SU(3) flavour singlet, ε_8 for nonet isosinglet, ε_{ns} for non-strange meson and ε_s for strange meson in Table 6.5 and the following discussions. On this basis, $S_2(988)$ is a natural candidate for the regular $s\bar{s}$ ground state. Direct confirmation for this assignment could be sought in precision data on radiative ϕ decay: $\phi \rightarrow \gamma S_2$. This process would provide γ rays of some 20 MeV (the mass difference between ϕ and S_2) with a spread of only a few MeV from the ϕ width. This should yield a clear signal readily distinguishable from the continuum. With S_2 as the lowest $s\bar{s}$ state in the quark model then it is natural to

identify $\varepsilon(900)$ as its non-strange counterpart on the basis of $|g_\pi/g_K|$. However, there is a problem with this ideal mixing assignment because naively one expects a mass-splitting of several hundred MeV (cf. $M_\phi^2 - M_\omega^2 \simeq 0.43\ GeV^2$). This descrepancy may be caused by additional mechanisms which shift the $s\bar{s}$ level down in mass and weaken its coupling [219].

Having identified the $S_2(988)$ and $\varepsilon(900)$ as the candidates for the two ideally mixed quark model states, we now consider the roles of our remaining states. From Tables 6.4-5 we see that $S_1(993)$ is compatible with an SU(3) singlet identification. It is thus a prime candidate within our spectrum for the I = 0 scalar glueball (see Section 7.4). To check this significant assignment we need additional and more refined data of the kind we have already discussed in Section 5.1, This could be usefully supplemented by new high precision experiments on dimeson production reactions like $K^-p \to K\bar{K}\Lambda$. In principle, one can seek for specific evidence that S_1 is a glueball by looking at the $\gamma\gamma$ excitations of S_1 which is supposed to be suppressed in the framework of parton model (Section 3.2.2). However, there are complications such as enhancements through anomalous couplings (Section 3.2.2) and final state interactions (cf. $\gamma\gamma \to \pi^0\pi^0$ in the f-region). We will return to the gluonium interpretation of S_1 later.

The last state to be identified is the $\varepsilon'(1420)$ [205] of Table 6.4. Its parameters could well undergo revision since it occurs at the upper end of our energy range where unconsidered channels start to play an appreciable role (note also that there have been claims for additional

structure [216][171], cf. Section 6.1). Again from the ratio of couplings we assign ε' to the ε_{ns} in Table 6.5. It is perhaps the first $q\bar{q}$ radial excitation of ε_{ns}. Etkin et al's S(1730) [166] could be the corresponding ε_s if it is confirmed.

We summarize the outcome of the above discussion as follows: The resonance content of the I = 0 S-wave below 1.5 GeV primarily couples to $\pi\pi$ and $K\bar{K}$. It comprises

(a) A narrow resonance $S_1(993)$ very close to $K\bar{K}$ threshold

$$E_R \simeq 0.993 - 0.023i \qquad (g_\pi \simeq 0.23,\ g_K \simeq 0.28)$$

which manifests itself via sheet II and sheet III poles A and C (details in Tables 6.1-2).

(b) A $K\bar{K}$ bound state $S_2(988)$ yielding pole B ($g_\pi \simeq 0$, $g_K \simeq 0.35$)

(c) An $\varepsilon(900)$

$$E_R \simeq 0.905 - 0.37i \qquad (g_\pi \simeq 0.48,\ g_K \simeq 0.28)$$

which corresponds to sheet II and sheet III poles D and E (cf. Tables 6.1-2)

(d) An $\varepsilon'(1420)$

$$E_R \simeq 1.42 - 0.23i \qquad (g_\pi \simeq 0.56,\ g_K \simeq 0.10)$$

corresponding to poles F and G. (cf. Tables 6.1-2)

The way our spectral assignments for the I = 0 scalars would fit into the overall pattern for the lower meson families is displayed in Table 6.6. (Note that these numbers differ from those in Ref. 219 by an insignificant amount.)

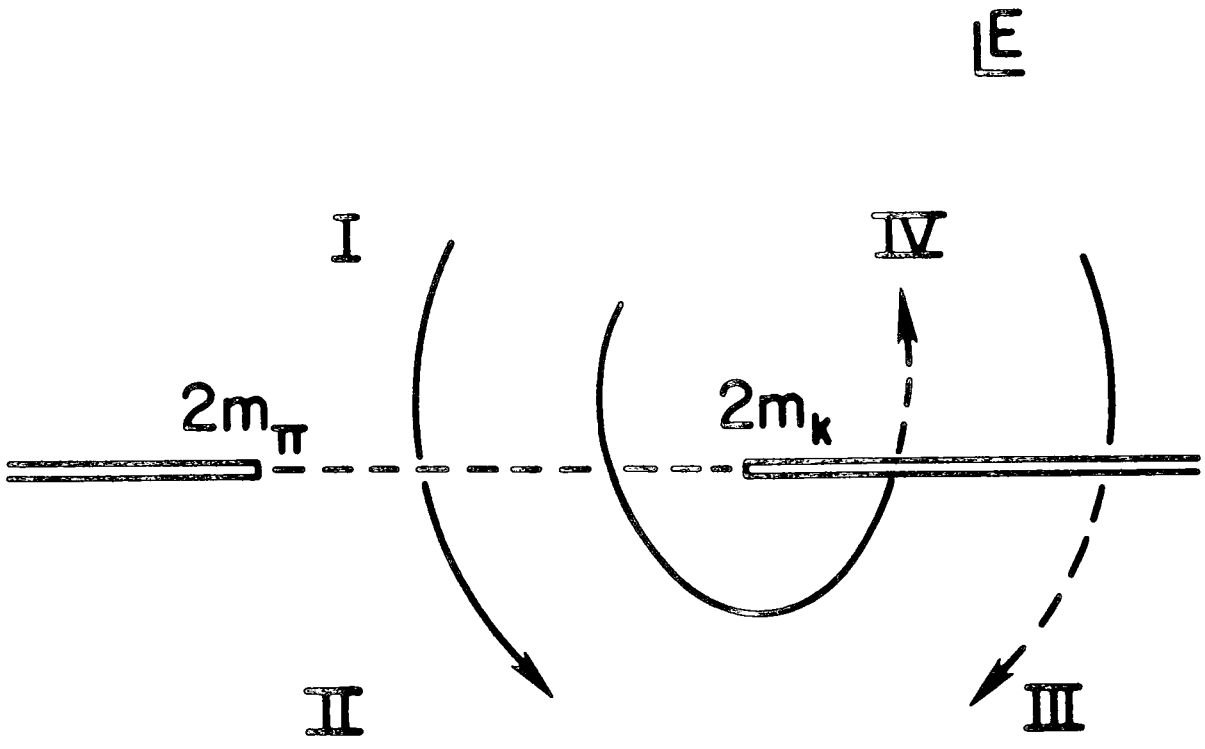

Sheet Structure of the Energy Plane

Figure 6.1 Sheet structure of the energy plane.

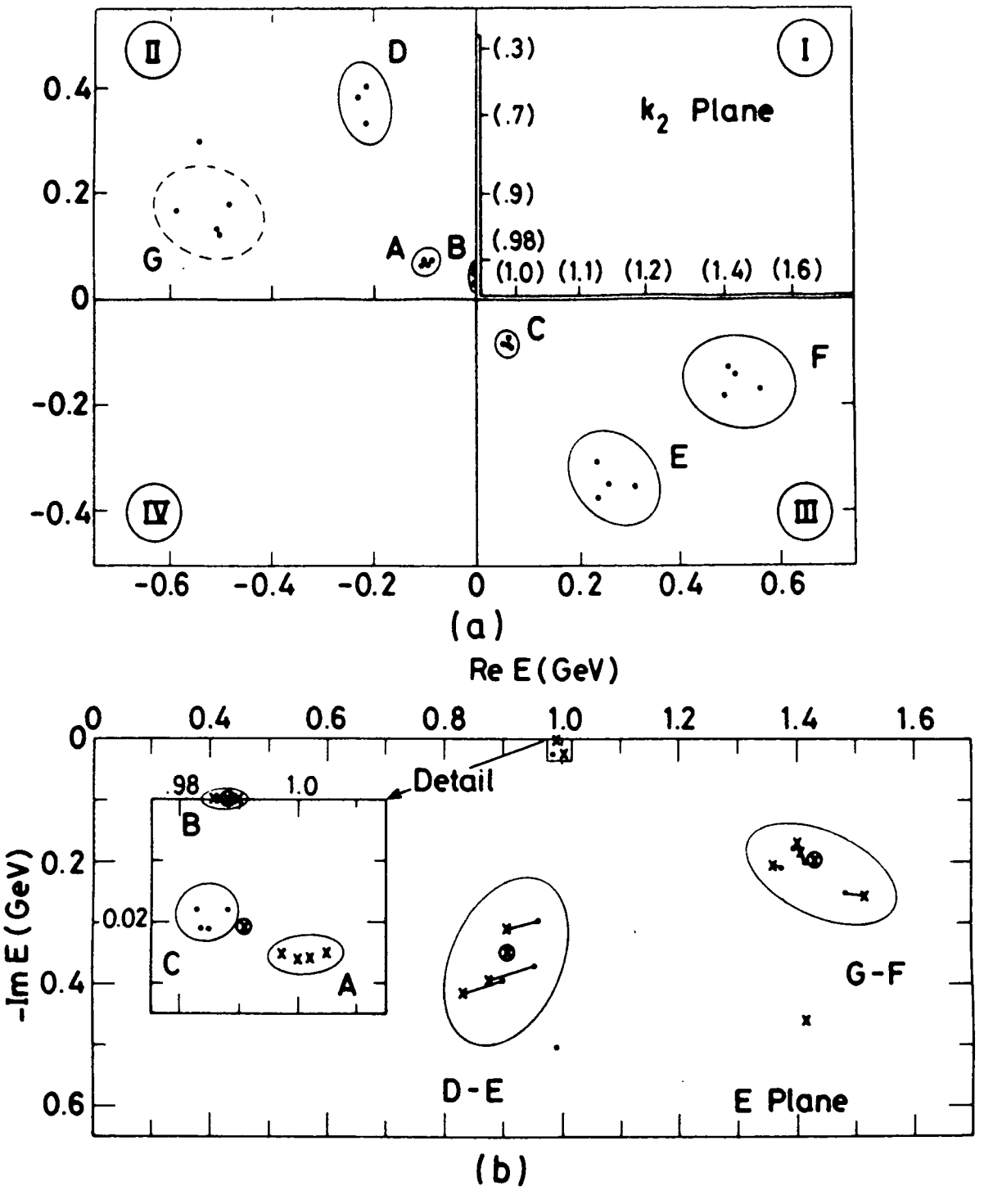

Figure 6.2 Positions of the 7 poles A-G for representative solutions (cf. Table 6.1):

(a) plotted in k_2-plane (corresponding real energies shown in brackets),

(b) plotted in E-plane with insert showing $K\bar{K}$ threshold region enlarged: X for sheet II, • for sheet III. The curved patches indicate spread among solutions.

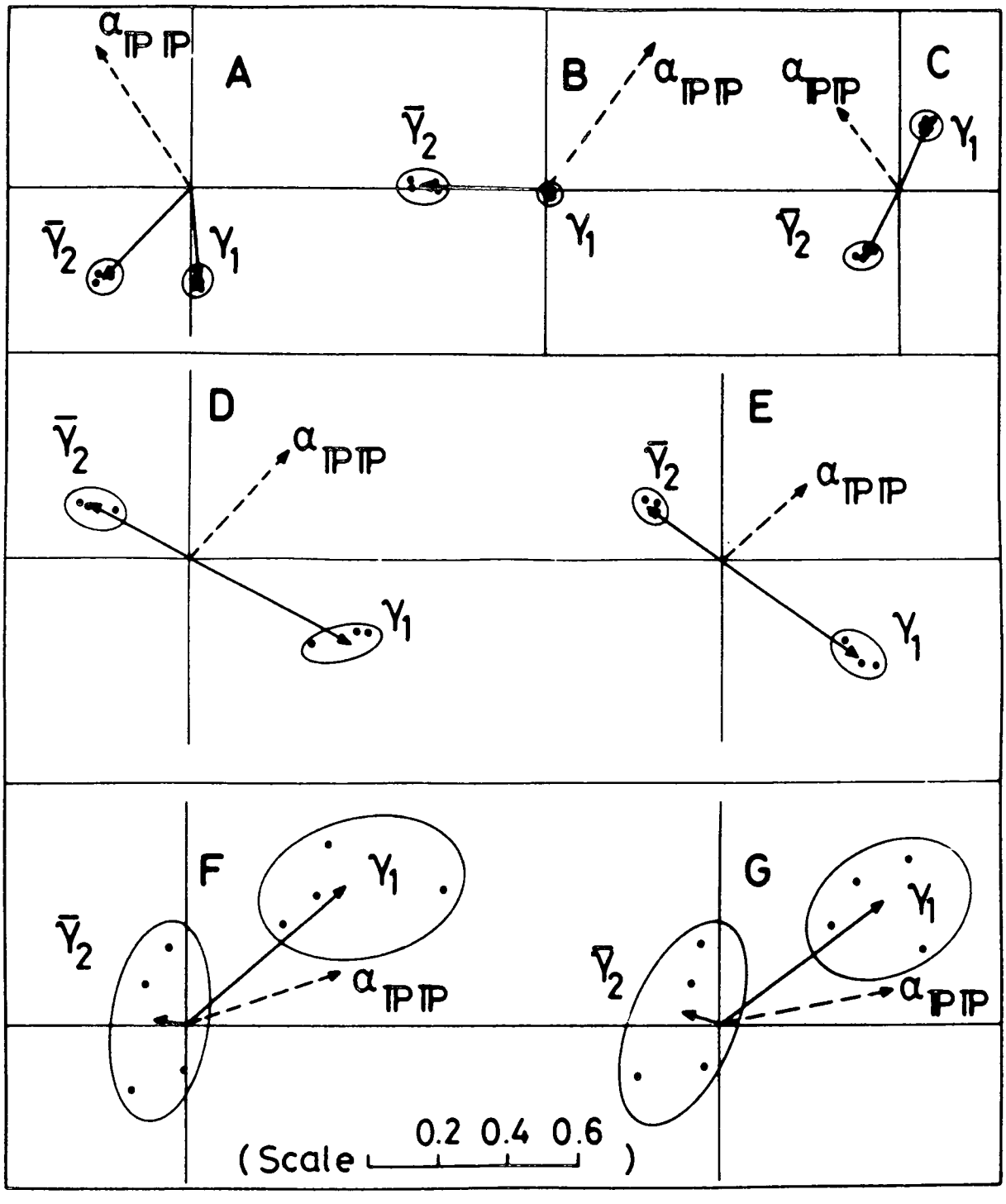

Figure 6.3 Complex residues γ_1 and $\bar{\gamma}_2$ ($\equiv -\gamma_2$)(cf. Eqn. 6.2) corresponding to poles of Figure 6.2. Dots correspond to individual solutions (Table 6.1), full lines to vector averages of these and dashed vectors to associated $I\!P\,I\!P$ couplings $\alpha_{I\!P\,I\!P} \equiv \alpha_1\gamma_1 + \alpha_2\gamma_2$.

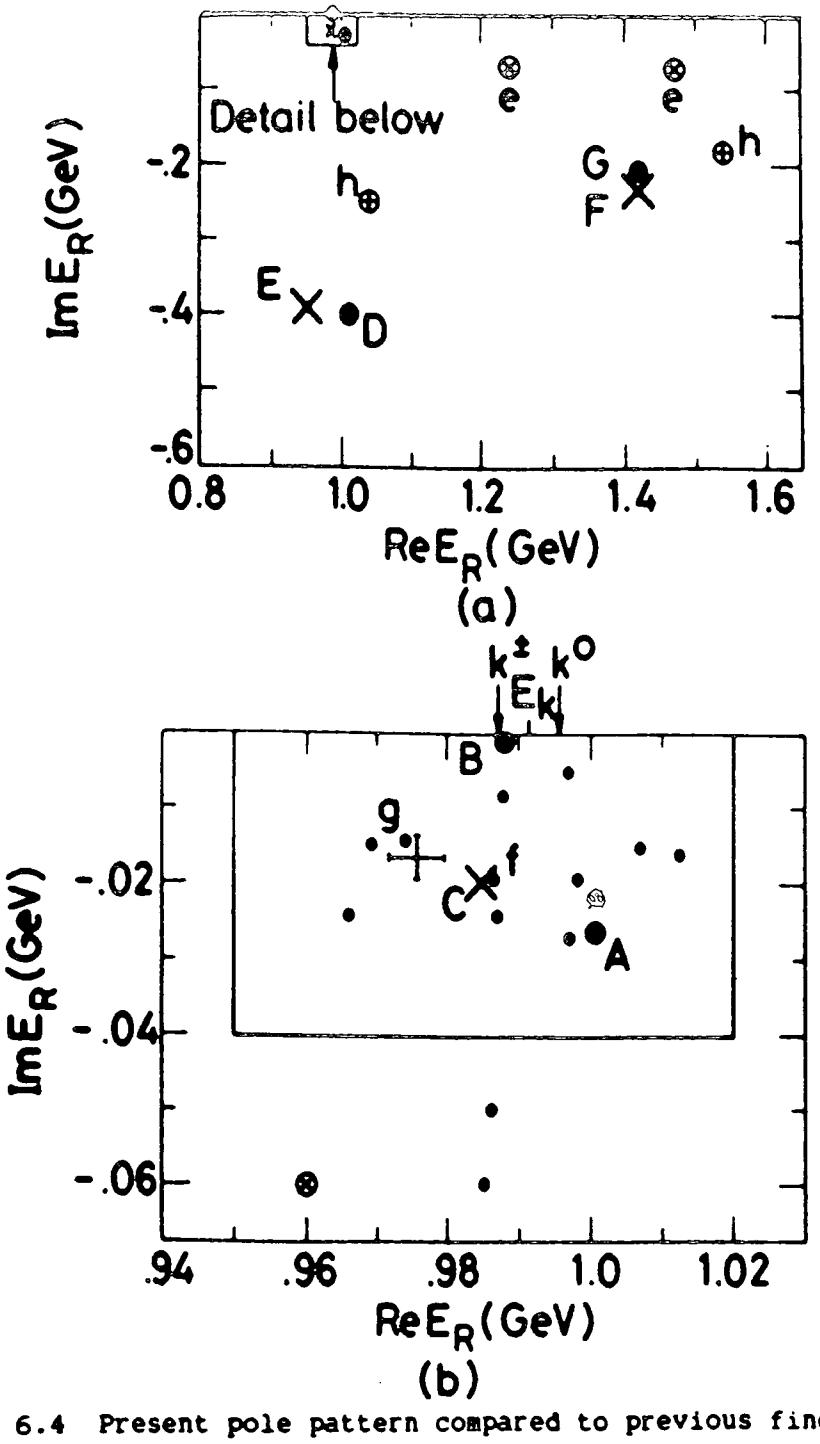

Figure 6.4 Present pole pattern compared to previous findings as listed in Ref. 169: (a) overview (b) detail for the $K\bar{K}$ threshold region. Notations: the average pole locations (Table 6.2): • (Sheet II), X (Sheet III); in (a) points labelled 'h' and 'e' are from Refs. 159 and 216 respectively; in (b) the cross with error bars depict PDG average [Ref. 169], 'g' the value inferred from Ref. 193, 'f' the outcome of the one-pole fit of Ref. 212 and ⊗ that from the associated two-pole fit [212].

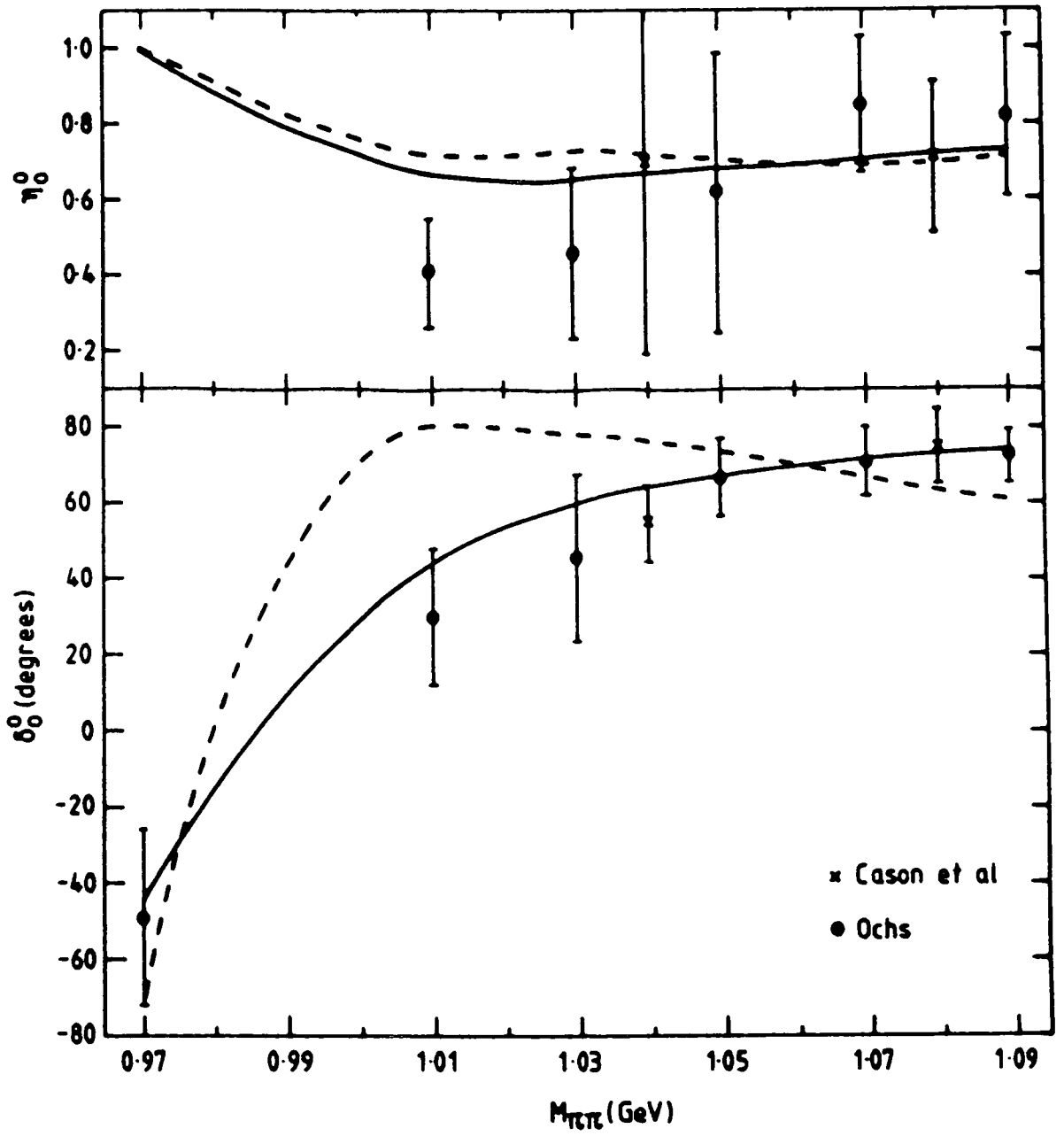

Figure 6.5 The $\pi\pi$ I = 0 S-wave phase-shift, δ_0^0 , and inelasticity η_0^0 (denoted by δ_{11} , η_{11} iin the text) above $K\bar{K}$ threshold up to 1.1 GeV showing the CERN-Munich results as analysed by Ochs [159] and the preferred B solution of Cason et al [161]. The curves show a typical 2-pole (dotted lines) and 3-pole (solid lines) Jost function fit (cf. Figure 5.4).

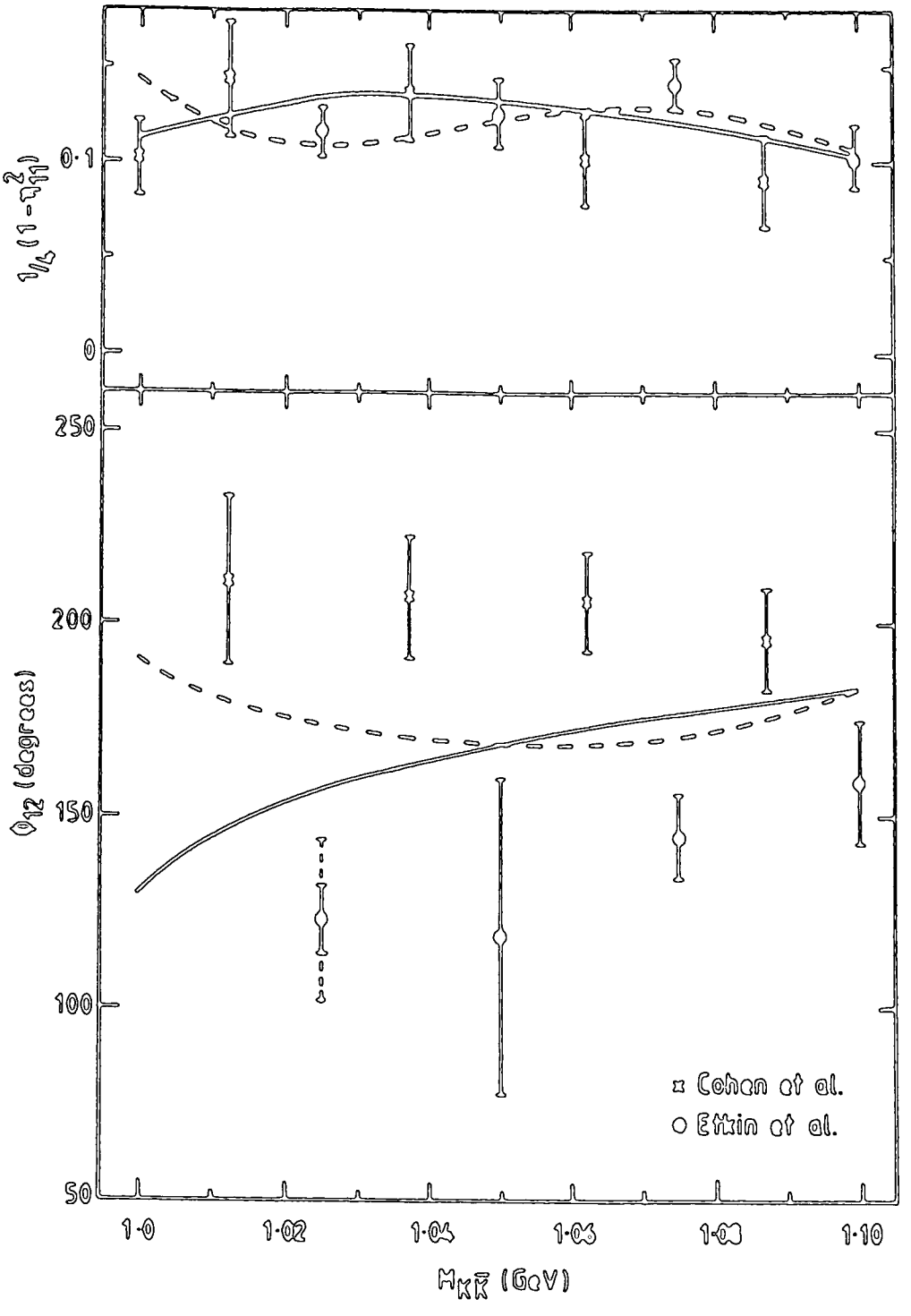

Figure 6.6 The I = 0 S-wave magnitude, $(1/4)(1 - \eta_{11}^2)$, and its phase ϕ_{12} for $\pi\pi \to K\bar{K}$ above $K\bar{K}$ threshold up to 1.1 GeV from Cohen et al [164](x) and Etkin et al [166](o). Again the curves show a typical 2-pole (dotted lines) and 3-pole Jost function fit (cf. Figure 5.7).

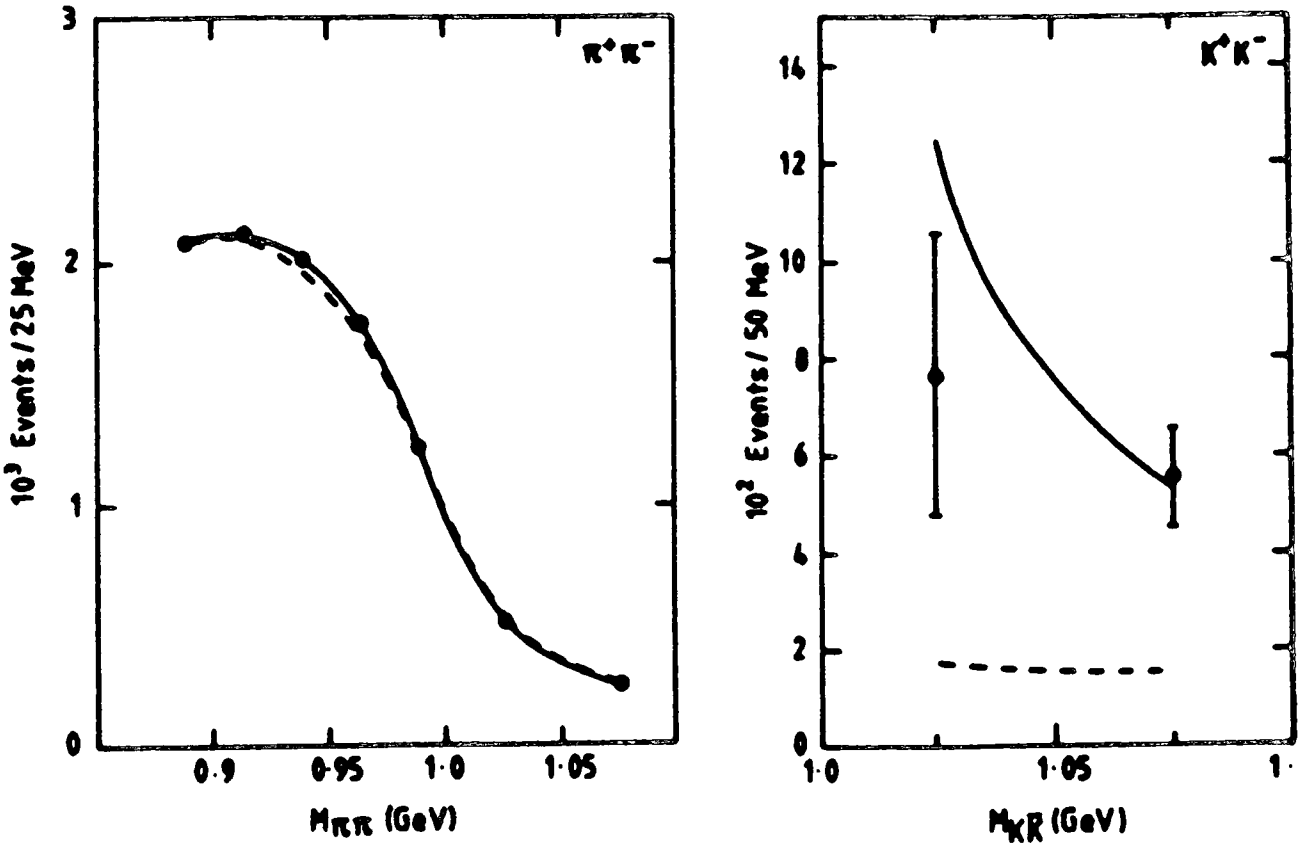

Figure 6.7 Mass spectrum of centrally produced S-wave $\pi\pi$ and $K\bar{K}$ events in pp -> pp(MM) from the AFS Collaboration [69] in the region of 0.87 to 1.1 GeV are shown. The 2-pole and 3-pole Jost function fits are shown in dotted and solid lines respectively (cf. Figures 5.9-10).

Solution						
Pole	Sheet	K_1	K_3	M	K_1'	average
A	II	1.002-0.026i	1.005-0.025i	0.997-0.025i	1.000-0.026i	1.001-0.026i
B	II	0.986	0.990	0.990	0.987	0.988
C	III	0.984-0.021i	0.988-0.018i	0.983-0.018i	0.984-0.021i	0.985-0.020i
D	II	0.88-0.40i	0.91-0.31i	(1.42-0.46i)	0.83-0.42i	0.87-0.38i
E	III	0.95-0.37i	0.96-0.30i	(0.99-0.50i)	0.90-0.39i	0.94-0.35i
F	III	1.48-0.26i	1.40-0.18i	1.37-0.26i	1.42-0.20i	1.42-0.23i
G	II	1.52-0.26i	1.40-0.17i	1.36-0.26i	1.40-0.18i	1.42-0.22i
χ^2/NDF		1.3	1.3	1.3	1.4	

Table 6.1 Pole positions, E_R(GeV), for various solutions described in the text.

Pole	E_R(GeV)	γ_1(GeV)	($\|\gamma_1\|$)	γ_2(GeV)	($\|\gamma_2\|$)	$\alpha_{\mathbb{P}\mathbb{P}\mathbb{P}}$
A	1.001-0.026i	0.02-0.26i	(0.27)	0.25+0.25i	(0.35)	0.9
B	0.988	0.011-006i	(0.01)	0.35-.01i	(0.35)	1.0
C	0.985-.020i	0.07+0.18i	(0.19)	0.09+0.18i	(0.20)	0.6
D	0.87-0.38i	0.44-0.21i	(0.49)	0.27-0.13i	(0.30)	0.7
E	0.94-0.35i	0.39-0.26i	(0.47)	0.21-0.14i	(0.25)	0.6
F	1.42-0.23i	0.43+0.36i	(0.56)	0.08-0.01i	(0.08)	0.9
(G)	1.42-0.22i	0.45+0.32i	(0.55)	0.10-0.03i	(0.10)	1.0

Table 6.2 Average pole positions, residues and $\mathbb{P}\mathbb{P}\mathbb{P}$ couplings, $\alpha_{\mathbb{P}\mathbb{P}\mathbb{P}}$, for the specimen solutions ($\alpha_{\mathbb{P}\mathbb{P}\mathbb{P}} \equiv |\alpha_1\gamma_1 + \alpha_2\gamma_2|$).

Parameters	(1,2)	1	2
Re k_{2A}	-0.0211	-0.0224	-0.0266
Im k_{2A}	0.0366	0.0358	0.0260
Re k_{2B}			
Im k_{2B}			
Re k_{2C}	0.1411	0.1381	0.1611
Im k_{2C}	-0.2371	-0.2338	-0.2723
Im Y_0	-0.9737	-0.9799	-0.6364
Re Y_1	1.0700	1.0250	0.7283
Im Y_1	5.5240	5.2790	8.2110
Im Y_2	4.9580	3.0600	5.0820
Re Y_3	43.680	40.300	45.670
Im Y_3	-39.640	-54.540	-51.050
Im Y_4	286.700	287.200	258.100
Re Y_5	-665.500	-686.800	-620.800
Im Y_5	-689.100	-1046.000	-989.200
Im Y_6	-2814.000	-2373.000	-3496.000
α_1^0	-0.2217	-0.2191	-0.3442
α_1^1	-1.6815	-1.6743	-1.6345
α_1^2	1.0207	1.0061	1.1154
α_2^0	0.2173	0.2176	0.2465
α_2^1	-0.1963	-0.1941	-0.1793
α_2^2	-0.1847	-0.1926	-0.1966
N_{Data}	47	39	37
N_{Parm}	20	20	20
χ^2	96	70	49
χ^2/d.f.	3.6	3.7	2.9

Table 6.3a

Parameters	(1,2)	1	2
Re k_{2A}	-0.0723	-0.0692	-0.0798
Im k_{2A}	0.0729	0.0706	0.0615
Re k_{2B}	-0.0029	-0.0028	-0.0037
Im k_{2B}	-0.0023	0.0025	0.0027
Re k_{2C}	0.0439	0.0452	0.0549
Im k_{2C}	-0.0754	-0.0752	-0.0660
Im Y_0	0.7803	0.6982	1.1160
Re Y_1	0.2202	0.2186	0.2708
Im Y_1	-0.4832	-1.2600	2.1840
Im Y_2	-0.7452	-0.6004	-0.3509
Re Y_3	-2.0200	-2.4940	-1.8500
Im Y_3	-13.3000	-29.8100	-18.7100
Im Y_4			
Re Y_5			
Im Y_6			
Im Y_6			
α_1^0	0.3557	0.3573	0.3554
α_1^1	0.2566	0.3776	0.0453
α_1^2			
α_2^0	3.4158	3.3619	3.1684
α_2^1	-3.7337	-3.7229	-3.5495
α_2^2	1.2077	1.2503	1.2409
N_{Data}	47	39	37
N_{Parm}	17	17	17
χ^2	66	37	22
χ^2/d.f.	2.2	1.7	1.1

Table 6.3b

Table 6.3 Parameters of the Jost function fits. The four significant figures are to allow an accurate reproduction of the fit. The 1, 2 for the $\pi\pi \to K\bar{K}$ data sets refer to Cohen et al [164] and Etkin et al [166] respectively.

(a) 2-pole Jost function fits,

(b) 3-pole Jost function fits.

Resonance	Poles	E_R(GeV)	g_π(GeV)	g_K(GeV)	$\lvert g_\pi/g_K \rvert$
$S_1(993)$	A,C	0.993-0.021i	0.23	0.28	0.8
$S_2(988)$	B	0.988	0.01	0.35	0.03
$\epsilon(900)$	D,E	0.905-0.37i	0.48	0.28	1.7
$\epsilon'(1420)$	G,F	1.42 -0.23i	0.56	0.09	6.2

Table 6.4 I = 0 S-wave resonances below 1.6 GeV from the global fits.

Scalar designation	Simple constituent model[90] realization	Final Dimeson State - P_1P_2		
		$\pi\pi$	$K\bar{K}$	$\eta_8\eta_8$
ϵ_1	$(u\bar{u}+d\bar{d}+s\bar{s})/\sqrt{3}$ or gg	0.87	1	-0.5
ϵ_8	$(u\bar{u}+d\bar{d}-2s\bar{s})/\sqrt{6}$	-1.73	1	-1
ϵ_{ns}	$(u\bar{u}+d\bar{d})/\sqrt{2}$	1.73	1	0.33
ϵ_s	$s\bar{s}$	0	1	-0.67

Table 6.5 Relative branching amplitudes for $S \to P_1P_2$ in SU(3) according to various idealized composition possibilities.

J^{PC}	I=1	I=0	I=½	I=0	Candidate for glue dominated states	Candidates for radial recurrences
(ideal scheme)	$V(m_0)$	$S(m_0)$	$K(m_0+\Delta)$	$S'(m_0+2\Delta)$	-	-
0^{-+}	$\pi(138)$	$\eta(550)$	K(496)	$\eta'(958)$	$\iota(1440)$	$\pi(1300), K(1400)$ $\eta(1275)$
1^{--}	$\rho(770)$	$\omega(783)$	$K^*(892)$	$\phi(1020)$		$\rho(1590), \phi(1680)$
2^{++}	$A_2(1320)$	f(1270)	K(1425)	f'(1525)	$\theta(1720)$	f(1810)
1^{++}	$A_1(1275)$ or (1056)	D(1285)	$Q_A(1270)$ $Q_B(1406)$	E(1420)		
1^{+-}	B(1235)	H(1190)				
0^{++}	$\delta(983)$	$\epsilon(900)$	$\kappa(1350)$	$S_2(988)$	$S_1(993)$	$\epsilon'(1420), S(1730)$

Table 6.6 Provisional placement of the I = 0 scalar assignments in the low-lying meson spectrum.

CHAPTER SEVEN

DICUSSION AND CONCLUSIONS

7.1 DISCUSSION

We have seen from the naive simulations in Chapter 2 that the idea of valence gluons seems to be valid. The mass spectra of glueballs and hybrids described in Section 1.3.3 are based on this valence gluon concept. We therefore use the term 'simple constituent model' to extend the concept of quark model states (cf. Section 1.2) to include systems with constituent gluons. The spectral assignments presented in Chapter Six is within the framework of this simple constituent model and soley depends on how we interpret and identify resonances in our solutions. We have already emphasized in Section 5.3 and Appendix A.III that the poles in the K- and M- matrix parametrizations are not the same as physical resonances. We have also pointed out in Section 5.3 (see also Appendix A.III) that the K- and M- matrix pole near 1 GeV is needed for the rapid structures in the region. Before this analysis the rapid structures were thought to be caused by the S* on a broad rising background (Section 4.2.1) and leads to the speculation that there is a one-to-one correspondence between the number of poles in parametrization and the number of physical resonances in amplitudes. We have proved beyond doubt that this is not the case by obtaining solutions with one, two and three poles in our parametrizations. The role of these multi K- and M- matrix poles are explained in Section 5.3. According to this

discussion we have to question the validity of the BNL resonance assignments (Section 3.3) where the three K-matrix poles are taken to be distinct physical resonances. Furthermore, if our view is correct (i.e. the BNL resonances may have been misidentified) then some of the proposed explanations for the BNL resonances (Section 3.3) would become highly speculative as they have accepted the BNL's interpretation. Indeed the $\phi\phi$ enhancement in BNL is similar to the case we study in that the situation is complicated by overlapping resonances in the region of interest. (The 3 close by K-matrix poles in the BNL analysis is an indication of rich structures). In fact that complexity in our case is greater because of the presence of the strongly coupled $K\bar{K}$ channel. This brings us back to the spectral assignments and the S* puzzle (Section 3.4.4). We have identified the $S_2(988)$ as the $K\bar{K}$ molecule on the ground that it does not have an associated pole or a mirror image. A familiar example of such situation is the $\Lambda(1405)$ pole which also sits on top of the threshold in KN and $\pi\Sigma$ scattering [221].

In connection with this is the interesting suggestion from Weinstein and Isgur [78] that a bootstrap effect would operate in the I = 0 and I = 1 $K\bar{K}$ systems. However, this idea has been invoked mainly to explain anomalous features of $\iota(1440)$ decay to $\delta\pi$ (Section 3.4.1.2).

Before returning to the S* phenomenon, one further suggestion on the interpretation of resonances is the P-matrix [222] concept of Jaffe and Low. Although motivated at the parton level (the underlying idea is that constituent model states sometimes have unphysical boundary conditions) this again involves a transmutation of the physical

scattering amplitudes at the hadron level so as to derive quantities directly comparable with constituent model states (see Appendix E). We have searched for the poles of the P-matrix with our solutions as input and the pole positions are listed in Table 7.1 for the K_1 and K_3 fits. This does not appear to clarify the dynamics in the present situation as the P-matrix poles are not similar to our resonances. However, it is interesting to note that there are two close by P-matrix poles in the 1 GeV region indicating perhaps some rich structure.

7.2 THE S* PHENOMENON

We have, by considering a number of reactions leading to $\pi\pi$ and $K\bar{K}$ final states, performed a new amplitude analysis of I = 0 scalar dimeson production from $\pi\pi$ threshold to beyond 1.6 GeV. The resonance spectrum that emerges comprises two broad objects $\varepsilon(900)$ and $\varepsilon'(1420)$ similar to those found in previous analyses and <u>two</u> narrow resonances $S_1(993)$ and $S_2(988)$ corresponding to the S* phenomenon. Attributing the S* effect to two resonances rather than, as previously, to single object is the principal novelty of our solution. As discussed in Chapter Six, the $S_1(993)$ forms a very plausible candidate for the long sought ground state scalar glueball which we will discuss in more detail later. The $S_2(988)$ which we assign as the $s\bar{s}$ ground state is an almost stable particle with very tiny width (though the coupling to $\pi\pi$ that we find for this pole is very small, corresponding to a width of some 10 keV, a determination of its exact width would require much more precise data) therefore can only cause local effects in the amplitudes. Its effect on

the phase shift would therefore not be noticable in experimental data because of binning. Consequently, the previous explanation for the classic S* phenomenon in which a narrow resonance sits on top of a rising background is in some sense still valid. This time the narrow resonance is not the classic S*(975) quoted in the latest PDG [169] but is the $S_1(993)$ scalar glueball. The rising background is provided by the broad $\varepsilon(900)$ and $\varepsilon'(1420)$. In making these identifications for the background, we have in effect married two of the scenarios for the S* discussed in Section 3.4.4, i.e. the background is either comprised of a very broad $\varepsilon(1300)$ or a broad S-matrix pole ε at 700 MeV. This is in a way rather satisfactory because the two scenarios were obtained from analysing subsets of our data and that they are contained in our solutions is an expected consequence rather than a surprise. Furthermore, our extensive investigation of the dynamics in the S* region using the Jost function in Section 6.1.1 has revealed that among the present input, it is predominantly the new DPE data on $\mathbb{P}\mathbb{P} \to \pi\pi$, $K\bar{K}$ and its interplay with traditional $\pi\pi$ processes that require the additonal B pole, the $S_2(988)$. This $S_1(993)$ has been mistaken as the $s\bar{s}$ $S_2(988)$ in all the previous analyses because they did not have the necessary constraints provided by the AFS data (see Chapter 4 for our formalism). We now consider the nature of $S_2(988)$ in more details.

7.3 THE $S_2(988)$ AS A $K\bar{K}$ MOLECULE

We have already explained the ideas behind our spectral assignment of the $S_2(988)$ in Chapter Six. Here we summarize the phenomenological implications of such assignment. We have mentioned earlier the idea of Weinstein and Isgur (explained in Section 3.4.1.2) that there is a $K\bar{K}$ residual interaction, $V_{K\bar{K}}$, binding the $K\bar{K}$ together to form a molecule. Furthermore, their idea is based on the study of the stability of four-quark bound states which turns out that they only exist as light $K\bar{K}$ bound states [78]. This immediately brings to mind the S* puzzle (Section 3.4.4) in which the old classic S* is singled out as the most probable four-quark bound state or a $K\bar{K}$ molecule. In fact it is rather difficult to say whether the parton content of a $K\bar{K}$ molecule is $s\bar{s}$ or $s\bar{s}s\bar{s}$ as we do not have a reliable scheme to distinguish such different types of resonances (see Ref. 219 for a useful discussion). Our $s\bar{s}$ assignment of the $S_2(988)$ is based on the simple quark model in which S_2 is taken as the ideally mixed partner of the non-strange $\varepsilon(900)$ because of its coupling ratio (Section 6.2.1). It is the lack of a mirror pole image that qualifies S_2 as a $K\bar{K}$ molecule. Having identified the two isoscalars required by the simple quark model, we are left with the $S_1(993)$ which is identified as the scalar glueball (a SU(3) singlet) because of its couplings. We next elaborate on this important finding of our analysis.

7.4 THE $S_1(993)$ AS THE GROUND STATE SCALAR GLUEBALL

As we have stressed, the $S_1(993)$ offers a potential solution to an outstanding problem of spectroscopy - the identity of the hypothesized scalar glueball. For this, the $S_1(993)$ forms a very plausible candidate. Of course (as discussed in Section 6.2.1), further experimental evidence is needed to confirm this assignment. If the $S_1(993)$ does prove to be the lowest mass glueball, not only will this vindicate the prediction of bag modellers, gluon condensate calculations and lattice computers of the pure gauge sector, but will serve as a calibration fixing the crucial missing parameter needed to normalize their whole glueball spectrum (see Section 1.3). We consider below how the gluonium identification of $S_1(993)$ compares with other gluonium candidates discussed in Chapter 3.

As mentioned in Chapter 3, hard gluon channels like the radiative J/ψ decays and DPE processes are thought to be ideal for gluonium production because according to the OZI rule (Section 3.2.4) only gluon rich states occur as resonances in these OZI forbidden channels. Such is the prime motivation for the AFS experiment in which the DPE mechanism is presumed to favour glueball production. If $S_1(993)$ is indeed a glueball, the $\mathbb{P}\,\mathbb{P}$ couplings that we find (Table 6.2 end column), provide no support for this notion. This may be a problem for OZI systematists but does not detract from DPE as an exploratory tool. The empirical OZI rule may even be inconsistent with unitarity (cf. Eqn. 3.5). We have ignored any intrinsic difference between gluon and quark channels in our

formalism (Chapter 4) as they will automatically show up in their respective couplings. Furthermore, we believe that so tight is the relationship required by unitarity on the $\pi\pi$ and $K\bar{K}$ final state interactions (Eqn. 4.14-15) that there is nothing new which has not been seen in the classic $\pi\pi$ data. Though the high statistics AFS data do not provide scope for new effects (contrary to the belief of the OZI systematists), they can supplement the classic meson-meson scattering results. Our philosophy is amply verified by the $I\!P\,I\!P$ coupling listed in Table 6.2 [Figure 5.11]. The glueball identification of $S_1(993)$ is solely based on the couplings obtained from our global analysis subject to unitarity constraints. This is the only justificable way of indentifying resonances in multi-channel situations and not by looking for peaks in cross-sections. As explained in Chapter 4, final state interactions can distort the appearance of a resonance and we could be misguided by the shape of its cross-section. The fundamental difference between our $S_1(993)$ and the g_Ts, $\iota(1440)$ and $\theta(1690)$ glueball candidates (Chapter 3) is the way in which they are identified. The $S_1(993)$ is an ideal SU(3) singlet and there is no need to invoke flavour symmetry breaking schemes to justify its gluonium status as has been done for other glueball candidates (cf. Section 3.4.1.1).

While we are still on the subject of couplings, let us consider the $\gamma\gamma$ coupling of S_1 obtained from fitting $\gamma\gamma \rightarrow \pi\pi$ (Figure 5.22). Glueballs are usually thought to have suppressed photon couplings (Section 3.2.2) but these can be changed either through mixing (Section 3.4.1.4) or anomalous couplings (Section 3.2.2 and

3.4.4). Since we have already assigned the S_2 and ε as the ideally mixed partners there is no scope for mixing between the gluonium S_1 and the S_2 and ε quark mesons. It is interesting to note that the deviation from ideal mixing in the 0^- channel could be understood in terms of mixing through the axial anomaly (Section 3.4.1.4(III)). In the scalar channel, there is the trace anomaly [Eqn. 1.24] which in principle can induce a mixing of this kind but this does not seem to happen in our spectrum. If our assignments are correct then it would be a problem for those who advocate the Effective Lagrangian (Section 1.3.2) approach in which such mixing is inevitable (Section 3.4.1.5 and 3.4.2.8(II)). Furthermore, the deviation from ideal mixing in the pseudoscalar channel would be more difficult to understand as the anomaly mixing idea could not be generalized to the scalar channel. Nevertheless, the scalar glueball can acquire a substantial $\gamma\gamma$ coupling through the trace anomaly (see Section 3.2.2 and Ref. 22). The rise of the $\gamma\gamma$ coupling in Figure 5.22 seems to suggest this is indeed what happens. Naively, one would expect the curves of the $\gamma\gamma$ and $\mathbb{P}\,\mathbb{P}$ couplings [Figures 5.11,5.22] to be very similar as is suggested by the similarity of their mechanisms, Figure 5.1. The trace anomaly therefore seems only to enhance the $\gamma\gamma$ coupling of the scalar glueball $S_1(993)$ and not to induce mixing. However, as we remarked in Section 5.4.2, the present $\gamma\gamma \rightarrow \pi\pi$ data do not agree with each other so the argument presented here is just a speculation. Finally, our $S_1(993)$ does not suffer, like other gluonium candidates, from being possibly a radial excitation, some kind of giant resonance state or hybrid (See Chapter 3 for examples). It is simply

too light for all of these. Furthermore, as explained in Section 3.4.1.2, the lightest four-quark bound state is believed to appear in the form of a $K\bar{K}$ molecule. The $S_1(993)$ is clearly not a four-quark bound state. The $S_1(993)$ in our solution is therefore a very strong candidate for the ground state scalar glueball. As remarked earlier, the $S_1(993)$ has previously been misidentified as a $q\bar{q}$ state, the S*(975), leading to speculations that the ground state glueball would either be very narrow or very broad (see Section 3.4.4). We now understand why it has been missing for so long! The hidden glueball scenario advocated in Ref. 137 turns out to be our $S_2(988)$ - a $K\bar{K}$ molecule.

7.5 CONCLUSIONS

As we explained, the novel features of our amplitude are the presence of two narrow resonances $S_1(993)$ and $S_2(988)$. The discovery of the extra $S_2(988)$ has freed the $S_1(993)$, which used to be known as the S*, to be identified as a plausible candidate for the ground state glueball. The additional B pole of S_2 is predominantly required by the consistency of the AFS data with the classic meson scattering reactions (cf. Chapter 6). As we discussed, much more direct signatures of the extra resonance would show in various reactions producing $K\bar{K}$ final state if only the precision were sufficient. Even with existing data, $\pi\pi \to K\bar{K}$ information are an important ingredient to our fit and, as mentioned, very significant discrepancies remain among the published results, notably regarding the relative phase of the $\pi\pi \to K\bar{K}$ amplitude below

1200 MeV. Our overall solution, which fits the highly structured $\mathbb{P}\mathbb{P} \to \pi\pi$ information so well, disfavours the flat phase alternative for $\mathfrak{Y}(\pi\pi \to K\bar{K})$. Only experiment can decide which is correct. Unfortunately, the large effort needed to repeat existing experiments is unlikely to be forthcoming quickly. In the short term, resources would probably be better directed to studying new reactions like $K^-p \to \Lambda(\Sigma)K^0_S K^0_S$ or in accumulating better statistics on $\mathbb{P}\mathbb{P} \to K\bar{K}$.

We have seen from our analysis the power of the DPE approach to meson spectroscopy. The AFS experiment has provided us invaluable data on the DPE processes. An unanticipated benefit of the DPE approach to meson production is its emphasis on low partial waves in contrast to traditional OPE reactions like $\pi N \to \pi\pi N$ in which the higher waves dominate (eg. the ρ). It is to be hoped that more and better data of this kind will come from the SPS and/or Tevatron colliders in the future.

Other 'production reactions' (in our terminology this includes various heavy flavour decays) are beginning to provide useful information on scalar final states. At present, the data are restricted both statistically and in the mass range explored and partial wave separation is usually lacking. It was not therefore appropriate to proceed as we did with the AFS results and let the production data help select the strong interaction amplitudes. Instead, we merely sought to demonstrate consistency, only allowing the characteristic reaction couplings ($\alpha^{(c)}$ of Eqn. 4.22 above) to vary. The reactions we have studied are, $\gamma\gamma \to \pi\pi$, $\psi' \to J/\psi\pi\pi$, $\Upsilon'(\Upsilon'') \to \Upsilon\pi\pi$ and $J/\psi \to \phi\pi\pi$.

Information on this latter process and its companion decay $J/\psi \rightarrow \phi K\bar{K}$ will shortly be greatly enhanced. It may then be appropriate to emulate the treatment of the AFS data and I hope this can be done in the near future.

For the higher mass range that we explore, information is needed on other coupled channels like 4π and $\eta\eta$. The latter has been quite extensively explored in a recent experiment at CERN [171]. According to the accompaning (somewhat restricted) amplitude analysis, the partial wave structure is very different from that reported in this thesis, in particular the S-wave cross-section peaks at 1200 and 1600 MeV with a sharp dip in-between. The difference of this spectrum from that found for $\pi\pi$ and $K\bar{K}$ final states, although formally possible, seems unlikely and merits further investigation.

I have reported in this thesis the complex features of our global fits (namely the 7 $\mathcal{K}$-matrix poles for 4 resonances), and have gone to some length to justify the number of $\mathcal{K}$-matrix poles required and explain our resonance assignments. Another way of identifying resonances in this complicated situation, which arrives at the same conclusions, is the 'λ-tracking' method of David Morgan presented in Ref. 219. Finally, our extensive analysis does reveal definite evidence for dynamics beyond the naive quark model with three states in the 1 GeV region. This richness may prove a key signature of non-perturbative QCD.

7.6 Table

K_1	K_3
0.648	0.638
0.993	0.997
1.069	1.063
1.295	1.297
1.629	1.655

Table 7.1 Poles (in units of GeV) of the P-matrix (see Ref. 222 and Appendix E) for the K_1 and K_3 solutions.

APPENDIX A

K- and M- matrix formalism

The idea of these formalisms is to express the constraints implied by coupled channel unitarity in a transparent way. The M-matrix formalism is first introduced in A.I as a trivial generalization of fulfilling single channel unitarity. The conversion to the K-matrix formalism is explained in A.II. The details of our parametrizations are given in A.III and A.IV. In A.V we discuss a simplified version of the three channel formalism. The last Section A.VI deals with the derivations of couplings.

A.I Introduction to the M-matrix formalism

Recall the Eqn. 4.6 for the single channel $\pi\pi \to \pi\pi$ amplitude $\mathcal{T}_{11}$ can be expressed in terms of a real function M_{11} $(= 1/K_{11})$ as in Eqn. 4.28, i.e.

$$\mathcal{T}_{11} = \frac{1}{\rho_1(\cot\delta - i)} = \frac{1}{M_{11} - i\rho_1} \qquad (A.1)$$

where ρ_1 is the threshold factor introduced in Section 4.2. These equivalent expressions for $\mathcal{T}_{11}$ obviously satisfy the single channel elastic unitarity constraint $\text{Im}\,\mathcal{T}_{11} = \rho_1|\mathcal{T}_{11}|^2$. The discontinuity in $\mathcal{T}_{11}$ implied by this relation for $s > 4m_1^2$ is explicitly exhibited in the ρ_1 factor in Eqn. A.1 with M_{11} a real analytic function of s. We next generalise Eqn. A.1 to the coupled channel case. For the two channels 1

and 2 (eg. $\pi\pi$ and $K\bar{K}$) there are two threshold factors ρ_1 and ρ_2, $\rho_i = \sqrt{(1 - 4m_i^2/s)}$. We do not concern ourselves with the distinction between charged (i.e. K^+K^-) and neutral (i.e. K^0K^0) channels for the moment. Though the M_{11} in Eqn. A.1 has no cut at channel 1 threshold, it must have a discontinuity corresponding to channel 2 which because of cut plane analyticity will occur through explicit factors of ρ_2. To exhibit these right hand cut structures in $\mathfrak{J}_{11}$ we need to express $\mathfrak{J}_{11}$ in terms of real functions of s, ρ_1 and ρ_2. This can be achieved by re-parametrizing the single channel case by

$$\mathfrak{J}_{11} = \frac{D_{11}(s)}{N_{11}(s) - i\rho_1 D_{11}(s)} \qquad (A.2)$$

and generalising this to the two channel situation by

$$\mathfrak{J}_{11} = \frac{D_{11}(s,\rho_2)}{N_{11}(s,\rho_2) - i\rho_1 D_{11}(s,\rho_2)} \qquad (A.3)$$

We can further expand D_{11} and N_{11} as:

$$D_{11}(s,\rho_2) = a(s) + i\rho_2 b(s)$$

$$N_{11}(s,\rho_2) = c(s) + i\rho_2 d(s)$$

where a, b, c and d are real functions of s, since below channel 2 threshold $i\rho_2$ is real and so N_{11}, D_{11} are. Eqn. A.3 then becomes

$$\mathfrak{J}_{11} = \frac{a(s) + i\rho_2 b(s)}{c(s) + i\rho_2 d(s) - i\rho_1 a(s) + \rho_1\rho_2 b(s)} \qquad (A.4)$$

Now let's examine what happens in each energy regime. When $s < 4m_1^2$, the $\mathfrak{J}_{ij}$ are real having no discontinuities. There the $\rho_{1,2}$ are

imaginary, and $\mathcal{J}_{11}$ guaranteed real provided a, b, c and d are all real functions.

When $4m_1^2 < s < 4m_2^2$, elastic unitarity requires Im $\mathcal{J}_{11} = \rho_1 |\mathcal{J}_{11}|^2$. This is assured by the form Eqn. A.3. Of the four real functions a, b, c, d, one is arbitrary since we can clearly divide the numerator and denominator of Eqn. A.4 by any real function. It is now convenient to express Eqn. A.4 in terms of three other real functions M_{ij} (i,j = 1,2) defined by:

$$M_{11} = \frac{d}{b}$$

$$M_{12} = M_{21} = \frac{\sqrt{bc - ad}}{b}$$

$$M_{22} = \frac{-a}{b} \qquad \text{(A.5)}$$

We then have

$$\mathcal{J}_{11} = \frac{M_{22} - i\rho_2}{(M_{11} - i\rho_1)(M_{22} - i\rho_2) - M_{12}^2} \qquad \text{(A.6)}$$

Because of the symmetry property of the labels 1 and 2, we can immediately write down $\mathcal{J}_{22}$, i.e.

$$\mathcal{J}_{22} = \frac{M_{11} - i\rho_1}{(M_{11} - i\rho_1)(M_{22} - i\rho_2) - M_{12}^2} \qquad \text{(A.7)}$$

To obtain a similar expression for $\mathcal{J}_{12}$ we consider the energy region of $s > 4m_2^2$, where ρ_1 and ρ_2 are real. The coupled channel unitarity then [Eqn. 4.14] requires that

$$\text{Im}\, \mathcal{J}_{11} = \rho_1 |\mathcal{J}_{11}|^2 + \rho_2 |\mathcal{J}_{12}|^2 \qquad \text{(A.8)}$$

and $$\text{Im}\, \mathcal{J}_{12} = \rho_1 \mathcal{J}^*_{11} \mathcal{J}_{12} + \rho_2 \mathcal{J}^*_{12} \mathcal{J}_{22} \qquad \text{(A.9)}$$

Substituting Eqns. A.6-7 into Eqns. A.8-9 we obtain

$$\mathcal{J}_{21} = \mathcal{J}_{12} = \frac{-M_{12}}{(M_{11} - i\rho_1)(M_{22} - i\rho_2) - M_{12}^2} \qquad \text{(A.10)}$$

Note that the sign in front of M_{12} is ambiguous because of the non-linearity of Eqn.A8 and the linearity of Eqn.A9. We have chosen the negative sign as our convention. All the unitarity constraints in Eqn. 4.14 are trivially satisfied with the forms of $\mathcal{J}_{ij}$ given in Eqns. A.6-7 and Eqn. A.10. Furthermore, all the $\mathcal{J}_{ij}$ elements have the same denominator as required by unitarity. Summarizing the Eqns. A.6-7 and Eqn. A.10 in matrix form we have the M-matrix formalism,

$$\underset{\sim}{\mathcal{J}} = [\underset{\sim}{M} - i\underset{\sim}{\rho}]^{-1}$$

Here, $\underset{\sim}{\rho}$ is the diagonal matix with diagonal elements ρ_1 , ρ_2 . $\underset{\sim}{M}$ is a real symmetrix matrix with elements M_{ij} , i = 1,2.

A.II The K-matrix formalism

From Eqn. 4.28 or Eqn. A.1 we have for single channel

$$\mathcal{J}_{11} = \frac{1}{\frac{1}{K_{11}} - i\rho_1} \qquad \text{(A.11)}$$

which suggests that we can express $\mathcal{J}_{11}$ as a function of M_{11} or its inverse $1/K_{11}$ and vice versa. Instead of going through all the previous procedures in A.I we immediately write down the K-matrix formalism for coupled channel with $\underset{\sim}{K} = \underset{\sim}{M}^{-1}$;

and show how the K- and M- matrix formalism are related.

In terms of the K-matrix elements

$$\mathcal{T}_{11} = \frac{K_{11} - i\rho_2(K_{11}K_{22} - K_{12}^2)}{Den} \qquad (A.12)$$

$$\mathcal{T}_{12} = \frac{K_{12}}{Den} \qquad (A.13)$$

$$\mathcal{T}_{22} = \frac{K_{22} - i\rho_1(K_{11}K_{22} - K_{12}^2)}{Den} \qquad (A.14)$$

where $Den = 1 - i\rho_1 K_{11} - i\rho_2 K_{22} - \rho_1\rho_2[K_{11}K_{22} - K_{12}^2]$ is the common denominator. Equating Eqns A.6-7 and Eqn A.10 with Eqns. A.12-14 we obtain the following equalities between the K- and M- matrix elements;

$$M_{11} = \frac{K_{22}}{\det K}$$

$$M_{12} = \frac{-K_{12}}{\det K}$$

$$M_{22} = \frac{K_{11}}{\det K} \qquad (A.15)$$

with $\det K = K_{11}K_{22} - K_{12}^2$. The K-matrix formalism obviously satisfies the coupled channel unitarity constraints of Eqn. 4.14. We next consider the K-matrix parametrization in more details.

A.III More on the K-matrix formalism

As discussed in Section 4.2.1 a simple Breit-Wigner resonance with mass E_R has a 90^0 phase shift, i.e. $\delta = 90^0$, on resonance.

For a single channel

$$\rho_1 \mathcal{T}_{11} = \frac{1}{(1/\rho_1 K_{11}) - i} = \frac{1}{\cot\delta - i} \qquad (A.16)$$

therefore K_{11} must have a pole at $s = E_R^2$ because cot $(\pi/2)$ is zero at the resonance. This is the reason why the positions of the K-matrix poles are sometimes interpreted as resonances. However, this is only true when the resonance occurs with no nearby resonance or threshold. The S^* is the best known example in which the phase shift δ reaches $\pi/2$ at a position which cannot be identified with that of the resonance because of a rising background (cf. Sections 3.4.4 and 4.2.1).

To illustrate the complications arising in the coupled channel case we consider $\mathcal{T}_{11}$ as an example. For $4m_1^2 < s < 4m_2^2$, ρ_1 is real and ρ_2 is imaginary or $\rho_2 = i|\rho_2|$. From Eqn. A.12 we have

$$\rho_1 \mathcal{T}_{11} = \frac{1}{\left(\dfrac{1 + |\rho_2| K_{22}}{\rho_1 K_{11} + \rho_1 |\rho_2| \det K}\right) - i} = \frac{1}{\cot\delta - i} \qquad (A.17)$$

This time cot δ does not necessary go to zero at the position of K-matrix pole. This scheme of identifying resonance becomes more complicate if the resonance occurs above the $K\bar{K}$ threshold with ρ_1 and ρ_2 both real. As is well-known the proper process-independent criterion is to identify the masses and widths of resonances with the complex positions of the poles of the $\mathcal{T}$(or S)- matrix. To be more precise, we rewrite Eqn. 4.7 for a simple Breit-Wigner resonance as

$$\rho \mathcal{T} = \frac{E_R \Gamma}{E_R^2 - s - iE_R \Gamma}$$

The zero of $\mathcal{D}$ occurs at $s = E_R^2 - iE_R\Gamma$. Since we have seen in A.I that all $\mathcal{T}_{ij}$ elements in the coupled channel $\mathcal{T}$-matrix have the same denominator, the poles of the $\mathcal{T}$-matrix are universal as resonances ought to be.

A.IV Parametrizations

Here we describe first the K-matrix parametrization given in Eqn. 4.33 and then explain how one goes from the K-matrix to the M-matrix parametrization. Since the phase shift rises sharply near a resonance (see Section 4.2.1) or an openning of a new threshold, it is helpful in fitting data to introduce a pole in the K-matrix to generate such structure. This pole of course does not necessary correspond to any physical entity. Indeed, the number of K-matrix poles is not necessarily the same as the number of physical resonances as discussed in Section 5.3 where we perform one- and three- pole fits and obtain the same resonance structures. Here we only address the technicalities of the parametrizations.

To illustrate the essential ingredients of the K-matrix parametrization we rewrite Eqn. 4.33 in a simplified form with only one K-matrix pole,

$$K_{ij} = (s - s_0)\left[P_{ij} + \frac{f_i f_j}{(s_1 - s)(s_1 - s_0)}\right] \qquad (A.18)$$

where s_0 is the Adler zero [157] and s_1 is the position of the K-matrix pole. The P_{ij} polynomials characterise 'backgrounds' and are smooth

functions of s. The form of Eqn. 4.29 suggests that the Adler zero of the $\mathcal{T}$-matrix can be parametrized by a simply factor $(s - s_0)$ in the K-matrix. The extra factor $(s - s_0)$ in the denominator of the pole term is to ensure that the coefficients are the same as the residues at the pole, i.e. $s = s_1$.

From Eqns A.12-14 we observe that the determinant of the K-matrix (det $\underset{\sim}{K}$) appears in both the numerators and denominators of the $\mathcal{T}$-matrix elements. Since det $\underset{\sim}{K}$ is quadratic it therefore contains products of the pole terms, i.e. double poles. To achieve the cancellation of the double poles we demand the pole terms in Eqn. A.18 be factorizable (i.e. with the coefficients (or residues) given in Eqn. 4.33 or Eqn. A.18). The double pole cancellation goes as follows:

$$K_{11}K_{22} = (s - s_0)^2\left[P_{11}P_{22} + P_{11}\frac{f_2f_2}{(s_1 - s)(s_1 - s_0)} + P_{22}\frac{f_1f_1}{(s_1 - s)(s_1 - s_0)} + \frac{f_1^2f_2^2}{(s_1 - s)^2(s_1 - s_0)^2}\right]$$

$$K_{12}^2 = (s - s_0)^2\left[P_{12}^2 + 2P_{12}\frac{f_1f_2}{(s_1 - s)(s_1 - s_0)} + \frac{f_1^2f_2^2}{(s_1 - s)^2(s_1 - s_0)^2}\right]$$

and the double pole term disappears in det $\underset{\sim}{K}$. The essence of the cancellation lies in the factorizability of the pole and the generalization of the cancellation to K-matrix with multi-poles are most straight forward. Of course, terms like $1/(s_1 - s)(s_2 - s)$ etc do not count as double poles.

Having explained the philosophy behind the K-matrix parametrization, we now explain how the form of the K- and M- matrix parametrizations given in Eqns. 4.33,35, are related. Since $\underset{\sim}{M} = \underset{\sim}{K}^{-1}$ this implies that

$$\underset{\sim}{M} = \frac{1}{\det \underset{\sim}{K}} \begin{bmatrix} K_{22} & -K_{12} \\ -K_{21} & K_{11} \end{bmatrix}$$

As the det $\underset{\sim}{K}$ is quadratic and contains the factor $(s - s_0)^2$, the M-matrix elements must have a pole to account for the Adler zero of the $\mathcal{T}$-matrix. Furthermore, if det K = 0 then one also needs to introduce an extra pole in the M-matrix parametrization. Apart from these, the M-matrix elements can have as many poles as there are in the K-matrix elements. Again, we simplify the parametrization of Eqn. 4.35 to illustrate its essence;

$$M_{ij} = \frac{a_{ij}}{s - s_0} + \left[P'_{ij} + \frac{f'_i f'_j}{s_1 - s} \right] \qquad (A.19)$$

This time there is no need for a $(s - s_0)$ factor in the denominator of the $(s_1 - s)$ pole term as the coefficients are guaranteed to be the residues of the poles. The M-matrix poles are given in factorizable forms hence there will be no double poles in the $\mathcal{T}$-matrix elements. From Eqns. A.6-7 and Eqn. A.10 we see that there is no double counting for the Adler zero pole term as well.

A.V Three channel -> Two channel formalism

Recall in Section 4.2.2, Eqn, 4.13, we have introduced an averaged $\rho_2 = (1/2)(\rho_2^n + \rho_2^c)$. The reason for this is to separate the Etkin

$\pi\pi \rightarrow K^0K^0$ [166] ($\rho_2 = \rho_2^n$), Cohen $\pi\pi \rightarrow K^+K^-$ [164] ($\rho_2 = \rho_2^c$) and AFS $I\!P\,I\!P \rightarrow K^+K^-$ ($\rho_2 = \rho_2^c$) from the rest of the data [158][159][161][162] (with the averaged ρ_2). We have only done this for the $K\bar{K}$ channel because we know from experiment [Figure 5.7] that the $K\bar{K}$ channel has a strong coupling in $\pi\pi$ scattering. Data in the $K\bar{K}$ threshold region may therefore be sensitive to the small mass difference between the K^+K^- and K^0K^0. The separation of K^+K^- and K^0K^0 are fine tuning exercises and the results reported in Chapters Five and Six are not very different from our previous analysis [144] in which we used the effective kaon mass $4m_2^2 = 0.98277\ GeV^2$ in ρ_2 .

In carrying out the separation of the K^+K^- and K^0K^0 channel we have in effect performed a simplified 3 coupled channel $\pi\pi$, K^+K^-, K^0K^0 analysis. To illustrate the connection between the simplified 3 coupled channel and coupled channel formalism, we consider the K-matrix formalism as an example, in particular $\mathcal{J}_{11}$.

Putting the averaged ρ_2 into Eqn. A.12 we get in the coupled channel case,

$$\mathcal{J}_{11} = \frac{K_{11} - i0.5(\rho_2^c+\rho_2^n)(K_{11}K_{22}-K_{12}^2)}{1-i\rho_1 K_{11} - i0.5(\rho_2^c+\rho_2^n)K_{22} - \rho_1 0.5(\rho_2^c+\rho_2^n)(K_{11}K_{22}-K_{12}^2)} \qquad (A.20)$$

To obtain $\mathcal{J}_{11}$ in the 3 coupled channel we denote $\pi\pi$, K^+K^- and $K^0\bar{K}^0$ by 1, 2 and 3 respectively; and use the letter L for the 3x3 K-matrix while keeping the symbol K for the 2x2 K-matrix. The three coupled channel amplitudes (denoted by $\mathcal{J}'$) is given by

$$\underset{\sim}{\mathcal{J}}' = \underset{\sim}{L}\,(\underset{\sim}{I} - i\underset{\sim}{\rho}\cdot\underset{\sim}{L})^{-1}$$

where the diagonal matrix $\underset{\sim}{\rho}$ has elements ρ_1 , ρ_2^c and ρ_2^n . Based on the assumption that the K^+K^- and K^0K^0 channels are identical dynamically, apart from the difference in their thresholds, is accounted for by ρ_2^c and ρ_2^n , making the following identifications

$$L_{13} = L_{12} \quad ; \quad L_{23} = L_{22} \quad \text{and} \quad L_{33} = L_{22}$$

We then have for $\mathcal{J}'_{11}$

$$\mathcal{J}'_{11} = \frac{L_{11} - i(\rho_2^c+\rho_2^n)(L_{11}L_{22}-L_{12}^2)}{1-i\rho_1 L_{11} - i(\rho_2^c+\rho_2^n)L_{22} - \rho_1(\rho_2^c+\rho_2^n)(L_{11}L_{22}-L_{12}^2)} \qquad \text{(A.21)}$$

To connect the 3 and 2 coupled channel K-matrix formalism we equate Eqns. A.20 and A.21 to obtain the following identities;

$$L_{11} = K_{11} \quad , \quad L_{12} = (1/\sqrt{2})K_{12} \quad , \quad L_{22} = (1/2)K_{22}$$

i.e. $$L_{11}L_{22} - L_{12} = (1/2)\det \underset{\sim}{K}$$

Hence by making the separation of ρ_2^c and ρ_2^n we have performed a simplified 3 coupled channel analysis.

We need to make sure that after separating ρ_2^c and ρ_2^n , the $\mathcal{J}$-matrix amplitudes in the coupled channel formalism still satisfy unitarity. The region where unitarity may be violated is $4m^2_{K^+} < s < 4m^2_{K^0}$ i.e. ρ_2^c is real and ρ_2^n is imaginary. We again use the $\pi\pi \to \pi\pi$ channel as an example. In the 3 coupled channel formalism, the unitarity equation for $\pi\pi \to \pi\pi$ in the region of $4m^2_{K^+} < s < 4m^2_{K^0}$ is simply

$$\text{Im}\,\mathcal{J}'_{11} = \rho_1|\mathcal{J}'_{11}|^2 + \rho_2^c|\mathcal{J}'_{12}|^2 \qquad \text{(A.22)}$$

with $$\mathcal{J}'_{12} = \frac{L_{12}}{1-i\rho_1 L_{11} - i(\rho_2^c+\rho_2^n)L_{22} - \rho_1(\rho_2^c+\rho_2^n)(L_{11}L_{22}-L_{12}^2)}$$

In terms of the coupled channel Eqn. A.22 becomes

$$\text{Im } \mathfrak{J}_{11} = \rho_1 |\mathfrak{J}_{11}|^2 + \rho_2^c |(1/\sqrt{2})\mathfrak{J}_{12}|^2$$
$$= \rho_1 |\mathfrak{J}_{11}|^2 + 0.5\rho_2^c |\mathfrak{J}_{12}|^2 \qquad \text{(A.23)}$$

where the $1/\sqrt{2}$ factor comes from $L_{12} = (1/\sqrt{2})K_{12}$. Putting $\rho_2^n = i|\rho_2^n|$ in Eqn. A.20 one obtains the following equality;

The numerator of $(\text{Im } \mathfrak{J}_{11} - \rho_1 |\mathfrak{J}_{11}|^2) = -0.5\rho_2^c \det K + 0.5\rho_2^c K_{11}K_{22}$

$$= 0.5\rho_2^c K_{12}^2$$

Hence the coupled channel K-matrix formalism still satisfies the necessary unitarity conditions after the separation of ρ_2^c and ρ_2^n in ρ_2. As a final comment, the converstion of all the K-matrix formalism in this section to the M-matrix formalism is straight forward with the help of Eqn. A.15.

A.VI Couplings and Pole Searchings

In Section 6.1 we use the idea of a k_2-plane to separate the sheet structures of the complex energy plane. For a single channel there is only one threshold factor ρ_1 which gives rise to two energy sheets I and II, see Figure A.1. For two channels there are two threshold factors ρ_1 and ρ_2 which then give rise to four energy sheets I, II, III and IV, see Figure A.2.

In defining the sheet structures we have used the effective masses for the pions and kaons in ρ_1 and ρ_2 to avoid introducing extra sheet strucutres (which would not lead to any new physics not already included in the k_2-plane, Figure 6.2a). Sheet I is known as the physical sheet

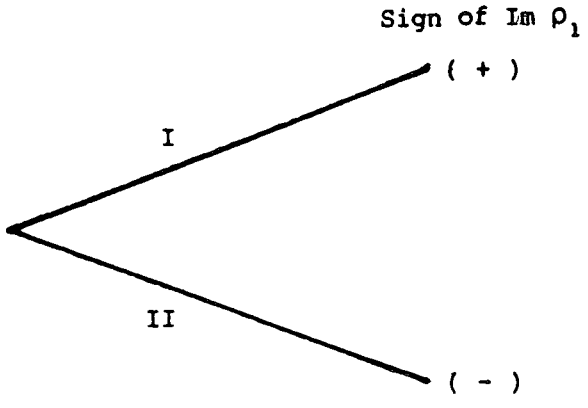

Figure A.1 Sheet structures for single channel.

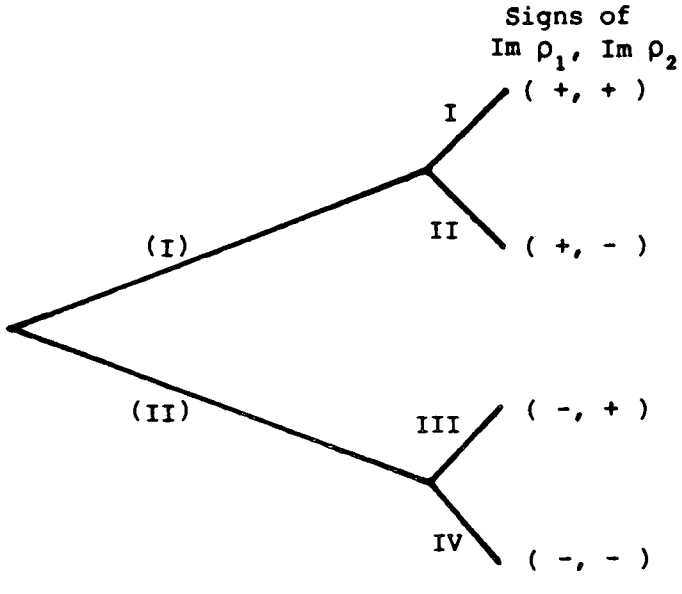

Figure A.2 Sheet structures for two channels (single channel in brackets).

because it contains the real energy axis below the branch point (cf. Section 4.2.3) and does not have poles. The poles on the unphysical sheets are found by searching the zeros of the common denominator of the $\mathcal{J}$-matrix with the appropriate signs of Im ρ_1 and Im ρ_2. The pole positions reported in Chapter Six were obtained in this fashion.

Finally, we come to the couplings or residues, γ, of the poles in our $\mathcal{J}$-matrix amplitudes. In the proximity of poles, s_R, the $\mathcal{J}_{ij}$ elements can be written as

$$\mathcal{J}_{ij} = \frac{\gamma_i \gamma_j}{s_R - s}$$

$$\gamma_i \gamma_j = \lim_{s \to s_R} (s_R - s)\mathcal{J}_{ij} \qquad \text{(A.24)}$$

To obtain $\gamma_i\gamma_j$ we need analytic expressions for $\lim_{s \to s_R} (s_R - s)\,\mathcal{J}_{ij}$. Since the denominator, Den (cf. Eqns. A.12-14), of the $\mathcal{J}_{ij}$ elements vanishes at the pole position s_R, we can expand Den in a Talyor series about $s = s_R$, i.e.

$$\text{Den}(s) = (s - s_R)\text{Den}^1(s) + (1/2)(s - s_R)^2\text{Den}^2(s) + \ldots\ldots \qquad \text{(A.25)}$$

where $\text{Den}^n(s) = \frac{\partial^n}{\partial s^n}\text{Den}(s)$. Substituting Eqn. A.25 into Eqn. A.24 one obtains for the K-matrix formalism the following expressions;

$$\gamma_1^2 = \frac{-K_{11} + i\rho_2(K_{11}K_{22} - K_{12}^2)}{\text{Den}^1(s)}$$

$$\gamma_1\gamma_2 = \frac{-K_{12}}{\text{Den}^1(s)}$$

$$\gamma_2^2 = \frac{-K_{22} + i\rho_1(K_{11}K_{22} - K_{12}^2)}{\text{Den}^1(s)}$$

The effective kaon mass $4m_K^2 = 0.98277$ is used in ρ_2 for consistency (same as the ρ_2 in pole searching).

In the case of the M-matrix formalism we get

$$\gamma_1^2 = \frac{-M_{22} + i\rho_2}{\Delta^1(s)}$$

$$\gamma_1\gamma_2 = \frac{M_{12}}{\Delta^1(s)}$$

$$\gamma_2^2 = \frac{-M_{11} + i\rho_1}{\Delta^1(s)}$$

where $\Delta(s) = (M_{11} - i\rho_1)(M_{22} - i\rho_2) - M_{12}^2$

and $\Delta^1(s) = \frac{\partial}{\partial s}\Delta(s)$.

APPENDIX B

The $\mathfrak{I}_{12}$ amplitude

In this short appendix we derive the expression for $\mathfrak{I}_{12}$, Eqn. 5.2, from the first principle. The expression for $\mathfrak{I}_{11}$, Eqn. 5.1, is derived in Section 4.2.2 and we are going to use $\mathfrak{I}_{11}$ and the unitarity equation, Eqn. 4.14 to obtain Eqn. 5.2. The coupled channel unitarity equation for $\pi\pi \rightarrow \pi\pi$ reads:

$$\mathrm{Im}\,\mathfrak{I}_{11} = \rho_1 |\mathfrak{I}_{11}|^2 + \rho_2 |\mathfrak{I}_{12}|^2$$

$$\Rightarrow \quad \rho_2 |\mathfrak{I}_{12}|^2 = \mathrm{Im}\,\mathfrak{I}_{11} - \rho_1 |\mathfrak{I}_{11}|^2$$

with

$$\rho_1 |\mathfrak{I}_{11}|^2 = \frac{1 + \eta_{11}^2 - 2\eta_{11}\cos 2\delta_{11}}{4\rho_1}$$

and

$$\mathrm{Im}\,\mathfrak{I}_{11} = \frac{1 - \eta_{11}\cos 2\delta_{11}}{2\rho_1}$$

$$\Rightarrow \quad \rho_2 |\mathfrak{I}_{12}|^2 = \frac{1 - \eta_{11}^2}{4\rho_1}$$

$$\Rightarrow \quad |\mathfrak{I}_{12}|^2 = \frac{1 - \eta_{11}^2}{4\rho_1\rho_2}$$

$$\Rightarrow \quad \mathfrak{I}_{12} = \frac{\sqrt{(1 - \eta_{11}^2)}\, e^{i\phi_{12}}}{2\sqrt{\rho_1\rho_2}}$$

APPENDIX C

The Jost Function

C.I Introduction

Let's consider the diagonal S-matrix elements in the K-matrix formalism which are given by

$$S_{11} = 1 + 2i\rho_1 \mathcal{T}_{11}$$

$$= \frac{1 + i\rho_1 K_{11} - i\rho_2 K_{22} + \rho_1\rho_2(K_{11}K_{22} - K_{12}^2)}{1 - i\rho_1 K_{11} - i\rho_2 K_{22} - \rho_1\rho_2(K_{11}K_{22} - K_{12}^2)} \qquad (C.1)$$

and

$$S_{22} = \frac{1 - i\rho_1 K_{11} + i\rho_2 K_{22} + \rho_1\rho_2(K_{11}K_{22} - K_{12}^2)}{1 - i\rho_1 K_{11} - i\rho_2 K_{22} - \rho_1\rho_2(K_{11}K_{22} - K_{12}^2)} \qquad (C.2)$$

One observes from Eqns. C.1 and C.2 that the signs of ρ_1 and ρ_2 in the numerators are opposite to those of the ρ_1 and ρ_2 in the denominators. One can therefore express S_{11} and S_{22} as ratios of a function of ρ_1 and ρ_2. Such function is known as the Jost function, ϕ, which is defined as (cf. Eqn. 6.4)

$$\phi(\rho_1,\rho_2) = d(s)[1 - i\rho_1 K_{11} - i\rho_2 K_{22} - \rho_1\rho_2(K_{11}K_{22} - K_{12}^2)]$$

where d(s) is some arbitrary real function. Hence

$$S_{11} = \frac{\phi(-\rho_1,\rho_2)}{\phi(\rho_1,\rho_2)} \qquad (C.3)$$

and

$$S_{22} = \frac{\phi(\rho_1,-\rho_2)}{\phi(\rho_1,\rho_2)} \qquad (C.4)$$

The d(s) function has to be real because the imaginary signs in the S- or $\mathcal{J}$- matrix are attached only to the threshold factors ρ_1 and ρ_2 which are physical quantities. Furthermore, d(s) is an arbitrary function because it is always cancelled in the S- and $\mathcal{J}$- matrix elements. We next demonstrate that this is indeed the case. We proceed with the proof by defining

$$\psi_+ = [\phi(\rho_1,\rho_2) + \phi(\rho_1,-\rho_2)]/2$$

$$= d(s)(1 - i\rho_1 K_{11})$$

and

$$\psi_- = [\phi(\rho_1,\rho_2) - \phi(\rho_1,-\rho_2)]/(2\rho_2)$$

$$= d(s)(-iK_{22} - \rho_1 \det K)$$

$$\Rightarrow \quad K_{11} = \frac{-\operatorname{Im}\psi_+}{\rho_1 \operatorname{Re}\psi_+} \tag{C.5}$$

$$K_{22} = \frac{-\operatorname{Im}\psi_-}{\operatorname{Re}\psi_+} \tag{C.6}$$

$$\det K = \frac{-\operatorname{Re}\psi_-}{\rho_1 \operatorname{Re}\psi_+} \tag{C.7}$$

and

$$K_{12} = +\sqrt{K_{11}K_{22} - \det K} \tag{C.8}$$

Since $\operatorname{Re}\psi_+ = d(s)$ and the denominators of the S- or $\mathcal{J}$- matrix elements are given by $\phi(\rho_1,\rho_2)/d(s)$, we see immediately that the S- or $\mathcal{J}$- matrix can be written as functions of $\phi(\pm\rho_1,\pm\rho_2)/d(s)$. Hence the function d(s) never enters any physical quantities and is therefore arbitrary.

C.II Separation of resonance and background in S-matrix

The prime virtue of the ϕ-representation is that the numerator of the S-matrix elements are related to their common denominator. It is natural to maintain this property in separating resonance and background effects by expressing ϕ as a product;

$$\phi = \phi^r \phi^b \qquad (C.9)$$

Eqns. C.3-4 imply that the diagonal S-matrix elements will also be factorized. We illustrate this below by considering a single pole situation, say at $k_2 = k_A$, i.e.

$$\phi = (k_2 - k_A)e^{-i\delta_b} \qquad (C.10)$$

where $k_2 = \rho_2(E/2)$. Substituting Eqns. C.10 into C.3 we get

$$S_{11} = \frac{-(k_2 + k_A^*)}{(k_2 - k_A)} e^{2i\delta_b} \qquad (C.11)$$

Note that the identity

$$\phi(-\rho_1, \rho_2) = \phi^*(\rho_1^*, -\rho_2^*)$$

has been used to obtain the above expression. We can generalise Eqn. C.10 to multi-pole situations and express ϕ as product of zeros and an exponential function as background. Eqn. 6.5 in Section 6.1.1 is therefore a generalization of Eqn. C.10 with three S-matrix poles. There is no problem in writing the zero terms as $(1 - k_2/k_{2A})$ etc instead of $k_2 - k_A$ as in Eqn. C.10. The complex k_2 factor in $k_2(1 - k_2/k_{2A})$ can be absorbed into the exponential background leading to the simple form of Eqn. 6.5.

APPENDIX D

Derivation of SU(3) couplings

To obtain the SU(3) couplings in Table 6.5 we use the SU(3) isoscalar factors given in Ref. 169 by making the following identifications;

$1 \to 8 \times 8$

$$(NK - \Xi K)/2 \to (K\bar{K})/\sqrt{2}$$

$$(\sqrt{3/8})(\Sigma\pi) \to (\sqrt{3/8})(\pi\pi)$$

$$-(\Lambda\eta)/\sqrt{8} \to -(\eta_8\eta_8)/\sqrt{8}$$

$8_1 \to 8 \times 8$

$$(NK - \Xi K)/\sqrt{10} \to (K\bar{K})/\sqrt{5}$$

$$-(\sqrt{3/5})(\Sigma\pi) \to -(\sqrt{3/5})(\pi\pi)$$

$$-(\Lambda\eta)/\sqrt{5} \to -(\eta_8\eta_8)/\sqrt{5} \qquad \text{(D.1)}$$

$$\varepsilon_8 = (\sqrt{2/3})\varepsilon_1 + \varepsilon_8/\sqrt{3}$$
$$= (u\bar{u} + d\bar{d})/\sqrt{2}$$

$$\varepsilon_s = \varepsilon_1/\sqrt{3} - (\sqrt{2/3})\varepsilon_8$$
$$= s\bar{s} \qquad \text{(D.2)}$$

Let the amplitude for $\varepsilon_1 \to P_i P_j$ be α, $\varepsilon_8 \to P_i P_j$ be β (P stands for pseudoscalar) we then have from (D.1) and (D.2) the following amplitudes;

$$\begin{aligned}
\varepsilon_{ns} &\to \pi\pi && (\sqrt{2/3})(\sqrt{3/8})\alpha - (1/\sqrt{3})(\sqrt{3/5})\beta \\
\varepsilon_{ns} &\to K\bar{K} && (\sqrt{2/3})(1/\sqrt{2})\alpha + (1/\sqrt{3})(1/\sqrt{5})\beta \\
\varepsilon_{ns} &\to \eta_8\eta_8 && -(\sqrt{2/3})(1/\sqrt{8})\alpha - (1/\sqrt{3})(1/\sqrt{5})\beta \\
\varepsilon_{s} &\to \pi\pi && (1/\sqrt{3})(\sqrt{3/8})\alpha + (\sqrt{2/3})(\sqrt{3/5})\beta \\
\varepsilon_{s} &\to K\bar{K} && (1/\sqrt{3})(1/\sqrt{2})\alpha - (\sqrt{2/3})(1/\sqrt{5})\beta \\
\varepsilon_{s} &\to \eta_8\eta_8 && -(1/\sqrt{3})(1/\sqrt{8})\alpha + (\sqrt{2/3})(1/\sqrt{5})\beta \qquad \text{(D.3)}
\end{aligned}$$

By OZI rule $\varepsilon_s \not\to \pi\pi$

$$\Rightarrow \quad \alpha/\sqrt{8} + (\sqrt{2/5})\beta = 0$$

$$\Rightarrow \quad \alpha = -4\beta/\sqrt{5} \qquad \text{(D.4)}$$

The coupling ratios given in Table 6.5 can then be derived by substituting (D.4) into (D.3), i.e.

$\varepsilon_{ns} \to \pi\pi$	$-(3/\sqrt{5})\beta$	$\varepsilon_s \to \pi\pi$	0
$\varepsilon_{ns} \to K\bar{K}$	$-(3/\sqrt{15})\beta$	$\varepsilon_s \to K\bar{K}$	$-(\sqrt{6/5})\beta$
$\varepsilon_{ns} \to \eta_8\eta_8$	$(1/\sqrt{15})\beta$	$\varepsilon_s \to \eta_8\eta_8$	$(\sqrt{8/15})\beta$

APPENDIX E

The P-matrix

The P-matrix was first introduced by Jaffe and Low [140] as a link between the discrete states of the quark model and physical scattering states. In a simple potential model, the poles of the P-matrix correspond to the bound states of the system i.e. their wavefunctions vanish at the boundary. In general, the P-matrix is simply related to the S-matrix (cf. Eqn. 2.3 in Ref. 140) given by Eqn. E.1. To search for the P-matrix poles in our amplitudes we need to express the P-matrix denominator, Δ_p, in terms of our parametrizations, the K-matrix in particular. Let us first express Δ_p in terms of the S-matrix. From Eqn. 2.3 in Ref. 104 we have

$$S = -e^{-ikb}\frac{1 - (i/\sqrt{k})P(1/\sqrt{k})}{1 + (i/\sqrt{k})P(1/\sqrt{k})}e^{-ikb} \qquad (E.1)$$

i.e.

$$-i\left[1 + e^{ikb}Se^{ikb}\right]\left[1 - e^{ikb}Se^{ikb}\right]^{-1} = (1/\sqrt{k})P(1/\sqrt{k}) \qquad (E.2)$$

For 2 coupled channel, e^{ikb} is a 2x2 diagonal matrix with elements e^{ik_ib} ($k_i = \sqrt{E^2/4 - m_i^2}$, $i = 1, 2$). The denominator Δ_p depends only on the determinant of the inverse matrix $(1 - e^{ikb}Se^{ikb})^{-1}$ in Eqn. E.2 which is given by

$$1 - e^{2ik_1b}S_{11} - e^{2ik_2b}S_{22} + e^{2ik_1b}e^{2ik_2b}(S_{11}S_{22} - S_{12}^2) \qquad (E.3)$$

In general, the S-matrix can be written as

$$S = \begin{bmatrix} \eta e^{2i\delta_1} & i\sqrt{(1-\eta^2)}e^{i(\delta_1+\delta_2)} \\ i\sqrt{(1-\eta^2)}e^{i(\delta_1+\delta_2)} & \eta e^{2i\delta_2} \end{bmatrix} \qquad (E.4)$$

using $\underset{\sim}{S} = \underset{\sim}{I} + 2i\sqrt{\underset{\sim}{\rho}}\,\underset{\sim}{J}\,\sqrt{\underset{\sim}{\rho}}$.

Substituting the S-matrix elements in Eqn. E.4 into Eqn. E.3 we obtain

$$\Delta_p \propto 1 - e^{2ik_1b}\eta e^{2i\delta_1} - e^{2ik_2b}\eta e^{2i\delta_2} + e^{2ik_1b}e^{2ik_2b}e^{2i\delta_1}e^{2i\delta_2}$$

$$\propto e^{-i(k_1b+\delta_1)}e^{-i(k_2b+\delta_2)} - \eta e^{i(k_1b+\delta_1)}e^{-i(k_2b+\delta_2)}$$

$$-\eta e^{-i(k_1b+\delta_1)}e^{i(k_2b+\delta_2)} + e^{i(k_1b+\delta_1)}e^{i(k_2b+\delta_2)}$$

$$\propto \cos(k_1b+\delta_1+k_2b+\delta_2) - \eta\cos(k_1b+\delta_1-k_2b-\delta_2) \qquad \text{(E.5)}$$

which is just Eqn. 4.5 in Ref. 104.

From $S_{11} = \eta e^{2i\delta_1}$ $\qquad$ $S_{22} = \eta e^{2i\delta_2}$

$$\Rightarrow \quad \frac{S_{11}}{S_{22}^*} = e^{2i(\delta_1+\delta_2)}$$

Using the K-matrix expressions for S_{11} & S_{22} given by Eqns. C.1-2 in Appendix C we have for $s > 4m_K^2$ (i.e. k_i , ρ_i ; i = 1, 2 are all real)

$$\frac{S_{11}}{S_{22}^*} = \frac{1 + i\rho_1K_{11} + i\rho_2K_{22} - \rho_1\rho_2\det K}{1 - i\rho_1K_{11} - i\rho_2K_{22} - \rho_1\rho_2\det K} = e^{2i(\delta_1+\delta_2)}$$

Either directly from Eqn. E.3 or by substituting Eqns. C.1-2 and Eqn. E.6 into Eqn. E.5 we obtain

$$\Delta_p \propto 1 - e^{2ik_1b}\,\frac{1 + i\rho_1K_{11} - i\rho_2K_{22} + \rho_1\rho_2\det K}{\text{Den}}$$

$$- e^{2ik_2b}\,\frac{1 - i\rho_1K_{11} + i\rho_2K_{22} + \rho_1\rho_2\det K}{\text{Den}}$$

$$+ e^{2ik_1b}e^{2ik_2b}\,\frac{1 + i\rho_1K_{11} + i\rho_2K_{22} - \rho_1\rho_2\det K}{\text{Den}}$$

where $\text{Den} = 1-i\rho_1K_{11}-i\rho_2K_{22}-\rho_1\rho_2\det K$ is the common S-matrix denominator. Since from Eqn. E.2 we observe that the numerator of the P-matrix depends also on the S-matrix elements, we can therefore factor out the common S-matrix denominator Den to obtain

$$\Delta_p \propto e^{-ik_1b}e^{-ik_2b}\,(1 - i\rho_1K_{11} - i\rho_2K_{22} - \rho_1\rho_2\det K)$$
$$- e^{ik_1b}e^{-ik_2b}\,(1 + i\rho_1K_{11} - i\rho_2K_{22} + \rho_1\rho_2\det K)$$
$$- e^{-ik_1b}e^{ik_2b}\,(1 - i\rho_1K_{11} + i\rho_2K_{22} + \rho_1\rho_2\det K)$$
$$+ e^{ik_1b}e^{ik_2b}\,(1 + i\rho_1K_{11} + i\rho_2K_{22} - \rho_1\rho_2\det K) \qquad (E.7)$$

Grouping the coefficients in front of 1, ρ_1K_{11} , ρ_2K_{22} and $\rho_1\rho_2\det K$ together we arrive at the expression

$$\Delta_p \propto \sin(k_1b)\sin(k_2b) + \cos(k_1b)\sin(k_2b)\rho_1K_{11}$$
$$+ \cos(k_1b)\sin(k_2b)\rho_2K_{22} + \cos(k_1b)\cos(k_2b)\rho_1\rho_2\det K \qquad (E.8)$$

In the case of $4m_1^2 < s < 4m_2^2$, k_1 and ρ_1 are real but k_2 and ρ_2 are imaginary (i.e. $k_2 = i|k_2|$ and $\rho_2 = i|\rho_2|$) we then have

$$\Delta_p \propto e^{-ik_1b}e^{k_2b}\,(1 - i\rho_1K_{11} + |\rho_2|K_{22} - i\rho_1|\rho_2|\det K)$$
$$- e^{ik_1b}e^{k_2b}\,(1 + i\rho_1K_{11} + |\rho_2|K_{22} + i\rho_1|\rho_2|\det K)$$
$$- e^{-ik_1b}e^{-k_2b}\,(1 - i\rho_1K_{11} - |\rho_2|K_{22} + i\rho_1|\rho_2|\det K)$$
$$+ e^{ik_1b}e^{-k_2b}\,(1 + i\rho_1K_{11} - |\rho_2|K_{22} - i\rho_1|\rho_2|\det K) \qquad (E.9)$$

Grouping the coefficients in front of 1, ρ_1K_{11} , $|\rho_2|K_{22}$ and $\rho_1|\rho_2|\det K$ we obtain

$$\Delta_p \propto \sin(k_1b)\sinh(|k_2|b) + \cos(k_1b)\sinh(|k_2|b)\rho_1K_{11}$$
$$+ \cosh(|k_2|b)\sin(k_1b)|\rho_2|K_{22}$$
$$+ \cos(k_1b)\cosh(|k_2|b)\rho_1|\rho_2|\det K \qquad (E.10)$$

The pole positions given in Table 7.1 correspond to the zeros of Eqns. E.8,10 with b = 7 GeV^{-1}.

References

[1] W.Heisenberg - Zeit. fur Phys. 77, 1, (1932).

[2] M.Gell-Mann and Y.Ne'eman - 'The Eightfold Way', Benjamin, (1964).

[3] M.Gell-Mann - Phys. Lett. 8, 214, (1964).
G.Zweig - CERN report 8182/TH 401, (1964), (unpublished).
R.H.Dalitz - Proc. Oxford Conf. on Elementary Particles (1965), eds. R.G.Moorhouse et al., Rutherford Laboratory, (1966).

[4] F.E.Close - 'An Introduction to Quarks and Partons', Academic Press, (1979).

[5] O.W.Greenberg - Phys. Rev. Lett. 13, 598, (1964).

[6] R.L.Jaffe - Phys. Rev. D15, 267, (1977).

[7] R.P.Feynman - 'Quantum Electrodynamics', Benjamin, (1961).

[8] C.N.Yang and R.Mills - Phys. Rev. 96, 191, (1954).

[9] H.D.Politzer - Phys. Rev. 14C, 129, (1974).

[10] M.R.Pennington - Rep. on Prog. Phys. 46, 393, (1983).

[11] D.J.Gross and F.Wilczek - Phys. Rev. Lett. 30, 1354, (1973).
H.D.Politzer - Phys. Rep. 14, 129, (1974).

[12] F.Halzen and A.D.Martin - 'Quarks and Leptons', Wiley, (1984).

[13] Cheng and Li - 'Gauge Theory of Elementary Particle Physics', Oxford, (1984).

[14] N.N.Bogoliubov and O.S.Parasiuk - Acta. Math. 97, 227, (1957).
K.Hepp - Comm. Math. Phys. 2, 301, (1966).
W.Zimmermann - 'Lectures on Elementary Particles and Quantum Field Theory', Proc. 1970 Brandeis Summer Institute, editors: S.Deser et at., MIT Press.

[15] E.C.G.Stueckelberg and A.Peterman
- Helv. Phys. Acta, 26, 499, (1953).

[16] G.t'Hooft - Nucl. Phys. B33, 173, (1971); ibid B35, 167, (1971).

[17] J.D.Bjorken - Proc. 3rd Int. Symp. on Electron + Photon Interactions, Stanford.
R.P.Feynman - Phys. Rev. Lett. 23, 1415, (1969).
J.D.Bjorken and E.A.Paschos - Phys. Rev. D10, 2973, (1969).

[18] R.P.Feynman - 'Photon-Hadron Interaction', Benjamin. (1972).

[19] C.G.,Jr.Callan and D.Gross - Phys. Rev. Lett. 22, 156, (1969).

[20] J.D.Bjorken - Phys. Rev. 179, 1547, (1969).

[21] H.Fritzsch and M.Gell-Mann - Proc. of XVI Int. Conf. on High Energy Physics, Fermilab (1972), vol.2, p.135.
H.Fritzsch and P.Minkowski - Nuovo Cimento. 30A, 393, (1975).
P.G.O.Freund and Y.Nambu - Phys. Rev. Lett. 34, 1645, (1975).
R.Jaffe and K.Johnson - Phys. Lett. 60B, 201, (1976).
J.Kogut, D.Sinclair and L.Susskind
- Nucl. Phys. B114, 199, (1976).
J.Bjorken - SLAC Summer Institute on Particle Physics, SLAC - PUB - 2372, (1979).

[22] S.R.Sharpe - Proc. 6th Int. Conf. on Elementary Particle Physics, Vanderbilt University (1984), editors: R.S.Panvini and G.B.Word, AIP, New York (1984).

[23] J.F.Donoghue, K.Johnson, B.A.Li - Phys. Lett. 99B, 416, (1981).

[24] C.N.Yang - Phys. Rev. 77, 242, (1950).

[25] T.D.Lee - Phys. Lett. D19, 1802, (1979).
F.E.Close and R.Horgan - Nucl. Phys. B164, 413, (1980).
F.E.Close and S.Monaghan - Phys. Rev. D23, 2098, (1981).

[26] T.Barnes - Z. Phys. C10, 275, (1981).
J.Cornwall and A.Soni - Phys. Lett. 120B, 431, (1983).

[27] B.Berg - preprint; CERN TH 3978, (1984).
M.Creutz - 'Quarks, Gluons and Lattices and Monte Carlo Simulations', World Scientific, Singapore, (1983).

[28] M.Teper - Int. Europhysics Conf. on High Energy Physics, Brighton, editors: J.Guy and C.Costain, (1983).
Preprint; LAPP - TH - 91 (1983).
K.Ishikawa, A.Sato, G.Schierholz and M.Teper
- Z. Phys. C21, 167, (1983).

[29] R.P.Feynman and A.R.Hibbs - 'Quantum Mechanics and Path Integrals', McGraw-Hill, (1965).

[30] K.Wilson - Phys. Rev. D10, 2445, (1974).

[31] N.Isgur and J.Paton - Phys. Lett. 124B, 247, (1983).

[32] M.A.Shifman, A.I.Vainshtein and VI.Zakharov - Nucl. Phys. B147, 385, 448, (1979).

[33] V.A.Novikov, M.A.Shifman, A.I.Vainshtein and V.I.Zakharov - Nucl. Phys. B191, 301, (1981).

[34] K.G.Wilson - Phys. Rev. 179, 1499, (1969).

[35] M.A.Shifman, A.I.Vainshtein and V.I.Zakharov - Nucl. Phys. B165, 45, (1980).

[36] S.Narison - preprints; CERN TH 3989/84, PM 85/2.

[37] M.A.Shifman - Z. Phys. C9, 347, (1981).

[38] E.Noether - Nachr. Kgl. Geo. Wiss Gottinger 235, (1918).

[39] S.L.Adler - Phys. Rev. 177, 2426, (1969).
J.S.Bell and R.Jackiw - Nuovo Cimento. 60A, 47, (1969).

[40] R.Crewther - Phys. Rev. Lett. 28, 1421, (72).
M.Chanowitz, and J.Ellis - Phys. Lett. 40B, 397, (1972).
J.Collins, A.Duncan and S.Joglekar - Phys. Rev. D16, 438, (1977).

[41] S.Coleman - 'New Phenomena in Subnuclear Physics' - Part A, editor: Zichichi, Plenum, (1977).

[42] E.Witten - Nucl. Phys. B156, 269, (1979).
- and references therein.

[43] F.E.Close - Int. Europhysics Conf. on High Energy Physics, Brighton, editors: J.Guy and C.Costain, (1983) - and references therein.

[44] I.I.Balitsky, D.Dyakanov and A.Yung - Phys. Lett. 112B, 71, (1982).
J.Gowaerts, F.de Viron, J.Pestieau and J.Weyers - Louvain report, (1983).

[45] T.Barnes and F.E.Close and F.de Viron - Nucl. Phys. B224, 241, (1983).

[46] M.Chanowitz and S.Sharpe - Nucl. Phys. B222, 211, (1983).

[47] M.R.Pennington - 'A New ABC of QCD', Lecture delievered at the School for Young High Energy Physicists, Rutherford Appleton Laboratory. (1983).

[48] G.Altarelli and G.Parisi - Nucl. Phys. B126, 298, (1977).

[49] T.Regge - Nuovo Cimento. 14, 951, (1959).
P.D.B.Collins - 'Regge Theory and High Energy Physics', Cambridge University Press, (1977).
P.D.B.Collins and A.D.Martin - 'Hadron Interactions', Adam Hilger.

[50] P.C.Bosetti et al. - Nucl. Phys. B142, 1, (1978).

[51] J.F.Donoghue - Proc. 1984 Yukon Advanced Study Institute, 'The Quark Structure of Matter', editors:N.Isgur, G.Karl and P.J.O'Donnel, World Scientific, Singapore.

[52] A more rational notation for mesons has recently been proposed and implemented in the latest PDG [169]. The changes impinge considerably on the states of present concern. Since this thesis has to present a number of unfamiliar spectroscopic concepts I have adhered to the old notatons to prevent the readers having to grapple with two types of novelty at once. To re-orient to the new terminology the reader should substitute

$S(975) \rightarrow f_0(975)$ $\quad \iota(1440) \rightarrow \eta(1440)$

$\delta(980) \rightarrow a_0(980)$ $\quad \theta(1690) \rightarrow f_2(1720)$

$\varepsilon(1300) \rightarrow f_0(1300)$ $\quad f(1270) \rightarrow f_2(1270)$

[53] C.E.Carlson, J.J.Coyne, P.M.Fishbane, F.Gross and S.Meshkov - Phys. Lett. 99B, 353, (1981).

[54] M.Chanowitz - Proc. XIVth Int. Conf. on Multiparticle Dynamics at High Energies, Lake Tahoe, 1983, editors: J.F.Gunion and P.M.Yager, World Scientific.

[55] P.M.F.Fishbane and S.Meshkov - Comm. Nucl. Part. Phys. 13, 325, (1984).

[56] C.Heusch - Proc. 1984 Yukon Advanced Institute, 'The Quark Structure of Matter', editors: N.Isgur, G.Karl and P.J.O'Donnell, World Scientific.

[57] J.J.de Swart - Rev Mod. Phys. 35, 916, (1963).

[58] H.J.Lipkin - Phys. Lett. 109B, 326, (1982).

[59] F.J.Gilman - Phys. Rev. 4C, 95, (1972).
M.Gourdin - Phys. Rev. 11C, 29, (1974).

[60] S.Okubo - Phys. Lett. 5, 163, (1963).
V.Zweig - CERN report No. 8419/TH 412, (unpublished).
J.Iizuka - Prog. Theor. Phys. Supplement No. 37-38, p.21, (1966).

[61] S.J.Lindenbaum - Int. Europhysics Conf. on High Energy Physics, Brighton, editors: J.Guy and C.Costain, (1983).
- preprint; BNL 36738, (1984).

[62] D.Robson - Nucl. Phys. B130, 328, (1977).

[63] J.Perrier - preprint; SLAC-PUB-3436, (1984).

[64] K.Konigsmann - preprint; DESY 86-009, (1986).

[65] P.B.Mackenzie and G.P.Lepage
- Phys. Rev. Lett. 47, 1244, (1981).
S.J.Brodsky, G.P.Lepage and P.B.Mackenzie
- Phys. Rev. D28, 228, (1983).

[66] F.E.Low - Phys. Rev. D12, 163, (1975).
S.Nussinov - Phys. Rev. Lett. 34, 1286, (1975).
- Phys. Rev. D14, 246, (1976).
D.M.Chew and G.F.Chew - Phys. Lett. 53B, 191, (1974).
D.Robson - Nucl. Phys. B130, 328, (1977).

[67] R.Waldi, K.R.Schubert and K.Winter - Z. Phys. C18, 301, (1983).

[68] A.Breakstone et al. - Z. Phys. C27, 205, (1985).

[69] T.Akesson et al. - Nucl. Phys. B264, 154, (1986).

[70] Etkin et al. - Phys. Rev. Lett. 49, 1620, (1982).

[71] F.Caruso, A.F.S.Santoro, M.H.G.Souza and C.O.Escobar - Phys. Rev. D30, 69, (1984).

[72] A.D.Martin and M.R.Pennington - Phys. Lett. 86B, 93, (1979). - Nucl. Phys. B169, 216, (1980). B.R.Martin and D.Morgan - Nucl. Phys. B176, 355, (1980).

[73] S.Ono and O.Pene - Z. Phys. C21, 109, (1983).

[74] B.A.Li and K.F.Liu - Phys. Rev. D28, 1636, (1983).

[75] B.A.Li and K.F.Liu - Phys. Lett. 118B, 435, (1982). - Phys. Lett. 124B, 550(E), (1983).

[76] R.L.Jaffe - Phys. Rev. D15, 281, (1977).

[77] S.D.Drell and T.M.Yan - Phys. Rev. Lett. 25, 316, (1970).

[78] J.Weinstein and N.Isgur - Phys. Rev. Lett. 48, 659, (1982). - Phys. Rev. D27, 588, (1983).

[79] G.Karl, W.Roberts and N.Zagury - Phys. Lett. 149B, 403, (1984).

[80] H.Gomm - Phys. Rev. D30, 1120, (1984).

[81] G.Altarelli - Phys. Rep. 81, 1, (1982).

[82] D.Hitlin - Proc. 1983 Int. Symp. on Lepton and Photon Interactions at High Energies, editors: D.G.Cassel and D.L.Kreinick, Cornell.

[83] C.Edwards et al. - Phys. Rev. Lett. 40, 458, (1982).

[84] K.F.Einsweiler - Ph.D thesis, SLAC-278, (1984).

[85] D.Scharre et al. - Phys. Lett. 97B, 329, (1980). J.D.Richman - Proc. of XXth Rencontre de Moriond, editor: J.Tran Thanh Van, Editions Frontieres, (1985).

[86] J.E.Augustin et al. - Physica Scripta 23, 623, (1981).

[87] G.S.Abrams - Phys. Rev. Lett. 43, 477, 481, (1979). W.Davies-White et al. - Nucl. Instr. Methods 160, 227, (1979).

[88] D.Bernstein et al. - Nucl. Instr. Methods 226, 301, (1984). J.Roehrig et al. - Nucl. Instr. Methods 226, 319, (1984).

[89] M.Oreglia et al. - Phys. Rev. D25, 2259, (1982).
E.D.Bloom and C.W.Peck - Ann. Rev. Nucl. Part. Sci. 33, 143, (1983).

[90] C.Edwards et al. - Phys. Rev. Lett. 49, 259, (1982).

[91] P.Baillon et al. - Nuovo Cimento. A50, 393, (1967).
- Jour. Phys. C3, 86, (1982).

[92] S.U.Chung et al. - Phys. Rev. Lett. 55, 779, (1985).
A.Ando et al. - KEK-preprint; 85-15.

[93] C.Dionisi et al. - Nucl. Phys. B169, 1, (1980).
T.A.Armstrong et al. - Phys. Lett. 146B, 273, (1984).

[94] M.Chanowitz and S.R.Sharpe - Phys. Rev. 132B, 413, (1983).

[95] C.E.Carlson, T.H.Hansson and C.Peterson
- Phys. Rev. D27, 2167, (1983).
- Phys. Rev. D30, 1594, (1984).

[96] B.Berg and A.Billoire - Nucl. Phys. B221, 109, (1983).

[97] K.Ishikawa, M.Teper and G.Schierholz
- Phys. Lett. 116B, 429, (1982).
- Z. Phys. C21, 167, (1983).

[98] M.Chanowitz - Phys. Rev. Lett. 46, 981, (1981).

[99] N.Stanton et al. - Phys. Rev. Lett. 42, 346, (1979).

[100] J.D.Richman - Ph.D thesis, CALT - 68 - 1231, (1985).

[101] K.Ishikawa - Phys. Rev. Lett. 46, 978, (1981).

[102] For a general discussion see Ref. 54. See also Ref. 98.

[103] W.F.Palmer and S.S.Pinsky - Phys. Rev. D27, 2219, (1983).

[104] J.M.Cornwall and A.Soni
- Phys. Rev. D32, 764, (1985).

[105] M.Frank, N.Isgur, P.J.O'Donnel, and J.Weinstein
- Phys. Lett. 158B, 442, (1985).
- Phys. Rev. D32, 2971, (1985).

[106] M.Tanimoto - Phys. Lett. 116B, 198, (1982).

[107] J.F.Donoghue and H.Gomm - Phys. Lett. 121B, 49, (1983).

[108] J.F.Donoghue - Phys. Rev. D30, 114, (1984).

[109] C.E.Carlson and T.H.Hansson - Nucl. Phys. B199, 441, (1981).

[110] J.L.Rosner - Phys. Rev. D27, 1101, (1983).

[111] N.Isgur - Phys. Rev. D13, 122, (1976).

[112] W.F.Palmer, S.S.Pinsky and C.Bender
- Phys. Rev. D30, 1002, (1984).

[113] M.Frank and P.J.O'Donnell - Phys. Rev. D29, 921, (1984).
- Phys. Lett. 144B, 451, (1984).

[114] H.J.Lipkin and I.Cohen - Phys. Lett. 135B, 215, (1984).

[115] H.Goldberg - Phys. Rev. Lett. 44, 363, (1980).
- Phys. Rev. D22, 2286, (1980).
K.Senba and M.Tanimoto - Phys. Lett. 106B, 215, (1981).

[116] G.Veneziano - Nucl. Phys. B159, 213, (1979).

[117] R.Sinha - preprint; Rochester, DOE/ER/13065-431, (1986).

[118] J.Schechter and Y.Ueda - Phys. Rev. D3, 176, (1971).
- Phys. Rev. D3, 2874, (1971).
- and references therein.

[119] C.Rosenzweig, J.Schechter and G.Trahern
- Phys. Rev. D21, 3388, (1980).
P.DiVecchia and G.Veneziano - Nucl. Phys. B171, 253, (1980).
E.Witten - Ann. Phys. 128, 363, (1980).
P.Nath and R.Arnowitt - Phys. Rev. D23, 473, (1981).

[120] C.Rosenzweig, A.Salomone, and J.Schechter
- Phys. Rev. D24, 2545, (1981).

[121] C.Rosenzweig, A.Salomone, and J.Schechter
- Nucl. Phys. B206, 12, (1982).

[122] N.Wermes - Proc. 5th Int. Conf. on Phys. in Collision, Autun, France, 1985; SLAC-PUB-3730, (1985).

[123] J.L.Rosner and S.F.Tuan - Phys. Rev. D27, 1544, (1983).

[124] H.J.Schnitzer - Nucl. Phys. B207, 131, (1982).
S.Ono - Phys. Rev. D28, 558, (1983).

[125] J.Schechter - Phys. Rev. D21, 3393, (1980).

[126] J.Schechter - Phys. Rev. D27, 1109, (1983).

[127] K.F.Einsweiler - Ph.D thesis, SLAC - 278, (1984).
- Proc. Int. Europhysics Conf. on High Energy Physics, Brighton, editors: J.Guy and C.Costain, (1983).

[128] S.Godfrey, R.Kokoski and N.Isgur
- Phys. Lett. 141B, 439, (1984).

[129] B.F.L.Ward - Phys. Rev. D31, 2649, (1985).

[130] A.Le Yaouanc, L.Oliver, O.Pene and J.C.Raynal
- Z. Phys. C28, 309, (1985).

[131] See Ref.78 and Section 3.4.1.2.

[132] F.Biron et al. - Nuovo Cimento. 80A, 363, (1984).

[133] S.S.Gershtein et al. - Z. Phys. C24, 305, (1984).

[134] G.Mennessier, S.Narison and N.Paver - preprint; PM/85 - 7.

[135] V.A.Novikov, M.A.Shifman, A.I.Vainshtein and V.I.Zakharov
- Nucl. Phys. B165, 55, (1980).

[136] J.Ellis and J.Lanik - Phys. Lett. 150B, 289, (1985).

[137] S.R.Sharpe, M.R.Pennington and R.L.Jaffe
- Phys. Rev. D30, 1013, (1984).

[138] T.Barnes, F.E.Close and S.Monaghan
- Phys. Lett. 110B, 159, (1982).

[139] S.D.Protopopescu et al. - Phys. Rev. D7, 1279, (1973).
G.Mennessier - Z. Phys. C16, 241, (1983).

[140] R.L.Jaffe and F.E.Low - Phys. Rev. D19, 2105, (1979).

[141] N.A.Tornqvist - Phys. Rev. Lett. 49, 624, (1982).

[142] M.Voloshin and V.Zakharov - Phys. Rev. Lett. 45, 688, (1980).
V.Novikov and M.Shifman - Z. Phys. C8, 43, (1981).

[143] T.Barnes - Phys. Lett. 165B, 434, (1985).

[144] Some key results of the present analysis were reported in;
K.L.Au, D.Morgan and M.R.Pennington
- Phys. Lett. 167B, 229, (1986).

[145] G.F.Chew and F.E.Low - Phys. Rev. 113, 1640, (1959).

[146] C.J.Goebel - Phys. Rev. Lett. 1, 337, (1958).

[147] D.Morgan and M.R.Pennington - Phys. Lett. 137B, 411, (1984).

[148] D.H.Perkins - 'Introduction to High Enegy Physics', Addison-Wesley, (1982).

[149] K.M.Watson - Phys. Rev. 88, 1163, (1952).

[150] I.J.R.Aitchison - Nucl. Phys. A189, 417, (1972).

[151] S.L.Adler - Phys. Rev. 139, B1638, (1965).

[152] B.R.Martin, D.Morgan and G.Shaw - 'Pion-Pion Interactions in Particle Physics', Academic Press, (1976).

[153] Y.Nambu - Phys. Rev. Lett. 4, 380, (1960).
M.Gell-Mann and M.Levy - Nuovo Cimento. 16, 705, (1960).

[154] In the applications to follow, we need to apply Eqn. 4.22 below some of the thresholds, specifically below $K\bar{K}$ threshold for the two channel ($\pi\pi$ and $K\bar{K}$) case that we actually consider. The necessary analytic continuations are straightforwardly (and standardly) accomplished by substituting $i\rho_2$ by $-|\rho_2|$ in the explicit formulae for T_{11} and T_{12} (cf. Eqn. 4.34).

[155] R.Omnes - Nuovo Cimento. 8, 316, (1958).
G.Barton - 'Introduction to Dispersion Techniques in Field Theory', Benjamin, New York, (1965).

[156] For a recent example see:
L.M.Barkov et al. - Nucl. Phys. B256, 365, (1985).

[157] One can allow independent Adler zeros in K_{11} , K_{12} , K_{22} , but this has very little effect on our fits.

[158] G.Grayer et al. - Nucl. Phys. B75, 189, (1974).

[159] W.Ochs - Ph.D thesis submitted to Univ. of Munich, (1974).

[160] S.Protopopescu et al. - Phys. Rev. D7, 1280, (1973).

[161] N.M.Cason et al. - Phys. Rev. D28, 1586, (1983).

[162] A.D.Martin and M.R.Pennington - Ann. Phys. (NY), 114, 1, (1978).

[163] H.Becker et al. - Nucl. Phys. B151, 46, (1979).

[164] D.Cohen et al. - Phys. Rev. D22, 2595, (1980).

[165] W.Wetzel et al. - Nucl. Phys. B115, 208, (1976).
V.A.Polychronakos et al. - Phys. Rev. D19, 1317, (1979).
G.Costa et al. - Nucl. Phys. B175, 402, (1980).

[166] A.Etkin et al - Phys. Rev. D28, 1786, (1982).

[167] See Ref. 166 Figs. 8,9 for a useful compilation but beware of energy shifts.

[168] M.R.Pennington and C.Schmid - unpublished, (1970). Referenced in:
M.R.Pennington and S.Protopopescu - Phys. Rev. D7, 1429, (1973).

[169] Particle Data Group, Review of Particle Properties April 1986, editors; M.Augilar-N.Benitez et al. - Phys. Lett. 170B, 1, (1986).

[170] L.Gorlich et al. - Nucl. Phys. B174, 16, (1980).

[171] D.Alde et al. - Nucl. Phys. B269, 485, (1986).

[172] M.Alston-Garnjost et al. - Phys. Lett. 36B, 152, (1971).
W.Y.Lee - Proc. 1975 Int. Symp. on Lepton and Photon Interactions at High Energies, Standord, editor; W.T.Kirk.

[173] D.M.Chew and G.F.Chew - Phys. Lett. 53B, 191, (1974).
B.R.Desai, B.C.Shen and M.Jacob
- Nucl. Phys. B142, 258, (1978).
S.N.Ganguli and D.P.Roy - Phys. Rep. 67, 201, (1980).
G.Alberi and G.Goggi - Phys. Rep. 74, 1, (1981).

[174] Such an extrapolation is natural from B phenomenology as discussed in;
M.R.Pennington - Nucl. Phys. B137, 77, (1978).

[175] M.Poppe - DESY report 86-014 (Feb, 1986).

[176] P.C.Cecil - Ph.D thesis, Cavendish Lab., Cambridge, (1984) - preprint; Rutherford RAL-T-004 (1984).

[177] See for example;
H.Harari - Proc. Roy. Soc. London. A318, 355, (1970).

[178] I.G.Halliday - Nucl. Phys. B114, 157, (1976).

[179] T.Inami and R.G.Roberts - Nucl. Phys. B93, 497, (1975).

[180] M.R.Pennington - unpublished, (1984).

[181] In Ref. 144, we quoted results for the favoured Etkin et al [166] phases, ϕ_{12} .

[182] S.L.Adler - Phys. Rev. 137, B1022, (1965).
- Phys. Rev. 139, B1638, (1965).
S.L.Adler and R.F.Dashen - 'Current Algebras and Applications to Particle Physics', Benjamin, New York, (1968).

[183] D.Morgan and M.R.Pennington - Phys. Rev. D12, 1283, (1975).

[184] L.S.Brown and R.N.Cahn - Phys. Rev. Lett. 35, 1, (1975).
T-M Yan - Phys. Rev. D22, 1652, (1980).
Y-P Kuang and T-M Yan - Phys. Rev. D24, 2874, (1981).

[185] Mark II Collab: T.M.Himel - SLAC-PUB-223, (1979).

[186] Crystal Ball Collab: M.Oreglia et al.
- Phys. Rev. Lett. 45, 959, (1980).

[187] Argus Collab: H.Albrecht et al. - Phys. Lett. 134B, 137, (1984).

[188] CLEO Collab: D.Besson et al. - Phys. Rev. D30, 1433, (1984).

[189] CUSB Collab: V.Fonseca et al. - Nucl. Phys. B242, 31, (1984).

[190] Crystal Ball Collab: D.Gelphman et al.
- Phys. Rev. Lett. D32, 2893, (1985).

[191] CLEO Collab: J.Green et al. - Phys. Rev. Lett. 49, 617, (1982).

[192] CUSB Collab: G.Mageras et al. - Phys. Lett. 118B, 453, (1982).

[193] G.Gidal - Phys. Lett. 107B, 153, (1981).

[194] MK III preliminary results on $\psi' \to \phi\pi\pi$ etc. presented at XXIth Rencontre de Moriond, March 1986 by U.Mallik.

[195] DM2 preliminary results on $\psi' \to \phi\pi\pi$ etc. presented at XXIth Rencontre de Moriond, March 1986 by A.Falvard.

[196] The preliminary DM2 results presented at Moriond in 10 MeV bins appear to be shifted by some 10 MeV from those of our other $\pi\pi$, KK channels and so have not been included in these tentative fits. By the time the final results on these ψ decays are available, hopefully such problems will have been resolved.

[197] F.Vannucci et al - Phys. Rev. D15, 1815, (1977).

[198] M.R.Pennington - unpublished, (1976).

[199] Ch.Berger et al. - Z. Phys. C26, 199, (1984).

[200] A.Courau et al. - Nucl. Phys. B271, 1, (1986).

[201] Z.Ajaltouni et al - Contribution to 1985 Kyoto Lepton-Photon symposium referenced by;
H.Kolanoski - Proc. 1985 Int. Symp. on Lepton and Photon Interactions at High Energies, editors; M.Kanuma, K.Takahashi.

[202] H.Aihara et al. - Phys. Rev. Lett. 57, 404, (1986).

[203] D.H.Lyth - Nucl. Phys. B30, 195, (1971).

[204] G.Mennessier - Z. Phys. C16, 241, (1983).

[205] For earlier discussion of objects like our $\varepsilon'(1420)$ see especially
B.Hyams et al. - Nucl. Phys. B64, 134, (1974).
W.Ochs - Ref. 159
P.Estabrooks - Phys. Rev. D19, 2678, (1979).
A.B.Wickland et al. - Phys. Rev. Lett. 45, 1469, (1980).
For further references see Ref. 169 p.194.

[206] Here ρ_2 means $\begin{bmatrix} 0 & 0 \\ 0 & \rho_2 \end{bmatrix}$ with ρ_2 defined on sheet II; if it were defined on sheet III, a minus sign would be required.

[207] References to the points displayed may be found in Ref. 169 p.184.

[208] M.Alston-Garnjost et al. - Ref. 172.
S.M.Flatte et al - Phys. Lett. 38B, 232, (1972).

[209] G.Grayer et al. - 'ππ scattering - 1973' AIP Conf. Proc. No.13, editors; P.K.Williams and V.Hagopian, (1973), p.117.

[210] S.M.Flatte et al. - Ref. 208
- Phys. Lett. 63B, 224, (1976).

[211] D.Morgan - Phys. Lett. 51B, 71, (1974).

[212] Y.Fujii and M.Fukugita - Nucl. Phys. B85, 179, (1975).

[213] A.D.Martin, E.Ozmultu and E.J.Squires
- Nucl. Phys. B121, 514, (1977).

[214] A.C.Irving, A.D.Martin and P.J.Done - Z. Phys. C10, 45, (1981).

[215] We emphasize that all through this part of our discussion it is the number of T-matrix poles (required to describe the S* region) that is in question. This is not to be confused with alternative K-pole forms that we have experimented with for fitting.

[216] A.Etkin et al - Phys. Rev. D25, 2446, (1982).

[217] See Ref. 169 p.235.

[218] M.Kato - Ann. Phys. (NY) 31, 130, (1965).
See also Ref.212.

[219] K.L.Au D.Morgan and M.R.Pennington - preprint; RAL-86-076 (DTP-86-9), 1986.

[220] The symbols S, V, K, S' refer to the internal structure.

[221] R.H.Dalitz et al. - Proc. Intern. Conf. on hypernuclear and kaon physics (MPI, Heidelberg, 1982) Report MPIH-1982-V20, editor; B.Povh, p.201.

[222] R.L.Jaffe and F.E.Low - Phys. Rev. D19, 2105, (1979).